



## The HITRAN2020 molecular spectroscopic database

I.E. Gordon, L.S. Rothman, R.J. Hargreaves, R. Hashemi, E.V. Karlovets, F.M. Skinner, E.K. Conway, C. Hill, R.V. Kochanov, Y. Tan, et al.

### ► To cite this version:

I.E. Gordon, L.S. Rothman, R.J. Hargreaves, R. Hashemi, E.V. Karlovets, et al.. The HITRAN2020 molecular spectroscopic database. *Journal of Quantitative Spectroscopy and Radiative Transfer*, 2021, pp.107949. 10.1016/j.jqsrt.2021.107949 . hal-03388954

**HAL Id: hal-03388954**

**<https://hal.science/hal-03388954>**

Submitted on 17 Nov 2021

**HAL** is a multi-disciplinary open access archive for the deposit and dissemination of scientific research documents, whether they are published or not. The documents may come from teaching and research institutions in France or abroad, or from public or private research centers.

L'archive ouverte pluridisciplinaire **HAL**, est destinée au dépôt et à la diffusion de documents scientifiques de niveau recherche, publiés ou non, émanant des établissements d'enseignement et de recherche français ou étrangers, des laboratoires publics ou privés.

# The HITRAN2020 molecular spectroscopic database

I. E. Gordon<sup>a,\*</sup>, L. S. Rothman<sup>a</sup>, R. J. Hargreaves<sup>a</sup>, R. Hashemi<sup>a</sup>, E. V. Karlovets<sup>a</sup>, F. M. Skinner<sup>a</sup>, E. K. Conway<sup>a</sup>, C. Hill<sup>b</sup>, R. V. Kochanov<sup>a,c,d</sup>, Y. Tan<sup>a,e</sup>, P. Wcislo<sup>f</sup>, A. A. Finenko<sup>a,g</sup>, K. Nelson<sup>a</sup>, P. F. Bernath<sup>h</sup>, M. Birk<sup>i</sup>, V. Boudon<sup>j</sup>, A. Campargue<sup>k</sup>, K. V. Chance<sup>a</sup>, A. Coustenis<sup>l</sup>, B. J. Drouin<sup>m</sup>, J.-M. Flaud<sup>s</sup>, R. R. Gamache<sup>o</sup>, J. T. Hodges<sup>p</sup>, D. Jacquemart<sup>q</sup>, E. J. Mlawer<sup>r</sup>, A. V. Nikitin<sup>c</sup>, V. I. Perevalov<sup>c</sup>, M. Rotger<sup>t</sup>, J. Tennyson<sup>u</sup>, G. C. Toon<sup>m</sup>, H. Tran<sup>al</sup>, V. G. Tyuterev<sup>t,d</sup>, E. M. Adkins<sup>p</sup>, A. Baker<sup>n</sup>, A. Barbe<sup>t</sup>, E. Canè<sup>w</sup>, A. G. Császár<sup>y,z</sup>, O. Egorov<sup>c</sup>, A. J. Fleisher<sup>p</sup>, H. Fleurbaey<sup>k</sup>, A. Foltynowicz<sup>aa</sup>, T. Furtenbacher<sup>y</sup>, J. J. Harrison<sup>ab,ac,ad</sup>, J.-M. Hartmann<sup>v</sup>, V.-M. Horneman<sup>ae</sup>, X. Huang<sup>af</sup>, T. Karman<sup>a</sup>, J. Karns<sup>a,au,av</sup>, S. Kassi<sup>k</sup>, I. Kleiner<sup>al</sup>, V. Kofman<sup>aq</sup>, F. Kwabia-Tchana<sup>al</sup>, T. J. Lee<sup>ag</sup>, D. A. Long<sup>p</sup>, A. A. Lukashchuk<sup>c</sup>, O. M. Lyulin<sup>c</sup>, V. Yu. Makhnev<sup>am</sup>, W. Matt<sup>a,av</sup>, S. T. Massie<sup>ah</sup>, M. Melosso<sup>x</sup>, S. N. Mikhailenko<sup>c</sup>, D. Mondelain<sup>k</sup>, H. S. P. Müller<sup>ai</sup>, O. V. Naumenko<sup>c</sup>, A. Perrin<sup>al</sup>, O. L. Polyansky<sup>u,am</sup>, E. Raddaoui<sup>q</sup>, P. L. Raston<sup>aj,ak</sup>, Z. D. Reed<sup>p</sup>, M. Rey<sup>t</sup>, C. Richard<sup>j</sup>, R. Tóbiás<sup>y</sup>, I. Sadiek<sup>aa,an</sup>, D. W. Schwenke<sup>ag</sup>, E. Starikova<sup>c</sup>, K. Sung<sup>m</sup>, F. Tamassia<sup>w</sup>, S. A. Tashkun<sup>c</sup>, J. Vander Auwera<sup>ao</sup>, I. A. Vasilenko<sup>c</sup>, A. A. Vigin<sup>ap</sup>, G. L. Villanueva<sup>aq</sup>, B. Vispoel<sup>as,ar,o</sup>, G. Wagner<sup>i</sup>, A. Yachmenev<sup>at</sup>, S. N. Yurchenko<sup>u</sup>

<sup>a</sup>Center for Astrophysics |Harvard & Smithsonian, Atomic and Molecular Physics Division, Cambridge MA 02138, USA

<sup>b</sup>Nuclear Data Section, International Atomic Energy Agency, Vienna International Centre, PO Box 100, A-1400 Vienna, Austria

<sup>c</sup>V.E. Zuev Institute of Atmospheric Optics, Laboratory of Theoretical Spectroscopy, Russian Academy of Sciences, 634055 Tomsk, Russia

<sup>d</sup>QUAMER laboratory, Tomsk State University, 634050 Tomsk, Russia

<sup>e</sup>Hefei National Laboratory for Physical Science at Microscale, University of Science and Technology of China, Hefei, China

<sup>f</sup>Institute of Physics, Faculty of Physics, Astronomy and Informatics, Nicolaus Copernicus University in Torun, Grudziadzka 5, 87-100 Torun, Poland

<sup>g</sup>Department of Chemistry, Lomonosov Moscow State University, Moscow 119991, Russia

<sup>h</sup>Old Dominion University, Department of Chemistry, Norfolk VA, USA

<sup>i</sup>German Aerospace Center (DLR), Remote Sensing Technology Institute, Wessling, Germany

<sup>j</sup>Université de Bourgogne Franche-Comté, Laboratoire Interdisciplinaire Carnot de Bourgogne, UMR 6303 CNRS, Dijon Cedex, France

<sup>k</sup>University of Grenoble Alpes, CNRS, LIPhy, F-38000 Grenoble, France

<sup>l</sup>Laboratoire d'Etudes Spatiales et d'Instrumentation en Astrophysique, Paris Observatory, CNRS, PSL Univ., Sorbonne Univ., Paris

<sup>m</sup>Jet Propulsion Laboratory, Caltech, Pasadena CA, USA

<sup>n</sup>California Institute of Technology, Division of Astronomy, Pasadena CA, USA

<sup>o</sup>University of Massachusetts, Dept. of Environmental, Earth & Atmospheric Sciences, Lowell MA, USA

<sup>p</sup>National Institute of Standards and Technology, Chemical Sciences Division, Gaithersburg MD, USA

---

\*Corresponding Author

Email address: [igordon@cfa.harvard.edu](mailto:igordon@cfa.harvard.edu) (I. E. Gordon)



- <sup>q</sup> Sorbonne Université, CNRS, De la Molécule aux Nano-objets : Réactivité, Interactions et Spectroscopies, MONARIS, 75005 Paris, France
- <sup>r</sup> Atmospheric and Environmental Research, Lexington MA, USA
- <sup>s</sup> Institut des Sciences Moléculaires d'Orsay, CNRS, Université Paris-Sud, Université Paris-Saclay, Orsay F-91405, France
- <sup>t</sup> Groupe de Spectrométrie Moléculaire et Atmosphérique, UMR CNRS 7331, BP 1039, F-51687, Reims Cedex 2, France
- <sup>u</sup> Department of Physics and Astronomy, University College London, London, WC1E 6BT, UK
- <sup>v</sup> Laboratoire de Météorologie Dynamique/IPSL, CNRS, École polytechnique, Sorbonne Université, École normale supérieure, PSL Research University, F-91120 Palaiseau, France
- <sup>w</sup> Dipartimento di Chimica Industriale "Toso Montanari", Università di Bologna, Viale Risorgimento 4, Bologna 40136, Italy
- <sup>x</sup> Dipartimento di Chimica "Giacomo Ciamician", Università di Bologna, Via F. Selmi 2, 40126 Bologna, Italy
- <sup>y</sup> MTA-ELTE Complex Chemical Systems Research Group, Budapest, Hungary
- <sup>z</sup> Eötvös Loránd University, Institute of Chemistry, Budapest, Hungary
- <sup>aa</sup> Department of Physics, Umeå University, 901 87 Umeå, Sweden
- <sup>ab</sup> University of Leicester, Department of Physics and Astronomy, Leicester, UK
- <sup>ac</sup> University of Leicester, National Centre for Earth Observation, Leicester, UK
- <sup>ad</sup> University of Leicester, Leicester Institute for Space and Earth Observation, Leicester, UK
- <sup>ae</sup> Department of Physics, University of Oulu, FIN-90014, Finland
- <sup>af</sup> SETI Institute, Mountain View, CA 94043, USA
- <sup>ag</sup> Planetary Systems Branch, Space Science and Astrobiology Division, NASA Ames Research Center, Moffett Field, CA 94035, USA
- <sup>ah</sup> University of Colorado, Laboratory for Atmospheric and Space Physics, Boulder CO, USA
- <sup>ai</sup> I. Physikalisches Institut, Universität zu Köln, 50937 Köln, Germany
- <sup>aj</sup> Department of Chemistry and Biochemistry, James Madison University, Harrisonburg VA 22807, USA
- <sup>ak</sup> Department of Chemistry, University of Adelaide, South Australia, 5005, Australia
- <sup>al</sup> Laboratoire de Météorologie Dynamique/IPSL, CNRS, Sorbonne Université, École normale supérieure, PSL Research University, École polytechnique, F-75005 Paris, France
- <sup>am</sup> Institute of Applied Physics of Russian Academy of Sciences, Nizhny Novgorod, Russia
- <sup>an</sup> Leibniz Institute for Plasma Science and Technology (INP), Greifswald, Germany
- <sup>ao</sup> Université Libre de Bruxelles, Spectroscopy, Quantum Chemistry and Atmospheric Remote Sensing (SQUARES), C.P. 160/09, B-1050 Brussels, Belgium
- <sup>ap</sup> Obukhov Institute of Atmospheric Physics, Russian Academy of Sciences, Pyzhevsky per. 3, 119017 Moscow, Russia
- <sup>aq</sup> NASA Goddard Space Flight Center, Greenbelt MD, 20771, USA
- <sup>ar</sup> Research Unit Lasers and Spectroscopies (LLS), Institute of Life, Earth and Environment (ILEE), University of Namur (UNamur), B-5000, Namur, Belgique
- <sup>as</sup> Royal Belgian Institute for Space Aeronomy (BIRA-IASB), 1180 Brussels, Belgium
- <sup>at</sup> Center for Free-Electron Laser Science, Deutsches Elektronen-Synchrotron DESY, Notkestraße 85, 22607 Hamburg, Germany
- <sup>au</sup> Golisano College of Computing and Information Sciences, Rochester Institute of Technology, Rochester NY 14623, USA
- <sup>av</sup> Computer Science Department, State University of New York at Oswego, Oswego NY 13126, USA

---

## Abstract

The HITRAN database is a compilation of molecular spectroscopic parameters. It was established in the early 1970s and is used by various computer codes to predict and simulate the transmission and emission of light in gaseous media (with an emphasis on terrestrial and planetary atmospheres). The HITRAN compilation is composed of five major components: the line-by-line spectroscopic parameters required for high-resolution radiative-transfer codes, experimental infrared absorption cross-sections (for molecules not yet feasible for representation in a line-by-line form), collision-induced absorption data, aerosol indices of refraction, and general tables, including partition sums, that apply globally to the data. This paper describes the contents of the 2020 quadrennial edition of HITRAN. The HITRAN2020 edition takes advantage of recent experimental and theoretical data that were meticulously validated, in particular, against laboratory and atmospheric spectra. The new edition replaces the previous HITRAN edition of 2016 (including its updates during the intervening years).

All five components of HITRAN have undergone major updates. In particular, the extent of the updates in the HITRAN2020 edition ranges from updating a few lines of specific molecules to complete replacements of the lists and also the introduction of additional isotopologues and new (to HITRAN) molecules: SO, CH<sub>3</sub>F, GeH<sub>4</sub>, CS<sub>2</sub>, CH<sub>3</sub>I and NF<sub>3</sub>. Many new vibrational bands were added, extending the spectral coverage and completeness of the line lists. Also, the accuracy of the parameters for major atmospheric absorbers has been increased substantially, often featuring sub-percent uncertainties. Broadening parameters associated with the water vapor’s ambient pressure were introduced to HITRAN for the first time and are available now for several molecules.

The HITRAN2020 edition will continue taking advantage of the relational structure and efficient interface available at [www.hitran.org](http://www.hitran.org) and the HITRAN Application Programming Interface (HAPI). The functionality of both tools has been extended for the new edition.

*Keywords:* HITRAN; Spectroscopic database; Molecular spectroscopy; Spectroscopic line parameters; Absorption cross-sections; Collision-induced

## 1. Introduction

In the last fifty years, the HITRAN molecular spectroscopic database has provided scientists and engineers with the necessary data to predict and simulate the transmission and emission of light in gaseous media. The database is being updated regularly, and official “editions” have been released and described in corresponding papers [1–15]. In the last three decades, the database has been released on a quadrennial basis. This paper describes the new and/or updated data in the HITRAN2020 edition of the database.

There are countless applications of HITRAN in science and industry, including but not limited to atmospheric, astrophysical, and medical sciences, as well as pollution monitoring. With that being said, the primary goal of HITRAN is to assist interpretation and modeling of spectra in the terrestrial atmosphere. Multiple ongoing (e.g., OCO-2 [16], OCO-3 [17], TES [18], GOSAT [19], ACE [20], TROPOMI [21], GEMS [22]) and upcoming (e.g., FORUM [23], TEMPO [24], MethaneSat [25]) remote-sensing missions rely on spectral data quality in the HITRAN database. It is fair to generalize that remote-sensing missions equipped with spectrometers of *any* resolution use HITRAN data in the analyses of their retrievals. However, this point is often overlooked since HITRAN data are often being integrated into radiative-transfer codes that are in turn used by atmospheric scientists. Whereas articles describing the HITRAN database are among the most cited articles in geosciences (recent editions have typically been cited over 2000 times each), it is very often not cited when the radiative-transfer codes are being used, despite their heavy reliance on HITRAN. There are many radiative-transfer codes that have HITRAN data integrated into them or are more flexible and allow the user to input HITRAN-formatted files themselves, including LBLRTM [26], MODTRAN [27], GENLN [28], RFM [29], ARTS [30], GARLIC [31], kCARTA [32] and VLIDORT [33], to name a few. These codes are used not only for monitoring the concentrations and atmospheric profiles of

gases but also in climate models.

The second most prominent application of HITRAN is interpretation and modeling of spectra of planetary atmospheres including those of exoplanets. Many HITRAN-powered radiative-transfer codes listed above are used for both terrestrial and planetary atmospheres. There are also some planetary-designated codes (including NEMESIS [34], petitRADTRANS [35], PSG [36], Exo-transmit [37] and HELIOS-K [38]) that employ HITRAN data. One should keep in mind that not all of these (or terrestrial) codes employ the most recent versions of HITRAN. Therefore, one needs to be aware of the particular edition of HITRAN that is implemented in their chosen radiative-transfer code.

Naturally, the success of previous/current (for instance, Venus Express [39, 40], ExoMars [41, 42], Cassini [43], and Hershel [44]) as well as future (including JWST [45] and ARIEL [46]) space missions depend on the quality and extent of reference molecular parameters, including spectral parameters in the HITRAN database. In turn, ground-based telescopes need HITRAN not only to interpret their observations of astrophysical objects, but also to subtract the effect of the terrestrial atmosphere [47]. Keeping the aforementioned applications in mind, HITRAN also plays an integral role in undergraduate and graduate courses on molecular spectroscopy and/or radiative transfer.

The greatly improved observational and retrieval capabilities of terrestrial and planetary remote-sensing missions have thus placed critical new requirements of HITRAN. Among the needs are: improved accuracy of all spectroscopic parameters, global consistency of line intensities, improved line-shape parameters (and the means by which they are represented), the addition of missing molecular bands and trace gas species, representation of phenomena that are impacting the retrievals including collision-induced absorption (CIA) bands, advanced line-shape formalisms, line-mixing, and pressure broadening by gases different than air and self.

The HITRAN project is rising to the challenge through an extensive scientific collaboration among spectroscopists, atmospheric scientists, and data scientists. State-of-the-art theoretical and experimental values have been rigor-

ously evaluated, and semi-empirical procedures have been developed for where the data were not available. The data have gone through validation against alternative sources, laboratory and field data when available. Figure 1 in the HITRAN2012 paper [14] provides an overview of the typical validation process. In this current paper, we describe the updates and extension of the database and associated software tools towards meeting the goals of remote sensing and planetary communities, and in parallel, assisting many other applications. For instance, atmospheric scientists would be interested in improved quality of spectroscopic parameters of ozone, which, as described in Section 2.3 will yield better consistency between different spectral regions. They will also appreciate the addition of parameters associated with the broadening of spectral lines by ambient pressure of water vapor [48] described in multiple subsections. This will also be welcomed by the exoplanetary community that models spectra of exoplanets with “steamy” atmospheres. In general, the planetary community and combustion researchers will be interested in learning about the extension of the number of gases that now have broadening parameters due to ambient pressure of  $\text{H}_2$ , He,  $\text{CO}_2$ , and  $\text{H}_2\text{O}$ . Medical experts who analyze human breath for markers of different diseases will appreciate improved relative intensities of the  $^{14}\text{NO}$  and  $^{15}\text{NO}$  transitions described in Section 2.8 and the addition of the  $\text{CS}_2$  molecule described in Section 2.53. Cometary scientists will also appreciate the latter. These are just a few relatively random examples of the gargantuan extent of the updates in this edition and the rationale for doing these updates.

Before the release of the HITRAN2016 edition, we had restructured the database into a relational database format in order to accommodate the need for additional parameters and flexibility of their representation [49, 50]. Many of these parameters can already be retrieved from the dynamic and user-friendly web interface *HITRANonline* (at [www.hitran.org](http://www.hitran.org)), which as of early March, 2021 has over 18 800 registered users in the initial five and a half years of it being made available. This new versatility allows one to request either the familiar HITRAN-format ASCII files (for those users that will not require advanced parameters), but also user-defined formats that can accommodate new features

and parameters. The HITRAN Application Programming Interface (HAPI) [51] that was released with HITRAN2016 has also been updated for increased capabilities and speed of calculations.

The HITRAN compilation in its current state comprises five components that encompass different parametrizations of various molecular phenomena required as spectroscopic input into the radiative-transfer models. The updates to these five portions of HITRAN, as well as the underlying system of data structure with accompanying internet user interface and an application programming interface (API), will be discussed in the following sections: (1) Section 2 is dedicated to the original and most popular component, which is a line-by-line section that provides spectroscopic parameters for high-resolution molecular absorption and radiance calculations (from the microwave through the ultraviolet region of the spectrum). (2) A second component described in Section 3 relates to experimental (mostly infrared) absorption cross-sections. These cross-sections are generally representing absorption by molecules that have very dense spectra or many low-lying vibrational modes. (3) Collision-induced absorption datasets for multiple collisional pairs are described in Section 4. (4) Tables of aerosol refractive indices are described in Section 5. (5) Global data that apply in a general manner to the archive is another important part of the database including its particular component, Total Internal Partition Sums (TIPS), are described in Section 6. The updates to the HITRAN website, underlying structure and HAPI are also described in Section 6.

The high temperature, HITEMP, database described by Rothman et al. [52] was established to provide substantially more transitions (compared to HITRAN), which become necessary for modeling radiative transfer of high-temperature environments [53]. These additional transitions are not required for typical atmospheric applications and are therefore not included in HITRAN. Recently, the number of molecules available through HITEMP (see [www.hitran.org/hitemp/](http://www.hitran.org/hitemp/)) has been extended to include nitrogen oxides [54] and methane [55]. An in-depth description of HITEMP is beyond the scope of this work; nevertheless, it is often the case that updates of HITRAN and HITEMP are

performed at the same time using the same data sources (such as for NO [54]). Therefore, a brief description of corresponding HITEMP updates are included in Section 2 for N<sub>2</sub>O, CH<sub>4</sub>, NO, NO<sub>2</sub>, and OH.

In order to better understand the discussion in this paper it is important to understand the HITRAN definitions of the parameters and formalisms, which can be found in the documentation section of the HITRAN website <https://hitran.org/docs/definitions-and-units/>. New users of the database should also be aware that all of the HITRAN editions (including this one) do not strictly adhere to the SI system for both historical and application-specific reasons. Thus cm<sup>-1</sup> (reciprocal centimeter, the unit of the quantity wavenumber) is seen throughout, as is atm (atmosphere) for pressure (in SI units of Pascals, 101 325 Pa = 1 atm). Also, the symbol  $\nu$  is used throughout for line position in cm<sup>-1</sup>, thereby dropping the tilde ( $\tilde{\nu}$ ) that is the official designation of wavenumber. The HITRAN unit for intensity is traditionally expressed as cm<sup>-1</sup>/(molecule cm<sup>2</sup>) rather than simplifying to the equivalent cm molecule<sup>-1</sup>. However, both notations are used throughout this paper.

A number of abbreviations have been used throughout this paper when describing data, instruments, and methods that have been used to update the HITRAN database. These are described in the text when used, but a list of these abbreviations is also provided in Appendix A.

## 2. Line-by-line modifications

An overview of changes and additions to the line-by-line section for each isotopologue in the database with respect to the HITRAN2016 edition is provided in Table 1. Isotopologues are given in order of their descending abundance for each individual molecule. The molecular abundance values in HITRAN are calculated based on the terrestrial atomic abundances selected from Ref. [56]. It is important to remember that the intensities in the HITRAN database are scaled by these abundances. Note that although for many molecules the amount of lines and spectral ranges have not changed, many parameters were updated or

added. In the subsequent subsections dedicated to individual molecules, detailed accounts of those changes are provided.

Table 1: Molecules and isotopologues represented in line-by-line portion of HITRAN.

Molecule	Isoto- pologue	HITRAN2016			HITRAN2020	
		Abundance <sup>a</sup>	Spectral Range <sup>b</sup>	# of lines	Spectral Range <sup>b</sup>	# of lines
(1) H <sub>2</sub> O	H <sub>2</sub> <sup>16</sup> O	9.973×10 <sup>-1</sup>	0–25 711	146 878	0–42 000	319 886
	H <sub>2</sub> <sup>18</sup> O	2.000×10 <sup>-3</sup>	0–19 918	39 903	0–19 992	42 178
	H <sub>2</sub> <sup>17</sup> O	3.719×10 <sup>-4</sup>	0–19 946	27 544	0–19 946	27 544 <sup>c</sup>
	HD <sup>16</sup> O	3.107×10 <sup>-4</sup>	0–19 936	56 430	0–19 935	56 430
	HD <sup>18</sup> O	6.230×10 <sup>-7</sup>	0–10 729	10 664	0–10 729	10 664
	HD <sup>17</sup> O	1.159×10 <sup>-7</sup>	0–10 703	6366	0–10 703	6366
	D <sub>2</sub> <sup>16</sup> O	2.420×10 <sup>-8</sup>	0–12 797	23 488	0–12 797	23 196 <sup>c</sup>
(2) CO <sub>2</sub>	<sup>12</sup> C <sup>16</sup> O <sub>2</sub>	9.842×10 <sup>-1</sup>	158–14 076	173 024	158–19 909	174 412
	<sup>13</sup> C <sup>16</sup> O <sub>2</sub>	1.106×10 <sup>-2</sup>	332–13 735	70 577	332–13 735	69 870
	<sup>16</sup> O <sup>12</sup> C <sup>18</sup> O	3.947×10 <sup>-3</sup>	1–12 678	127 850	1–12 678	122 142
	<sup>16</sup> O <sup>12</sup> C <sup>17</sup> O	7.340×10 <sup>-4</sup>	0–12 727	77 941	0–12 727	73 942
	<sup>16</sup> O <sup>13</sup> C <sup>18</sup> O	4.434×10 <sup>-5</sup>	2–9213	43 782	2–9213	41 059
	<sup>16</sup> O <sup>13</sup> C <sup>17</sup> O	8.246×10 <sup>-6</sup>	9–8062	25 175	9–8062	23 607
	<sup>12</sup> C <sup>18</sup> O <sub>2</sub>	3.957×10 <sup>-6</sup>	482–8163	10 522	482–8163	10 498
	<sup>17</sup> O <sup>12</sup> C <sup>18</sup> O	1.472×10 <sup>-6</sup>	491–8194	15 878	498–8194	15 623
	<sup>12</sup> C <sup>17</sup> O <sub>2</sub>	1.368×10 <sup>-7</sup>	535–6933	6518	535–6933	6493
	<sup>13</sup> C <sup>18</sup> O <sub>2</sub>	4.446×10 <sup>-8</sup>	2245–4751	2916	539–6687	2926
	<sup>18</sup> O <sup>13</sup> C <sup>17</sup> O	1.654×10 <sup>-8</sup>	549–4915	4190	549–4915	3980
	<sup>13</sup> C <sup>17</sup> O <sub>2</sub>	1.538×10 <sup>-9</sup>	575–3615	1501	575–3615	1501
(3) O <sub>3</sub>	<sup>16</sup> O <sub>3</sub>	9.929×10 <sup>-1</sup>	0–6997	289 340	0–6997	289 340
	<sup>16</sup> O <sup>16</sup> O <sup>18</sup> O	3.982×10 <sup>-3</sup>	0–2768	44 302	0–2768	44 302
	<sup>16</sup> O <sup>18</sup> O <sup>16</sup> O	1.991×10 <sup>-3</sup>	1–2740	18 887	1–2740	18 887

*Continued on next page*



Table 1 – *Continued from previous page*

Molecule	Isoto	HITRAN2016			HITRAN2020	
	pologue	Abundance <sup>a</sup>	Spectral Range <sup>b</sup>	# of lines	Spectral Range <sup>b</sup>	# of lines
	$^{16}\text{O}^{16}\text{O}^{17}\text{O}$	$7.405 \times 10^{-4}$	0–2122	65 106	0–2122	65 106
	$^{16}\text{O}^{17}\text{O}^{16}\text{O}$	$3.702 \times 10^{-4}$	0–2101	31 935	0–2101	31 935
(4) $\text{N}_2\text{O}$	$^{14}\text{N}_2^{16}\text{O}$	$9.903 \times 10^{-1}$	0–7797	33 074	0–7797	33 265
	$^{14}\text{N}^{15}\text{N}^{16}\text{O}$	$3.641 \times 10^{-3}$	5–5086	4222	5–5086	4222
	$^{15}\text{N}^{14}\text{N}^{16}\text{O}$	$3.641 \times 10^{-3}$	4–4704	4592	4–4704	4592
	$^{14}\text{N}^{14}\text{N}^{18}\text{O}$	$1.986 \times 10^{-3}$	0–4672	116 694	0–10364	116 694
	$^{14}\text{N}_2^{17}\text{O}$	$3.693 \times 10^{-4}$	550–4430	1705	550–4430	1705
(5) $\text{CO}$	$^{12}\text{C}^{16}\text{O}$	$9.865 \times 10^{-1}$	3–14 478	1344	3–14 478	1344 <sup>c</sup>
	$^{13}\text{C}^{16}\text{O}$	$1.108 \times 10^{-2}$	3–12 231	1042	3–12 231	1042 <sup>c</sup>
	$^{12}\text{C}^{18}\text{O}$	$1.978 \times 10^{-3}$	3–12 205	920	3–12 205	920 <sup>c</sup>
	$^{12}\text{C}^{17}\text{O}$	$3.679 \times 10^{-4}$	3–10 295	800	3–10 295	800 <sup>c</sup>
	$^{13}\text{C}^{18}\text{O}$	$2.223 \times 10^{-5}$	3–8078	674	3–8078	674 <sup>c</sup>
	$^{13}\text{C}^{17}\text{O}$	$4.133 \times 10^{-6}$	3–8168	601	3–8168	601 <sup>c</sup>
(6) $\text{CH}_4$	$^{12}\text{CH}_4$	$9.883 \times 10^{-1}$	0–11 502	313 943	0–11 502	325 431
	$^{13}\text{CH}_4$	$1.110 \times 10^{-2}$	0–11 319	77 626	0–11 319	79 931
	$^{12}\text{CH}_3\text{D}$	$6.158 \times 10^{-4}$	7–6511	54 550	7–6511	54 550
	$^{13}\text{CH}_3\text{D}$	$6.918 \times 10^{-6}$	959–1695	4213	959–1695	4213
(7) $\text{O}_2$	$^{16}\text{O}_2$	$9.953 \times 10^{-1}$	0–57 028	15 263	0–57 028	15 367
	$^{16}\text{O}^{18}\text{O}$	$3.991 \times 10^{-3}$	1–56 670	2965	1–56 670	3120
	$^{16}\text{O}^{17}\text{O}$	$7.422 \times 10^{-4}$	0–14 537	11 313	0–14 538	11 313
(8) $\text{NO}$	$^{14}\text{N}^{16}\text{O}$	$9.940 \times 10^{-1}$	0–9273	103 701	0–23 727	251 898
	$^{15}\text{N}^{16}\text{O}$	$3.654 \times 10^{-3}$	1609–2061	699	0–15 630	67 370

*Continued on next page*

Table 1 – *Continued from previous page*

Molecule	Isoto	HITRAN2016			HITRAN2020	
	pologue	Abundance <sup>a</sup>	Spectral Range <sup>b</sup>	# of lines	Spectral Range <sup>b</sup>	# of lines
	<sup>14</sup> N <sup>18</sup> O	$1.993 \times 10^{-3}$	1602–2039	679	0–15 503	67 370
(9) SO <sub>2</sub>	<sup>32</sup> S <sup>16</sup> O <sub>2</sub>	$9.457 \times 10^{-1}$	0–4092	72 459	0–4160	549 200
	<sup>34</sup> S <sup>16</sup> O <sub>2</sub>	$4.195 \times 10^{-2}$	0–2500	22 660	0–3465	147 577
	<sup>33</sup> S <sup>16</sup> O <sub>2</sub>	$7.464 \times 10^{-3}$	–	–	0–2625	76 402
	<sup>16</sup> O <sup>32</sup> S <sup>18</sup> O	$3.792 \times 10^{-3}$	–	–	0–2793	208 183
(10) NO <sub>2</sub>	<sup>14</sup> N <sup>16</sup> O <sub>2</sub>	$9.916 \times 10^{-1}$	0–3075	104 223	0–7978	171 057
	<sup>15</sup> N <sup>16</sup> O <sub>2</sub>	$3.646 \times 10^{-3}$	–	–	0–1660	5860
(11) NH <sub>3</sub>	<sup>14</sup> NH <sub>3</sub>	$9.959 \times 10^{-1}$	0–10 349	65 828	0–10 349	76 614
	<sup>15</sup> NH <sub>3</sub>	$3.661 \times 10^{-3}$	0–5180	1320	0–5180	13 791
(12) HNO <sub>3</sub>	H <sup>14</sup> N <sup>16</sup> O <sub>3</sub>	$9.891 \times 10^{-1}$	0–1770	950 863	0–1770	950 863
	H <sup>15</sup> N <sup>16</sup> O <sub>3</sub>	$3.636 \times 10^{-3}$	0–923	58 107	0–923	58 107
(13) OH	<sup>16</sup> OH	$9.975 \times 10^{-1}$	0–19 268	30 772	0–43 408	55 698
	<sup>18</sup> OH	$2.000 \times 10^{-3}$	0–329	295	0–329	295
	<sup>16</sup> OD	$1.554 \times 10^{-4}$	0–332	912	0–332	912
(14) HF	H <sup>19</sup> F	$9.998 \times 10^{-1}$	24–32 351	8088	24–32 351	8088
	D <sup>19</sup> F	$1.557 \times 10^{-4}$	13–20 829	11 920	13–20 829	11 920
(15) HCl	H <sup>35</sup> Cl	$7.576 \times 10^{-1}$	8–20 231	8891	8–20 231	8891
	H <sup>37</sup> Cl	$2.423 \times 10^{-1}$	8–20 218	8907	8–20 218	8907
	D <sup>35</sup> Cl	$1.180 \times 10^{-4}$	5–15 265	17 761	5–15 265	17 761
	D <sup>37</sup> Cl	$3.774 \times 10^{-5}$	5–15 246	17 690	5–15 246	17 690

*Continued on next page*

Table 1 – *Continued from previous page*

Molecule	Isotope pologue	HITRAN2016			HITRAN2020	
		Abundance <sup>a</sup>	Spectral Range <sup>b</sup>	# of lines	Spectral Range <sup>b</sup>	# of lines
(16) HBr	H <sup>79</sup> Br	$5.068 \times 10^{-1}$	13–16 033	3028	13–16 033	3028
	H <sup>81</sup> Br	$4.931 \times 10^{-1}$	13–16 031	3029	13–16 031	3029
	D <sup>79</sup> Br	$7.894 \times 10^{-5}$	7–8780	1453	7–8780	1453
	D <sup>81</sup> Br	$7.680 \times 10^{-5}$	7–8777	1455	7–8777	1455
(17) HI	H <sup>127</sup> I	$9.998 \times 10^{-1}$	10–13 907	3160	10–13 907	3160
	D <sup>127</sup> I	$1.557 \times 10^{-4}$	5–7625	1588	5–7625	1588
(18) ClO	<sup>35</sup> Cl <sup>16</sup> O	$7.559 \times 10^{-1}$	0–1208	5721	0–1208	5721
	<sup>37</sup> Cl <sup>16</sup> O	$2.417 \times 10^{-1}$	0–1200	5780	0–1200	5780
(19) OCS	<sup>16</sup> O <sup>12</sup> C <sup>32</sup> S	$9.374 \times 10^{-1}$	0–7822	18 264	0–7822	21 776
	<sup>16</sup> O <sup>12</sup> C <sup>34</sup> S	$4.158 \times 10^{-2}$	0–7796	6846	0–7796	7424
	<sup>16</sup> O <sup>13</sup> C <sup>32</sup> S	$1.053 \times 10^{-2}$	0–6660	3275	0–6660	3395
	<sup>16</sup> O <sup>12</sup> C <sup>33</sup> S	$7.399 \times 10^{-3}$	0–6631	3005	0–6632	3005
	<sup>18</sup> O <sup>12</sup> C <sup>32</sup> S	$1.880 \times 10^{-3}$	0–4046	1640	0–4046	1640
	<sup>16</sup> O <sup>13</sup> C <sup>34</sup> S	$4.675 \times 10^{-4}$	–	–	1951–2039	221
(20) H <sub>2</sub> CO	H <sub>2</sub> <sup>12</sup> C <sup>16</sup> O	$9.862 \times 10^{-1}$	0–3100	40 670	0–3100	40 670 <sup>c</sup>
	H <sub>2</sub> <sup>13</sup> C <sup>16</sup> O	$1.108 \times 10^{-2}$	0–117	2309	0–117	2309 <sup>c</sup>
	H <sub>2</sub> <sup>12</sup> C <sup>18</sup> O	$1.978 \times 10^{-3}$	0–101	1622	0–101	1622 <sup>c</sup>
(21) HOCl	H <sup>16</sup> O <sup>35</sup> Cl	$7.558 \times 10^{-1}$	1–3800	8877	1–3800	8877
	H <sup>16</sup> O <sup>37</sup> Cl	$2.417 \times 10^{-1}$	1–3800	7399	1–3800	7399
(22) N <sub>2</sub>	<sup>14</sup> N <sub>2</sub>	$9.927 \times 10^{-1}$	11–9355	1107	11–9355	1107

*Continued on next page*

Table 1 – *Continued from previous page*

Molecule	Isoto	HITRAN2016			HITRAN2020	
	pologue	Abundance <sup>a</sup>	Spectral Range <sup>b</sup>	# of lines	Spectral Range <sup>b</sup>	# of lines
	<sup>14</sup> N <sup>15</sup> N	$7.478 \times 10^{-3}$	11–2578	161	11–2578	161
(23) HCN	H <sup>12</sup> C <sup>14</sup> N	$9.851 \times 10^{-1}$	0–17 586	58 108	0–17 586	131 031
	H <sup>13</sup> C <sup>14</sup> N	$1.107 \times 10^{-2}$	2–3405	652	2–5401	57 882
	H <sup>12</sup> C <sup>15</sup> N	$3.622 \times 10^{-3}$	2–3420	646	2–3420	646
(24) CH <sub>3</sub> Cl	<sup>12</sup> CH <sub>3</sub> <sup>35</sup> Cl	$7.489 \times 10^{-1}$	0–3198	110 462	0–3198	110 462
	<sup>12</sup> CH <sub>3</sub> <sup>37</sup> Cl	$2.395 \times 10^{-1}$	0–3198	109 113	0–3198	109 113
(25) H <sub>2</sub> O <sub>2</sub>	H <sub>2</sub> <sup>16</sup> O <sub>2</sub>	$9.950 \times 10^{-1}$	0–1731	126 983	0–1731	126 983
(26) C <sub>2</sub> H <sub>2</sub>	<sup>12</sup> C <sub>2</sub> H <sub>2</sub>	$9.776 \times 10^{-1}$	13–9890	22 866	13–10 737	74 335
	H <sup>12</sup> C <sup>13</sup> CH	$2.197 \times 10^{-2}$	613–6589	285	613–9857	2120
	H <sup>12</sup> C <sup>12</sup> CD	$3.046 \times 10^{-4}$	1–789	7512	1–789	7512
(27) C <sub>2</sub> H <sub>6</sub>	<sup>12</sup> C <sub>2</sub> H <sub>6</sub>	$9.770 \times 10^{-1}$	225–3001	54 460	225–3099	74 743
	<sup>12</sup> CH <sub>3</sub> <sup>13</sup> CH <sub>3</sub>	$2.195 \times 10^{-2}$	285–919	7107	285–919	7107
	<sup>12</sup> C <sub>2</sub> H <sub>5</sub> D	$9.131 \times 10^{-4}$	–	–	681–3207	39 271
(28) PH <sub>3</sub>	<sup>31</sup> PH <sub>3</sub>	$9.995 \times 10^{-1}$	0–3602	22 190	0–3660	104 759
(29) COF <sub>2</sub>	<sup>12</sup> C <sup>16</sup> O <sup>19</sup> F <sub>2</sub>	$9.865 \times 10^{-1}$	725–2002	168 793	697–2001	168 793
	<sup>12</sup> C <sup>16</sup> O <sup>19</sup> F <sub>2</sub>	$1.108 \times 10^{-2}$	686–815	15 311	687–815	15 311
(30) SF <sub>6</sub>	<sup>32</sup> S <sup>19</sup> F <sub>6</sub>	$9.502 \times 10^{-1}$	580–996	2 889 065	580–996	2 889 065
(31) H <sub>2</sub> S	H <sub>2</sub> <sup>32</sup> S	$9.499 \times 10^{-1}$	2–11 330	36 561	3–11 330	36 556 <sup>c</sup>

*Continued on next page*

Table 1 – *Continued from previous page*

Molecule	Isotope	HITRAN2016			HITRAN2020	
		Abundance <sup>a</sup>	Spectral Range <sup>b</sup>	# of lines	Spectral Range <sup>b</sup>	# of lines
	H <sub>2</sub> <sup>34</sup> S	4.214×10 <sup>-2</sup>	5–11 227	11 352	6–11 227	11 452 <sup>c</sup>
	H <sub>2</sub> <sup>33</sup> S	7.498×10 <sup>-3</sup>	5–11 072	6322	6–11 071	6220 <sup>c</sup>
(32) HCOOH	H <sup>12</sup> C <sup>16</sup> O <sup>16</sup> OH	9.839×10 <sup>-1</sup>	10–1890	62 684	10–1889	187 596
(33) HO <sub>2</sub>	H <sup>16</sup> O <sub>2</sub>	9.951×10 <sup>-1</sup>	0–3676	38 804	0–3676	38 804
(34) O	<sup>16</sup> O	9.976×10 <sup>-1</sup>	68–159	2	69–158	2
(35) ClONO <sub>2</sub>	<sup>35</sup> Cl <sup>16</sup> O <sup>14</sup> N <sup>16</sup> O <sub>2</sub>	7.496×10 <sup>-1</sup>	763–798	21 988	763–798	21 988
	<sup>37</sup> Cl <sup>16</sup> O <sup>14</sup> N <sup>16</sup> O <sub>2</sub>	2.397×10 <sup>-1</sup>	765–791	10 211	765–791	10 211
(36) NO <sup>+</sup>	<sup>14</sup> N <sup>16</sup> O <sup>+</sup>	9.940×10 <sup>-1</sup>	3–2531	1270	4–2530	1270
(37) HOBr	H <sup>16</sup> O <sup>79</sup> Br	5.056×10 <sup>-1</sup>	0–316	2177	0–316	2177
	H <sup>16</sup> O <sup>81</sup> Br	4.919×10 <sup>-1</sup>	0–316	2181	0–316	2181
(38) C <sub>2</sub> H <sub>4</sub>	<sup>12</sup> C <sub>2</sub> H <sub>4</sub>	9.773×10 <sup>-1</sup>	620–3243	59 536	620–3242	59 536
	<sup>12</sup> CH <sub>2</sub> <sup>13</sup> CH <sub>2</sub>	2.196×10 <sup>-2</sup>	614–3181	18 095	615–3180	18 095
(39) CH <sub>3</sub> OH	<sup>12</sup> CH <sub>3</sub> <sup>16</sup> OH	9.859×10 <sup>-1</sup>	0–1408	19 897	0–1407	19 897
(40) CH <sub>3</sub> Br	<sup>12</sup> CH <sub>3</sub> <sup>79</sup> Br	5.010×10 <sup>-1</sup>	794–1706	18 692	794–1706	18 692
	<sup>12</sup> CH <sub>3</sub> <sup>81</sup> Br	4.874×10 <sup>-1</sup>	796–1697	18 219	795–1967	18 219
(41) CH <sub>3</sub> CN	<sup>12</sup> CH <sub>3</sub> <sup>12</sup> C <sup>14</sup> N	9.739×10 <sup>-1</sup>	890–946	3572	890–946	3572

*Continued on next page*

Table 1 – *Continued from previous page*

Molecule	Isotope	HITRAN2016			HITRAN2020	
		Abundance <sup>a</sup>	Spectral Range <sup>b</sup>	# of lines	Spectral Range <sup>b</sup>	# of lines
(42) CF <sub>4</sub>	<sup>12</sup> C <sup>19</sup> F <sub>4</sub>	9.889×10 <sup>-1</sup>	582–1519	842 709	582–1519	842 709
(43) C <sub>4</sub> H <sub>2</sub>	<sup>12</sup> C <sub>4</sub> H <sub>2</sub>	9.560×10 <sup>-1</sup>	0–1303	251 245	0–1303	251 245
(44) HC <sub>3</sub> N	H <sup>12</sup> C <sub>3</sub> <sup>14</sup> N	9.633×10 <sup>-1</sup>	0–760	180 332	0–3361	226 369
(45) H <sub>2</sub>	H <sub>2</sub>	9.997×10 <sup>-1</sup>	15–27 185	3480	15–27 185	3480 <sup>c</sup>
	HD	3.114×10 <sup>-4</sup>	3–36 406	5129	3–36 406	11 575
(46) CS	<sup>12</sup> C <sup>32</sup> S	9.396×10 <sup>-1</sup>	1–2586	1088	1–2586	1088
	<sup>12</sup> C <sup>34</sup> S	4.168×10 <sup>-2</sup>	1–1359	396	1–1359	396
	<sup>13</sup> C <sup>32</sup> S	1.056×10 <sup>-2</sup>	1–1331	396	1–1331	396
	<sup>12</sup> C <sup>33</sup> S	7.417×10 <sup>-3</sup>	1–156	198	1–156	198
(47) SO <sub>3</sub>	<sup>32</sup> S <sup>16</sup> O <sub>3</sub>	9.434×10 <sup>-1</sup>	0–2825	14 295	0–2825	14 295
(48) C <sub>2</sub> N <sub>2</sub>	<sup>12</sup> C <sub>2</sub> <sup>14</sup> N <sub>2</sub>	9.708×10 <sup>-1</sup>	200–307	71 775	200–307	71 775
(49) COCl <sub>2</sub>	<sup>12</sup> C <sup>16</sup> O <sup>35</sup> Cl <sub>2</sub>	5.664×10 <sup>-1</sup>	793–900	164 437	793–900	164 437
	<sup>12</sup> C <sup>16</sup> O <sup>35</sup> Cl <sup>37</sup> Cl	3.622×10 <sup>-1</sup>	800–892	145 477	800–892	145 477
(50) SO	<sup>32</sup> S <sup>16</sup> O	9.479×10 <sup>-1</sup>	–	–	0–6060	1494
(51) CH <sub>3</sub> F	<sup>12</sup> CH <sub>3</sub> <sup>19</sup> F	9.884×10 <sup>-1</sup>	–	–	1067–1291	1499
(52) GeH <sub>4</sub>	<sup>74</sup> GeH <sub>4</sub>	3.652×10 <sup>-1</sup>	–	–	648–2270	12 209
	<sup>72</sup> GeH <sub>4</sub>	2.741×10 <sup>-1</sup>	–	–	649–2270	12 141

*Continued on next page*

Table 1 – *Continued from previous page*

Molecule	Isotopologue	HITRAN2016		HITRAN2020	
		Abundance <sup>a</sup>	Spectral Range <sup>b</sup> # of lines	Spectral Range <sup>b</sup> # of lines	
	<sup>70</sup> GeH <sub>4</sub>	$2.051 \times 10^{-1}$	–	–	649–2271 12 091
	<sup>73</sup> GeH <sub>4</sub>	$7.755 \times 10^{-2}$	–	–	649–2270 12 170
	<sup>76</sup> GeH <sub>4</sub>	$7.755 \times 10^{-2}$	–	–	649–2270 12 266
(53) CS <sub>2</sub>	<sup>12</sup> C <sup>32</sup> S <sub>2</sub>	$8.928 \times 10^{-1}$	–	–	23–6467 53 770
	<sup>32</sup> S <sup>12</sup> C <sup>34</sup> S	$7.921 \times 10^{-2}$	–	–	196–4543 7322
	<sup>32</sup> S <sup>12</sup> C <sup>33</sup> S	$1.409 \times 10^{-2}$	–	–	611–4567 3612
	<sup>13</sup> C <sup>32</sup> S <sub>2</sub>	$1.003 \times 10^{-2}$	–	–	1–4426 30 288
(54) CH <sub>3</sub> I	<sup>12</sup> CH <sub>3</sub> <sup>127</sup> I	$9.884 \times 10^{-1}$	–	–	693–3274 105 473
(55) NF <sub>3</sub>	<sup>14</sup> N <sup>19</sup> F <sub>3</sub>	$9.963 \times 10^{-1}$	–	–	2–2201 2 717 795

<sup>a</sup> Abundances are calculated from terrestrial atomic abundances in Ref. [56]. Line intensities in the HITRAN database have been scaled by these isotopologue abundances.

<sup>b</sup> Spectral ranges are given in cm<sup>−1</sup>.

<sup>c</sup> Although spectral ranges and amount of lines is unchanged with respect to HITRAN2016, there are changes to spectral parameters of lines for these isotopologues.

The definitions of the uncertainty indices used in HITRAN for spectral parameters in the line-by-line representation are defined in Table 2. Uncertainty and reference indices are now given for all parameters in HITRAN except for the Einstein-A coefficients (which usually share the same source and uncertainty as the intensities), lower-state energies and quantum numbers. It should be remarked that the code 0 in Table 2 might lend itself to two different meanings in the case of line position or air pressure-induced shift. It means that either the uncertainty in the shift reported is greater than 1 cm<sup>−1</sup> or was not reported. The word “default” or “constant” (code 1 in Table 2) means a constant value, and the word “average” or “estimate” (code 2 in Table 2) means an average

or empirical value. This Table will be frequently referred to across different subsections of section 2.

Table 2: The uncertainty codes used by the HITRAN database (as presented in HITRAN*Nonline*) is produced based on Table 5 of the HITRAN2004 paper [12]. There are two types of uncertainty code corresponding to absolute uncertainty in  $\text{cm}^{-1}$  (used for the line position and pressure-induced line shift parameters) and relative uncertainty in % (used for the line intensity and line-shape parameters).

Code	Absolute uncertainty range	Code	Relative uncertainty range
0	$\geq 1$ or Unreported	0	Unreported or unavailable
1	$\geq 0.1$ and $< 1$	1	Default or constant
2	$\geq 0.01$ and $< 0.1$	2	Average or estimate
3	$\geq 0.001$ and $< 0.01$	3	$\geq 20\%$
4	$\geq 0.0001$ and $< 0.001$	4	$\geq 10\%$ and $< 20\%$
5	$\geq 0.00001$ and $< 0.0001$	5	$\geq 5\%$ and $< 10\%$
6	$\geq 0.000001$ and $< 0.00001$	6	$\geq 2\%$ and $< 5\%$
7	$\geq 0.0000001$ and $< 0.000001$	7	$\geq 1\%$ and $< 2\%$
8	$\geq 0.00000001$ and $< 0.0000001$	8	$< 1\%$
9	$\geq 0.000000001$ and $< 0.00000001$		

### 2.1. $H_2O$ : Water Vapor (molecule 1)

Considering that water vapor is the major absorber of light in the terrestrial atmosphere, it is difficult to overstate the importance of the quality and extent of spectroscopic parameters for this molecule in HITRAN. The details surrounding the previous (HITRAN2016) water vapor compilation can be found in the corresponding paper [15]. To briefly summarize, the wavelength range has now been extended to approximately 400 nm, and the study used *ab initio* calculated line lists as its initial starting point. Whenever possible, line positions were replaced with accurate experimental data or wavenumbers generated from a MARVEL-based [57, 58] set of empirical energy levels [59]. The bulk of the intensities were of *ab initio* origin, but in many places experimental data were used (taken most notably from Refs. [60–71]). This approach substantially reduces the number of missing lines (from an atmospheric perspective) in all isotopologues and, in general, it enhances the quality of the line parameters. Similar to the earlier two editions (HITRAN2008 [13] and HITRAN2012 [14]), HITRAN2016 [15] continued to utilize the “Diet” algorithm [72] for broaden-



ing parameters, supplemented with the newest experimental data. Moreover, parameters determined for the advanced Hartmann–Tran (HT) profile [73, 74] were incorporated into the database, where available from Ref. [65]. Remote-sensing experiments in the IR region have identified that the HITRAN2016 water vapor compilation results in smaller residuals when compared with previous editions (see Ref. [42] for instance). Nevertheless, a number of issues have been found. One of the sources of discrepancies predominantly manifests itself in the NIR to visible parts of the spectrum and is associated with erroneous broadening and shifting parameters of experimental origin. Unfortunately, one of the “Diet” algorithm features that was designed to eliminate outliers was inadvertently turned off in the HITRAN2016 edition. This has resulted in some of the issues reported in the visible region by Baker et al. [75]. Another problem concerned the incorrect quantum assignment of certain transitions, which, while not having adverse affects on atmospheric retrievals, were not accurate from a spectroscopic perspective. In the new edition, these issues have been eliminated. Moreover, the water database was extended into the UV region, and the general quality of the parameters was improved overall. The details of the update are given below.

#### 2.1.1. $H_2^{16}O$

The water-vapor line lists for HITRAN2020 have received a significant update compared to HITRAN2016 [15]. The entire process of developing the HITRAN2020 line list for the principal isotopologue is presented as a flowchart in Fig. 1. Within the text below, we will describe the steps in significantly more detail.

In Ref. [76], an *ab initio* dipole moment surface (DMS), underpinned by high-level electronic-structure calculations, was developed, designed to create highly-accurate spectra extending all the way to the dissociation limit in the near ultraviolet. The motivation for this work came in part from the forthcoming launch of NASA’s TEMPO (Tropospheric Emissions Monitoring of Pollution) satellite [77], which carries a short-wavelength instrument that aims to accu-

rately monitor the chemical composition in the air across the North American continent. TEMPO will retrieve water-vapor column densities in the 440–450 nm spectral interval, a region that is often used for water retrievals [78–80]; however, the interference of water-vapor absorption features in the near ultraviolet needs to be accounted for when targeting trace gases such as formaldehyde.

Atmospheric observations from Lampel et al. [81] indicate that the “POKAZATEL” [82] line list underestimates the magnitude of absorption features at near-ultraviolet wavelengths (363 nm) by a factor of 2.6 – a potential source of error for TEMPO retrievals. A noteworthy point is that the HITRAN2016 line list extends only to 400 nm and the source of transition intensities that underpins a large portion of the visible transitions are variational in nature and these use a similar DMS [83] to that used in the creation of the POKAZATEL line list, hence the requirement to update the transition frequency limit and *ab initio* data sources.

Conway et al. [84] calculated  $\text{H}_2^{16}\text{O}$  and  $\text{H}_2^{18}\text{O}$  line lists that extended to the HITRAN2016 frequency limits and compared the new *ab initio* intensities against a large quantity of experimental sources, most of which feature in the HITRAN2016 line list. It became evident that the new *ab initio* spectra from Conway et al. provide more accurate and reliable transition intensities than other available *ab initio* line lists, particularly at short wavelengths. More recently, Conway et al. created a new near-ultraviolet line list [85] that extends to dissociation and this provides the correct amount of absorption at 363 nm, while also adhering to the upper limit absorption thresholds proposed by Lampel et al. through atmospheric observations [86], and to that of Wilson et al. [87] through experimental measurements. What cannot be replicated by the *ab initio* spectra are the measured spectra of Du et al. [88] and Pei et al. [89]. The magnitude of the water-vapor cross sections reported both by Du et al. and Pei et al. are significantly larger than the *ab initio* predictions; meaning, for example, that they would adversely perturb atmospheric retrievals of ozone.

To create the HITRAN2020  $\text{H}_2^{16}\text{O}$  line list we started with the *ab initio* spectra from Conway et al. While semi-empirical potential energy surfaces

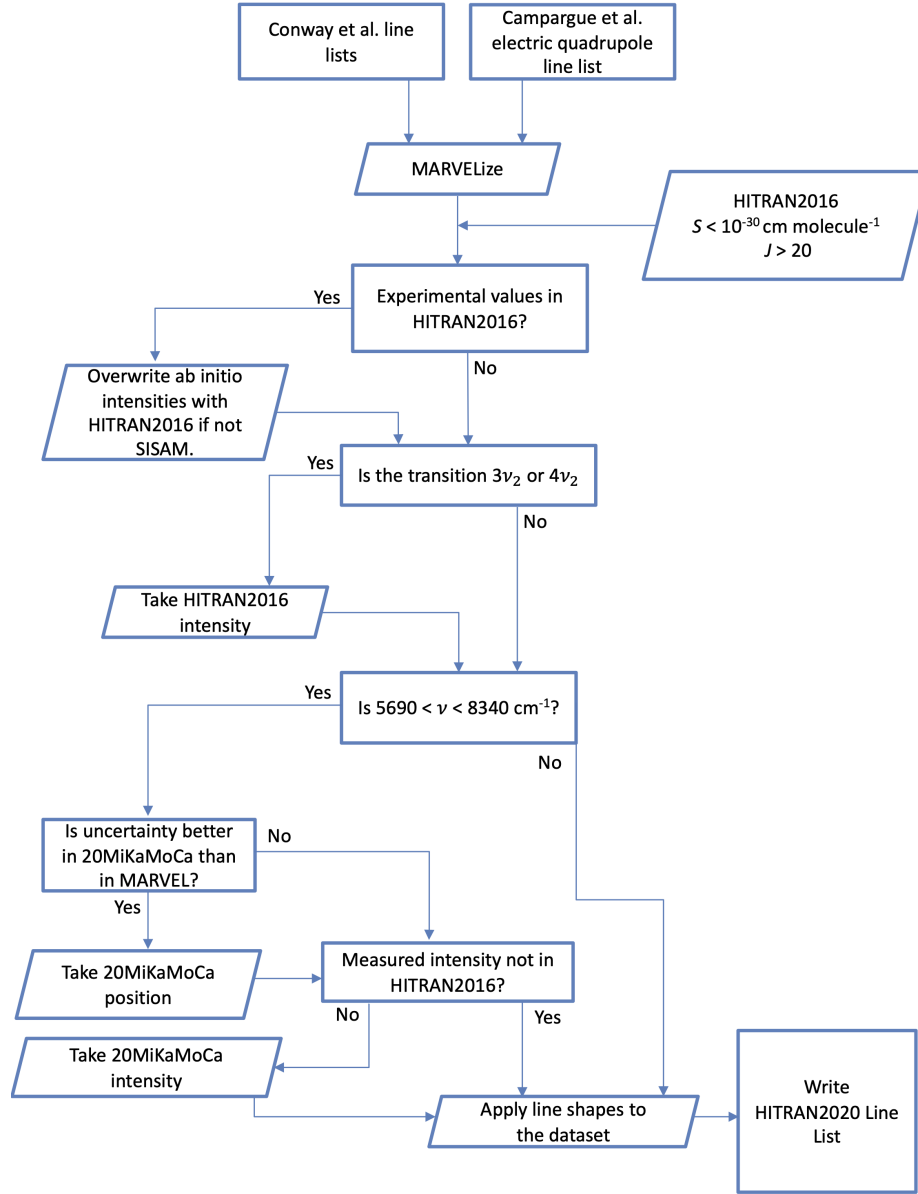


Figure 1: A flowchart describing the development of the HITRAN2020 line list for the principal isotopologue of water vapor. The Mikhailenko et al. [90] line list is abbreviated to “20MiKaMoCa” within the chart shown above.

capable of predicting energy levels to a hundredth [91] and even a thousandth of a wavenumber are gradually appearing [92], they are still far less accurate than

their experimental counterparts, which make use, for example, of frequency-comb and Lamb-dip techniques. The MARVEL (Measured Active Rotational-Vibrational Energy Levels) methodology [57, 58] utilizes the framework provided by spectroscopic networks [93] and high-quality experimental measurements of line positions. Highly-accurate experimental measurements of line positions [94] were utilized during the latest MARVEL attempts to analyze water spectra. These accurate measurements can simultaneously improve the accuracy of the majority of energy levels [94] involved in connected transitions. Furtenbacher et al. released a much improved set of highly accurate  $\text{H}_2^{16}\text{O}$  energy levels [95, 96], named the “W2020” dataset, containing 19 225 empirical energy levels derived from 286 987 non-redundant experimental ro-vibrational transitions. Utilizing the labels and the transition wavenumbers of the W2020 set the information in the *ab initio* line list was updated. Conway et al. [97] recently applied the Hoes–Taylor theorem [98] to theoretical spectroscopy and showed that the projection of the total angular momentum ( $J$ ) onto the body fixed axis ( $k$ ) can be considered a good quantum number once the square of the projected component’s wave-function amplitude is greater than one-half ( $\Psi_k^2 > 0.5$ ). The theory was tested using the DVR3D [99] nuclear motion code on the water and ozone molecules. The asymmetric-top quantum numbers  $K_a$  and  $K_c$  were determined to a high degree of fidelity up to dissociation. We used these results to label states in the visible and near ultraviolet where MARVEL does not yield this information.

Mikhailenko et al. [90] also released an empirical line list that spans  $5690 - 8340 \text{ cm}^{-1}$ , and we compared their results to the *ab initio* calculations of Conway et al. It was found that high overtones of  $\nu_2$ , notably  $3\nu_2$  and  $4\nu_2$ , were not accurately represented in the new *ab initio* calculations. Hence, for these bands, we replaced the calculated results of Conway et al. with what was already present in HITRAN2016. In our own comparisons, we detected a small number of discrepancies in the transition frequencies created by the latest empirical (MARVEL) energy levels to those present in the empirical line list. In such cases, we chose the source that has the lowest uncertainty associated with it

and also considered the type of experiment used to derive the value in the empirical line list.

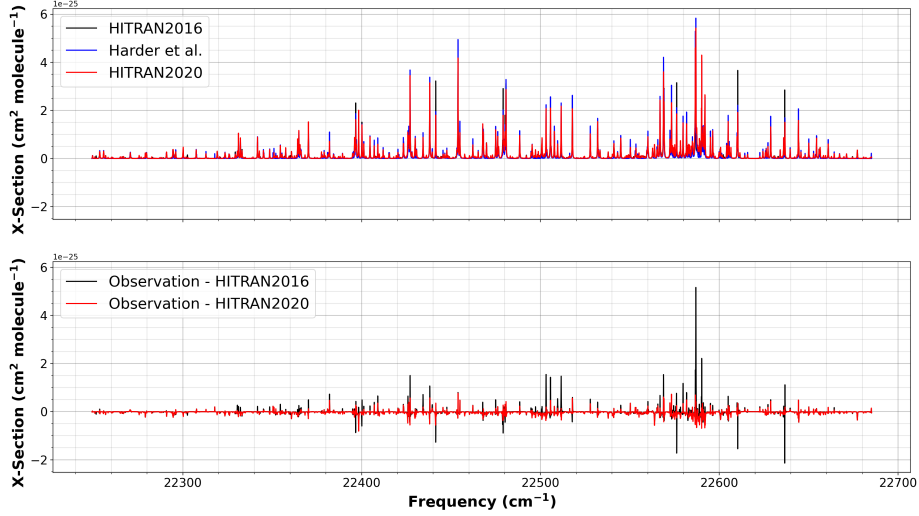


Figure 2: Comparison of the HITRAN2020 and HITRAN2016 [15] line lists against the observed water-vapor cross sections reported by Harder et al. [100].

In the next step, we focused on overwriting the *ab initio* intensities with high-quality experimental measurements wherever it was deemed appropriate. Experimental measurements in the IR which were performed at the Deutsches Zentrum für Luft und Raumfahrt (DLR) [65, 101, 102] were analyzed by Birk et al. [103] and deficiencies were observed in the *ab initio* data of Lodi et al. [83], particularly in the  $\nu_1$  band. The same deficiencies in  $\nu_1$  are present in the Conway et al. *ab initio* data but improvements are evident in many other bands [84], especially for those near  $1\ \mu\text{m}$ . Differences between the experimental [65] and the new *ab initio* data were found in the relative intensities for  $\nu_2$  (ca. 1%) and  $2\nu_2$  (ca. 1.5%). The differences occur in the upper wavenumber range of the bands and increase with wavenumber. In the case of the  $\nu_3$  fundamental, the average difference worsens from 0.18% with the calculation of Lodi et al. to  $-1.08\%$  with the *ab initio* data of Conway et al. The  $3\nu_3$  band also showed similar behavior, with the mean residuals increasing from  $-0.7\%$  using the Lodi et al. line list to  $-3.9\%$ . The latter one is the only band in the  $1\text{-}\mu\text{m}$  region

where no improvement was observed. For these bands, we scaled the *ab initio* intensities from Conway et al. to match the experimental measurements better, and while they will be overwritten with the experimental data later on, where no measurement is available this scaling improves the accuracy of the calculations. Further investigations indicated that the underlying electronic structure calculations were the culprit of such irregularities [104] and Conway et al. showed for the  $\nu_2$  fundamental how changing the spectrum-fitting profile can result in different transition parameters – in particular, intensities.

All experimental intensity measurements in the HITRAN2016 line list, with the exception of the SISAM [60] data (excluding any  $3\nu_2$  and  $4\nu_2$  measurements), are transcribed into HITRAN2020 [61–71]. Comparisons [84] between the new *ab initio* intensities and the intensity measurements within the SISAM data set in the infrared region exhibited a skewed appearance. This is not the first instance of such a structure being attributed to Kitt Peak water-vapor spectra [62, 103, 105]. If we detected an experimentally determined value for an intensity in the empirical list of Mikhailenko et al., the *ab initio* intensity was overwritten by the experimental datum.

For the first time, electric quadrupole (E2) transitions for the water molecule were identified in experimental spectra, made possible by the availability of an E2 *ab initio* line list [106, 107]. The E2 transitions have now been added to the HITRAN2020 line list (only for the principal isotopologue). This room temperature E2 line list for  $\text{H}_2^{16}\text{O}$  ranges from 0 to  $10\,000\text{ cm}^{-1}$  and contains 6227 lines with intensities stronger than  $10^{-30}\text{ cm/molecule}$ . It was generated using MARVEL line positions and lower-state energies and theoretical transition intensities computed using a high-level *ab initio* electric quadrupole moment and a state-of-the-art variational approach [108, 109]. The character in the last field of lower-state rotational (“local”) quanta (i.e. preceding the error code for the line positions) in the traditional 160 character “.par” format will carry a label “q” to denote these transitions. It should be noted that E2 type transitions are typically 6–8 orders of magnitude weaker than electric dipole transitions [106].

The HITRAN2016 line list included a large number of highly-accurate tran-

sition wavenumber measurements from the SISAM data set. Comparisons of these data to derived MARVEL transition frequencies indicated that the transition wavenumbers derived from the most recent version of the MARVEL data [96] match the SISAM values to within their uncertainty. The predicted MARVEL line positions are therefore selected as the preferable source of data because, apart from their validated accuracy, they also would provide consistency throughout the database.

The accuracy of the HITRAN2020 line list in the visible region is significantly better than that of its predecessor, HITRAN2016. Harder et al. [100] reported water-vapor absorption spectra in the 22 100–22 700  $\text{cm}^{-1}$  interval through atmospheric observations. Using the HITRAN Application Programming Interface (HAPI) [51], we have generated cross sections at a temperature of 288 K using the Voigt profile at a resolution of 0.03  $\text{cm}^{-1}$ . In Fig. 2, it becomes clear that the HITRAN2020 line list is significantly better suited for retrieving water in the visible region. It has already been reported that the HITRAN2016 water line list has spectroscopic errors in the visible range [110] and the HITRAN2020 edition offers substantial improvements. The errors were a collection of irregularities in line shape parameters and inaccurate *ab initio* transition intensities.

To extend this comparison between HITRAN2020 and HITRAN2016 in the visible between 9000 – 20 000  $\text{cm}^{-1}$ , we generated two telluric models using the Planetary Spectrum Generator (PSG) [36], each generated with the two respective line lists, and compared these models to a high SNR telluric spectrum extracted from solar observations detailed in Baker et al. [75]. The atmospheric profile used to generate the model was evaluated for the appropriate location and elevation of the observation site in Göttingen, Germany as well as the corresponding observation time of June 17, 2015 UTC 10:50:30.5. The water-vapor abundance and surface pressure were adjusted by fitting the model to a subset of the data between 13 679.89–13 698.63  $\text{cm}^{-1}$ . The results of this comparison are shown in Fig. 3. The residual root mean square (RMS) for each model comparison shows overall improvements in HITRAN2020. This is partly due to fixes of the strongest residuals seen in Fig. 3, which includes the few

missing lines reported in Baker et al. 2020 [75]. Some residuals are found that worsened in HITRAN2020. This includes lines between 11 900–12 300  $\text{cm}^{-1}$ , which are due to an offset in the transition energies that is being investigated and will be resolved in a later release. Similar results are found by redoing this analysis using a transmission spectrum of the atmosphere at Kitt Peak [111] also derived from solar observations, but extracted using a different method to that used in Baker et al.

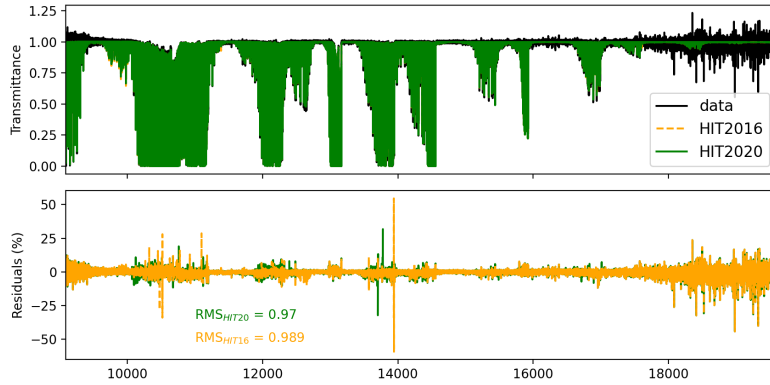


Figure 3: Comparison of the HITRAN2020 and HITRAN2016 [15] line lists through modeling the terrestrial atmospheric transmittance. Models were generated with the Planetary Spectrum Generator (PSG) [36] and compared to a telluric spectrum extracted from a high-resolution solar spectrum as described by Baker et al. [75].

### 2.1.2. $\text{H}_2^{18}\text{O}$

The HITRAN2020 line list for  $\text{H}_2^{18}\text{O}$  also begins with the *ab initio* line list from Conway et al., which extends to 20 000  $\text{cm}^{-1}$ . In their comparisons against the experimental transition intensities present in the HITRAN2016 line list, discrepancies were observed that were not evident in any of the  $\text{H}_2^{16}\text{O}$  comparisons. A large amount of scatter was observed in intensity comparisons to measurements in the SISAM data [60], while a large, 20% shift was observed in the Tanaka et al. [112] intensities present in HITRAN2016. No such discrepancies were detected for the principle isotopologue covering the same regions. Considering that the *ab initio* line lists for  $\text{H}_2^{16}\text{O}$  and  $\text{H}_2^{18}\text{O}$  were calculated using



very similar PESs and the same DMS, the source of the discrepancies is more likely to be associated with experiments. Therefore, the Tanaka et al. data is not included in the HITRAN2020 release.

Comparisons against new experimental spectra measured by Mikhailenko et al. [113] between 16 400 to 17 200  $\text{cm}^{-1}$ , that was not present in HITRAN2016, were also performed [84]. While Mikhailenko et al. noticed that the HITRAN2016 data missed particularly strong transitions in the region, most from *ab initio* calculations [114], the new *ab initio* calculations were not missing such transitions.

In addition to releasing a much improved set of  $\text{H}_2^{16}\text{O}$  energy levels, Furtenbacher et al. [96] also released an updated set of empirical energy levels for both  $\text{H}_2^{18}\text{O}$  and  $\text{H}_2^{17}\text{O}$  as part of their W2020 dataset. Hence, to develop the  $\text{H}_2^{18}\text{O}$  line list for HITRAN2020 we considered the *ab initio* line list from Conway et al. and updated the *ab initio* energy levels with the latest MARVEL data. Furtenbacher et al. also utilized the method of Polyansky et al. [115] to generate so-called pseudo-experimental energy levels. Use of these semi-empirical levels for both  $\text{H}_2^{18}\text{O}$  and  $\text{H}_2^{17}\text{O}$  will be considered as a possible further improvement in a future release.

Following this, we proceeded to update the calculated transition intensities with the measured data present in HITRAN2016 [62, 67–70, 116], with the exception of the SISAM (aside from the measured  $3\nu_2$  and  $4\nu_2$  bands) and Tanaka et al. data. In addition, we also supplement the line list with newly measured intensities from Mikhailenko et al. [113].

### 2.1.3. $\text{H}_2^{17}\text{O}$

The HITRAN2016  $\text{H}_2^{17}\text{O}$  line list possessed several small issues [96], mostly related to spectroscopic assignment of states. There were forbidden transitions between ortho–para states, rotational parity was equal for several upper and lower-states, and the list possessed several duplicate transitions. To address these issues, we have updated the energy levels (hence the transition frequencies) with the latest MARVEL data and remedied these transition assignments.

#### 2.1.4. $HD^{16}O$ , $HD^{18}O$ and $HD^{17}O$

The HITRAN2016  $HD^{16}O$ ,  $HD^{18}O$  and  $HD^{17}O$  line lists also possessed several issues related to forbidden transitions. To address these issues, we have updated the transition assignments. Positions and intensities have not been altered from HITRAN2016.

#### 2.1.5. $D_2^{16}O$

The  $D_2^{16}O$  line list in HITRAN2016 was based on a preliminary version of the line list from Kyuberis et al. [117]. This list was found to contain some ambiguous assignments and therefore for HITRAN2020 the published list from Kyuberis et al. [117] was used.

#### 2.1.6. *Line-shape parameters for water vapor*

Line-shape parameters, including the half-width,  $\gamma$ , and the line shift,  $\delta$ , their associated errors, and the temperature dependence of these parameters have been added to the water vapor transitions discussed above. The algorithm becomes rather involved due to the fact that the data availability varies greatly with isotopologue but basically follows the “Diet” procedure of Gordon et al. [72]. Line-shape parameters for  $H_2O$ -air and self-collision systems were added for all the isotopologues of water vapor, although for self-collisions only the half-widths are considered. It is important to note that in the official release of HITRAN2020, only values associated with the power law of temperature dependencies were considered for water vapor. When the shift does not change sign over the temperature range of the calculations (see below), the power law temperature dependence,  $m$ , was also determined. However, when possible, the temperature dependence of the half-width and the line shift were generated using the Gamache–Vispoel double power law (DPL) model [118] and will be considered for the database update in the future. The infrastructure for this is already setup [119] but large effort is required to validate and populate these parameters as mentioned in section 7.1.1.

The line-shape data were taken from a number of sources. Beginning with an

updated version of the measurement database of Gamache and Hartmann [120], which contains data for the seven water-vapor isotopologues in HITRAN, data of known high quality for  $\gamma$  and  $\delta$  were extracted and put into a “priority” data file. It is important to emphasize that in that priority data, apart from the laboratory values, parameters determined from the fits of the atmospheric spectra were also employed. For instance, Mlawer et al. [121] have identified issues with broadening parameters for a couple of dozen of lines in the FIR region and have suggested alternative values based on the retrievals. These values were used in the HITRAN2020 update in the priority data.

Next, an intercomparison of the measurement data was performed, and the inconsistent references and individual outliers were filtered from the air-broadening database. The intercomparison of  $\text{H}_2\text{O}$ -air data and  $\text{H}_2\text{O} - \text{H}_2\text{O}$  data were redone and average values from the intercomparison of data were determined and stored in files for the half-widths and the line shifts. All the lines for which an intercomparison could not be done, i.e. a single datum for a transition, were written to separate files for the half-widths and the line shifts.

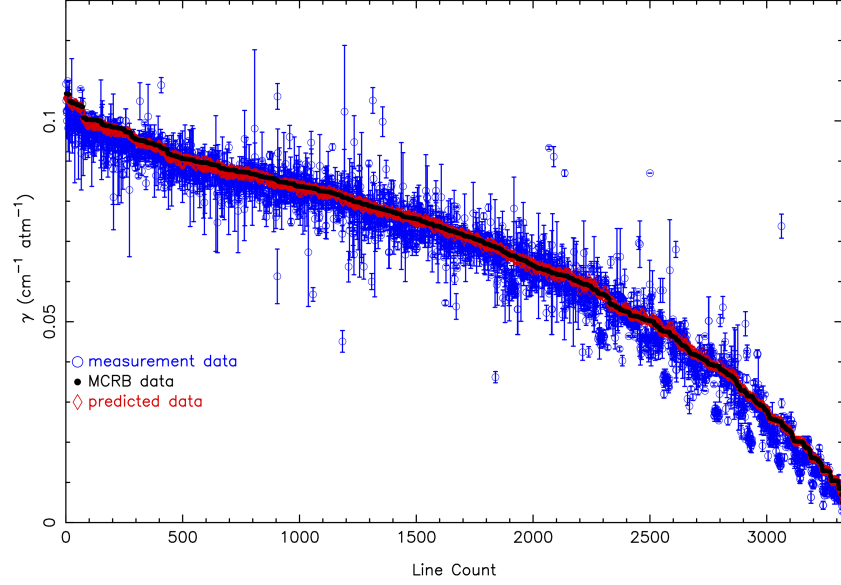
Subsequently, theoretical calculations of the line-shape parameters were considered. Taking the Modified Complex Robert–Bonamy (MCRB) calculations of Vispoel et al. [122] for the  $\text{H}_2\text{O} - \text{N}_2$  collision system and similar calculations for the  $\text{H}_2\text{O} - \text{O}_2$  collision system, the line-shape information for the  $\text{H}_2\text{O}$ -air collision system were produced by  $\gamma_{\text{air}} = 0.79 \times \gamma_{\text{N}_2} + 0.21 \times \gamma_{\text{O}_2}$  with a similar formula for the line shift. Note the calculations considered 13 temperatures from 200-3000 K;  $\gamma$  and  $\delta$  were determined for these 13 temperatures so that the temperature dependence could be determined. These MCRB calculations were made for 10 782 rotational transitions for the rotational band and for bands with one to four  $\nu_1$ ,  $\nu_2$ , and  $\nu_3$  vibrational quanta exchanged, giving some 140 000 calculated transitions. These data make up the calculated  $\text{H}_2\text{O}$ -air line-shape files for the  $\text{H}_2^{16}\text{O}$ ,  $\text{H}_2^{18}\text{O}$ ,  $\text{H}_2^{17}\text{O}$  isotopologues. For these three isotopologues, the self-broadening Complex Robert–Bonamy calculations that were added to previous HITRAN databases were used. For the HDO and  $\text{D}_2\text{O}$  isotopologues self-broadened data are from the calculations in Refs. [123–125].

Next in the algorithm was the use of accurate predicted values of  $\gamma$ ,  $\delta$ , and the temperature dependence of each. Gamache and Hartmann, working from Robert–Bonamy theory, derived a formula that can accurately predict  $\gamma$  and  $\delta$  [126] at any temperature. This routine has been successfully applied to H<sub>2</sub>O-air [127], CO<sub>2</sub>-x, where x = N<sub>2</sub>, O<sub>2</sub>, air, CO<sub>2</sub> [128], H<sub>2</sub>O-H<sub>2</sub> [129], and H<sub>2</sub>O-N<sub>2</sub> [130], and the predicted values agree well with the calculated or measured ones with a standard deviation 5% for the H<sub>2</sub>O studies and 1% for the CO<sub>2</sub> studies. A prediction routine was developed based on the H<sub>2</sub>O-air MCRB data (H<sub>2</sub><sup>16</sup>O, H<sub>2</sub><sup>18</sup>O, H<sub>2</sub><sup>17</sup>O) and the prediction coefficients determined at the 13 temperatures allowing the temperature dependence to also be determined. These data make the predicted part of the H<sub>2</sub>O-air database.

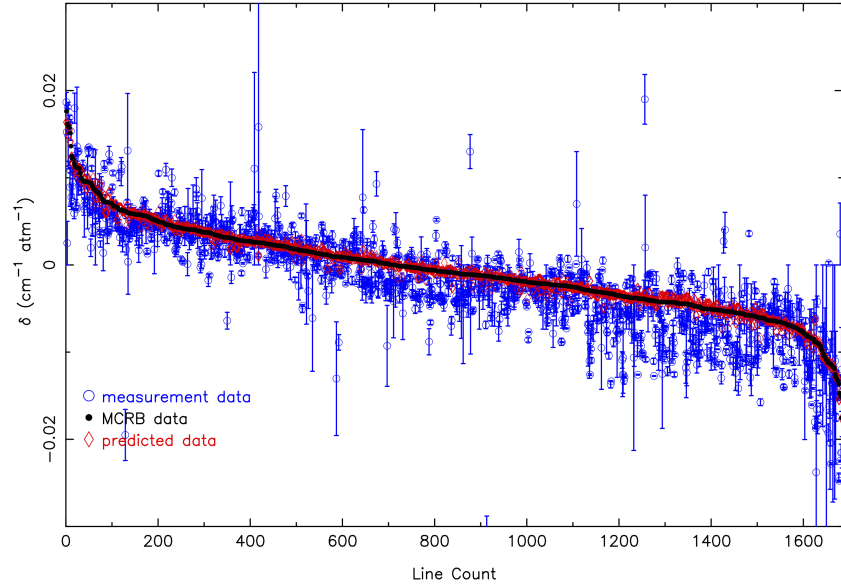
Figures 4a and 4b show the agreement of the MCRB calculations and the values from the prediction routine compared with the measurement database. Shown are the measured  $\nu_2$  transitions (blue open circle symbols with error bars), the MCRB calculated values (black solid circle symbols), and the prediction algorithm values (red open diamond symbols). Figure 4a shows the air-broadened half-width in cm<sup>-1</sup>atm<sup>-1</sup> versus a line count and Fig. 4b is a similar figure for the line shifts. As can be seen, there is excellent agreement for both the MCRB calculated values and the predicted values.

Lastly, for transitions that are not in the above databases, the half-width is estimated by using the rotation band value if it is available, i.e. neglecting the vibrational dependence. However, there are a large number of H<sub>2</sub>O transitions in the HITRAN database that do not have attributions. These are transitions generally taken from *ab initio* calculations where only the rotational quantum number  $J$  and parity are “good” quantum numbers. For these transitions, the rotation band calculations were taken and half-widths as a function of  $J''$  were determined. These data were extrapolated to  $J'' = 50$ . Note, because of the very strong vibrational dependence of the line shift, no comparable average values can be determined. These data are the last component of the database of line shape information.

This general procedure was done in three groups: (H<sub>2</sub><sup>16</sup>O, H<sub>2</sub><sup>18</sup>O, H<sub>2</sub><sup>17</sup>O),



(a)



(b)

Figure 4: (a) half-widths and (b) line shifts in  $\text{cm}^{-1} \text{atm}^{-1}$  for transitions in the  $\nu_2$  band from the measurement database (blue open circle symbols with measurement error bars), the MCRB calculated values (black solid circle symbols), and values from the prediction algorithm (red open diamond symbols) versus a line count ordered on the magnitude of the MCRB half-widths. (For interpretation of the references to color in this figure legend, the reader is referred to the web version of this article.)

(HD<sup>16</sup>O, HD<sup>18</sup>O, HD<sup>17</sup>O) and (D<sub>2</sub><sup>16</sup>O) for air- and self-collisions, producing the isotopologue-dependent files: priority, intercomparison, single measurement, MCRB, predicted, and  $J$  average. It was possible to do the temperature dependence of the  $J$ -average values only for the first group. This procedure assumes that the line-shape data for the oxygen-16, 18, and 17 species of water are the same, which has been well demonstrated by measurement and calculation.

These data sets were taken and Python dictionaries were made using the ro-vibrational quantum numbers as the key. A Python algorithm was written that loads into memory, for all isotopologues of H<sub>2</sub>O, the database dictionaries described above and then reads the HITRAN2020 water-vapor line file and selectively adds the line-shape data to each transition in the prioritized scheme discussed above. A summary of the line-shape data is presented in Table 3.

It is important to note that all the parameters described above are for the Voigt line shape. However, non-Voigt line shapes and specifically HT profile have also been accommodated. HITRAN2016 already contained many of these parameters, but more have been added in the HITRAN2020 edition, specifically in the 2.3- $\mu$ m region. The data are based on the new H<sub>2</sub>O/HDO database in the spectral range 4190–4340 cm<sup>-1</sup> (2.39–2.30  $\mu$ m) that was generated within the framework of the ESA project SEOM-IAS (Scientific Exploitation of Operational Missions — Improved Atmospheric Spectroscopy Databases), ESA/AO/1-7566/13/I-BG. A detailed publication is in preparation [131]. This work was already reported in HITRAN2016 [15], but only line intensities were entered into the database.

In the 4190–4340 cm<sup>-1</sup> region, several Fourier-Transform transmittance spectra of pure and air-broadened water vapor at low and high temperatures were measured and analyzed. These measurements were dedicated to water-vapor parameters to be used in TROPOMI/S5-P retrievals. The analysis was based on a multi-spectrum fit using the HT profile. Line positions, intensities, self- and air-broadened line-shape parameters including speed-dependence and Dicke narrowing parameters as well as their temperature dependence were retrieved

Table 3: Summary of line-shape data for water vapor used for HITRAN2020.

$\gamma$ (H <sub>2</sub> O-air)	H <sub>2</sub> <sup>16</sup> O	H <sub>2</sub> <sup>18</sup> O	H <sub>2</sub> <sup>17</sup> O	HD <sup>16</sup> O	HD <sup>18</sup> O	HD <sup>17</sup> O	D <sub>2</sub> <sup>16</sup> O
Priority data	4681	4414	3391	3 172	919	722	
Intercomparison data	2629	2579	2076	16	16	16	
Single measured datum	5407	4477	2699	566	541	452	222
MCRB data	24 453	7116	3418	23 266	6599	4093	
Predicted data	133 123	18 446	7679	13 892	1215	456	
$J''$ Average values	145 593	5146	8281	15 518	1374	627	22 973
$\delta$ (H <sub>2</sub> O-air)							
Priority data	3600	3379	2553	2947	697	500	
Intercomparison data	701	700	678				
Single measured datum	3271	2795	1743				116
MCRB data	25 695	8282	4304	37 956	8590	5237	0
Predicted data	133 992	21 868	9983				
PL $n$ (H <sub>2</sub> O-air)*							
Priority data	4359	4100	3135	3025	772	575	
Intercomparison data	250	250	245	3	3	3	
Single measured datum	33	23	20				
MCRB data	26 167	8744	4605				
Predicted data	139 445	23 915	11 258				
$J''$ Average values	149 632	5146	8281	53 402	9889	5788	23 195
DPL $\gamma$ T dep (H <sub>2</sub> O-air)**							
MCRB data	29 207	11 706	6945				
Predicted data	140 778	25 265	12 280				
PL $\delta$ T dep (H <sub>2</sub> O-air)*							
MCRB data	25 286	9792	5753				
Predicted data	119 145	20 927	10 107				
DPL $\delta$ T dep (H <sub>2</sub> O-air)**							
MCRB data	29 229	11 714	6949				
Predicted data	140 771	25 256	12 289				
$\gamma$ (H <sub>2</sub> O-H <sub>2</sub> O)							
Intercomparison data	5358	5100	3661	118	90	24	
Single measured datum	16 859	11 703	5651	4533	1119	938	
MCRB data	1607	1526	1234	3741	3300	2200	1531
Rotation band data							15 853
Average values	296 062	23 849	16 998	48 038	6155	3404	5811

\* power law data

\*\* Gamache–Vispoel temperature dependence model. Not included in the official release of HITRAN2020, but will be evaluated for future updates. See Ref. 10.1016/j.jqsrt.2019.106676 for parametrisation of temperature dependencies.

in the analysis. The line-shape parameters are available in the HITRAN2020 database. The data as well as the measurements can also be downloaded from Zenodo [102, 132].

The new 2.3- $\mu\text{m}$   $\text{H}_2\text{O}$  data together with the new 2.3- $\mu\text{m}$   $\text{CH}_4$  data described in section 2.6 have been validated by ground-based solar occultation measurements by Frank Hase, KIT, Karlsruhe, Germany. Figure 5 shows residuals applying HITRAN2012, HITRAN2016, and the new database. The residuals are smallest for the new database. Remaining residuals are caused by imperfect modeling of solar lines.

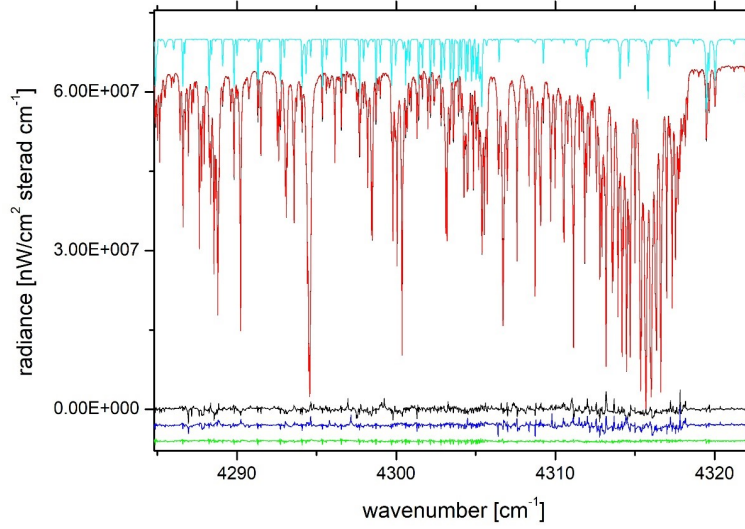


Figure 5: Solar occultation spectrum (red) and residuals for different spectroscopic databases, green: new line list, black: HITRAN2012, blue: HITRAN2016, light blue: solar transmission spectrum. Courtesy Frank Hase, KIT, Karlsruhe, Germany.



## 2.2. CO<sub>2</sub>: Carbon Dioxide (molecule 2)

Current and planned atmospheric remote sensing instruments set a very challenging level of 0.3% accuracy on the retrieved CO<sub>2</sub> column [133], which in turn places stringent requirements on the quality of spectroscopic parameters for this molecule.

The HITRAN2016 line list for the twelve stable isotopologues of carbon dioxide has proven to be an overall improvement over the previous editions of the database (see, for instance, Ref. [42]). However, a number of remaining or new issues were identified as described below. For the HITRAN2020 database, these issues were addressed while a number of previously missing bands above 8000 cm<sup>-1</sup> were added.

### 2.2.1. CO<sub>2</sub> line positions and intensities

The details of the update for line positions and intensities will be described in a dedicated publication in this special issue [134]. Here we briefly summarize important points. Before describing the new data, it is worth recalling that, below 8000 cm<sup>-1</sup>, the line positions for CO<sub>2</sub> transitions in HITRAN2016 were predominantly based on the update to the 2015 version of the Carbon Dioxide Spectroscopic Database (CDSD-296) [135]. The line intensities were mostly of *ab initio* origin [136] based on the work of Zak et al. [137–139] except for the bands that were identified as “sensitive” [137], where CDSD intensities were preferred.

### 2.2.2. Improved line positions and “new” bands

The majority of the CO<sub>2</sub> line positions in the HITRAN2020 database were updated using the line positions from the new 2019 version of CDSD-296 for atmospheric applications [140]. It should be noted that the slightly corrected and updated version of the CDSD-296 database uploaded at [ftp://iaof.ru/pub/CDSD-296/cdsd-296\\_version\\_1.rar](ftp://iaof.ru/pub/CDSD-296/cdsd-296_version_1.rar) was used. The differences with CDSD-296 published in Tashkun et al. [140]: 1.  $\Delta P = 6$  region of the <sup>16</sup>O<sup>12</sup>C<sup>18</sup>O isotopologue was recalculated using the new set of effective dipole moment pa-

rameters; 2. A total of 226 lines with  $\Delta l_2 = 4$  of the  $^{12}\text{C}^{16}\text{O}_2$ ,  $^{13}\text{C}^{16}\text{O}_2$ , and  $^{16}\text{O}^{12}\text{C}^{18}\text{O}$  isotopologues were added. The lower-state energies and the uncertainty codes of the line positions were also transferred from CDSD-296 [140] to HITRAN2020.

The line parameters for the principal isotopologue above  $8000\text{ cm}^{-1}$  were extended by including the new bands from the high-temperature line list from Yurchenko et al. [141] (with appropriate intensity cut off). The assignments for these  $\text{CO}_2$  lines were achieved by using the CDSD-296 [140] and NASA Ames [142] databases. The vibrational assignments were replaced with “-2-2-2-20” when the states were not assigned. Uncertainty codes 3 for the line positions and 4 for the line intensities (see Table 2) were used in the case of the newly added  $\text{CO}_2$  lines.

Also, the 30022-00001 and 30023-00001 bands of the  $^{16}\text{O}^{12}\text{C}^{18}\text{O}$  isotopologue, missing in HITRAN2016 [15] and CDSD-296 [140], were included in the HITRAN2020 line list. The line positions for these bands were computed up to  $J = 34$  using the spectroscopic constants obtained by the fit to the measured line positions from Karlovets et al. [143]. In Ref. [143], it was also shown that the R-branch intensities of the 00041-01101 band of the  $^{12}\text{C}^{16}\text{O}_2$  isotopologue are in good agreement with the Ames values while HITRAN2016 values are largely overestimated. This band is missing in CDSD2019 [140] and included in HITRAN2016 from an old version of CDSD [144]. The line intensities for the three described above bands were updated using the NASA Ames database [142]. Uncertainty code 4 for line positions and uncertainty code 4 for line intensities (see Table 2) were updated for these bands in the HITRAN2020  $\text{CO}_2$  line list. An overview of the HITRAN2020 line lists for all 12 isotopologues of carbon dioxide in natural abundance is plotted in Fig. 6.

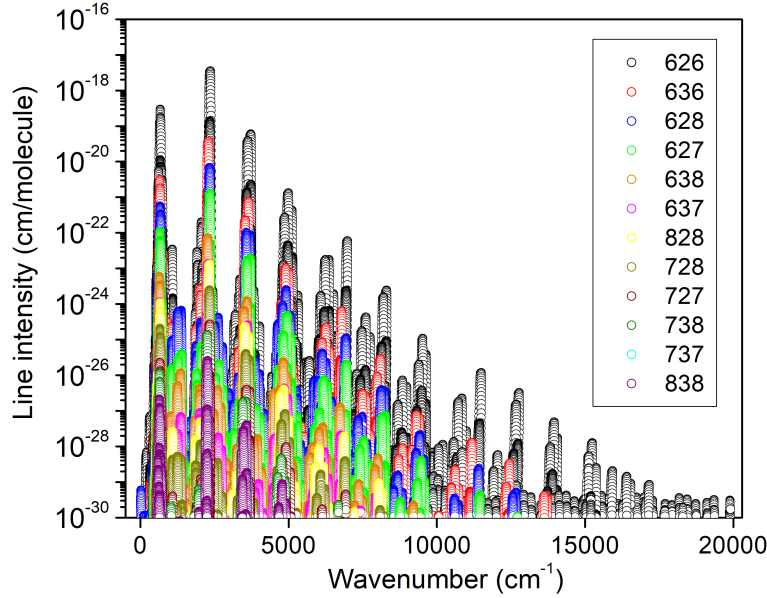


Figure 6: Overview of the HITRAN2020 line lists for all 12 naturally abundant isotopologues of carbon dioxide.

### 2.2.3. Addressing the issues found in HITRAN2016

Most of the HITRAN2016 CO<sub>2</sub> issues were identified by comparisons against laboratory and atmospheric spectra obtained with Fourier Transform Spectrometers (FTS) at the Kitt Peak National Observatory, MkIV balloon, and Total Carbon Column Observing Network (TCCON) [145, 146]. In particular, it was shown that:

- Comparisons with the Kitt Peak laboratory spectrum demonstrated 10–15% rotationally dependent errors in the *ab initio* intensities of the 40002–01101 band of <sup>12</sup>C<sup>16</sup>O<sub>2</sub> isotopologue near 4800 cm<sup>-1</sup>. This region is probed by the OCO-2 instrument [147], so it is important, although it is worth pointing out that the intensities of this hot band are about two orders of magnitude weaker than the strongest lines in that region. This

comparison helped to identify a systematic issue in the *ab initio* calculations [137] when calculating intensities for the transitions that involve either of the interacting 40002 and 21113 vibrational states which are affected by Coriolis interaction.

- In the 1800-2000  $\text{cm}^{-1}$  region, the amount of  $\text{CO}_2$  retrieved with HITRAN2016 is about 5% larger than that retrieved with previous line lists [13, 14]. The biggest deviations in this region were observed for the 11102-00001 band. Two bands 11101-00001 and 11102-00001 borrow the intensities from the strong 00011-00001 band via Coriolis interaction. The CDSD-296 [135] line positions and intensities were used in the previous line lists [13, 14] while HITRAN2016 used the UCL *ab initio* line intensities [137]. It was shown in Ref. [140] that the *ab initio* AMES line intensities [142] for the 11101-00001 band deviate considerably from the observations. The same conclusion is valid for the UCL *ab initio* line intensities [137] of this band.
- The TCCON spectra cover the 3950  $\text{cm}^{-1}$  to 9500  $\text{cm}^{-1}$  region. The HITRAN2016 line lists reduce the  $\text{CO}_2$  retrieved from the 6220  $\text{cm}^{-1}$  and 6338  $\text{cm}^{-1}$  windows by 0.5% and 1.5% respectively, raising additional concerns of consistency at the required level of accuracy. This issue is associated with the line intensities in the 30012-00001 band and is discussed below.

Critical validation tests for the spectroscopic data were carried out to find problems due to insufficient accuracy of line parameters in some of the bands in the  $\text{CO}_2$  line list using available experimental works and the existing theoretical and semi-empirical databases, including NASA Ames [142], UCL [137–139], and CDSD-296 [140]. All updates for the  $\text{CO}_2$  line positions and intensities described above are discussed in Ref. [134].

In the HITRAN2016 line list below 8000  $\text{cm}^{-1}$ , a number of inconsistencies in the rotational structure in the so-called “sensitive bands” (as defined by Zak et al. [137]) due to the mixing of CDSD [135] and UCL [137–139] line intensities

were revealed in Cavity Ring-Down Spectroscopy (CRDS) measurements of  $^{18}\text{O}$  and  $^{13}\text{C}$  enriched and “natural”  $\text{CO}_2$  near  $1.74\text{ }\mu\text{m}$  [148–150]. They concern the perpendicular bands of the  $\Delta P = 9$  series of transitions ( $P = 2V_1 + V_2 + 3V_3$  is the polyad number,  $V_i$  are the vibrational quantum numbers). It leads to apparent inconsistency in the rotational structure with strong intensity variation between successive  $J$  values or even missing transitions (due to falling below the intensity cut-off) as shown, as example, in Fig. 9 of Ref. [148]. Validation tests were carried out for the bands from Refs. [148–150] and the other bands affected by this problem due to the mixing of CDS and *ab initio* intensities in the HITRAN line list using literature values and those from the different  $\text{CO}_2$  databases. Alternative sources of data for each problematic band were identified. See more details in Ref. [134].

#### 2.2.4. New experimental data with sub-percent uncertainty

A number of very accurate measurements have become available after the release of HITRAN2016. Here we make use of the most recent CRDS measurements from NIST [151, 152] and FTS measurements from DLR (reported in this special issue by Birk et al. [153] with the corresponding measurements and line parameter database made available on Zenodo [154]). The results of these works were used to improve the HITRAN line intensities for several NIR bands of the principal isotopologue of  $\text{CO}_2$ . It is interesting to note that in these works it was found that for these particular bands (discussed below) the rotational distribution of the *ab initio* intensities from Zak et al. [137] used in HITRAN2016 was very accurate; however different band scaling factors were recommended. In Refs. [151, 152], the reported intensity uncertainty is better than 0.1%. Fleurbaey et al. [151] showed that a constant scaling of  $1.0069 \pm 0.0002$  of HITRAN2016 values in the 20013–00001 band of  $\text{CO}_2$  ( $\lambda = 2.06\text{ }\mu\text{m}$ ) is consistent with experiment, therefore we have performed this scaling in HITRAN2020. Similarly accurate line intensity measurements for the 3001*i*–00001 ( $i = 2\text{--}4$ ) bands reported by Long et al. [152] were used to improve the  $\text{CO}_2$  line intensities near  $1.6\text{ }\mu\text{m}$ . It was shown in Ref. [152] that their results

and the *ab initio* calculations of Zak et al. [137] agree at the 0.06% level for the 30013–00001 (also targeted by the OCO-2 mission) and 30014–00001 bands, but there is a systematic discrepancy of about 1.1% for the 30012–00001 band. Following these results, the HITRAN2016 line intensities were scaled to the experimental band-dependent scaling factors from Long et al. [152]. Uncertainty code 8 (see Table 2) for the line intensities was given for the corresponding bands in the HITRAN2020 line list.

Ambient temperature FTS measurements of pure CO<sub>2</sub> have been conducted at the German Aerospace Center (DLR) with a Bruker IFS 125HR in the range 6000–7000 cm<sup>−1</sup> [153]. Line intensity accuracies of 0.15% have been reported for the strongest bands in that spectral region. They also covered the 3001*i*–00001 bands, but this time including the 30011–00001 band. The corresponding factor 1.0061 was used to scale the intensities of the 30011–00001 band of the <sup>12</sup>C<sup>16</sup>O<sub>2</sub> isotopologue according to DLR measurements [153]. Good agreement between measurements of intensities of the 30013–00001 and 30014–00001 bands in Ref. [153] and Ref. [152] were found. Nevertheless, for the 30012–00001 band the differences outside of the stated uncertainties were reported. However, these differences are still small, <0.5%. Further investigations will be carried out for future updates of the database. Although this band is not being targeted by the OCO-2 mission it is used in LIDAR applications (see Ref. [155], for instance), therefore it is important to minimize possible uncertainties.

The line intensities of the 00031–00001 band of the principal isotopologue near 1.4 μm came from CDS-296 [135] in the HITRAN2016 edition, because this band was identified as “sensitive” in the *ab initio* calculations [137]. The comparison of the CDS line intensities with the DLR measurements [153] showed rotationally dependent deviations up to 4% for the 00031–00001 band. In the HITRAN2020 line list, the UCL line intensities [137] of the 00031–00001 band were scaled by the factor of 1.1217 to match the line intensities measured by Birk et al. [153]. Also, the HITRAN2016 line intensities of the 10032–10002 and 01131–01101 relatively weak hot bands located near 6900 cm<sup>−1</sup> were compared to the DLR measurements [153]. It was found that the line intensities

of the 10032–10002 band in HITRAN2016 should be scaled by a factor of 1.1346 while the line intensities of the 01131–01101 band should be scaled by a factor of 1.0022.

#### *2.2.5. Introduction of magnetic dipole transitions*

Previously all editions of HITRAN provided only electric dipole transitions for CO<sub>2</sub>. In this edition, the line parameters of the  $\nu_2+\nu_3$  magnetic dipole band of the <sup>12</sup>C<sup>16</sup>O<sub>2</sub> isotopologue were introduced into HITRAN for the first time. These new data will help spectral studies of carbon dioxide-rich planetary atmospheres. This band is forbidden in electric dipole absorption, but it is allowed in electric quadrupole and in magnetic dipole absorptions. The first observation of the  $\nu_2+\nu_3$  band of <sup>12</sup>C<sup>16</sup>O<sub>2</sub> at 3.3  $\mu$ m was made in the atmosphere of Mars (Trokhimovskiy et al. [156]) by the ExoMars Trace Gas Orbiter ACS instrument (Korablev et al. [41]). This band is located in a CO<sub>2</sub> transparency window and identified as a magnetic dipole band (Perevalov et al. [157]). Detailed spectroscopic studies of this band providing the selection rules for the vibration-rotation transitions, as well as the line position and intensity measurements are given in Refs. [156, 157]. The vibrational transition magnetic dipole moment of the  $\nu_2+\nu_3$  band was fitted to the line intensities measured with a Bruker IFS 125 HR FTS and a 30 m base multipass gas cell of the V.E.Zuev Institute of Atmospheric Optics SB RAS (Borkov et al. [158]). Using the obtained vibrational transition magnetic dipole moment and the set of the effective Hamiltonian parameters (Majcherova et al. [159]), the line positions and intensities of this band were generated. The maximum line intensities are on the order of  $3 \times 10^{-28}$  cm/molecule. The calculated line intensities for five R-branch lines of this band (R26-R32 and R36) are in a good agreement with the values measured independently by CRDS [160]. In the HITRAN2020 database, the calculated line parameters of this band are presented up to  $J = 64$  corresponding to the intensity cut-off  $10^{-30}$  cm/(molecule at 296 K. The line position uncertainty code 4 and line intensity uncertainty code 4 (see Table 2) are used for this band. It should be noted that line intensities of this band

retrieved from laboratory spectra [158] are about two times smaller than those recovered from the Martian atmosphere spectra [156]. To distinguish these transitions in the HITRAN2020 CO<sub>2</sub> line list, a letter “m” is introduced into the quantum notation of these magnetic dipole CO<sub>2</sub> transitions in the field dedicated to upper state rotational (“local”) quanta (see HITRAN2004 paper [12] for the description of the .par format).

#### 2.2.6. CO<sub>2</sub> line-shape parameters

The approach we have taken to populate the line-shape parameters of CO<sub>2</sub> broadened by air and CO<sub>2</sub> (self-broadening) is described in the study by Hashemi et al. [161], where different comparisons of the parameters and various validation tests are carried out to demonstrate how the appropriate data sets were chosen for the HITRAN2020 edition. In this section, we highlight these updates and we explain the slight modification (regarding Ref. [161]) based on the new measurements.

The update to the line-shape parameters of CO<sub>2</sub> in the HITRAN2020 edition can be summed into three components:

- revising the Voigt profile (VP) [162] parameters that belong into the ‘.par’ format file.
- addition of the air and self speed-dependent Voigt (SDV) [163–165] parameters for all the transitions of CO<sub>2</sub>.
- updating the already-existing CO<sub>2</sub> line-mixing package developed by Lamouroux et al. [166], and addition of the first-order line-mixing to the database.

These parameters are listed in Table 4 for the Voigt and speed-dependent Voigt parameters group in two separate sets.



Table 4: The VP and SDV line-shape parametrization and their notation in HITRAN*Nonline* and HAPI<sup>a</sup>.

VP parameters <sup>b</sup>	Common notation	Symbol (units)	Database notation
Half-widths	$\gamma_{\text{air}}$	$\gamma_{\text{air}}$ ( $\text{cm}^{-1}\text{atm}^{-1}$ )	gamma_air
	$\gamma_{\text{self}}$	$\gamma_{\text{self}}$ ( $\text{cm}^{-1}\text{atm}^{-1}$ )	gamma_self
Temp. dep. half-widths	$n_{\text{air}}$	$n_{\text{air}}$ (unitless)	n_air
	$n_{\text{self}}$	$n_{\text{self}}$ (unitless)	n_self
Line shifts	$\delta_{\text{air}}$	$\delta_{\text{air}}$ ( $\text{cm}^{-1}\text{atm}^{-1}$ )	delta_air
	$\delta_{\text{self}}$	$\delta_{\text{self}}$ ( $\text{cm}^{-1}\text{atm}^{-1}$ )	delta_self
First-order line-mixing	$Y_{\text{air}}$	$Y_{\text{air}}$ ( $\text{cm}^{-1}$ )	Y_air
	$Y_{\text{self}}$	$Y_{\text{self}}$ ( $\text{cm}^{-1}$ )	Y_self
SDV parameters <sup>b</sup>	Common notation	Symbol (units)	Database notation
Half-widths	$\gamma_0\text{-air}(\text{SDV})$	$\gamma_{\text{SDV}_0\text{-air}}$ ( $\text{cm}^{-1}\text{atm}^{-1}$ )	gamma_SDV_0_air_296
	$\gamma_0\text{-self}(\text{SDV})$	$\gamma_{\text{SDV}_0\text{-self}}$ ( $\text{cm}^{-1}\text{atm}^{-1}$ )	gamma_SDV_0_self_296
Temp. dep. half-widths	$n_{\gamma_0}\text{-air}(\text{SDV})$	$n_{\text{SDV\_air}}$ (unitless)	n_SDV_air_296
	$n_{\gamma_0}\text{-self}(\text{SDV})$	$n_{\text{SDV\_self}}$ (unitless)	n_SDV_self_296
Speed dep. half-widths	$\gamma_2\text{-air}(\text{SDV})$	$\gamma_{\text{SDV}_2\text{-air}}$ ( $\text{cm}^{-1}\text{atm}^{-1}$ )	gamma_SDV_2_air_296
	$\gamma_2\text{-self}(\text{SDV})$	$\gamma_{\text{SDV}_2\text{-self}}$ ( $\text{cm}^{-1}\text{atm}^{-1}$ )	gamma_SDV_2_self_296
Temp. dep. speed dep.	$n_{\gamma_2}\text{-air}(\text{SDV})$	$n_{\gamma_{\text{SDV}_2\text{-air}}}$ (unitless)	n_gamma_SDV_2_air_296
	$n_{\gamma_2}\text{-self}(\text{SDV})$	$n_{\gamma_{\text{SDV}_2\text{-self}}}$ (unitless)	n_gamma_SDV_2_self_296
Line shifts	$\delta_0\text{-air}(\text{SDV})$	$\delta_{\text{SDV}_0\text{-air}}$ ( $\text{cm}^{-1}\text{atm}^{-1}$ )	delta_SDV_0_air_296
	$\delta_0\text{-self}(\text{SDV})$	$\delta_{\text{SDV}_0\text{-self}}$ ( $\text{cm}^{-1}\text{atm}^{-1}$ )	delta_SDV_0_self_296
First-order line-mixing	$Y_{\text{air}}(\text{SDV})$	$Y_{\text{SDV\_air}}$ ( $\text{cm}^{-1}$ )	Y_SDV_air_296
	$Y_{\text{self}}(\text{SDV})$	$Y_{\text{SDV\_self}}$ ( $\text{cm}^{-1}$ )	Y_SDV_self_296
Temp. dep. first-order	$n_Y\text{-air}(\text{SDV})$	$n_{Y_{\text{SDV\_air}}}$ (unitless)	n_Y_SDV_air_296
line-mixing	$n_Y\text{-self}(\text{SDV})$	$n_{Y_{\text{SDV\_self}}}$ (unitless)	n_Y_SDV_self_296

<sup>a</sup> The notations presented here are common notations often encountered in this paper (although sometimes they slightly differ, for instance (SDV) is dropped if there is a dedicated SDV section where parameter is presented), symbols/notation that user can select on HITRAN*Nonline*, and "database notation" is referring to actual names of the parameters in the SQL structure. The latter are used by HAPI for instance to download a particular parameter.

<sup>b</sup> The speed dependence and the temperature dependence of the line shift parameters are not presented in this table because of the lack of accurate measurements for these parameters.

### 2.2.7. Revising the Voigt profile parameters

The Voigt air- and self-broadened half-widths ( $\gamma_{\text{air}}$  and  $\gamma_{\text{self}}$ , respectively) of CO<sub>2</sub> lines and their temperature exponent parameters were re-assessed since the vibrational dependence of the line widths was found to be excessive for some of the CO<sub>2</sub> bands in the HITRAN2016 line list. The concern was that the line widths, calculated for the HITRAN2016 edition, were influenced by some of the less accurate measurements. Additionally, the Lorentzian widths, were retrieved using various line-shape profiles for different bands, and were used in the algorithm [128]. This discrepancy in the line widths using different line-shape models, which can alternate by about 5% [167–169], may have been inadvertently ascribed to a large vibrational dependence of the width parameters. For the bands probed by the OCO-2 mission (1.6  $\mu\text{m}$  and 2.06  $\mu\text{m}$  regions), the HITRAN2016 half-widths belonged to the experimental values of Ref. [170] obtained with the SDV profile without supplying the speed-dependent parameters in the database. To investigate the magnitude of the vibrational-dependence of the broadening parameters in HITRAN2016, the laboratory-measured widths and theoretical values for several bands were collected and examined for CO<sub>2</sub> lines using the VP [161]. Not uncommon for a linear molecule, a relatively weak vibrational dependence was revealed. Accordingly, with regard to updates of the line widths and their temperature dependences for the HITRAN2020 edition, the vibrational dependence of these parameters was ignored, and new values were produced for the air- and self-broadening parameters based on the measured data in Refs. [171, 172] using semi-empirical models (the Padé approximants) described in Ref. [161].

Moreover, the air- and self-shifts ( $\delta_0$ ) in HITRAN2016 (calculated using the semi-classical routine in Ref. [128]) for P- and R-branches were not asymmetric. To produce the rotational and vibrational dependence of shift parameters, the empirical model introduced by Hartmann [173] is implemented to determine the air- and self-shifts of lines for all the vibrational bands of CO<sub>2</sub>. With regard to this approach, the shifts of CO<sub>2</sub> lines can be obtained from the available

measured shift parameters for one band and, after properly determining the fitting coefficients explained in Refs. [161, 173], the shift values can be expanded to the non-measured bands and transitions.

#### *2.2.8. Air and self speed-dependent Voigt parameters*

To reach the accuracy that is required in atmospheric CO<sub>2</sub> retrievals, it is imperative to include more refined line-shape parameters such as the air and self speed dependence of the line broadening and shift parameters together with their temperature dependences. The air-broadening parameters of CO<sub>2</sub> were determined from requantized classical molecular dynamics simulations (rCMDS) [174] using the SDV profile as presented in Table 1 of the supplemental files from Ref. [161] with adequate coverage of the rotational transitions and an extensive set of the required SDV parameters. The results were extrapolated using the Padé approximants and applied to all the bands of CO<sub>2</sub> for the air-broadening, air-speed dependence of width ( $\gamma_2$ -air), and their temperature dependences. Isotopic dependence of the broadening parameters was ignored and therefore the same approach was used for all 12 isotopologues. Comparison of the temperature dependence of the half-widths and the temperature dependence of the speed-dependent parameter in Ref. [161] revealed that the temperature exponents for  $\gamma_0$  and  $\gamma_2$  parameters were not the same. Using HAPI, the SDV parameters were checked by modeling the laboratory spectra, and the corresponding residuals (experiment-calculations) confirmed the validity of the parameters [161]. It is noteworthy that for verifying the parameters, we have also examined the measurements which were issued after the release of the Ref. [161] data and in general very good agreement was found between HITRAN2020 and these measurements that will be published in the near future. See for example Ref. [175].

For updating the self-broadening half-widths ( $\gamma_0$ -self) of CO<sub>2</sub> and the self speed dependence ( $\gamma_2$ -self) of CO<sub>2</sub> using the SDV profile originally, the measured self-broadening by Predoi-Cross et al. [176] and the self speed-dependence measured by Daneshvar et al. [177] were used in Ref. [161]). However, for the

HITRAN2020 edition, the very recent high-accuracy measurements of Birk et al. [153] was used where the authors have provided the self-broadening parameters for several bands in the 1.6  $\mu\text{m}$  region. These data potentially allow for assessing the vibrational dependence of the self-half-width parameters. Figure 7 presents the self-broadening parameters as a function of  $m$  for different bands. The agreement between the measured self-broadening in Ref. [176] and the measured data by Birk et al. [153] for the 30013 – 00001 band is considerably satisfying. The measured self-broadening of Ref. [177] for the 21102 – 00001 band is also comparable with those of 30013 – 00001 band values.

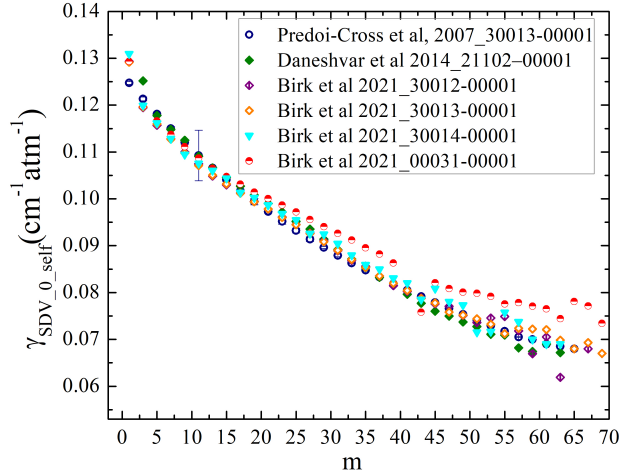


Figure 7: The self-broadening parameters for CO<sub>2</sub> transitions at 296 K using the SDV profile. The values by Predoi-Cross et al. [176] are compared with the measurement of Ref. [177]. The Birk et al. [153] values are presented for different bands as well.

Among the various bands measured in Ref. [153], for the 30011–00001, 30012–00001, 30013–00001, and 30014–00001 bands the vibrational dependence is principally smaller than 1%. However, several data fall outside of the regular pattern for the lines with  $J > 30$  of the 00031–00001 band. An appreciable difference of about 10% for the self-broadening parameters, when comparing the 00031–00001 and 30013–00001 band lines, indicates the vibrational depen-

dence of the self-widths. Therefore for HITRAN2020, the  $3\nu_3$  band was treated separately, and for all other bands no vibrational dependence has been assumed at the moment and the 30013-00001 band results were used. The measured self-shifts of Ref. [153] were used to update the self-shifts for the measured bands.

Similarly, for updating the self speed-dependence of widths, the measured data of Ref. [153] were used to avoid mixing the data from different sources. Figure 8 displays the  $\gamma_2$ -self parameters for different bands and, as can be seen after  $m > 35$ , the values deviate from each other. The Padé approximants were used for extrapolating the 30013-00001 band results from Ref. [153] to all the bands except for the 00031-00001 band. After more high-quality experiments become available in various bands, it would be worth attempting to determine the vibrational dependence of the half-widths, their temperature, and speed-dependences.

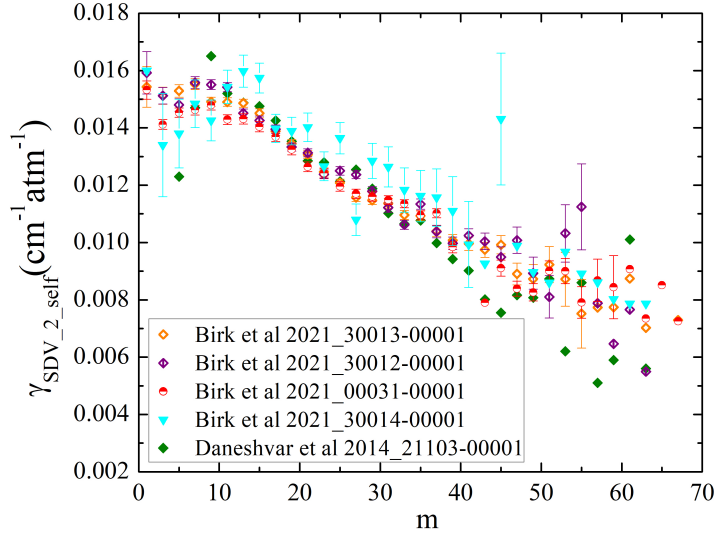


Figure 8: The self speed-dependence of width parameters for CO<sub>2</sub> transitions at 296 K using the SDV profile. The measured values for different bands by Birk et al. [153] and Daneshvar et al. [177] are compared.

### 2.2.9. Updating the CO<sub>2</sub> line-mixing package

The FORTRAN code by Lamouroux et al. [166] is used for predicting the line-mixing effect in all the bands of CO<sub>2</sub> either accounting for the full line-mixing (using the VP) or the first-order approximation (using the VP and SDV profiles). The update to the CO<sub>2</sub> line-mixing package is specified in Ref. [161] and the modifications to the line positions, intensities [134] and the relevant line-shape parameters [161] for the HITRAN2020 edition were addressed to update the package. Also, the partition functions were calculated employing TIPS2017 [178]. Moreover, the first-order line-mixing and its temperature dependence were implemented in HAPI to be taken into account with different line-shape profiles [51]. Based on the analyses performed using the measured laboratory spectra in Ref. [161], similar residuals were obtained when the transmission spectra were generated using i) the VP accounting for full line-mixing, and ii) the SDV modeled with first-order line-mixing. For instance, for the examined regions when only the P- and R-branch lines were present, the difference was on the order of 0.1% at 296K. Compared to HITRAN2016, an improvement of about 0.5% in the calculated residuals was achieved when using the new spectroscopic parameters and including line-mixing (implied by figures 13, 16, 18, and 19 of Ref. [161]).

For the purpose of atmospheric validation, the CO<sub>2</sub> line-mixing package was used to calculate the absorption coefficients (ABSCO tables) in the 4700–5100 cm<sup>-1</sup> region corresponding to the so-called “strong band” in the OCO-2 mission. The ABSCO tables are produced using both Voigt profile accounting for the first-order and full line-mixing, and the speed-dependent Voigt including the first-order line-mixing which are available at Zenodo [179]. As illustrated in Fig. 9, the generated tables were preliminarily tested by the OCO-2 science team through comparison of modeled spectra to TCCON measurements of atmospheric transmission.

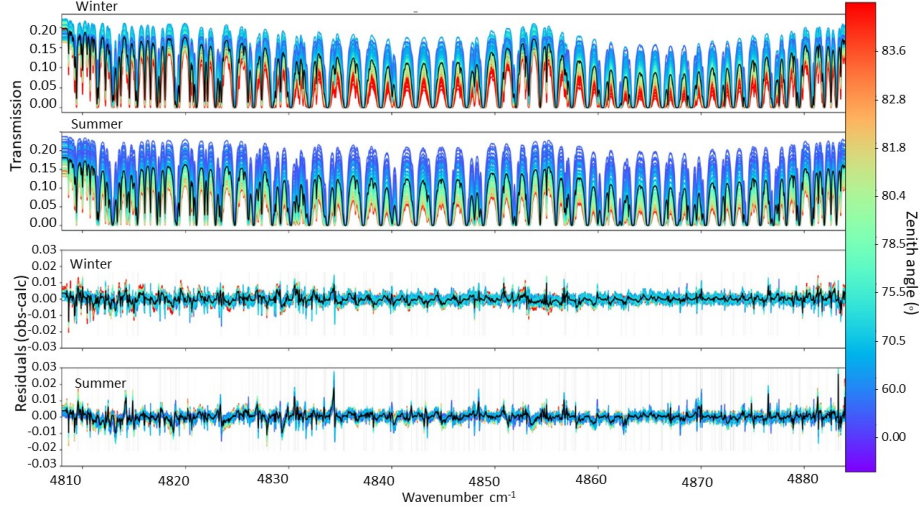


Figure 9: Atmospheric transmission spectra (upper two panels) and model residuals (lower two panels) in the  $2.06 \mu\text{m}$  band region for the summer and winter seasons for different zenith angles (in degree). The modeled spectra were calculated by F. A. Oyafuso at Jet Propulsion Laboratory, California Institute of Technology, Pasadena, using the ABSCO tables produced by the updated line-mixing package for HITRAN2020 using the Voigt profile plus the full line-mixing effect. In both sets of upper and lower panels, the black lines represent the average transmission and residuals (observations - calculations), respectively.

The mean transmissions and mean residuals are shown with the black line. The third panel (from the top) shows the residuals for the summer which are larger than the winter residuals.

All of the verification investigations [161] confirmed that including the first-order line-mixing parameters is a quick method for calculating the cross-sections with a reasonable improvement in the residuals. Nevertheless, wherever the Q-branch lines are present, the first-order approximation fails to correctly model the spectra, and ultimately, it creates negative absorption coefficients. Therefore, for the more compact spectral regions, the application of full line-mixing is recommended. The current form of the line-mixing code does not support the formulation of the SDV profile accounting for the full line-mixing effect because of the complexity of the calculation. This issue will be studied for the forthcoming releases of the database. Furthermore, for future editions, we plan to add the HT profile [73] parameters to the database of carbon dioxide param-

eters, which will be valuable in enhancing the retrieval accuracy if the proper functional forms are adopted in the radiative transfer codes.

#### *2.2.10. Introducing water-vapor broadening parameters*

The predominant importance of water vapor in the terrestrial atmosphere, and its key role in the Earth’s climate system, mean the water spectrum has been the subject of numerous studies. At the same time the collisional broadening effects introduced by water vapor on other molecules are required in order to accurately characterize and model spectra of the atmospheres with significant amounts of water vapor. Furthermore, the collisional broadening of spectral lines by water vapor is much larger than that by nitrogen and oxygen. Therefore, we introduced the pressure-broadening parameters including the temperature-dependent exponents due to water vapor in the HITRAN database through semi-empirical models based on the third- to fourth-order Padé approximant. The first part of this work was reported for the lines of CO<sub>2</sub>, N<sub>2</sub>O, CO, CH<sub>4</sub>, O<sub>2</sub>, NH<sub>3</sub>, and H<sub>2</sub>S [48].

The water vapor broadening parameters ( $\gamma_{\text{H}_2\text{O}}$ ) and their temperature dependence exponents ( $n_{\text{H}_2\text{O}}$ ) for CO<sub>2</sub> transitions were determined using a semi-empirical approach by fitting accurate parameters to a Padé approximant. The collected data sets included early theoretical calculations from Rosenmann et al. [180, 181] and the more recent experimental results from Sung et al. [182], Wallace et al. [183] and Delahaye et al. [184]. The fitted half-widths of water vapor broadening are valid up to  $J \leq 121$ . The new Padé function approach is advantageous over extend the standard polynomial functions as it overcomes the convergence issues for high rotational  $J$  transitions, which can become significant at high temperatures. Meanwhile, the temperature-dependent exponents for water vapor broadening of CO<sub>2</sub> are also included in the updating water-vapor broadening parameter data sets.



### 2.3. $O_3$ : Ozone (molecule 3)

Ozone plays a crucial role in the chemistry of the terrestrial atmosphere. Its concentrations and vertical distribution are among key factors that drive the quality of human life on earth, both as a protector from harmful UV radiation and as a pollutant. Not surprisingly, it is actively monitored by satellite [18, 20, 21, 185], balloon [186, 187], and ground-based spectrometers [188] operating from the MW to UV parts of the spectrum.

Although ozone was one of the first gases introduced into HITRAN, and there is no lack of laboratory measurements (see, for instance, review by Barbe et al. [189]) or theoretical calculations, it remains one of the most challenging line lists in the database. In particular, a major challenge is related to obtaining self-consistency in band intensities of ozone in various spectral intervals. This is mandatory to avoid discrepancies in the atmospheric ozone retrieval using different spectral windows. In this context, the previously available line-by-line compilations were not fully satisfactory, as shown by laboratory and atmospheric validations [190].

The IR measurements of line intensities of ozone are very challenging. Usually, relative uncertainties in line intensities obtained via fits of observed spectra with effective spectroscopic models could be significantly smaller than the absolute uncertainties. This is because the dynamic range in line intensities is very large, making it necessary to use spectra obtained at different pressure/path length conditions in the fit. As ozone is an unstable species, the partial pressure conditions are difficult to control precisely, which is one of the main factors contributing to inconsistencies between absolute band intensities in different spectral intervals. Related issues for laboratory measurements have been discussed in Refs. [191–196] and references therein. Therefore simultaneous measurements in the MW or UV regions are usually carried out, because the intensities of low- $J$  MW lines can be directly linked to the permanent dipole moment of the molecule, which is known very precisely. The UV standards were considered to be well-calibrated. Also, due to relatively small rotational constants, the IR spectra of ozone are quite congested. Consequently, only a

restricted number of the non-blended lines could be accurately measured. Complete line lists for a given band system are typically produced by calculations using empirically-fitted parameters of the effective Hamiltonian (EH) and effective dipole transition moment (EDTM) parameters [189, 197]. This implies the increase of uncertainties for extrapolated/interpolated ranges.

As described in the previous section devoted to carbon dioxide, modern *ab initio* calculations allow the determination of precise intensity values for many molecules, except for so-called “sensitive” bands or lines that for molecules like carbon dioxide are not very frequent. Unfortunately, for ozone, it is not always the case, and although a great many calculated intensities are of very good quality, the amount of lines where intensities can not be calculated reliably from first principles is quite large due to severe resonance perturbations, many of which are caused by the “dark” states [189]. Nevertheless as will be shown below, *ab initio* calculations could be employed for many transitions or serve as a validation tool.

Ozone data in HITRAN2016 [15] was a substantial improvement compared to previous editions in many spectral regions [42]. Following the release of HITRAN2016, Drouin et al. [193] measured the MW and IR bands at 10  $\mu\text{m}$  simultaneously and found an excellent consistency (better than 1%) between these bands when using HITRAN2016. Assuming that the intensities of the strongest lines in the pure rotational band should be known on a sub-percent level, Drouin et al. [193] concluded that the intensities in the 10  $\mu\text{m}$  band in HITRAN2016 are therefore also of excellent quality. However, Birk et al. [198] have shown that the MW intensities in HITRAN were too weak by  $\sim 3.8\%$ , which in the context of the conclusions of Drouin et al. [193] implies that the same scaling should apply to the 10  $\mu\text{m}$  band. These findings have paved the way to a extensive international campaign for remeasuring and recalculating spectral parameters of ozone in all spectral regions from the MW to UV. Although not all of these works have been published, the new data had gone through intensive evaluation procedures, including comparisons with laboratory, ground-based, satellite, and balloon measurements. It was concluded that a combination of data from new

laboratory and theoretical sources had yielded much better consistency of the intensities of ozone bands but also increased quality of all parameters of individual lines. This is undoubtedly one of the highlights of HITRAN2020. Below we describe three sets of infrared experimental and theoretical data in the IR region and how they were combined (based on the validations) to form the HITRAN2020 ozone line list. UV data are still only available in cross-sections, and the new dataset is described in Section 3.2.1.

### 2.3.1. New “S&MPO\_2020d” line list

In December 2020, a new update for the S&MPO Reims-Tomsk line list (<http://smpo.iao.ru>, <http://smpo.univ-reims.fr>) [189] was made, featuring substantial changes in line intensities [199, 200] and line positions [201] not only for the principal but also for minor isotopologues [202, 203]. The line positions and lower-state energies in S&MPO are based on empirical Hamiltonian models, while the intensities are mostly empirical or semi-empirical, which in the new edition often includes corrections based on *ab initio* calculations.

#### 2.3.1.1. $^{16}\text{O}^{16}\text{O}^{16}\text{O}$ : *ab initio* intensity corrections and empirical line positions.

*Ab initio* calculations of ozone have significantly advanced over the years, which enables one to improve the modeling of collisional processes [204, 205] and of vibrational dynamics [206, 207] using the PES [208] obtained at a high level of electronic structure theory. Recently, it was shown [199] that line intensity calculations by variational method from the *ab initio* dipole moment surfaces (DMS) of Tyuterev et al. [209] can help to resolve controversies among previously reported  $^{16}\text{O}^{16}\text{O}^{16}\text{O}$  data sets in MW, 5 and 10  $\mu\text{m}$  ranges.

A comparison of results from Ref. [209] with very accurate FTS intensity measurements of Barbe et al. (GSMA, Reims) and preliminary data from Refs. [194, 195] of Janssen, Jacquemart et al. (LERMA/MONARIS, Paris) in the 5 and 10  $\mu\text{m}$  ranges and with Stark-effect data in the MW [210] have shown an average agreement within 0.3–1.0% for strong lines between *ab initio* theory

and these experiments. The tight scatter in these results made it evident that the HITRAN2016 intensities must be increased by 2.5% to 4.5% in the corresponding regions. This was also consistent with the results reported by the DLR group [196] and Drouin et al. [193, 198]. For the 2020 update of the S&MPO line list (and ultimately HITRAN2020 in selected spectral regions), we have extended *ab initio* intensity corrections for 31 bands including 14 cold and 17 hot bands in the range from 0 to 4300  $\text{cm}^{-1}$  using the dipole moment surfaces from Ref. [209]. The corresponding details of calculations will be described in the dedicated publication in this special issue [200]. The summary of changes in line intensities between S&MPO\_2020d and HITRAN2016 is shown in Figure 10.

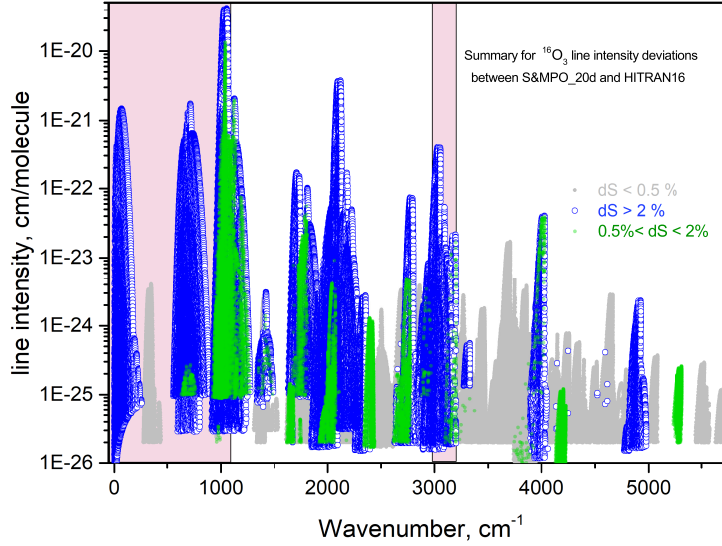


Figure 10: Summary for the line intensity deviations  $dS = (S_{\text{S\&MPO\_20d}} - S_{\text{HIT2016}})/S_{\text{HIT2016}}$  in % for the ozone  $^{16}\text{O}_3$  transitions in 0–5791  $\text{cm}^{-1}$  range. Each point or circle in the Figure corresponds to a line in log scale. Most of changes with  $dS > 2\%$  correspond to *ab initio* intensity correction as described in Ref. [200]. Shaded area correspond to the spectral regions where S&MPO\_20d was not used for the HITRAN2020 ozone database.

The target accuracy of line intensities for unstable species like ozone is currently considered as being within 1% for strong and about 3 or 5% for weak transitions. At this level of accuracy, the best *ab initio* calculations can be

competitive with precise experimental measurements [199]. However, it is well known that *ab initio* calculations for multi-electron molecules are not able to achieve experimental high-resolution accuracy in line positions (0.001–0.0001  $\text{cm}^{-1}$ ) because this corresponds to relative precision requirements in wavenumbers of  $10^{-7}$  or  $10^{-8}$ . In a previous release of the S&MPO database [192], the line positions were computed from empirically-fitted EH parameters except for the cases where effective models do not provide experimental accuracy because of the large number of strongly coupled bands and “dark states” perturbations [189]. Empirical corrections to line positions and energy levels must then be accounted for. For the current S&MPO\_20d version, we have introduced three types of changes in line positions in the range 0–5500  $\text{cm}^{-1}$ . Part of these changes corresponded to a simple update of old EH parameters from the past S&MPO releases by more recent ones: this concerns MW and  $\nu_2$  ranges, as well as the 4000  $\text{cm}^{-1}$  range [211].

Furthermore, a new list including both line positions and intensities was generated for the strongest  $\nu_1/\nu_3$  bands using unpublished EH and EDTM parameters [201] obtained from the analyses of GSMA/Reims spectra at 10  $\mu\text{m}$ . In particular, the line positions with large  $K_a > 20$  rotational quantum numbers were improved for the  $\nu_3$  band. The third type of change concerns empirical corrections of line positions near 2700  $\text{cm}^{-1}$  and in the 2900–5500  $\text{cm}^{-1}$  range. Following the recent analysis of Mikhailenko and Barbe [211], the most significant corrections concern the complex band system (103)/(004)/(310)–(000) near 4000  $\text{cm}^{-1}$  and in the corresponding hot bands. Some other corrections concern “exotic” accidental resonance perturbations like those involving the (040) and (050) states. Note that a line position correction in one range resulted in many more “induced” corrections in other ranges via the shifts in energy levels. Finally, a limited number of line intensities were empirically adjusted, particularly in the ranges near 3000  $\text{cm}^{-1}$  and 5000  $\text{cm}^{-1}$  [201]. Overall, in the spectral range of 0–5791  $\text{cm}^{-1}$ , the S&MPO\_20d list contains 312 669 lines versus 278 586 lines in HITRAN2016. There are 273 233 common lines in both lists, 87 481 of which have deviations in line position  $d\nu > 0.0003 \text{ cm}^{-1}$  and 136 163 have deviations

in line intensities  $dS > 2\%$ . A summary of lists for 25 newly generated weak hot bands is presented in Table 5. A global Table including band statistics versus HITRAN2016 is given in the Supplementary Materials

Table 5: New (with respect to HITRAN2016) S&MPO.20d bands of the principle isotopologue of ozone in “natural” abundance in the range 0–5791  $\text{cm}^{-1}$ . Minimum and maximum wavenumbers  $\nu_{\min}$  and  $\nu_{\max}$ , number of lines  $N$  and sum of line intensities within individual bands  $S_\nu$ . Note that only S&MPO lines that were adapted for HITRAN are those above 1180  $\text{cm}^{-1}$  and outside of 2975–3205  $\text{cm}^{-1}$  range

$v'$	$v''$	$\nu_{\min}, \text{cm}^{-1}$	$\nu_{\max}, \text{cm}^{-1}$	$N$	$S_\nu, \text{cm/mol}$
0 1 2	0 0 2	618.779	733.136	420	1.297E-23
1 1 1	1 0 1	646.832	727.301	254	7.086E-24
2 1 0	2 0 0	675.024	709.057	54	1.517E-24
0 0 3	2 0 0	950.562	1000.782	4	1.003E-25
1 3 0	2 0 0	951.144	1004.815	2	5.343E-26
2 1 0	0 0 2	954.526	1009.611	2	8.830E-26
1 0 2	0 3 0	955.060	987.713	2	2.277E-25
3 0 0	2 0 0	1059.350	1157.311	249	9.420E-24
2 0 1	1 0 1	1093.352	1156.125	39	9.705E-25
2 2 0	0 2 1	1139.984	1187.006	164	4.218E-24
3 0 0	0 0 2	1155.052	1208.551	12	2.628E-25
2 2 0	1 1 0	1761.375	1817.097	92	3.032E-24
2 0 2	0 0 2	1994.841	2105.185	82	2.899E-24
2 0 2	0 3 0	2011.499	2043.890	2	4.439E-26
2 3 0	2 0 0	2015.029	2062.849	5	1.524E-25
0 5 0	0 2 0	2020.866	2073.526	4	6.219E-25
3 0 1	1 0 1	2154.827	2159.443	6	1.271E-25
0 2 2	0 0 1	2320.650	2365.711	191	2.514E-24
1 2 1	0 0 1	2423.376	2435.536	29	4.182E-25
2 2 0	1 0 0	2476.903	2484.720	15	1.717E-25
0 5 0	0 1 0	2718.726	2771.609	4	6.880E-25
2 2 0	0 1 0	2794.977	2922.083	488	2.933E-23
0 5 0	0 0 0	3419.165	3472.267	4	2.591E-25
3 0 2	0 0 1	4069.803	4143.464	905	5.364E-23
3 0 2	1 0 0	4109.876	4143.008	3	3.816E-26

A summary of line position corrections and new lines is given in Figure 11. A detailed description will be presented in a dedicated publication in this special issue [201].

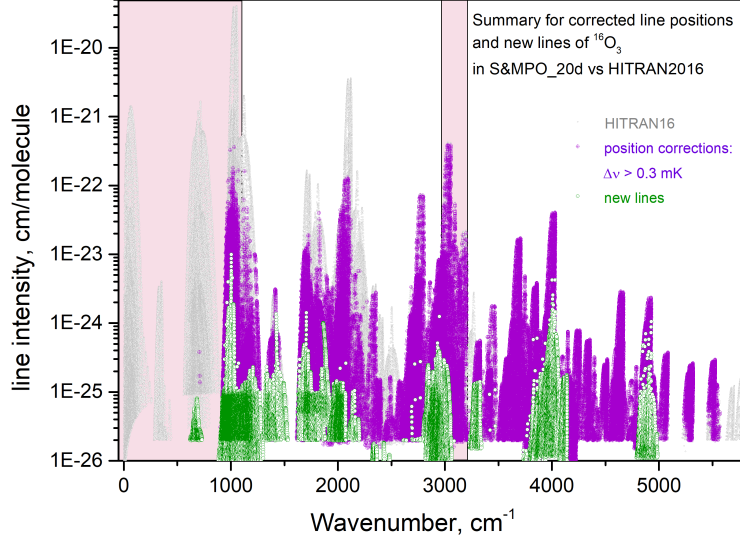


Figure 11: Summary for newly added hot bands (in green) and line position corrections [201]. The transitions for the  $^{16}\text{O}_3$  ozone in  $0\text{--}5791 \text{ cm}^{-1}$  range corrected by more than  $d\nu = \nu(\text{S\&MPO\_20d}) - \nu(\text{HIT2016}) > 0.0003 \text{ cm}^{-1}$  are indicated in magenta. Each point or circle in the Figure corresponds to a line in log scale. Shaded area correspond to the spectral regions where S&MPO\_20d was not used for the HITRAN2020 ozone database.

An example of an improvement for the transmittance calculation near  $4000 \text{ cm}^{-1}$  using the S&MPO\_20d list including recent results of analysis [211] with the subsequent *ab initio* corrections for intensities [200] is given in Figure 12.

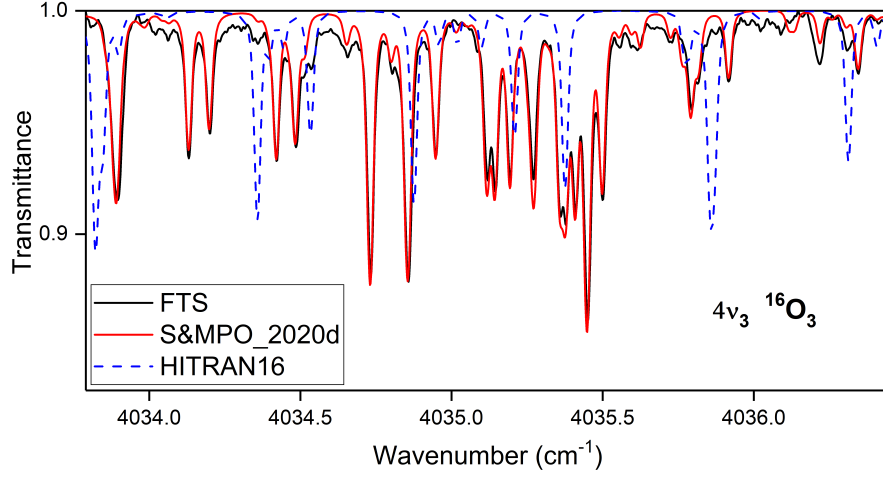


Figure 12: Example of an improvement of the comparison with experimental FTS laboratory spectra using a simulation with the new S&MPO\_20d (hence HITRAN2020 in this region) line list in the range of the  $4\nu_3$  band.

It is instructive to compare the S&MPO\_20d line list with other most recent data based on accurate laboratory intensity measurements. Tables 6 and 7 show an excellent agreement for RMS and mean deviations in line-by-line intensities with the DLR list described in Subsection 2.3.2 in the  $10\ \mu\text{m}$  range. On the full sample of the common lines of these lists, the sums of intensities  $S_\nu$  gives very close values with a deviation of only 0.07% for the strongest ozone band  $\nu_3$  and of 0.25% for  $\nu_1$  (see Table 6). A systematic off-set is almost negligible – between 0.1% and 0.2% for the mean intensity values. For the strong and medium lines, the RMS deviation is significantly smaller for the dominant band  $\nu_3$  within about 0.25% (Figure 13). The deviation increases to an RMS of 0.5% when extending to medium lines including the sample of 1000 transitions (see Table 7). As expected, the scatter increases for weak lines, though many of these weak lines have not been actually measured and rely on extrapolations.



Table 6: Comparison of integrated intensities for the cold bands in the 10  $\mu\text{m}$  range between S&MPO\_20d and DLR line lists for the principle isotopologue, for the common sample of transitions.

Band	$N$	$\nu_{\min}$	$\nu_{\max}$	S&MPO $S_\nu$	DLR $S_\nu$	$\Delta(S_\nu)$
$\nu_3$	6212	980.042	1219.990	1.398E-17	1.397E-17	0.07 %
$\nu_1$	5991	980.126	1219.838	5.287E-19	5.274E-19	0.25 %

Table 7: Comparison of RMS and mean intensity deviations between S&MPO\_20d and DLR line lists  $^{16}\text{O}_3$  for strong lines of the  $\nu_1$  and  $\nu_3$  bands

Band	$N$	$S_{\min}$	$S_{\max}$	RMS( $S$ ), %	Mean( $S$ ), %
$\nu_3$	500	9.4E-21	4.2E-20	0.24	0.08
	1000	2.0E-21	4.2E-20	0.50	0.15
$\nu_1$	500	3.0E-22	3.4E-21	0.60	0.23
	1000	1.6E-22	3.4E-21	0.88	0.13

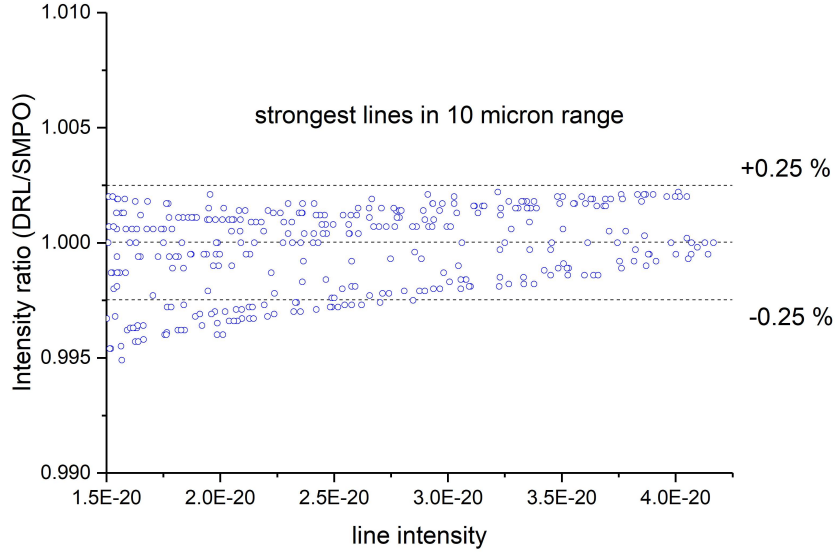


Figure 13: Ratio of intensities  $S(\text{DLR})/S(\text{S\&MPO.20d})$  for the strongest lines in the 10  $\mu\text{m}$  range

Another accurate set of intensities in the 5 and 10  $\mu\text{m}$  ranges have been recently obtained in Refs. [194, 195]. Preliminary comparison between the *ab*

*initio* and empirical list fitted to LERMA spectra [195] was reported in [199] where only 50 of the strongest transitions were included. Table 8 summarizes the results of an extended comparison with a complete set of experimental lines determined by Jacquemart et al. [195] from LERMA spectra using a speed-dependent line profile. At  $10\mu\text{m}$ , this also gives a sub-percent RMS deviation including lines of three measured bands  $\nu_3$ ,  $\nu_1$  and  $\nu_2 + \nu_3 - \nu_2$ . at  $5\mu\text{m}$  the agreement for two measured bands  $\nu_1 + \nu_3$ ,  $2\nu_3$  is slightly better with an RMS deviation of 0.67%. Table 8 describes a systematic offset between 0.5% and 0.6% in both ranges for  $S_\nu$ , and for the mean deviations. These differences are shown for the strong lines in Figure 14.

Table 8: Comparison of RMS, mean and integrated deviations for line intensities between the S&MPO\_20d list and experimental values from LERMA [195] in the 10 and 5  $\mu\text{m}$  ranges for  $^{16}\text{O}_3$

Range	Bands	$N$	$\Delta(S_\nu)^a$	RMS( $S$ )	Mean ( $S$ )
10 $\mu\text{m}$	$\nu_3$ , $\nu_1$ , $\nu_2 + \nu_3 - \nu_2$	497	-0.62%	0.98%	-0.53%
5 $\mu\text{m}$	$\nu_1 + \nu_3$ , $2\nu_3$	319	-0.56%	0.67%	-0.52%

<sup>a</sup>relative deviations of sums of all line intensities for the range

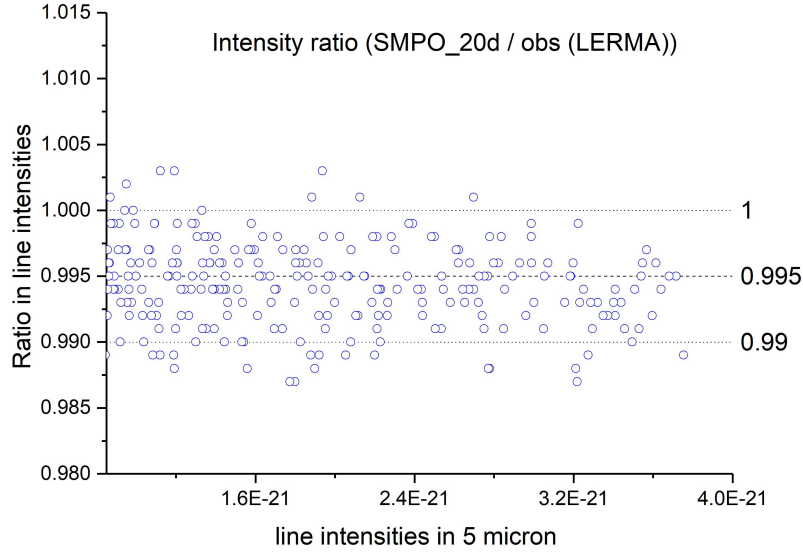


Figure 14: Ratio of intensities  $S(\text{S\&MPO}_{20\text{d}}) / S(\text{LERMA}_{\text{obs}})$  for the strongest lines in the  $5\ \mu\text{m}$  range.

Interestingly, on the common sample of measured lines, the LERMA(obs) gives almost exactly the same ratio  $S_{\nu}(10\ \mu\text{m})/S_{\nu}(5\ \mu\text{m})$  as the S\&MPO-20d line list testifying to a perfect intensity consistency of the two data sets between these spectral ranges, which are of primary importance for atmospheric applications.

*2.3.1.2.  $^{16}\text{O}^{16}\text{O}^{18}\text{O}$  isotopologue.* About thirty ozone spectra enriched with  $^{18}\text{O}$  were recorded with the GSMA FTS spectrometer using different cell lengths,  $^{18}\text{O}/^{16}\text{O}$  oxygen isotopic mixtures, and different pressures varying from 4 to 20 Torr. The analyses of the spectra in the range between  $900$  and  $3850\ \text{cm}^{-1}$  allowed us to extend essentially the information about ro-vibrational transitions and energy levels of the  $^{16}\text{O}^{16}\text{O}^{18}\text{O}$  isotopologue, belonging to the  $C_s$  point group. The assignment and modeling have been carried out using EH and EDTM operators with the help of theoretical predictions on the band centers,

rotational constants and some coupling parameters. The latter ones have been derived from *ab initio* potential energy surface (PES) [208] using the MOL\_CT code [212] in the standard format of EH [192, 213] of the S&MPO system. We fixed the coupling term values to the predicted ones for the complete polyads of observed bands below  $2500\text{ cm}^{-1}$  to characterize the intensity transfer among the observed bands. Above  $2500\text{ cm}^{-1}$ , our effective models include only those coupling terms, which correspond to the observed perturbations. In total, 9976 ro-vibrational transitions belonging to the 15 bands of  $^{16}\text{O}^{16}\text{O}^{18}\text{O}$  were assigned and modeled with average accuracy of the order of  $10^{-3}\text{ cm}^{-1}$ . The set of 7030 corresponding upper-state ro-vibrational energy levels were determined. The calculated line list of 51 100 transitions has been introduced in the S&MPO information system. We provide the HITRAN2020 database with a line list of 49 148 transitions for 13 observed bands of  $^{16}\text{O}^{16}\text{O}^{18}\text{O}$  up to  $\Delta\nu = 3$ . The corresponding information is summarized in Table 9.

*2.3.1.3.  $^{16}\text{O}^{16}\text{O}^{17}\text{O}$  and  $^{16}\text{O}^{17}\text{O}^{16}\text{O}$  isotopologues.* The 5 and 10  $\mu\text{m}$  ranges of the  $^{17}\text{O}$ -substituted ozone isotopologue were reinvestigated using GSMA Fourier spectra. The line positions for 15 transitions in the  $\nu_3$  band in HITRAN2016 data for the  $^{16}\text{O}^{17}\text{O}^{16}\text{O}$  isotopomer were shifted by an order of  $10^{-3}\text{ cm}^{-1}$  with respect to the experimental spectrum. The spectral line parameters for this isotopic species were included in the HITRAN database during almost two decades from different sources: the  $\nu_1$  and  $\nu_3$  bands from Ref. [214] and  $\nu_1 + \nu_3$  from Ref. [215]. In these calculations, different parameters for the ground state have been used. In our work, the  $\nu_1$ ,  $\nu_3$  and  $\nu_1 + \nu_3$  bands of the  $^{16}\text{O}^{17}\text{O}^{16}\text{O}$  isotopomer were modeled simultaneously to improve the parameters of the ground state energy level. The analysis of the  $\nu_1 + \nu_3$  bands of  $^{16}\text{O}^{16}\text{O}^{17}\text{O}$  was also extended. The parameters allowed for the generation of new line lists in the corresponding spectral ranges. They are included in the S&MPO database and provided for the HITRAN2020 version.

Table 9: HITRAN2020 ozone update summary: isotopologues  $^{16}\text{O}^{16}\text{O}^{18}\text{O}$ ,  $^{16}\text{O}^{16}\text{O}^{17}\text{O}$  and  $^{16}\text{O}^{17}\text{O}^{16}\text{O}$

Isotopologue	Band	$N$	Region, $\text{cm}^{-1}$	$S_\nu$ , $\text{cm}\cdot\text{mol}^{-1}$
$^{16}\text{O}^{16}\text{O}^{18}\text{O}$	001-000	3694	961.88–1117.65	5.122E-20
	100-000	7216	973.69–1187.47	4.017E-21
	020-000	505	1342.89–1398.80	7.706E-25
	011-000	2474	1644.36–1720.54	2.033E-22
	110-000	4188	1663.38–1894.67	6.376E-23
	002-000	8149	1897.41–2113.39	6.941E-22
	101-000	3468	2017.37–2113.59	3.889E-21
	200-000	8635	2063.76–2274.12	2.354E-22
	111-000	1910	2701.72–2767.50	9.528E-23
	111-010	2166	2015.15–2084.74	3.835E-27
	003-000	1562	2930.52–3011.53	4.316E-22
	102-000	3241	2965.77–3123.18	1.221E-22
	201-000	1940	3103.03–3164.88	3.782E-23
	Total	49148	961.88–3164.88	6.101E-20
$^{16}\text{O}^{16}\text{O}^{17}\text{O}$	101-000	2135	2045.82–2121.62	6.078E-22
$^{16}\text{O}^{17}\text{O}^{16}\text{O}$	001-000	1157	968.30–1054.70	4.857E-21
	100-000	107	1082.60–1124.24	3.571E-23
	101-000	820	2029.66–2101.31	2.674E-22
Total		2084	968.30–2101.31	5.160E-21

### 2.3.2. $O_3$ DLR database

New mid infrared ozone measurements in the range 600–1200  $\text{cm}^{-1}$  were carried out within the framework of the ESA project SEOM-IAS, ESA/AO/1-7566/13/I-BG. A detailed publication is in preparation [196]. The goal of this task was to resolve discrepancies in retrieved atmospheric ozone amount between observations in the mid-infrared (MIR) and ultraviolet (UV). An important output of this effort is the new data described in this section and in the section on UV absorption cross-sections for  $O_3$  (see Section 3.2.1).

The new FTS transmittance measurements were carried out with a Bruker IFS 125 HR high resolution spectrometer in combination with a coolable four-window single-pass cell [216] of pathlength 22.15 cm which was also used for the UV measurements utilizing a different window pair. The same four-window cell was used under reproducible conditions for both the UV and MIR measurements, and absorption spectra were recorded under sealed-off conditions. Ozone was prepared from  $O_2$  in a silent discharge and purified and handled using procedures similar to those given in [217]. Because decomposition of ozone was negligible at the low temperatures considered, the sample number densities could be derived from absolute pressure and temperature measurements. The new measurements were recorded with high-column amounts and different temperatures (23 mbar at 293 K, 11 mbar at 234 K). These measurements were combined with four previously published ambient temperature measurements [217] with lower column amount, which were complementary to the new measurements. The availability of a new multi-spectrum fitting tool ([65] and reference cited therein) motivated re-analysis of the previous measurements and yielded improved results, especially when combined with the new measurements. Four  $N_2$ -broadened and three  $O_2$ -broadened ozone measurements at ambient temperature from [217] were re-analyzed with the multi-spectrum fitting tool, also yielding air broadening and shift parameters.

*2.3.2.1. Self-broadened spectra.* The primary goal of the line fitting was new line positions and intensities of the main isotopologue. The analysis has shown that for this purpose self broadening and self speed dependence have to be considered. All self-broadened spectra were analyzed simultaneously using multi spectrum fitting. The initial guess was HITRAN2016. The measurements were individually frequency-calibrated against HITRAN2012 ozone line positions. Lines were fitted in the intensity range  $1.0 \times 10^{-23}$  to  $4.0 \times 10^{-20}$  cm/molecule with statistical line intensity uncertainties  $<10\%$  for the weakest lines. The weaker lines are especially important for limb-sounding space instruments measuring ozone. An EH approach was applied to fit line positions and intensities of the fundamentals  $\nu_1$  and  $\nu_3$  simultaneously. Hot bands in the  $\nu_3$  region were also considered in the intensity analysis. Using the parameters from this analysis, the line positions and intensities were calculated, avoiding extrapolation. The calculated data were used to replace the HITRAN2016 values. In the case of  $\nu_2$ , a scalar (1.014) was fitted to match HITRAN2016 intensities to the experimental ones. All  $\nu_2$  intensities were replaced by scaled HITRAN2016 values. Experimental line positions for hot bands in the  $\nu_3$  region were used in the database for isolated lines when the line intensity statistical error was less than 10% and the difference to the HITRAN2016 line position was less than  $0.02 \text{ cm}^{-1}$ . In the case of the most abundant isotopologue, and lines in the  $\nu_3/\nu_1$  region where no predictions from the EH were available, the intensities were scaled by  $(1.023+1.017)/2$ . The two values were obtained by weighted fitting of the experimental line intensities against HITRAN for the  $\nu_1$  and  $\nu_3$  bands.

Data are given for three different regions:  $700\text{--}800 \text{ cm}^{-1}$  ( $\nu_2$ ),  $980\text{--}1070 \text{ cm}^{-1}$  (mainly  $\nu_3$ ),  $1070\text{--}1180 \text{ cm}^{-1}$  (mainly  $\nu_1$ ). Line positions and intensities of ozone isotopologues were fitted but not used for the final database. The isotopologue abundance differs from the natural abundance by more than 10% due to the kinetics in the ozone production in the silent discharge. Therefore, no reliable line intensities were available from the line fitting.

In Fig. 15 the ratios of Janssen et al. [194, 195] line intensities and DLR line intensities predicted by the EH for strong ozone  $\nu_3$  lines are shown. The mean ratio is 1.00689(21). This agreement is excellent. It should be noted that the DLR experimental data contain lines up to 100 times weaker than those of Janssen et al.

The measurement and line parameter databases can be downloaded from [218].

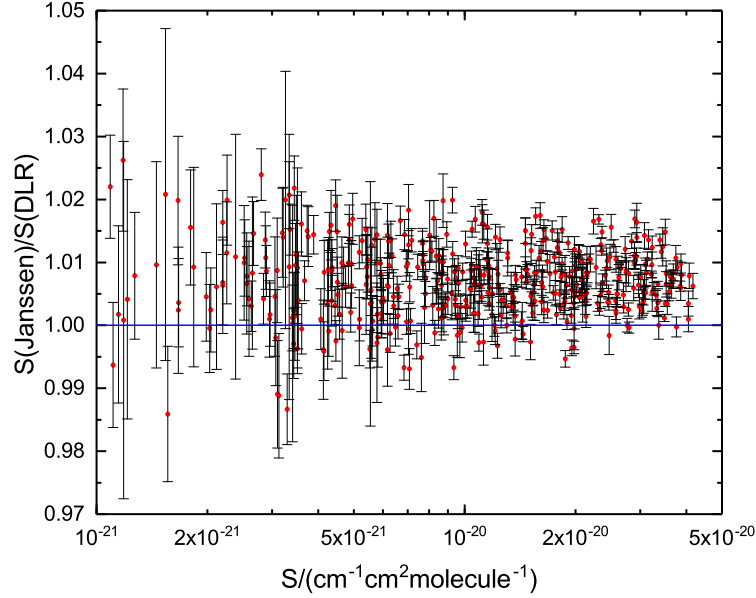


Figure 15: Ratio of Janssen et al. and DLR ozone  $\nu_3$  line intensities. Janssen et al.  $1\sigma$  uncertainties are shown.

*2.3.2.2. N<sub>2</sub>- and O<sub>2</sub>-broadened spectra.* Ambient temperature N<sub>2</sub>- and O<sub>2</sub>- broadened spectra were presented and analyzed in Ref. [217]. The air-broadened values were taken from polynomial representations and the resulting air-broadening parameters are given in the editions HITRAN2004 (and with some corrections in HITRAN2008) through HITRAN2016. These measurements had considerable



self-broadening contributions. The new measurements at high ozone pressure together with the old pure ozone measurements allowed for the determination of the self-broadening parameters to be more accurate than in the old analysis. The multi-spectrum fitting was thus applied for the N<sub>2</sub>- and O<sub>2</sub>-broadened measurements using the new self-broadening data to determine N<sub>2</sub>- and O<sub>2</sub>-broadening parameters on an individual line basis. In case of the weaker  $\nu_1$  and  $\nu_2$  bands, the data were too noisy but still confirmed the validity of the polynomials mentioned above. For the stronger  $\nu_3$  band, more accurate values are available. As in [217], a simple Voigt profile was used, neglecting speed dependence. Air-broadening parameters were calculated for the strong lines in the  $\nu_3$  region when the statistical uncertainty for the N<sub>2</sub> and O<sub>2</sub> broadening parameter was better than 4% and 8%, respectively.

N<sub>2</sub> and O<sub>2</sub> pressure shifts were obtained for several lines in the  $\nu_3$  region. Since absolute frequencies were not available, the shifts were calibrated with the accurate shifts of two lines determined by Minissale et al. [219]. Among the eight lines where Minissale et al. determined air-pressure shifts, two were also available in the DLR data set with sufficient precision. The calibration is accurate to 0.00024 cm<sup>-1</sup>/atm. A second-order polynomial in  $\gamma_{0,air}$  was found to be a reasonable representation of the shifts. In the case where the N<sub>2</sub> and O<sub>2</sub> pressure shifts both had smaller statistical uncertainties than 0.001 cm<sup>-1</sup>/atm, their resulting air shift was added into the database. For all other transitions in the  $\nu_3$  fundamental, the value calculated from the polynomial was entered.

*2.3.2.3. Error considerations.* Line position accuracy is the same as for HITRAN2012 through HITRAN2016 given for most lines ( $10^{-4}$ – $10^{-3}$  cm<sup>-1</sup>). For line intensity, several error sources have to be considered: number density, absorption path, temperature, instrumental line shape, line model, EH approach. The excellent agreement with Janssen et al. data (see Fig. 15) validates overall accuracy <1% for at least the stronger lines. Definitely, the integrated band intensities have

accuracies  $<1\%$  too. From comparison of experimental and predicted line intensities, it was assumed that for lines with intensities  $>3\times 10^{-23}$  the error was  $<1\%$ . Since the  $\nu_2$  band has no Coriolis perturbation in contrast to the  $\nu_1/\nu_3$  pair, the relative intensities in the  $\nu_2$  band in HITRAN2016 should be better than  $1\%$  for lines  $>3\times 10^{-23}$ . All new EH approach predictions in the  $\nu_1/\nu_3$  band  $<3\times 10^{-23}$ , and the  $\nu_2$  HITRAN2016 intensities  $<3\times 10^{-23}$  get 1–2% errors. For all other lines in the  $\nu_1/\nu_3$  region, which are scaled HITRAN2016, the error was set to 2–5%.

The error for  $\gamma_{0,air}$  in HITRAN2016 for lines based on the polynomial representation of [217] was 2–5%. The same error was given for the new data. It should be noted that this error bar is quite conservative and includes statistical and systematic uncertainties. Due to ignoring speed dependence, the broadening could be systematically too small by  $\approx 2\%$ .

For all lines in the  $\nu_3$  band, where the air shift was updated, an error of  $10^{-4}$  to  $10^{-3} \text{ cm}^{-1}/\text{atm}$  was estimated.

### 2.3.3. $O_3$ UCL line intensities

A synthetic line list calculated at the University College London for the principle isotopologue of ozone has been recently presented in Jacquemart et al. [220]. Variational calculation using a semi-empirical potential energy surface (PES) [221] and *ab initio* dipole moment surface (DMS) [199] produced very accurate values for the line intensities for the intense cold bands  $\nu_1$  and  $\nu_1+\nu_3$  as compared to recent measurements performed in LERMA [194, 195] respectively at 10 and 5  $\mu\text{m}$ . However, variational line positions are far away from their experimental values and complete assignment of rotational and vibrational quantum numbers are missing from variationally calculated line list. Corrections for intensities distorted by resonances in the variational calculation with *ab initio* DMS due to the artificial intensity stealing has been developed and

applied [220]. When resonances occur between levels, the distribution of the line intensities between the transitions involving the resonant levels is often incorrectly represented in variational calculations [114], but the sum of intensities is correct. As a consequence, based on the sum of variationally calculated intensities, the distribution has been corrected using the intensity distribution from HITRAN2016 for the transitions involved.

In the work of Jacquemart et al. [220], the complementary nature of EH models used in HITRAN2016 [15] (with full vibrational and rotational assignment and accurate line positions) and variational calculated intensities has been used to generate a line list between 0 and  $4930\text{ cm}^{-1}$  for the main isotopologue. Only transitions with an intensity cutoff of  $10^{-24}\text{ cm/molecule}$  at 296 K and with  $J$  values below 60 have been generated. Note that for 5% of the transitions generated for the line list (77 819 total transitions), the variationally-calculated intensities were corrected using the intensity distribution from HITRAN2016.

As already noted, the variationally-calculated line intensities have been found to be in very good agreement with recent measurements [194, 195] at 10 and  $5\text{ }\mu\text{m}$ : sub percent average discrepancies (as well as sub percent standard deviation associated with the averages values) are reached for the  $\nu_1$  and  $\nu_1+\nu_3$  bands for 476 and 316 common transitions respectively. The whole comparison file is available as supplemental data to Ref. [220]. An interesting case has been noticed concerning the  $2\nu_1-\nu_3$  band in the  $10\text{-}\mu\text{m}$  region. Indeed for this band, the average deviation between variational and HITRAN2016 intensities reaches 28% whereas recent measurements from Birk et al. [218] leads to intensities in better agreement with the variational calculation (average deviation 5.2%). In this region HITRAN2016 is based on the EH model from Flaud et al. [222] constructed when no measurements were available for this band. When accounting for the recent measurements by Birk et al. [218] in an EH model, the average discrepancy between the variationally calculated intensities and the EH calculated intensities from Flaud [223] is 3.3% (1SD equal to 2.1%). The  $2\nu_1-\nu_3$  band provides another example where the variationally-calculated intensities are of better quality than an EH prediction of intensities used in HITRAN2016.

This may be the case for most of the bands for which no measurements were performed or included in the EH model.

In order to be tested against atmospheric validations, a HITRAN2016 type line list has been generated where HITRAN2016 line intensities were replaced by the variationally calculated ones (eventually corrected as discussed in Ref. [220]) for transitions presented in Jacquemart et al. [220].

#### *2.3.4. O<sub>3</sub> Atmospheric Validations and choices for HITRAN2020*

The three line lists presented above were rigorously validated against laboratory, TCCON and balloon spectra by Toon [224]. The quality was accessed based on minimal RMS in selected spectral windows and consistency of the amount of ozone from window to window. It is important to stress again that not only intensities are different in the new line lists. With respect to HITRAN2016 the S&MPO line list contains new bands, updated line positions and intensities for four isotopologues, including the principal isotopologue; however line-shape parameters are same as in HITRAN2016. The DLR line list contains new line positions, intensities and line-shape parameters; however the isotopologue information is that from HITRAN2016. The UCL line list contains only new intensity information. It was found that in overlapping spectral ranges in most cases all three line lists supersede the HITRAN2016 line list in quality. An exception is only the region of the  $\nu_2$  fundamental, where the intensities in the S&MPO and UCL line lists seem to be inferior to those in HITRAN2016 and especially the DLR line list. Based on the validations presented in [224] and findings in Birk et al. [198], the following wavenumber-dependent selections have been made for the MW-IR transitions of ozone:

1. In the region of pure rotational transitions of all HITRAN isotopologues of ozone, the values from the JPL catalogue [225] were chosen. To take advantage of increased precision of MW transitions, it should be noted that the wavenumber format for ozone in the traditional “.par” format has been updated to F12.9 for transitions below  $1.0 \text{ cm}^{-1}$ , F12.8 for transitions  $1.0$

to  $10.0\text{ cm}^{-1}$ , and F12.7 for transitions  $10.0$  to  $100.0\text{ cm}^{-1}$  (as previously implemented for  $\text{HNO}_3$ ,  $\text{PH}_3$ ,  $\text{O}_2$  and  $\text{NO}^+$ ).

2. Below  $1180\text{ cm}^{-1}$  the DLR line list is used as is.
3. Above  $1180\text{ cm}^{-1}$  and up to  $5791\text{ cm}^{-1}$  new S&MPO line list is used except for the  $2975\text{--}3205\text{ cm}^{-1}$  region, where the RMS of the UCL line list are the lowest. Therefore in that window UCL line list is used. However, one should be aware that the retrieved amount of ozone with the latter list is noticeably lower compared to other regions.
4. Above  $5791\text{ cm}^{-1}$  HITRAN2016 line list is retained for HITRAN2020

#### 2.4. $\text{N}_2\text{O}$ : Nitrous Oxide (molecule 4)

Due to its prominent presence in the terrestrial atmosphere, nitrous oxide ( $\text{N}_2\text{O}$ ) has been the subject of many spectroscopic studies in different spectral ranges, enabling the remote-sensing measurements of  $\text{N}_2\text{O}$  concentrations. In HITRAN2020, intensities of the NIR bands have been updated, while a complete overhaul of the line-shape parameters has been carried out.

##### 2.4.1. $\text{N}_2\text{O}$ intensities in NIR

An update to the near-infrared  $\text{N}_2\text{O}$  line intensities has been performed based upon recent frequency-agile, rapid scanning cavity ring-down spectroscopy measurements of the  $4200 - 0000$  and  $5000 - 0000$  bands near  $1.6\text{ }\mu\text{m}$  [226]. A band-wide fit of these measurements has allowed for the range of  $|m|$  included for these bands to be increased from  $|m| \leq 46$  to  $|m| \leq 85$ . Furthermore, these measurements led to combined standard uncertainties near 1%, which is roughly a factor of five lower than the values found in HITRAN2016 [15] which were based on measurements from Toth [227]. We note that these new measurements (and hence HITRAN2020 intensity values for these bands) are roughly 5% greater than the values found in HITRAN2016 [15]. With that being said, good agreement was observed with the Fourier-transform spectroscopy measurements of Daumont et al. [228].

#### 2.4.2. $N_2O$ line shapes

In the description of the atmospheric retrievals by ACE-FTS, Boone et al. [229] have stressed the importance of revision of line-shape parameters for certain bands in HITRAN and the importance of including the non-Voigt parameters. This issue has been attended in the 2020 edition of the database, where we updated the  $N_2O$ -air and  $N_2O$ - $N_2O$  line-shape parameters using the Voigt and speed-dependent Voigt parameters, including the first-order line-mixing parameters [230] as presented in Table 4 of Section 2.2.

In updating the line-shape parameters of  $N_2O$ , we used the approach similar to the one used for updating the line-shape parameters of  $CO_2$ . This approach enabled providing both Voigt and the speed-dependent Voigt parameters (including first order line-mixing) for each transition (see Ref. [231] for more details).

The air- and self-broadening parameters (using VP), their temperature dependence, and the pressure shifts of  $N_2O$  in the HITRAN2016 database were based on the earlier studies from Refs. [232–235]. The vibrational dependence of the line widths was assumed negligible. The parameters were revised based on the recent high-quality experimental data from Adkins et al. [226]. The new NIST spectroscopic parameters were measured in the Near-IR region for the 4200–0000 and 5000–0000 bands obtained using their Multi-spectrum Analysis Tool for Spectroscopy (MATS) [236] using the line-shape functions defined in HAPI. The non-measured transitions were given an approximated value, estimated from the results reported in Ref. [231], where the Padé approximant functions were applied as a smoothing function over the measured transitions and extrapolated to the higher  $J$  lines in all the bands. The reported error codes for the measured lines correspond to the combined error type A (statistical) and B (systematic) error in the measurement. The temperature exponents of the air-broadening parameters were also updated using the Padé approximants fit to the data from Ref. [234]. For the self-broadening (the VP) parameters, there were not many measurements of  $N_2O$  available in the literature. In HITRAN2016,

these values were produced from the study by Toth [233]. For HITRAN2020, a fit of the recent measurement of  $\gamma_0$ -self half-widths by Werwein et al, [237] for the 0002–0000 band was used to extrapolate the results for all the transitions in all the bands [231].

The speed-dependent parameters were not provided in HITRAN2016 except for the  $\nu_3$  band of N<sub>2</sub>O-air [238], which were obtained from a multi-spectrum fit of FTS measurements. Note that these parameters were present under the HT profile parametrization in the HITRAN2016 edition. We used the air-broadened parameters measured by NIST [226] for the 5000 – 0000 band and expanded them for all the bands except for the  $\nu_3$  band, where the data from Ref. [238] were used for updating the air-broadening, air speed-dependence of width, air-shift, and the first-order line-mixing parameter for the measured transitions. Based on the uncertainties of the parameters reported by NIST, in smoothing the collisional air-broadening (for the SDV) and air-speed-dependence, only data with  $|m| \leq 40$  were included in the fit. For the temperature dependence of the air-broadening, we used Ref. [231] data to produce the temperature exponent for the SDV line widths. Also, in the absence of the measurement of the temperature exponent of  $\gamma_2$  (i.e.,  $n_{\gamma_2}$ ), the predicted ones for the half-width parameters were used.

With a similar fitting approach, we produced the results for the  $\gamma_0$ -self and  $\gamma_2$ -self (for the SDV profile) parameters based on the high-accuracy measured self-broadening using a diode laser spectrometer in Ref. [239] for eight transitions in the  $3\nu_1 + 2\nu_2$  band, acquired at room-temperature. In Ref. [231], it is described how the  $\gamma_0$ -self and  $\gamma_2$ -self were generated for the lines where these parameters were not measured.

We used the method proposed by Hartmann [173], which was successfully tested for the CO<sub>2</sub>-air and CO<sub>2</sub>-CO<sub>2</sub> systems [161], to calculate the pressure shifts of the transitions of air- and self-broadened N<sub>2</sub>O bands. Because there were not many measurements available for educating the model with the SDV and VP shifts for different bands, we used the same air- and self-shifts for the VP and SDV profiles to populate the database. The fitting coefficients

were presented in Ref. [231]. For the line shifts from these calculation, the uncertainty code 3 ( $> 20\%$ ) has been adopted.

The first-order line-mixing parameters of the  $\text{N}_2\text{O}$  lines were calculated using the Exponential Power Gap law (EPG) approximation [240] explained in Ref. [231] and provided for every transition in HITRAN separately for the VP and SDV profiles for  $\text{N}_2\text{O}$  broadened by air and  $\text{N}_2\text{O}$  [231]. It should be noted that the line-shape parameters were not updated for the  $^{14}\text{N}_2^{18}\text{O}$  isotopologue in the HITRAN2020 line list because of the ambiguities in assignments for some of the NIR bands discussed in the HITRAN2016 paper.

HAPI was used to validate the results against the laboratory spectra. By taking into account the line-mixing effect, the absorption coefficient for the mixture of  $\text{N}_2\text{O}$ -air at specific temperature  $T$  and pressure  $P$  was obtained. Using the new NIST parameters led to improvements in calculating the spectra both for the VP and SDV profiles as shown in Ref. [231].

Finally, every transition of  $\text{N}_2\text{O}$  now has  $\gamma_{\text{H}_2\text{O}}$  and  $n_{\text{H}_2\text{O}}$  parameters as described in Ref. [48].

#### 2.4.3. $\text{N}_2\text{O}$ in HITEMP

The addition of  $\text{N}_2\text{O}$  to HITEMP is described in Hargreaves et al. [54]. This  $\text{N}_2\text{O}$  line list was based on the Nitrous Oxide Spectroscopic Data Bank at 1000 K (NOSD-1000) [241]. Comparisons to PNNL spectra [242] in the region of the 1000–0110 band of  $^{14}\text{N}_2\text{O}$  required a correction to the effective dipole moment used to calculate intensities for NOSD-1000 (see Fig. 1 of Ref. [54]). To create the line list for HITEMP, a recalculated version of the NOSD line list was then merged with the  $\text{N}_2\text{O}$  data in HITRAN2016 [15].

The  $\text{N}_2\text{O}$  line list was added to HITEMP prior to the updates for HITRAN2020 described in Sections 2.4.1 and 2.4.2. To maintain consistency, updates to HITRAN will be incorporated into HITEMP in due course. Readers should refer to Hargreaves et al. [54] for a full description of the HITEMP line list for  $\text{N}_2\text{O}$ .



#### 2.4.4. Forthcoming updates

In its present status, the HITRAN line list for  $\text{N}_2\text{O}$  has room for improvement above  $8000\text{ cm}^{-1}$ . Data relative to the main isotopologue are limited to FTS data below  $7796\text{ cm}^{-1}$ , mostly from the Toth database [227, 243] and correspond to an intensity cut-off of  $2 \times 10^{-25}\text{ cm/molecule}$  at 296 K. The inclusion in the HITRAN dataset of the calculated line list of the  $^{14}\text{N}_2^{18}\text{O}$  isotopologue from Ref. [244] with an intensity cut-off of  $1 \times 10^{-29}\text{ cm/molecule}$  leads to a somewhat unusual situation. In spite of it being only forth in abundance,  $^{14}\text{N}_2^{18}\text{O}$  has largest amount of transitions in the HITRAN  $\text{N}_2\text{O}$  list, extending up to  $10\,363\text{ cm}^{-1}$ , while many NIR bands of the principal isotopologue are missing. This situation was illustrated in a recent CRDS study in the  $8325\text{--}8622\text{ cm}^{-1}$  region where the HITRAN line list includes only  $^{14}\text{N}_2^{18}\text{O}$  transitions (see Fig. 7 in Ref. [245]). In addition, there are no  $^{14}\text{N}^{15}\text{N}^{16}\text{O}$  and  $^{15}\text{N}^{14}\text{N}^{16}\text{O}$  transitions in the HITRAN and HITEMP lists (in the considered region) while the  $4\nu_3$  band of the  $^{14}\text{N}^{15}\text{N}^{16}\text{O}$  isotopologue is dominant in the  $8500\text{--}8550\text{ cm}^{-1}$  interval. Fortunately, many of these bands have been accurately measured in the recent literature, in particular by CRDS [243, 246–254]. Spectroscopic data available in the literature will be gathered and critically evaluated in order to significantly extend and improve the  $\text{N}_2\text{O}$  lists of the first four isotopologues in the next editions of the HITRAN and HITEMP databases.

#### 2.5. CO: Carbon Monoxide (molecule 5)

The HITRAN2016 [15] line list for carbon monoxide was based on the semi-empirical line list from Li et al. [255]. For the purpose of inclusion into HITRAN2016, the line list was truncated, and the line positions were replaced with updated calculation or state-of-the-art experimental data (see HITRAN2016 paper [15] for details). For the HITRAN2020 edition, the line positions have not been changed, but the intensity and line-shape data have been updated.

### 2.5.1. CO intensities

Intensities in Li et al. [255] were calculated using the piece-wise dipole moment function fitted to existing experimental and *ab initio* data. Therefore, it is not surprising that the values of the intensities are primarily driven by the quality of the experimental data used as input. Recent state-of-the-art experiments have either confirmed the quality of CO intensities in HITRAN or have issued recommendations for improvements.

Despite the fundamental band being by far the strongest band of CO, experimental and theoretical data for its intensities in the literature do not agree well. Devi et al. [256] found that the intensities of the principal isotopologue of CO in HITRAN differ by about two percent when compared to their measurements. For the HITRAN2020 edition, the intensities of the  $\Delta v = 1$  transitions of all isotopologues of CO in HITRAN were reduced by 2% following the recommendation of Ref. [256]. In the meantime, it is highly desirable that more experiments are carried out in this band.

Intensities of the second overtone in Li et al. [255] were primarily driven by the experimental values reported in Ref. [257] with sub-percent uncertainty. Recently the authors of Ref. [257] revised their experimental procedure, and their new measurements [258] suggest that HITRAN2016 intensities in this band are underestimated by about 2.6%. This assessment was corroborated by independent FTS measurements by Borkov et al. [259]. Therefore, in the HITRAN2020 edition, the intensities of the  $\Delta v = 3$  transitions of all isotopologues of CO in HITRAN were increased by 2.6%.

Another recent paper by Borkov et al. [260] is devoted to the third overtone of CO. There the authors find that although HITRAN intensities are within respective error bars, they may be systematically off by about 2%. However, an independent CRDS study by Bordet et al. [261] has confirmed HITRAN values

for this band to better than 1%. Therefore, the intensities in this band remain unchanged.

In the future, a better way to address the intensities in the fundamental and second overtone bands would be to refit the dipole moment function from Li et al. [255] with new experimental data and recalculate intensities. Ref. [255] notes that although their procedure should yield the same quality of results for all isotopologues (assuming no Born-Oppenheimer breakdown), comparisons with different experimental values yield different deviations for each of the six isotopologues. New experiments reported in Refs. [257, 259–261] do not resolve this issue. One possible explanation is that none of the experiments had a way of measuring the relative abundance of isotopologues in the sample. Experiments with controlled abundance are highly desirable to resolve this issue.

### 2.5.2. CO line-shapes

The line broadening and the pressure shift parameters of transitions of CO perturbed by air and by CO itself have been revised mainly based on a review performed in Ref. [231] on a variety of measurements. Compared to the HITRAN2016 line list, which included the speed-dependent parameters for only transitions of 2–0 band (up to  $J_{\max} = 29$ ), in the 2020 edition of the CO line list, every line includes the speed-dependent Voigt and the Rozenkranz line-mixing parameters [230] for both air- and self-broadened lines. The importance of including non-Voigt line shapes in atmospheric retrievals of CO has been highlighted by Hochstaffl et al. [262, 263]. Furthermore, the CO line-shape parameters for the important planetary broadeners such as CO-H<sub>2</sub>, CO-He, and CO-CO<sub>2</sub> were revised [264], while parameters associated with broadening by H<sub>2</sub>O was introduced for the first time as described in Ref. [48]. The summary of these modifications for the HITRAN2020 edition is given below:

#### 1. The CO-air broadened parameters:

- (a) For the air half-widths (the VP parameters), to evaluate the effect of vibration, the relative difference of the broadening parameters for

various measured bands were calculated and the average difference was well below 1% for different band values. Therefore, the broadening parameters were considered to be vibrationally independent. Then, the Padé approximants model, which is used extensively in this edition, was employed to fit all the measured air-broadening data for several bands, including Ref. [265] for the 1–0 band, Ref. [266] for the 2–0 band, and Ref. [267] for the 3–0 band simultaneously [231]. The fit coefficients are provided in Ref. [231] and the resulted broadening parameters were expanded to all the transitions of CO perturbed by air.

- (b) The update of the speed-dependent Voigt line-shape parameters heavily relies on the semi-empirical Padé approximant fits to the experimental data of Ref. [268]. For the air broadening (the SDV parameters), and the temperature dependence of the air-broadening parameters, the 2–0 band data measured by Devi et al. [268] were used in the fit, and the approximated values from the model were expanded for lines of every band. The air speed dependence of line widths were fitted as well using the same data source, and the corresponding  $\gamma_2$ -air parameters were estimated and attributed to each transitions. Wherever the measured SDV parameters were available, the original experimental results were used in populating the database. For instance, the Ref. [256] data were used for the lines of the 1–0 band and the measured parameters of Ref. [269] are used for updating the 2–0 band lines for different isotopologues of CO.

## 2. *The CO-CO broadened parameters:*

- (a) To find the values for the self-broadened half-widths (using the VP) for the high- $J$  transitions, the measurements for different bands were used (i.e. 1–0 band [270], 2–0 band [271–273], 3–0 band [274]). All these data were fitted simultaneously to estimate the self-broadening parameters for the lines that were not measured for all the bands except for the measured transitions in the 2–0 band, where the data

from Ref. [271] were used for the update.

- (b) The self-broadening parameters, their temperature exponents, and the speed-dependence of the broadening (the SDV profile parameters) were approximated using the measured line widths of Ref. [268] fitted to the Padé approximants model, and we imported the experimental values for different isotopologues reported in Refs. [256, 269] for the 1–0 and 2–0 bands, respectively.

3. *The CO-air and CO-CO pressure shifts:*

The air and self shifts (for both VP and SDV) were calculated employing the sophisticated vibrational-dependent approach of Hartmann [173] for all the transitions. The quality of the calculated shifts were validated by comparison of the shifts in different bands [231]. The measured air shifts for the transitions in the 1–0, 2–0, and 3–0 bands remained unchanged as they were reported in HITRAN2016. Also it should be emphasized that measured pressure self shifts of CO for the 1–0 [270], 2–0 [268], 3–0 [267] and 4–0 [261] bands were written into the database directly for the measured lines.

4. *The CO-air and CO-CO first-order line-mixing:*

The first-order line-mixing parameters were calculated based on the EPG formalism [240] using both the VP and SDV broadening parameters and provided for every transition. For the 2–0 band of the main isotopologue, the CO-air and CO-CO line-mixing were taken from the measurement of Ref. [268].

5. *Planetary perturbations:*

Broadening parameters due to pressure of “planetary” ( $\text{H}_2$ ,  $\text{CO}_2$ , He) gases were first introduced in HITRAN in 2016, based on the procedure described by Li et al. [255]. In this edition we update these parameters. For the update of the CO- $\text{H}_2$  broadening parameters and their temperature dependence, the data from Refs. [271, 275] were taken into the semi-empirical fitting models [264] and the results were extrapolated for every CO line. The line-shape parameters of CO perturbed by helium were

modified as well, based on Refs. [276–280], and the CO<sub>2</sub> pressure broadening and the temperature dependence of the broadening parameters of CO were generated from extrapolating the data from Ref. [281]. Finally, the pressure shift parameters for all three broadeners of CO were obtained based on the Hartmann semi-classical routine [173] and the values agree well with the available experimental data [264].

## 2.6. CH<sub>4</sub>: Methane (molecule 6)

HITRAN2016 provided substantial improvements in methane spectroscopy in many spectral regions (see, for instance, the Olsen et al. [42] validation of the ACE-FTS experiment). In general, the line positions and intensities were considerably improved, and the spectral coverage increased. Nevertheless, the spectroscopy of methane is still far from perfect. In this edition, several spectral regions have been improved. However, one of the largest issues that remain is the quality of the line shape parameters. In particular, the tetradecad region targeted by GOSAT and MethaneSat requires revision (as indicated, for instance, in Chesnokova et al. [282]) A major global revision of the methane line shape parameters is currently underway for Voigt and speed-dependent Voigt parametrizations, as well as the inclusion of line-mixing parameters. At present, this work is still ongoing and will not form part of the current update for methane. The improvements for HITRAN2020 concern updating line-shapes of individual transitions where major issues have been identified. Nevertheless, several spectral regions have received significant updates and are described below.

### 2.6.1. 3760–4100 cm<sup>-1</sup>

A new line list from Rodina et al. [283] was used to completely replace HITRAN data for the principal isotopologue in this spectral region. This line list is based on the analyses of the FTS experimental spectra recorded in Reims under different thermodynamic conditions. This line list improves the quality of spectroscopic parameters in this spectral region and contains assignments for

all lines, enabling easier conversion between temperatures.

#### *2.6.2. 4190–4315 cm<sup>-1</sup>*

This spectral region is important in remote sensing as it is used by TROPOMI and by TCCON to monitor both methane and carbon monoxide. Lorente et al. [284] evaluated HITRAN2008, HITRAN2016, and SEOM-IAS [102] databases against retrievals from TROPOMI. The sensitivity tests did not indicate an improved data quality when either of the spectroscopic databases was used. However, the RMS and  $\chi^2$  values were much improved with HITRAN2016 over HITRAN2008, with the SEOM-IAS data giving the best results. Indeed the SEOM-IAS [102] database is a very accurate line list, which, apart from accurate line positions and intensities, provides advanced line shape parameters including line-mixing. However, it is not completely assigned, and some of the existing assignments contradict the assignments in HITRAN and variational line lists. In addition, the line-mixing formalism used in that work is not yet adapted in HITRAN. This is the reason why only 122 lines from Ref. [102] were adapted for HITRAN2016. For HITRAN2020 substantially more lines were assigned and incorporated into HITRAN with all the other parameters. This, however, has both advantages and disadvantages. On the one hand, assignments allow one to use correct lower-state energies, which provides better applicability of the line list at different temperatures. On the other hand, parameters determined in a multi-spectrum fit of experimental data in Birk et al. [102] are somewhat correlated; therefore, the changes in lower-state energies could now conflict with other parameters determined in that study. In general, the specifics of the data proposed in Ref. [102] requires a dedicated software or precalculated cross-sections to be used in radiative transfer codes successfully. The authors of SEOM-IAS database are working on this approach.

#### *2.6.3. 8850–9180 cm<sup>-1</sup>*

A new line list from Nikitin et al. [285] was used to update HITRAN data for the principal isotopologue of methane in this spectral region. This line

list is based on the analyses of the FTS spectra that were recorded in Tomsk with a cell path length of 2.2 m under different thermodynamic conditions. This line list improves the quality of spectroscopic parameters in this spectral region and provides substantially more quantum assignment information than the HITRAN2016 list in this region, making conversions between temperatures more reliable.

#### 2.6.4. *Line shape parameters*

As it was already mentioned, a major revision of methane line shape parameters is underway and will be featured in near future updates to HITRAN2020. At the moment only a few dozen individual parameters that were deemed to be definite outliers have been updated. There is however one global update, which is an inclusion of the half-widths (and their temperature dependencies), due to the ambient pressure of water [48].

#### 2.6.5. *Future work*

Many other new experimental works on spectroscopy of different isotopologues of the methane molecule exist, that could benefit the HITRAN database, including (but not limited to) Refs. [286–298]. A very extensive effort is underway to evaluate new data against current HITRAN data and experimental and atmospheric spectra. Methane is a very complex molecule from the spectroscopic standpoint and it is not straightforward to make choices for individual parameters of individual lines. One interesting example is a pure rotational spectrum of CH<sub>3</sub>D. In the HITRAN2016 paper an argument was made regarding updating the intensity of these lines with results from Bray et al. [299]. Since then, the authors of this work have revised these values [300] but these data still disagree with *ab initio* calculations and other theoretical works, which are not in agreement between themselves either. More work is needed to understand these discrepancies.

The high-temperature theoretical line list for <sup>12</sup>CH<sub>4</sub> produced by Rey et al. [301] (and available online as part of the TheoReTS project [302]) has been used



to create a line list suitable for HITEMP [52]. The approach involved merging Rey et al. [301] with the HITRAN2016  $^{12}\text{CH}_4$  data [15]. A method was devised to compress the weak underlying *ab initio* transitions into “effective lines” so that the complete HITEMP line list can be used directly in radiative transfer calculations. For a full description of the HITEMP line list of  $^{12}\text{CH}_4$ , including validation against experimental works, readers are referred to Hargreaves et al. [55], which describes the addition to HITEMP. Users should be mindful that this HITEMP update was carried out before the  $^{12}\text{CH}_4$  updates described above for HITRAN2020. To maintain consistency, these updates will be incorporated into HITEMP in due course.

## 2.7. $\text{O}_2$ : Molecular Oxygen (molecule 7)

Due to the dominant presence and uniform mixing of oxygen in the terrestrial atmosphere, its spectral lines are often used as a benchmark for intensity calibration of atmospheric spectra taken by satellite and ground-based instruments. Although there is over a century of measurements and calculations of spectral parameters of oxygen, their quality was still not achieving the sub-percent goal in many important spectral bands. In this edition, major revisions of oxygen line lists have been carried out.

### 2.7.1. 1.27 $\mu\text{m}$ region

Spectroscopy of the  $a^1\Delta_g - X^3\Sigma_g^-$  band at 1.27  $\mu\text{m}$  is more complex [303] than that of the A-band at 0.76  $\mu\text{m}$ . It has more branches, a denser spectrum with overlapping lines, stronger underlying collision-induced absorption, and interfering emission features (air-glow) at the top of the terrestrial atmosphere due to the production of oxygen in the  $a^1\Delta_g$  state through photo-dissociation of ozone. Nevertheless, it is located closer (on the spectral scale) to the bands of  $\text{CO}_2$  and  $\text{CH}_4$  that are targeted by the remote-sensing missions and therefore has better benchmarking characteristics to remove systematic errors. In fact, the Total Carbon Cycle Observing Network (TCCON) [304], which is less sensitive to the emission contamination from the top of the atmosphere, already employs

this band. Sun et al. [305] have demonstrated that emission features could also be modeled accurately, and therefore, if one knows the spectroscopic parameters to the necessary degree of accuracy, this band can be used in remote sensing and is intended to be used by upcoming satellite missions, including MicroCarb [306] and MethaneSAT [25].

A major overhaul of the spectroscopic parameters for the  $a^1\Delta_g-X^3\Sigma_g^-$  band of the  $^{16}\text{O}_2$  and  $^{16}\text{O}^{18}\text{O}$  isotopologues was carried out for this edition. The details for the calculations of line positions and intensities will be provided in a separate paper, but a general overview is provided below.

The  $a^1\Delta_g-X^3\Sigma_g^-$  band consists of nine magnetic dipole (M1) branches (with  $\Delta J = 0, \pm 1$ ) and 15 electric quadrupole (E2) branches (with  $\Delta J = 0, \pm 1, \pm 2$ , therefore nine of these branches overlap with M1 ones). Typically E2 transitions are about six orders of magnitude weaker than M1 transitions. However, as explained in Gordon et al. [303], intensities of the E2 lines in this particular band are enhanced due to mixing of the different spin-components of the  $X^3\Sigma_g^-$  state with the  $b^1\Sigma_g^+$  state at around  $13\,000\text{ cm}^{-1}$  and to a lesser extent with much higher-lying  $^1\Pi$  states. These contributions affect each branch differently, and it is very hard to model these overlapping transitions. Therefore, in HITRAN2012 [14] and HITRAN2016 [15] only those E2 transitions with  $\Delta J = \pm 2$  were included based on measurements reported in Gordon et al. [303] and a model proposed by Mishra et al. [307]. The E2 lines overlapping with M1 lines were not included, therefore creating difficulty in modeling absorption due to M1+E2 lines on a sub-percent level as E2 contribution to the total intensity should be considered almost negligible for some of the bands, but up to 1.5% for others.

Gordon et al. (2021) make use of an extensive campaign of new measurements carried out in Grenoble and NIST. These measurements are a continuation of published works [308–310] that take advantage of the extremely sensitive CRDS setup equipped with the frequency combs. Intensities with the lowest uncertainties were used in the fit to the Mishra et al. [307] model for E2 transitions and the modified Balasubramanian and Bellary [311] model for M1

transitions. Modifications are connected to the Herman-Wallis-like rovibronic deviations that were modeled by introducing polynomials as a function of rotational quanta to the groups of transitions that are connected to the same spin component in the ground state.

Frequency comb-calibrated line positions from the new Grenoble and NIST experiments were also used to refit all the  $^{16}\text{O}_2$  and  $^{16}\text{O}^{18}\text{O}$  data involving the  $a^1\Delta_g$  and  $X^3\Sigma_g^-$  states simultaneously. Effectively, a systematic change by about  $2 \times 10^{-4} \text{ cm}^{-1}$  (slightly larger at  $J'' \geq 29$ ) was introduced with respect to the HITRAN2016 values that were based on Ref. [312].

The Voigt line shapes were taken from the analyses of the Grenoble data carried out in Tran et al. [309], while advanced line-shape parameters, including first-order line-mixing, are from the new study in NIST that updates data from Mendonca et al. [310]. No new studies have been carried out for the temperature dependencies of the width, but in order to satisfy TCCON retrievals, the previous values in HITRAN were multiplied by a factor of 0.93.

Figure 16 demonstrates how spectroscopic parameters in HITRAN affect the residuals of the TCCON spectra in Park Falls, WI (USA). The use of the HITRAN2020 line list clearly reduces the residuals to a sub-percent level.

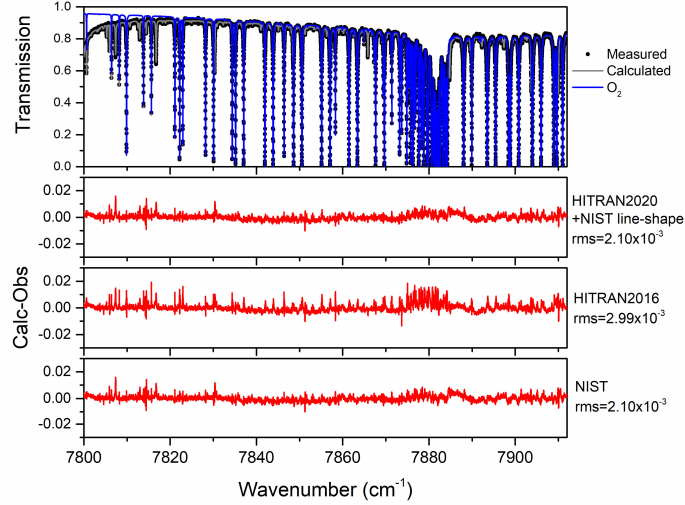


Figure 16: Comparison between measured transmissions from Park Falls FTS and simulations using different versions of the database.

### 2.7.2. A-band region

Updates to O<sub>2</sub> in the A-band region reflect ongoing efforts to improve the balance between line-mixing and collision-induced absorption that have been shown to bias surface pressure retrievals [313, 314]. The effort [314] which drives this update does not improve the precision of line positions which may be correlated with self-shift parameters [315]. Therefore this HITRAN update retains the positions produced from the updated global model of Yu et al. [312] and additional uncertainty is recommended for the self-shift parameters. Line intensities are changed up to 5% at higher  $J$  values due to a re-assessment of the high- $J$  data [316] used to determine Herman-Wallis terms utilized in the last two HITRAN editions [317]. Intensities in the present update, see Fig. 17, reflect a median value found in the FTS and CRDS datasets analyzed for production of ABSorption COefficient (ABSCO) tables used for the OCO missions [314]. The present adjustment appears larger with respect to HITRAN2016 than in comparison to HITRAN2012. Direct measurements of intensities have been performed subsequently by NIST after mitigating biases associated with the CRDS

signal digitization, and found the ABSCO table intensities to be consistent to approximately better than 1%. The intensity changes are largest for the weakest features, such that the total band intensity is less variant, changing 0.92% from ABSCO 5.0 [318] (HITRAN2016) to ABSCO 5.1 [314] (HITRAN2020).

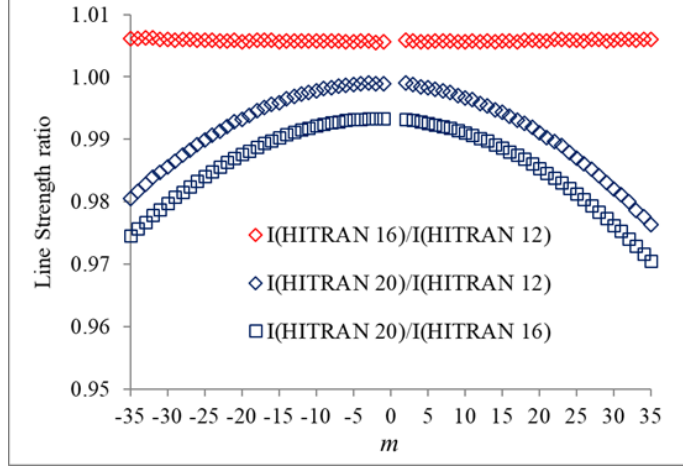


Figure 17: Ratios of intensities from ABSCO 5.1 [319] compared with HITRAN2016 and HITRAN2012. The HITRAN2016 update, which utilized a prior ABSCO release (5.0, [318], kept the Herman-Wallis factors from HITRAN2012 fixed. The changes are due to band scaling and the application of new Herman-Wallis factors.

Changes in the air-broadened half-width and its temperature-dependence parameter (both Voigt and speed-dependent Voigt) are subtle, the latter showing increases of a few percent at low  $m$  and decreases of a few percent at high  $m$ , whereas the former generally increased and present more variability. Changes in air-induced pressure shifts follow the same trends as air-broadened half-width, but with a clearer monotonic structure now presented in the P-branch. All of these air-induced line-shape parameters show significant deviations from monotonic behavior near the band head of the R-branch, where there are strong interactions with line-mixing model parameters. It is likely that the subtle  $J$ -dependent changes in widths and shifts are also attributable to the modified line-mixing model which re-proportioned the odd and even elements of the relaxation matrix. The allocation of a small weight (instead of zero weight) to

the odd elements produces a notable zigzag effect in the first-order Rosenkranz parameters provided with the HITRAN2020 database. The median of these elements closely traces prior Rosenkranz parameters except for a stronger slope in the R-branch vs.  $m$ .

#### *2.7.3. Corrections to the line-broadening parameters for the O<sub>2</sub> B-band*

The speed-dependent Voigt line-broadening parameters of the O<sub>2</sub> B-band adopted in the HITRAN2016 database from Domysławska et al. [320, 321] were treated as half-widths (while apparently the full-widths were reported in the original papers). This discrepancy was discovered by Sung et al. [322]. The speed-dependent Voigt parameters have now been corrected for this band.

#### *2.7.4. Water-vapor broadening parameters*

A variety of experimental methods have been applied to study the water-vapor broadening of O<sub>2</sub> lines including early O<sub>2</sub> Q-branch Raman spectroscopic studies for a wide temperature range (460 to 990 K) [323]. The pure rotational and A-band transitions have been studied using laser-based photoacoustic spectroscopy [324], frequency-multiplier spectrometers with a Zeeman-modulated absorption cell [325], radio-acoustic detection spectrometers [326], as well as Fourier transform spectroscopy [327]. A complete analysis for all collected experimental data were presented in Ref. [48]. The Padé approximant was applied to fit the collected data for transitions  $N'' \leq 35$ . There is an exception with  $N'' = 1$  which is treated separately due to the large spin splitting in the lowest rotational level.

#### *2.7.5. Future improvements in the 60 GHz band*

The band of oxygen at 60 GHz represents the manifold of transitions between spin components within the same rotational levels. It is an important band from an atmospheric perspective, and although line-positions, intensities, and to lesser extent Voigt parameters in HITRAN are of very high quality, the close proximity of transitions requires advanced line shape parameterizations that include line-mixing. The recent study by Koshelev et al. [328] is considered to

potentially introduce advanced line shape parameters for these “fine-structure” transitions.

## 2.8. NO: Nitric Oxide (molecule 8)

Nitric oxide (NO) plays a key role in tropospheric chemistry [329] and contributes significantly to air pollution [330]. Spectroscopic NO emissions from the upper-atmosphere require the consideration of high rotational transitions in radiative transfer models due to non-local thermodynamic equilibrium conditions [331].

Hargreaves et al. [54] provide a detailed description of the NO update for HITRAN2020 and HITEMP [52], therefore only a summary is provided here. In HITRAN2016 [15], the  $^{14}\text{N}^{16}\text{O}$  line list contained transitions from the electronic ground state  $X^2\Pi_{\Omega'}-X^2\Pi_{\Omega''}$  (with  $\Omega = 1/2$  and  $3/2$ ) for vibrational bands up to  $\Delta v = 5$  (with  $v'' = 5$ ). For  $^{15}\text{N}^{16}\text{O}$  and  $^{14}\text{N}^{18}\text{O}$ , only 699 and 679 lines of the 1–0 band were provided, respectively.

The comprehensive semi-empirical “NOname” line list [332], part of the ExoMol project [333], contains six isotopologues of NO ( $^{14}\text{N}^{16}\text{O}$ ,  $^{15}\text{N}^{16}\text{O}$ ,  $^{14}\text{N}^{18}\text{O}$ ,  $^{14}\text{N}^{17}\text{O}$ ,  $^{15}\text{N}^{17}\text{O}$ ,  $^{15}\text{N}^{18}\text{O}$ ). For  $^{14}\text{N}^{16}\text{O}$ , the NOname line list was created using an effective Hamiltonian by fitting to available experimental energies (with  $J < 99.5$ ,  $v < 28$ ) and combined with *ab initio* intensities. To allow extension to higher rotational levels and vibrational bands, a second variational model was also built by fitting to experimentally-obtained energy levels and positions using the *Duo* program for diatomic molecules [334].

The HITRAN and HITEMP update for  $^{14}\text{N}^{16}\text{O}$  was built around the NOname line list, but some adjustments were necessary. Discontinuities at the stitching point of the two methods used to create the NOname line lists, and intensity issues observed for  $\Delta v = 0$  (see Fig. 6 of Ref. [54]), required the effective Hamiltonian to be extended to higher rotational levels for the  $\Delta v = 0$  and  $\Delta v = 1$  bands [54]. Furthermore, comparisons to experimental observations required the NOname intensities for the  $\Delta v = 4$ ,  $\Delta v = 5$  and  $\Delta v = 7$  bands to be scaled by a factor of 1.35, 1.30 and 0.55, respectively.

For the 0-0 and 1-1 bands, positions and intensities from CDMS [335] replace the corresponding lines in the adjusted NOname line list. Any lines of the 0-0, 1-1, 1-0, 2-1, 2-0, and 3-1 bands with hyperfine splitting from HITRAN2016 (that were not replaced by CDMS data) have been retained. Further details for transitions with  $J \geq 99.5$  is given by Hargreaves et al. [54]. In addition, magnetic dipole transitions (identified by “m” in the local upper-state quanta in the HITRAN line-transition format) for the 0-0 band remain unchanged.

For HITRAN2020, an intensity threshold has been applied. Lines that remain less than  $1.0 \times 10^{-99}$  cm/molecule, or do not exceed  $1.0 \times 10^{-31}$  cm/molecule (at 100, 296, 500, 1000 or 2000 K) have been omitted from the HITRAN2020 line list. However, readers should be aware that the full  $^{14}\text{N}^{16}\text{O}$  line list is available via HITEMP [54]. Figure 18 provides an overview of the update for  $^{14}\text{N}^{16}\text{O}$ , which highlights the expanded spectral range (up to  $23\,727\text{ cm}^{-1}$ ) and the increase in vibrational band coverage (up to  $\Delta v \leq 14$ ,  $v' \leq 26$ ), when compared to HITRAN2016. To take advantage of increased precision of MW transitions, it should be noted that the wavenumber format for NO has been updated to F12.9 for transitions below  $1.0\text{ cm}^{-1}$ , F12.8 for transitions  $1.0$  to  $10.0\text{ cm}^{-1}$ , and F12.7 for transitions  $10.0$  to  $100.0\text{ cm}^{-1}$  (as previously implemented for  $\text{HNO}_3$ ,  $\text{PH}_3$ ,  $\text{O}_2$  and  $\text{NO}^+$ ).



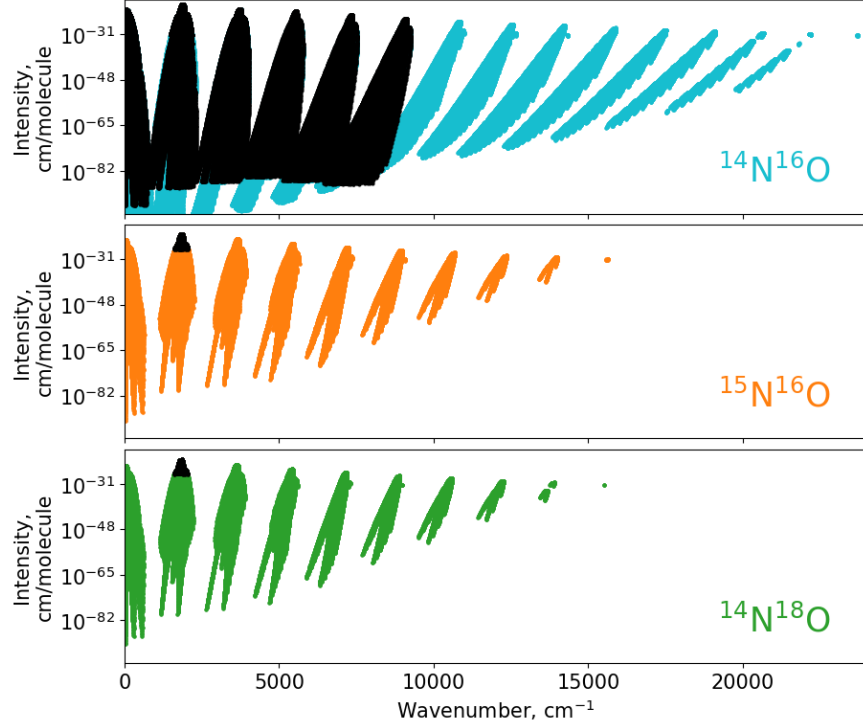


Figure 18: Overview of the  $^{14}\text{N}^{16}\text{O}$  (top),  $^{15}\text{N}^{16}\text{O}$  (middle) and  $^{14}\text{N}^{18}\text{O}$  (bottom) line lists in HITRAN2020, when compared to HITRAN2016 (indicated by black points).

Air- and self-broadening parameters of NO in HITRAN and HITEMP have been refit to available measurements, and are described in detail by Hargreaves et al. [54]. The air-broadening (where  $\gamma_{\text{air}} = 0.79\gamma_{\text{N}_2} + 0.21\gamma_{\text{O}_2}$ ) is calculated from rotationally-dependant  $\text{N}_2$  and  $\text{O}_2$  half-widths provided by separate Padé functions of the form

$$\gamma_x(m) = \frac{a_1 + c_1 m^2}{a_2 + b_2 m + c_2 m^2 + d_2 m^3} \quad (1)$$

for the  $\Omega = 1/2$  and  $3/2$  components. The HITEMP update includes transitions with maximum  $J = 184.5$ , so care was taken to ensure good performance at high- $J$ . The self-broadening half-widths were also revised as part of the HITRAN and HITEMP updates and were fit to the same functional form. The coefficients

for Eqn. 1 for N<sub>2</sub>-, O<sub>2</sub>- and self-broadening of the  $\Omega = 1/2$  and  $3/2$  components are given in Tab. 3 of Ref. [54].

In addition, the pressure-induced line shifts for air ( $\delta_{\text{air}}$ ) that are measured for the fundamental vibrational band [336] have been extended to additional vibrational bands (up to  $\Delta v = 6$ ) using the method outlined by Hartmann and Boulet [337]. This same method was previously applied to CO [255] for HITRAN2016.

The HITRAN2020 update for NO also includes the NOname line lists of <sup>15</sup>N<sup>16</sup>O and <sup>14</sup>N<sup>18</sup>O, with the same intensity thresholds as <sup>14</sup>N<sup>16</sup>O applied. The extended coverage when compared to HITRAN2016 is also shown in Fig. 18. Isotopologue analysis of human breath [338] highlighted issues for the intensities of <sup>15</sup>N<sup>16</sup>O in HITRAN2016. The present update contains intensities from NOname for each isotopologue and is therefore expected to address this issue. The <sup>14</sup>N<sup>17</sup>O, <sup>15</sup>N<sup>17</sup>O and <sup>15</sup>N<sup>18</sup>O NOname line lists have not been added to HITRAN.

NO also absorbs strongly in the near ultraviolet. In particular, in the 200–230 nm (44 000– 50 000 cm<sup>−1</sup>) region its spectrum overlaps those of ammonia, O<sub>2</sub> and O<sub>3</sub>. Qu et al. have recently developed a spectroscopic model which covers the  $\beta$ ,  $\gamma$  and  $\delta$  bands of NO [339] and associated line list [340] which will be considered for future inclusion in the database.

### 2.9. SO<sub>2</sub>: Sulfur Dioxide (molecule 9)

Sulfur dioxide is an abundant pollutant in the terrestrial atmosphere, being produced by natural (such as volcanoes [341]) and anthropogenic (including coal burning [342]) sources. Characterization of SO<sub>2</sub> is necessary for atmospheric chemistry and climate models, due to its large affect on sulfate aerosols [341]. It is present on Venus, contributing to the Venusian sulfur cycle [343], and SO<sub>2</sub> is also being actively searched for in the atmosphere of Mars [344, 345] as it is believed to play an important role in the atmospheres of rocky planets, including exoplanets [346].

### 2.9.1. Description of new line lists

Recent developments in SO<sub>2</sub> spectroscopy have laid the groundwork for a major update and expansion of the corresponding line list in HITRAN. In particular, semi-empirical line lists from Huang et al. [347], and Naumenko et al. [348], have been identified as major sources for the potential improvement. Both line lists actively employed *ab initio* intensities (sometimes adjusted with empirical values) and systematically verified energy levels available from MARVEL analyses. In the MARVEL work on the SO<sub>2</sub> molecule [57, 58], three sulfur isotopologues, <sup>32</sup>S<sup>16</sup>O<sub>2</sub>, <sup>33</sup>S<sup>16</sup>O<sub>2</sub>, and <sup>34</sup>S<sup>16</sup>O<sub>2</sub>, were analyzed, resulting in 15 130, 5852, and 10 893 validated empirical ro-vibrational energy levels, respectively [349]. The <sup>32</sup>S<sup>16</sup>O<sub>2</sub>, <sup>33</sup>S<sup>16</sup>O<sub>2</sub>, and <sup>34</sup>S<sup>16</sup>O<sub>2</sub> MARVEL datasets, collated from the literature, contain 40 269, 15 628, 31 080 ro-vibrational lines, respectively [349]. Both Huang et al. [347], (hereafter referred to as Ames) and Naumenko et al. [348] (hereafter referred to as Naumenko) line lists and their evaluations against available laboratory spectra are briefly described below.

From 2014 to 2016, NASA Ames-296K *ab initio* IR line lists were published for <sup>32</sup>S<sup>16</sup>O<sub>2</sub>, <sup>33</sup>S<sup>16</sup>O<sub>2</sub>, <sup>34</sup>S<sup>16</sup>O<sub>2</sub> [350, 351], and <sup>16</sup>O<sup>32</sup>S<sup>18</sup>O [352]. They were computed on a potential energy surface empirically refined with selected lines taken from HITRAN2012 (with line positions uncertainty codes  $\geq 4$  (see Table 2) [14] (unchanged in HITRAN2016 [15]), and an original *ab initio* dipole moment surface determined at the CCSD(T)/aug-cc-pV(Q+d)Z level of theory. Compared to the bands in HITRAN2012 [14], the agreement for intensities was usually better than 90-95% [350, 351]. The consistency of the Ames-296K line lists has been systematically investigated to explore the possibility of further improvements [353, 354]. Using the same potential and dipole surfaces, Underwood et al. [355] reported a hot <sup>32</sup>S<sup>16</sup>O<sub>2</sub> line list containing 1.3 billion lines. With more complete calculations at higher  $J$  values and extending to a higher energy range, the list was expected to provide the most complete coverage for 0-8000 cm<sup>-1</sup> and temperatures up to 2000 K.

Although line position predictions from the *ab initio* works described above

have matched recent experiments with  $\sigma_{\text{RMS}} = 0.01\text{--}0.02 \text{ cm}^{-1}$ , this accuracy is not sufficient for atmospheric applications. In order to improve the line positions, experimental line positions and Effective Hamiltonian (EH) models based upon ro-vibrational energy levels published between 2009 and 2017 were collected and analyzed for  $^{32}\text{S}^{16}\text{O}_2$  [356–363],  $^{33}\text{S}^{16}\text{O}_2$  [364, 365],  $^{34}\text{S}^{16}\text{O}_2$  [366–369], and  $^{16}\text{O}^{32}\text{S}^{18}\text{O}$  [370–374]. With  $J \leq 75$  (the limit of the Ames-296K line lists) and  $S_{296\text{K}} \geq 10^{-26} \text{ cm/molecule}$ , 26 464, 25 089, 20 820 lines can be matched for  $^{32}\text{S}^{16}\text{O}_2$ ,  $^{34}\text{S}^{16}\text{O}_2$ , and  $^{16}\text{O}^{32}\text{S}^{18}\text{O}$ , respectively. These “New Line Sets” and other  $^{32}\text{S}^{16}\text{O}_2$  and  $^{34}\text{S}^{16}\text{O}_2$  data from HITRAN2016 [15] were updated with reliable ground state EH models [361, 374, 375]. A complete list of observed and calculated energy levels of  $^{33}\text{S}^{16}\text{O}_2$  [376] was incorporated at this stage. The resulting energy levels and other published EH model based levels were taken as the “corrected” reference energy set. Transitions were extracted from the Ames-296K line lists if their lower and upper state energy levels could be matched and replaced by the reference set values. Those extracted lines formed the “Expanded Line Sets”. These contain 195 425/162 403/242 889/123 441 lines for  $^{32}\text{S}^{16}\text{O}_2$ / $^{34}\text{S}^{16}\text{O}_2$ / $^{16}\text{O}^{32}\text{S}^{18}\text{O}$ / $^{33}\text{S}^{16}\text{O}_2$ , in the range of 0–4151/3465/2974/2625  $\text{cm}^{-1}$ , with maximum  $K_a'' = 42/39/32/35$  for 16/13/11/6 vibrational states and 79/59/39/20 bands. Similarly, an “Ames+MARVEL” line set was extracted from the Ames-296K line lists by matching to the published MARVEL level set. These include 195 882/159 729/79 927 lines for  $^{32}\text{S}^{16}\text{O}_2$ / $^{34}\text{S}^{16}\text{O}_2$ / $^{33}\text{S}^{16}\text{O}_2$ , with maximum  $K_a'' = 35/29/22$ . Uniform criteria were adopted for both line sets: 1) line position difference  $\leq 0.10 \text{ cm}^{-1}$  (for  $E'$ ,  $E''$ , and transition wavenumber), 2) ro-vibrational quantum numbers match, 3)  $S_{296\text{K}} \geq 10^{-26} \text{ cm/molecule}$ . Compared to HITRAN2016 [15], many more  $^{32}\text{S}^{16}\text{O}_2$  bands have been added up to 4200  $\text{cm}^{-1}$ . However, the  $3\nu_1$ ,  $2\nu_1 + \nu_3$ , and  $\nu_1 + 2\nu_3$  bands of  $^{32}\text{S}^{16}\text{O}_2$  are still missing from the Ames line sets. See more details in Huang et al. [347].

The Ames line sets did not actively utilize the published experimental EH models (or the EH models published along with the MARVEL analysis) to derive a complete energy level set and use it in the match analysis, except for those of the ground states and  $^{33}\text{S}^{16}\text{O}_2$ . For example, the  $^{34}\text{S}^{16}\text{O}_2$  EH models of the

$3\nu_2$  and  $2\nu_1 + \nu_3$  states were published by Lafferty and Flaud [377] but they are not available in the Ames line set (nor the MARVEL level set). Therefore, in addition to the  $S_{296K}$  and  $J/K_a$  cutoffs, the effective coverage and quality are further restricted by the number and accuracy of reported measured lines and EH-based levels. Levels extrapolated from outdated EH models may coexist with those derived from the latest experiments. This potentially would result in a  $0.001\text{--}0.01\text{ cm}^{-1}$  discrepancy within the “Expanded Line Set”. Future updates to the Ames lists are planned that will fix such minor inconsistencies, enable provision of reliable uncertainty indices to line positions, and re-evaluate the intensities of the major isotopologues with an even more accurate dipole moment surface. Additional Ames-296K line list information for other isotopologues with combinations of isotopes  $^{17}\text{O}$ ,  $^{18}\text{O}$ ,  $^{33}\text{S}$ ,  $^{34}\text{S}$ ,  $^{35}\text{S}$ , and  $^{36}\text{S}$  [353, 354] is available at [huang.seti.org/S02/so2.html](http://huang.seti.org/S02/so2.html), including an “Expanded Line Set” reported for  $^{32}\text{S}^{18}\text{O}_2$  [347].

The Naumenko  $^{32}\text{S}^{16}\text{O}_2$  line list is based primarily on the experimental energy levels derived in the aforementioned MARVEL work by Tóbiás et al. [349]. Moreover, additional experimental energy levels obtained from the identification of the FTS spectra of  $\text{SO}_2$  from Vasilenko et al. [378] and Naumenko et al. [379] were also utilized. The uncertainty of the majority of the transition wavenumbers determined this way correspond to HITRAN uncertainty code 4 (see Table 2). For completeness, effective Hamiltonian calculations performed in Tóbiás et al. [349] were used for the rest of the lines which in turn have uncertainties in the range  $0.001\text{--}0.01\text{ cm}^{-1}$  (code 3).

The Naumenko et al. [348] line list employs *ab initio* intensity values from Underwood et al. [355]. Exceptions are for the  $\nu_1 + \nu_2$ ,  $\nu_2 + \nu_3$ ,  $\nu_1 + \nu_3$  and  $\nu_1 + \nu_2 + \nu_3$  bands, where intensity values are from the recent experimental data from Ulenikov et al. [373] and Borkov et al. [380]. The estimated uncertainties of the intensities are around 5–10% on average. Overall, the Naumenko et al. [348] line list ranges from  $0.025$  and  $4159\text{ cm}^{-1}$  and consists of 549 200 transitions with a  $10^{-27}\text{ cm/molecule}$  intensity cutoff.

### 2.9.2. Validation

Both  $^{32}\text{S}^{16}\text{O}_2$  line lists (Naumenko and Ames) were converted into the HITRAN format. This includes addition of air- and self-broadening data (as well as temperature dependence of the former) using the procedure derived by Tan et al. [381]. The Ames intensities were scaled by the HITRAN isotopic abundance 0.9457 (note that only the two most abundant isotopologues were available in HITRAN so far). The Naumenko line list contains only the principal  $^{32}\text{S}^{16}\text{O}_2$  isotopologue.

In addition, there were further requirements when generating the Ames  $^{32}\text{S}^{16}\text{O}_2$  line list following recommendations in that article. It was suggested using the  $^{32}\text{S}^{16}\text{O}_2$  “Ames+MARVEL” line list which uses MARVEL levels matched to Ames lines. Then supplement the  $^{32}\text{S}^{16}\text{O}_2$  “Ames+Marvel” line list with other transitions from the  $^{32}\text{S}^{16}\text{O}_2$  “Expanded” line list which uses matched Experimental and HITRAN Effective Hamiltonian (EH) model levels to Ames lines. The article also recommended applying cutoffs for  $J \leq 50$  and  $K_a \leq 25$  for the most reliable Ames-296K intensity. All recommendations were applied for the  $^{32}\text{S}^{16}\text{O}_2$  Ames line list [347] prior to comparisons with laboratory data. Line-to-line comparisons of all the  $^{32}\text{S}^{16}\text{O}_2$  spectral bands were generated to evaluate the position, intensity and lower-state energy differences between the Naumenko line list [348], the  $^{32}\text{S}^{16}\text{O}_2$  Ames line list [347] and the  $^{32}\text{S}^{16}\text{O}_2$  HITRAN2016 [15] line list.

The Naumenko and Ames line lists were compared against PNNL [242] laboratory data at 5°C, 25°C and 50°C with nitrogen as the buffer gas for each data set at a pressure of 1 atm. There is a degree of uncertainty for these comparisons in that the PNNL data are N<sub>2</sub>-broadened and HITRAN does not contain N<sub>2</sub>-broadening for SO<sub>2</sub>, therefore air-broadening has been used. Also, the PNNL [242] measurements are limited to frequencies  $\gtrsim 600 \text{ cm}^{-1}$ , making far-IR comparisons unavailable. In addition to the PNNL comparisons, the line lists were validated at high resolution against an FTS experimental spectrum of SO<sub>2</sub> recorded at Old Dominion University (ODU) in 2015 (using the exper-

imental setup previously described for CH<sub>4</sub> [382]). This spectrum covered the  $\nu_1 + \nu_3$  and  $2\nu_3$  bands of SO<sub>2</sub> with a sample pressure of 10 Torr (0.0132 atm), a temperature of 297 K, and a resolution of 0.015 cm<sup>-1</sup>.

The result of the <sup>32</sup>S<sup>16</sup>O<sub>2</sub> line list comparisons showed that in the majority of the bands where HITRAN had data, both line lists exhibited an improvement in residuals and contained multiple bands not previously available in HITRAN. With that in mind, the Ames line list [347] lacked some observable transitions. This is due to the  $J \leq 50$  and  $K_a \leq 25$  limits and a cutoff for intensities beyond 10<sup>-26</sup> cm/molecule. Sample comparisons to PNNL [242] laboratory data is available in Figs. 19 and 20. These figures include data from <sup>32</sup>S<sup>16</sup>O<sub>2</sub>, <sup>34</sup>S<sup>16</sup>O<sub>2</sub> in HITRAN2016 [15], <sup>32</sup>S<sup>16</sup>O<sub>2</sub>, <sup>34</sup>S<sup>16</sup>O<sub>2</sub> from Huang et al. [347], <sup>32</sup>S<sup>16</sup>O<sub>2</sub> from Naumenko et al. [348] supplemented by the <sup>34</sup>S<sup>16</sup>O<sub>2</sub> Huang et al. [347] line list.

The <sup>34</sup>S<sup>16</sup>O<sub>2</sub> isotopologue line list generated by Huang et al. [347] is available in several line list sets. One is labeled the “Expanded” set and another is labeled the “Ames+Marvel” set. As recommended by the article in Huang et al. [347], the following cutoffs were applied for  $J \leq 50$  and  $K_a \leq 25$ . In following the recommendations by the authors, the “Ames+Marvel” set was supplemented with other transitions from the “Expanded” set to generate the final <sup>34</sup>S<sup>16</sup>O<sub>2</sub> Huang et al. [347] line list.

The resulting <sup>34</sup>S<sup>16</sup>O<sub>2</sub> line list was evaluated by first converting it into HITRAN data format and then scaling the intensities by the HITRAN isotopic abundance 4.195×10<sup>-2</sup>. Next, line-by-line comparisons of the available  $\nu_1$ ,  $\nu_1 + \nu_3$  and  $\nu_3$  bands in HITRAN were used to evaluate the position, intensity and lower-state energy differences between the <sup>34</sup>S<sup>16</sup>O<sub>2</sub> Huang et al. [347] line list and the HITRAN2016 [15] <sup>34</sup>S<sup>16</sup>O<sub>2</sub> line list. As was the case for the principal isotopologue, the procedure derived by Tan et al. [381] was used to populate line-shape parameters. Additionally, the <sup>34</sup>S<sup>16</sup>O<sub>2</sub> Huang et al. [347] line list was supplemented into the <sup>32</sup>S<sup>16</sup>O<sub>2</sub> Huang et al. [347] line list prior to validations against the PNNL [242] and the ODU laboratory data. HITRAN2016 [15] contains only a few bands for this isotopologue, which is evident from these comparisons. However, the <sup>34</sup>S<sup>16</sup>O<sub>2</sub> Huang et al. [347] line list

contains many more transitions/bands and therefore provide a more complete  $^{34}\text{S}^{16}\text{O}_2$  line list.



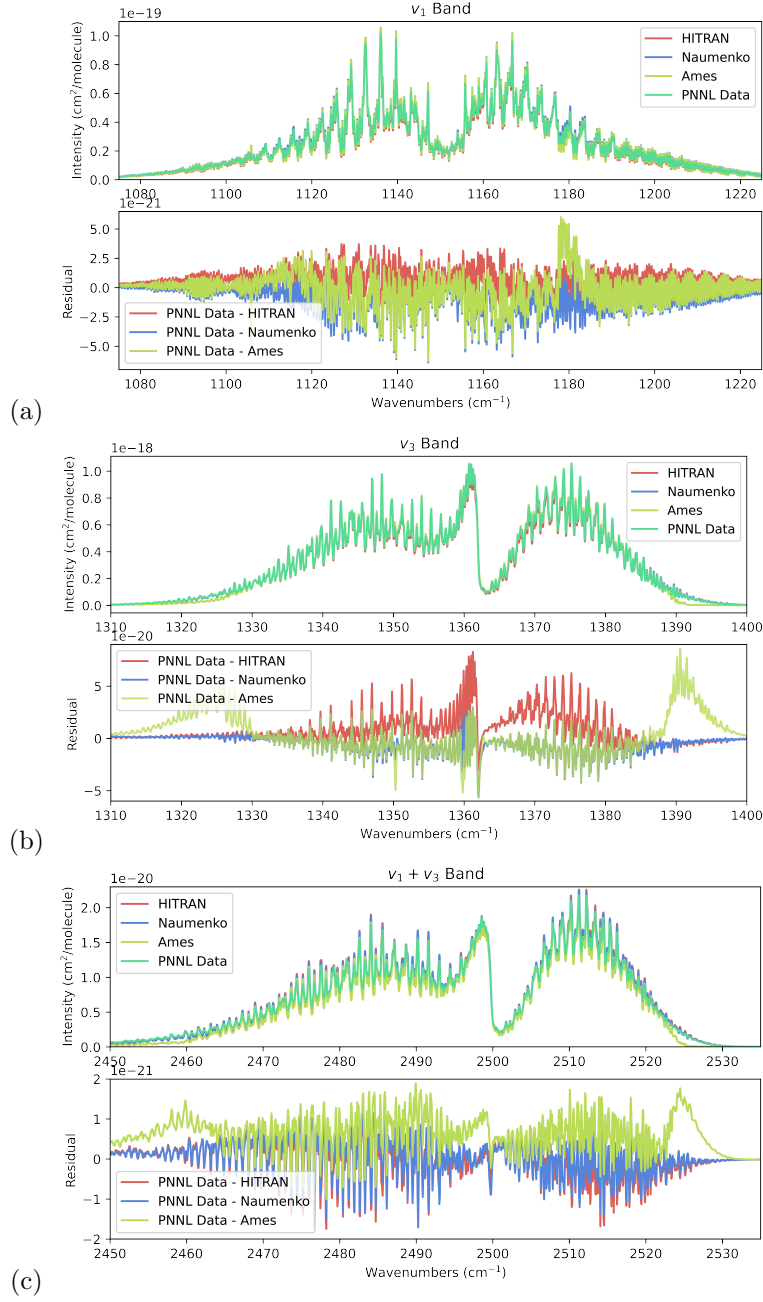


Figure 19: Validation of calculated spectra covering the  $\nu_1$ ,  $\nu_3$  and  $\nu_1 + \nu_3$  vibrational bands against PNNL laboratory data [242]. In each panel,  $^{32}\text{S}^{16}\text{O}_2$ ,  $^{34}\text{S}^{16}\text{O}_2$  HITRAN2016 data [15],  $^{32}\text{S}^{16}\text{O}_2$ ,  $^{34}\text{S}^{16}\text{O}_2$  Ames data [347], and  $^{32}\text{S}^{16}\text{O}_2$  Naumenko data [348] (supplemented by the  $^{34}\text{S}^{16}\text{O}_2$  Huang et al. [347] line list) have been compared to the PNNL  $\text{SO}_2$  spectrum at 25°C and 1 atm ( $\text{N}_2$  buffer gas).

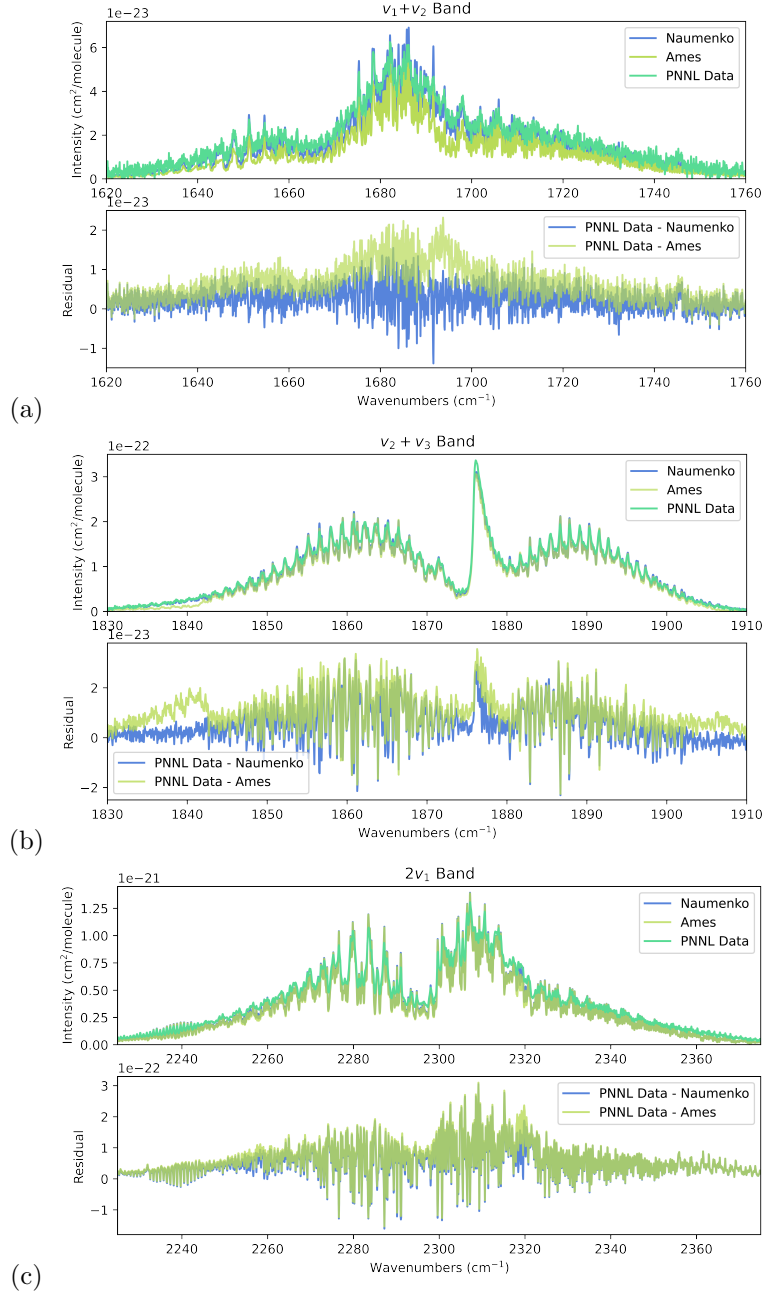


Figure 20: Validation of calculated spectra covering the  $\nu_1 + \nu_2$ ,  $\nu_2 + \nu_3$  and  $2\nu_1$  vibrational bands against PNNL laboratory data [242]. These bands were not previously included in HITRAN2016 [15]. In each panel, spectra calculated from  $^{32}\text{S}^{16}\text{O}_2$ ,  $^{34}\text{S}^{16}\text{O}_2$  Ames data [347], and  $^{32}\text{S}^{16}\text{O}_2$  Naumenko data [348] (supplemented by the  $^{34}\text{S}^{16}\text{O}_2$  Huang et al. [347] line list) have been compared to the PNNL laboratory SO<sub>2</sub> spectra at 25°C and 1 atm (N<sub>2</sub> buffer gas).

The  $^{33}\text{S}^{16}\text{O}_2$  isotopologue is available in several line list sets generated by Huang et al. [347]. One labeled the “Expanded” set and another labeled the “Ames+Marvel” set. As recommended by Huang et al. [347] the line list was limited to  $J \leq 50$  and  $K_a \leq 25$ . The “Ames+Marvel” set was used as a basis and then supplemented with additional transitions from the “Expanded” set to generate the final  $^{33}\text{S}^{16}\text{O}_2$  line list for HITRAN.

The resulting intensities of the  $^{33}\text{S}^{16}\text{O}_2$  line list were scaled by the HITRAN isotopic abundance  $7.464 \times 10^{-03}$ . The  $^{33}\text{S}^{16}\text{O}_2$  isotopologue was not included in HITRAN2016 [15], therefore the  $^{33}\text{S}^{16}\text{O}_2$  line list from Huang et al. [347] was added to HITRAN2020.

The  $^{16}\text{O}^{32}\text{S}^{18}\text{O}$  isotopologue was available in the “Expanded” line list generated by Huang et al. [347]. As recommended, the line list was limited to  $J \leq 50$  and  $K_a \leq 25$  and the resulting  $^{16}\text{O}^{32}\text{S}^{18}\text{O}$  intensities were scaled by the HITRAN isotopic abundance  $3.793 \times 10^{-03}$ . The  $^{16}\text{O}^{32}\text{S}^{18}\text{O}$  isotopologue was not included in HITRAN2016 [15], therefore the  $^{16}\text{O}^{32}\text{S}^{18}\text{O}$  line list from Huang et al. [347] was added to HITRAN2020.

As was the case for the two most abundant isotopologues, the air-broadening coefficients (and their temperature dependence), as well as self-broadening coefficients, were applied to the  $^{33}\text{S}^{16}\text{O}_2$  and  $^{16}\text{O}^{32}\text{S}^{18}\text{O}$  Huang et al. [347] line list using the procedure described by Tan et al. [381].

Finally, Fig. 21 compares the new HITRAN2020 line list for  $\text{SO}_2$  (for all isotopologues) against the previous  $\text{SO}_2$  line list in HITRAN2016 [15] and demonstrates the significant increase in spectral coverage.

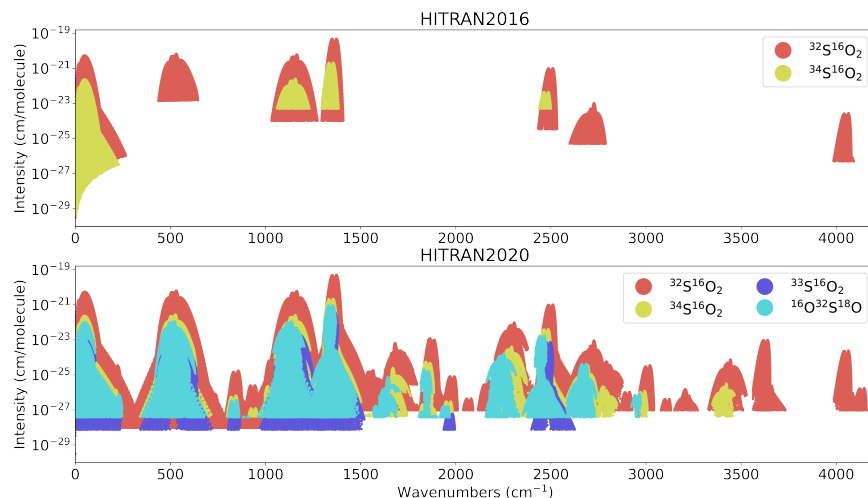


Figure 21: The HITRAN2016 SO<sub>2</sub> line list [15] is shown in the upper panel, which can be compared to the spectral coverage of the new HITRAN2020 SO<sub>2</sub> line list (using data from Refs. [347, 348] shown in the lower panel. These intensities have been scaled to their “natural” abundance (see Tab. 1) per HITRAN convention.

## 2.10. NO<sub>2</sub>: Nitrogen Dioxide (molecule 10)

Nitrogen dioxide (NO<sub>2</sub>) plays an important role in the photochemistry of Earth’s atmosphere. Combustion of fossil fuels at high temperatures (particularly from diesel engines), along with biomass burning and soil emissions are primary contributors to tropospheric NO<sub>2</sub> [383]. NO<sub>2</sub> also impacts air quality and is detrimental to human health [384], therefore concentrations are routinely monitored, such as during the COVID-19 lockdown in the UK [385].

For HITRAN2020, the NO<sub>2</sub> spectral coverage has been significantly extended. Figure 22 (left panel) displays an overview comparison of the <sup>14</sup>NO<sub>2</sub> line lists of HITRAN2016 and HITRAN2020. While HITRAN2016 contained only lines below 3074.153 cm<sup>-1</sup>, the present version has been extended into the NIR. Selected data from NDSD-1000 [386, 387] up to 4775 cm<sup>-1</sup> (with an intensity threshold of  $S = 1.0 \times 10^{-25}$  cm/molecule) have been added for HITRAN2020. Comparisons to PNNL absorption cross sections [242] over the 4060-4775 cm<sup>-1</sup> spectral region necessitated a scaling of the NDSD-1000 intensities by a factor of 3.5 in this region (see Hargreaves et al. [54] for further details).

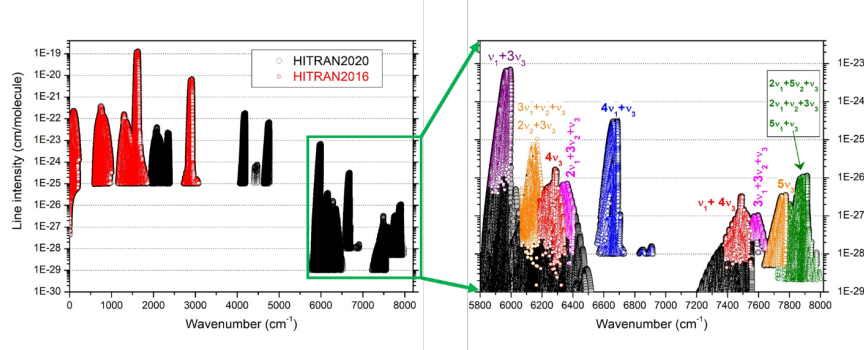


Figure 22: Overview of the  $\text{NO}_2$  line list for the main isotopologue,  $^{14}\text{N}^{16}\text{O}_2$ . *Left panel:* Comparison of the HITRAN2016 and HITRAN2020 versions (red and black circles, respectively). *Right panel:* Enlargement of the  $5800\text{--}8000\text{ cm}^{-1}$  region that has been updated using CRDS measurements. The HITRAN2020 update (black circles) has been overlaid by the original CRDS data for each band system [388–396], which are identified by color.

Data obtained from extensive CRDS measurements [388–396] in the  $5800\text{--}8000\text{ cm}^{-1}$  region has also been added for HITRAN2020. The CRDS measured line positions and intensities were used to fit effective Hamiltonian and effective dipole moment parameters for the separate groups of interacting bands [388–396]. The obtained sets of effective parameters were presently used for the generation of the HITRAN2020 lists. As illustrated in Fig. 22 (right panel), different intensity cutoffs were applied depending on the study (in some cases, the addition to HITRAN has been extrapolated beyond the observed data). The smallest intensity for this region is  $S = 1.0 \times 10^{-29}\text{ cm/molecule}$  and has increased the total number vibrational bands to 48 that are included in HITRAN for  $^{14}\text{NO}_2$ .

For the added bands, semi-empirical approaches [397, 398] were used for the calculation of the self- and air-broadening coefficients as well as their temperature exponents [386]. The empirical parameters used in these approaches were fitted to the measured self-broadening coefficients [399] and to the measured  $\text{N}_2$ - and  $\text{O}_2$ -broadening coefficients [400]. The vibrational dependence of the line-broadening coefficients was found to be small (less than 4%) [386] and thus neglected in the production of the  $\text{NO}_2$  line list.

It is worth noting that the minimum intensity of the  $^{14}\text{NO}_2$  line list is different below and above  $5000\text{ cm}^{-1}$ . However, the HITRAN list is not complete in both regions as some relatively strong bands are not provided due to the lack of measurements. New observations, such as of the  $\nu_1 + \nu_2 + \nu_3$  band near  $3600\text{ cm}^{-1}$  [401], will help to improve the completeness for future editions of HITRAN.

Finally, it should be mentioned that the statistical weights of the lower and upper states and the Einstein- $A$  coefficients for the  $\text{NO}_2$  HITRAN2016 bands with unresolved hyperfine structure were corrected.

#### *2.10.1. Addition of $^{15}\text{N}^{16}\text{O}_2$*

$^{15}\text{N}^{16}\text{O}_2$  is the second most abundant isotopologue of nitrogen dioxide, with a 0.003646 concentration of total  $\text{NO}_2$  [56]. The  $\nu_3$  band of  $^{15}\text{N}^{16}\text{O}_2$  is centered at  $1582.1029\text{ cm}^{-1}$  and becomes the first band of this isotopologue to be included into HITRAN.

The  $^{15}\text{N}^{16}\text{O}_2$  data included for HITRAN2020 contains 5860 transitions between  $1500.73\text{--}1660.45\text{ cm}^{-1}$  for the  $\nu_3$  fundamental band. These transitions have a maximum intensity of  $2.0 \times 10^{-26}\text{ cm/molecule}$ , with  $N_{\text{max}} = 77$  and  $K_a = 0\text{--}15$ . The line positions and intensities were generated during two analyses: Orphal et al. [402] used laboratory FTS spectra recorded at high-resolution ( $0.006\text{ cm}^{-1}$  unapodized) to generate a preliminary line list, which was later refined by Perrin et al. [403]. The  $^{15}\text{N}^{16}\text{O}_2$  line list was restricted to the strong  $\nu_3$  band, although the resonances that couple the strong  $\nu_3$  band with very dark  $2\nu_2$  and  $\nu_1$  bands were explicitly accounted for. Experimental data concerning absolute line intensities are presently unavailable for  $^{15}\text{N}^{16}\text{O}_2$ , therefore the line intensity calculation was performed using the transition moment constants which are quoted for the  $\nu_3$  band of  $^{14}\text{N}^{16}\text{O}_2$  in Ref. [404]. In parallel, the partition functions for  $^{15}\text{N}^{16}\text{O}_2$  were computed and are now available from the supplementary material of Ref. [401].

Perrin et al. [403] have used this line list to detect atmospheric  $^{15}\text{N}^{16}\text{O}_2$  for the first time from balloon-borne solar occultation spectra measured by the JPL

MkIV FTS. Their retrieved  $^{15}\text{NO}_2/^{14}\text{NO}_2$  ratio is within 5% of the expected 0.00364 isotopic value (at and altitude of 15–35 km) and validate the calculated intensities. Over the same altitude range the RMS spectral fitting residuals reduce significantly as a result of including the new  $^{15}\text{N}^{16}\text{O}_2$  line list. Thus improving the accuracy of retrievals for all gases that absorb in the 1550–1650  $\text{cm}^{-1}$  region (e.g.,  $^{14}\text{NO}_2$ ,  $\text{H}_2\text{O}$ ,  $\text{HDO}$ ,  $\text{O}_2$ ).

Future improvements for the  $\text{NO}_2$  line list can be achieved by using the line list for the 1153–4775  $\text{cm}^{-1}$  spectral region [401] generated from recently recorded high-resolution FTS measurements (and added to the GEISA database [405]). For the 6.2  $\mu\text{m}$  and 3.4  $\mu\text{m}$  spectral regions, Jacquinet-Husson et al. [405] fully updated the line lists for the first hot bands ( $\nu_2 + \nu_3 - \nu_2$  and  $\nu_1 + \nu_2 + \nu_3 - \nu_2$ , respectively) and also included the  $\nu_3$  and  $\nu_1 + \nu_3$  bands of  $^{15}\text{N}^{16}\text{O}_2$ . Several weak cold bands in the 2.2–4.9  $\mu\text{m}$  region together with several higher order hot bands in the 6.2  $\mu\text{m}$  and 3.4  $\mu\text{m}$  spectral regions are also included for  $^{14}\text{N}^{16}\text{O}_2$ , whenever possible. Finally, Perrin et al. [401] performed a validation of this new line list and inter-comparisons with the  $\text{NO}_2$  lists present in HITRAN and HITEMP [54] databases. The most significant differences concern vibration-rotation bands that have a weak IR signature for typical terrestrial atmospheric conditions, but for hot bands, may have an impact for  $\text{NO}_2$  in high-temperature gas conditions.

#### 2.10.2. $\text{NO}_2$ added to HITEMP

The HITEMP database [52] has been expanded to include  $\text{NO}_2$  [54] and is based on the NDSD-1000 line list [386, 387].  $\text{NO}_2$  was added to HITEMP prior to the 5800–8000  $\text{cm}^{-1}$  ( $^{14}\text{NO}_2$ ) and  $^{15}\text{NO}_2$  HITRAN additions described above. To maintain consistency, these updates will be incorporated into HITEMP in due course. Readers should refer to Hargreaves et al. [54] for a full description of the HITEMP line list for  $\text{NO}_2$ .

### 2.11. $\text{NH}_3$ : Ammonia (molecule 11)

Ammonia ( $\text{NH}_3$ ) is integral to global agriculture through its use as an industrial fertilizer [406]. Consequently, anthropogenic emissions are a large contributor to the atmospheric abundance [407], but enhancements can also occur through natural events such as wildfires [408]. The abundance of  $\text{NH}_3$  impinges on air quality [409] and its abundance can now be monitored over urban [410], industrial [411], and rural [412] regions using satellite observations. Furthermore,  $\text{NH}_3$  is a well known constituent of gas giants atmospheres and recent measurements from the Juno mission demonstrate complex weather processes with large-scale  $\text{NH}_3$  variability [413, 414]. The absorption of  $\text{NH}_3$  is also expected to contribute to the opacities of cool brown dwarfs [415] and exoplanets [416].

The “CoYuTe” *ab initio* line list has been calculated as part of the ExoMol project based on a spectroscopically determined PES and an *ab initio* DMS [417]. CoYuTe spans transitions with wavenumbers up to  $20\,000\text{ cm}^{-1}$  and is designed for use at temperatures up to  $1500\text{ K}$  [418]; even before improvement of the energy levels using MARVEL, it is significantly more accurate than the BYTe line list [419] used to populate earlier versions of HITRAN. In parallel there was an extensive update of the  $^{14}\text{NH}_3$  MARVEL database [420] which considered 46 115 transitions up to  $7500\text{ cm}^{-1}$  yielding 4936 unique, labelled empirical ro-vibrational energy levels. These MARVEL energy levels were used in the CoYuTe line list to ensure experimental accuracy in the wavenumbers of the vast majority of transitions lying below  $7000\text{ cm}^{-1}$  and above the HITRAN2016 intensity cut off. These new MARVEL energy levels and the CoYuTe line list were used to complement the HITRAN2016 dataset in which a significant number of lines were missed in the  $4000\text{--}7000\text{ cm}^{-1}$  region.

#### 2.11.1. Addition of bands below $5500\text{ cm}^{-1}$

The performance of the CoYuTe/MARVEL line list at modeling room-temperature experimental FTS spectra ( $0.01\text{ cm}^{-1}$  resolution) between  $2400\text{--}5500\text{ cm}^{-1}$  [421, 422] and  $4800\text{--}7500\text{ cm}^{-1}$  [423] (as well as lower resolution cross-sections



from PNNL [242]), has been compared to HITRAN2016 [15]. Throughout these spectral regions there were instances where CoYuTe/MARVEL provided position and/or intensity improvements when compared to HITRAN; however, there were also a number occasions when the HITRAN2016 data was favorable, with many instances where the performance were comparable. A more intensive and thorough assessment of the line-by-line improvements provided by the CoYuTe/MARVEL line list is planned for the future. At this time, only transitions from vibrational bands not previously contained in HITRAN are considered for inclusion. For  $\text{NH}_3$ , the lower-state energies in HITRAN refer to the lowest allowed lower-state energy and values in the CoYuTe/MARVEL line list have been reduced by  $0.7934 \text{ cm}^{-1}$ : the energy difference between the symmetric and anti-symmetric  $J'' = K'' = 0$  levels of the ground vibrational state.

A previous lack of assignments for  $\text{NH}_3$  in the  $5500\text{--}6350 \text{ cm}^{-1}$  spectral region means that the CoYuTe/MARVEL line list is missing the majority of transitions recently observed by Cacciani et al. [424]. Of the weak transitions in this range that were included in the CoYuTe/MARVEL, the predicted intensities appeared to be overestimated when compared to measured values. Therefore, only the CoYuTe/MARVEL transitions of selected bands  $< 5500 \text{ cm}^{-1}$  (with intensities  $> 1.0 \times 10^{-25} \text{ cm/molecule}$ ) were included as part of HITRAN2020. Figure 23 summarizes the new CoYuTe/MARVEL additions to HITRAN below  $5500 \text{ cm}^{-1}$ .

The CoYuTe/MARVEL lines that were not included as part of the present update will be thoroughly evaluated as a subsequent update to HITRAN2020. In addition, the intensities for the  $50\text{--}660 \text{ cm}^{-1}$  spectral region measured by [426] will also be considered.

### *2.11.2. The $5500\text{--}6350 \text{ cm}^{-1}$ region*

Transitions of  $\text{NH}_3$  for the  $5500\text{--}6300 \text{ cm}^{-1}$  spectral region were not previously included in HITRAN due to a lack of measurements, but this region is part of the  $1.6 \mu\text{m}$  atmospheric transparency window and allows for additional

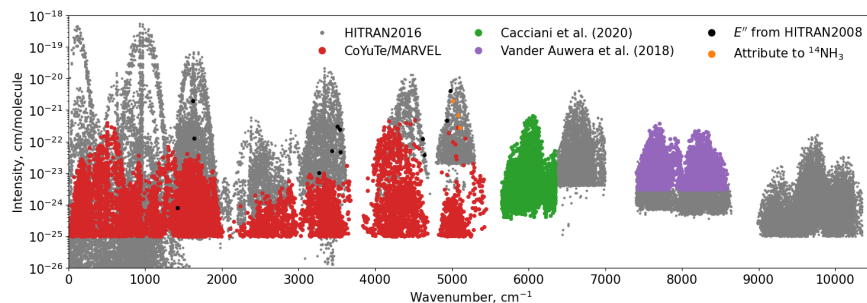


Figure 23: Overview of the  $^{14}\text{NH}_3$  data in HITRAN2020. The location of the CoYuTe/MARVEL, Cacciani et al. [424] and Vander Auwera and Vanfleteren [425] updates for  $\text{NH}_3$  and additional corrections are indicated on the plot.

opportunities for  $\text{NH}_3$  retrievals. Recently, Cacciani et al. [424] have analyzed an archived FTS spectrum of  $\text{NH}_3$  (1.8 Torr at  $21.5^\circ\text{C}$ ) between  $5500\text{--}6350\text{ cm}^{-1}$  recorded at Kitt Peak National Solar Observatory (NSO) in 1991 with a resolution of  $0.01\text{ cm}^{-1}$ . A multi-line fitting procedure was used to obtain the positions and intensities of 2779 lines, of which 1762 lines were assigned to 29 vibrational bands.

A small number of transitions (between  $6300\text{--}6350\text{ cm}^{-1}$ ) partially overlap the data provided by Sung et al. [427], which was included as part of HITRAN2012 [14]. Comparison of these intensities showed a systematic offset of  $\sim 10\text{--}15\%$  (within the uncertainty of the experiment), but a good agreement was found when compared to *ab initio* line intensities [418] for many more lines (see Fig. 9 or Ref. Cacciani et al. [424]). Therefore, the positions and intensities from Cacciani et al. [424] have been added to HITRAN, and replace the previous values [427] for the  $6300\text{--}6350\text{ cm}^{-1}$  overlap region. For inclusion to HITRAN, the lower-state energies in Cacciani et al. [424] have been reduced by  $0.7934\text{ cm}^{-1}$  to account for the lowest allowed lower-state energy.

### 2.11.3. The $7400\text{--}8600\text{ cm}^{-1}$ region

Relying on two high-resolution Fourier-transform spectra recorded at room temperature, the positions and intensities of 1936 lines of ammonia were measured in the range  $7400\text{--}8600\text{ cm}^{-1}$  [425]. These lines are not assigned and

lower-state energies are therefore not available. The line positions were calibrated using 145 water vapor lines observed in the ranges 5255–5536  $\text{cm}^{-1}$  and 7054–7398  $\text{cm}^{-1}$  and reference line positions reported by Toth [60] and available in HITRAN [15]. The accuracy of the calibrated line positions was estimated to range from 0.001 to 0.002  $\text{cm}^{-1}$  from the lower to the upper limits of the spectral range considered, while the accuracy of the line intensities was estimated to be around 10% or better. Line positions and intensities measured in the range 6800–7000  $\text{cm}^{-1}$  of the same two spectra with measurements reported by Sung et al. [427] agreed within these estimated accuracies (see Figs. 2 and 3 of [425]). Partially-assigned lines measured in the 7400–8640  $\text{cm}^{-1}$  range of a FTS spectrum recorded at NSO by C. De Bergh in 1980 [428] were incorporated in the 2016 update of HITRAN [15]. Comparisons of these line positions and intensities with the new measurements [425] put forward discrepancies within the uncertainties stated in HITRAN [15] for the line positions, but (significantly) larger for the intensities of strong lines ( $S > 10^{-22}$  cm/molecule; see Figs. 6 and 7 of [425]). Note that less-accurately measured positions and intensities of 1985 lines were also reported in the range 7400–8600  $\text{cm}^{-1}$  [425], leading to a combined total of 3921 lines.

The Vander Auwera and Vanfleteren [425] positions and intensities were compared to the empirical line list of Beale et al. [423]. Empirical lower-state energies have been matched to 578 lines of Vander Auwera and Vanfleteren [425] to improve the temperature extrapolation of this spectral range. For all other lines, a default value is used ( $E'' = 333 \text{ cm}^{-1}$ ). The performance of the Vander Auwera and Vanfleteren [425] line lists (all 3921 lines) was validated against HITRAN2016 by modeling a FTS spectrum of  $\text{NH}_3$  (5.0 Torr at 21.5°C) recorded at the NSO in 1980. (This same spectrum was previously analysed by Barton et al. [428] and the corresponding data added to HITRAN2016 [15]). This reanalysis for this work demonstrated that Vander Auwera and Vanfleteren [425] provided many improvements, such as for strong lines (as shown in Fig. 24c), but these comparisons also demonstrated that some blended features were better modelled by HITRAN2016 (Fig. 24b). The vast majority of

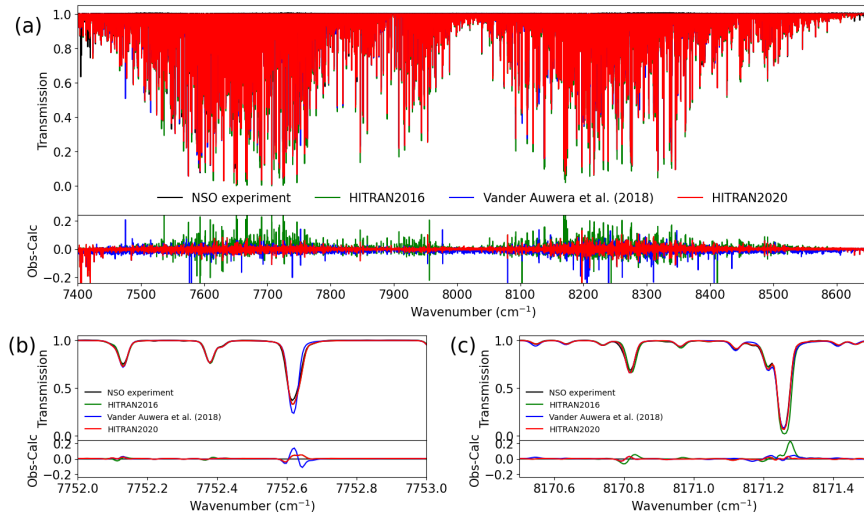


Figure 24: A demonstration of the improvements for the NH<sub>3</sub> line list in HITRAN2020 over the 7400–8600 cm<sup>-1</sup> spectral region (a), with zoomed in examples of when HITRAN2016 (b) or Vander Auwera and Vanfleteren [425] (c) contribute to the HITRAN2020 data. In each upper panel, a FTS NSO spectrum with 5.0 Torr of NH<sub>3</sub> at 21.5°C is compared to calculated spectra using the HITRAN2016 (using the data of Barton et al. [428]), Vander Auwera and Vanfleteren [425] and the combined HITRAN2020 line lists. The lower panels display the obs-calc residuals.

transitions in this region are unassigned, therefore the calculated spectra were assessed in their ability to reproduce the experimental observations. The parameters that provided the smallest residual were used for HITRAN2020. The NH<sub>3</sub> line list for HITRAN2020 is also included in the comparison plots of Fig. 24 and can be seen to have the smallest residual in each case.

Additional FTS spectra (10.0 Torr of NH<sub>3</sub> combined with a 0.5 m path length) measured by Beale et al. [423] also cover the 7400–8600 cm<sup>-1</sup> region. However, the SNR for this region was not sufficient to provide detailed comparisons. Nevertheless, the overestimation of strong line intensities identified by Vander Auwera and Vanfleteren [425] for HITRAN2016 (and shown in Fig. 24c) were clearly observed when comparing calculated spectra, with the HITRAN2020 calculated spectrum providing the smallest residual.

#### 2.11.4. Above 12 000 cm<sup>-1</sup>

The HITRAN NH<sub>3</sub> data currently extends up to 10 349 cm<sup>-1</sup>, but recent spectroscopic analyses have provided line lists into the NIR and visible regions.

Relying on NH<sub>3</sub> FTS absorption spectra covering the 0.793 μm region, the positions and intensities of 1114 ammonia lines observed in the 12 491–12 810 cm<sup>-1</sup> region have been measured [429]. This work will be considered for a future update of the database.

Zobov et al. [430] have reported analysis of the green and red bands of NH<sub>3</sub> for the 15 200–15 700 cm<sup>-1</sup> and 17 950–18 250 cm<sup>-1</sup> spectra regions, respectively, based on reanalysed Kitt Peak archive absorption spectra from 1980. Assignments were made up to  $J = 7$  and were used to refine the PES [417] used for the CoYuTe line list [418]. Irwin et al. [431] used the CoYuTe line list to model low- to medium-resolution spectra of Jupiter at visible wavelengths with promising results, although application to high-resolution studies is not recommended [418] and these data have not been added to HITRAN at this time.

#### 2.11.5. Additional updates and broadening parameters for <sup>14</sup>NH<sub>3</sub>

The lower-state energies of 12 transitions was noted to give an incorrect temperature extrapolation when used at higher temperatures [421]. To correct this issue, the lower-state energies of these transitions have been reverted to values from HITRAN2008 [13] and the assignment removed. In addition, it was noted by Yurchenko [432] that 3 lines at 5014.4776, 5084.8734, 5104.2963 cm<sup>-1</sup> identified as belonging to <sup>15</sup>NH<sub>3</sub> had intensities overestimated by (at least) an order of magnitude. These anomalous intensities are due to stronger coincident <sup>14</sup>NH<sub>3</sub> transitions and they have therefore been attributed to <sup>14</sup>NH<sub>3</sub> and the assignment has been removed. These corrected transitions are indicated in Fig. 23 along with the other HITRAN2020 updates for NH<sub>3</sub>.

The air- and self-broadening coefficients and temperature dependence from Nemtchinov [433] have been applied to all new transitions. To support the application of HITRAN data to modeling of planetary atmospheres, H<sub>2</sub>-, He- and CO<sub>2</sub>-broadening parameters were introduced for NH<sub>3</sub> as part of HITRAN2016

[434]. In addition, H<sub>2</sub>O-broadening parameters have since been added to HITRAN by [48]. These parameters are necessary for accurate modelling of the Jupiter’s atmosphere and have been validated against experimental measurements under Jovian conditions [435]. As part of this work, the self-broadening parameter for the  $R(0)$  ground state transition at  $4.67463\text{ cm}^{-1}$  was empirically adjusted to  $0.250\text{ cm}^{-1}/\text{atm}$ , for better agreement with observation.

#### 2.11.6. $^{15}\text{NH}_3$

Notwithstanding the recognized important role of  $^{15}\text{NH}_3$  in the determination of the  $^{15}\text{N}/^{14}\text{N}$  ratio in space [436] where ammonia is abundant in various environments and objects, the extent and quality of spectroscopic information contained in HITRAN2016 was not on par with that of  $^{14}\text{NH}_3$  (with an exception of the MW region).

Recently, the spectroscopic analysis of  $a$ ,  $s$  inversion levels of the bending states up to about  $3000\text{ cm}^{-1}$  has been completed for  $^{15}\text{NH}_3$  at experimental accuracy [437, 438], as a result of new high-resolution spectra recorded using the FTS at the Canadian Light Source (CLS) synchrotron and the Bomem DA8 interferometer in Bologna. Overall, 13 288 inversion-rotation-vibration transitions in the  $\nu_2$ ,  $2\nu_2$ ,  $\nu_4$ ,  $3\nu_2$ , and  $\nu_2 + \nu_4$  cold bands, in the  $2\nu_2 \leftarrow \nu_2$ ,  $2\nu_2 \leftarrow \nu_4$ ,  $\nu_4 \leftarrow \nu_2$ ,  $\nu_4 \leftarrow 2\nu_2$ ,  $3\nu_2 \leftarrow \nu_2$ ,  $3\nu_2 \leftarrow 2\nu_2$ ,  $3\nu_2 \leftarrow \nu_4$ ,  $3\nu_2 \leftarrow \nu_2 + \nu_4$ ,  $\nu_2 + \nu_4 \leftarrow \nu_2$ ,  $\nu_2 + \nu_4 \leftarrow 2\nu_2$ ,  $\nu_2 + \nu_4 \leftarrow 3\nu_2$  and  $\nu_2 + \nu_4 \leftarrow \nu_4$  hot bands, and the inversion-rotation transitions in the studied excited states have been assigned and analyzed [437, 438].

The experimental wavenumbers of the assigned transitions have been reproduced at experimental accuracy. This was achieved through a fit with an effective Hamiltonian that included all symmetry-allowed interactions between (and within) the studied excited states. This Hamiltonian is derived according to the most recent results of the principal isotopologue of ammonia [439, 440]. In both studies [437, 438] the experimental values have also been compared with their corresponding *ab initio* values calculated in Ref. [432].

The line positions calculated using the effective Hamiltonian are now in-

cluded as part of HITRAN2020. The line intensity of each transition is calculated from the *ab initio* Einstein-A coefficients computed in Yurchenko [432] for  $J \leq 18$ . The lower-state energies of Canè et al. [437, 438] have been reduced by  $0.7577 \text{ cm}^{-1}$  for HITRAN to account for the energy difference between the symmetric and anti-symmetric  $J'' = K'' = 0$  levels of the ground vibrational state. Isotopologue dependence of the line shape parameters was ignored, and the same algorithms that were used for the principal isotopologue for self-, air- [433],  $\text{H}_2$ , He,  $\text{CO}_2$  [434], and  $\text{H}_2\text{O}$  [48] broadening (and associated temperature dependencies) have also been applied for  $^{15}\text{NH}_3$ .

It should be noted, that the quantum number notation used for  $^{15}\text{NH}_3$  is currently dissimilar to the principal isotopologue in HITRAN. The global quantum number notation used for  $^{14}\text{NH}_3$  was updated in HITRAN2012 [14] to:  $v_1, v_2, v_3, v_4, L_3, L_4, L, \Gamma_{\text{vib}}$  (refer to Table 7 of Ref. [14] for parameter descriptions, but note that the order of the parameters in the “.par” file is as specified here). However, the global quantum number notation for  $^{15}\text{NH}_3$  remains as:  $v_1, v_2, v_3, v_4, S$  (parameter descriptions are given in Table 7 of Ref. [12]). For future editions of HITRAN the consistency of the quantum number notation between ammonia isotopologues will be addressed.

### 2.12. $\text{HNO}_3$ : Nitric Acid (molecule 12)

Unchanged.

### 2.13. $\text{OH}$ : Hydroxyl Radical (molecule 13)

The OH radical is a key species in atmospheric science. In the terrestrial troposphere, OH is the most important oxidizing agent for organic molecules, and in the upper atmosphere produces prominent airglow emission. Atmospheric OH abundances are measured by pure rotational transitions [441], vibration-rotation transitions (Meinel bands) [442], and by the  $A^2\Sigma^+ - X^2\Pi$  electronic transition [443]. OH is also prominent in many astronomical objects [444, 445] and is a strong emitter in high-temperature sources such as flames [446]. The line positions of the Meinel bands ( $X^2\Pi$  vibration-rotation bands) of  $^{16}\text{OH}$  were

updated using mainly calculated values from the PGOPHER [447] fit of Brooke et al. [448] for  $v = 0-13$  based on the earlier Bernath and Colin [449] analysis. Many data sources were included from the literature including some  $B^2\Sigma^+-X^2\Pi$  bands for the high vibrational levels ( $v > 10$ ). The maximum rotational levels reported were extrapolated to 5–10  $J$  values beyond the last observed level and range from 60.5 for  $v = 0$  to 13.5 for  $v = 13$ .

Noll et al. [442] analyzed Meinel band airglow spectra recorded with the astronomical echelle spectrograph UVES at the European Southern Observatory. The line positions agreed very well with the line list provided by Brooke et al. [448] except for some transitions involving higher rotational levels of  $v = 5$  and 6. The observed lines of Noll et al. were then included in the Brooke et al. fit using the same number of line parameters. The spectroscopic constants changed slightly, and a new line list was created with PGOPHER for HITRAN2020.

The line positions for the  $A^2\Sigma^+-X^2\Pi$  electronic transition of  $^{16}\text{OH}$  in HITRAN2020 are based on the analysis of Yousefi et al. [450]. Data from the literature was used for  $v' = 0-4$  in the  $A^2\Sigma^+$  state, and the  $X^2\Pi$  state constants for  $v'' = 0-9$  were held constant at the values determined by Brooke et al. [448]. The primary source of these data was the  $A^2\Sigma^+-X^2\Pi$  0–0, 1–1, and 2–2 bands analyzed by Stark et al. [451] from Fourier transform emission spectra and recalibrated using the frequency comb measurements of Fast et al. [452]. PGOPHER was used to make a line list for all  $A-X$  bands with  $\Delta v \leq 5$  and extrapolated to 5 to 7  $J$ 's higher than the observed values which range from  $J = 12.5$  ( $v' = 4$ ) to 30.5 ( $v' = 0$ ).

The line strengths for the Meinel bands are those calculated by Brooke et al. [448] from two *ab initio* dipole moment functions and the RKR potential curve. The Herman-Wallis effect was taken into account by calculating  $N$ -dependent dipole matrix elements using LeRoy's LEVEL program [453]. LEVEL does not include electron spin (Hund's case (b) matrix elements) while PGOPHER uses  $J$ -dependent matrix elements (Hund's case (a)) as input. As described by Brooke et al., the LEVEL output was transformed into the Hund's case (a) dipole matrix elements for PGOPHER. The line list intensities were validated



by comparison with the observed Herman-Wallis effect in the 2-0 band emission spectrum.

Noll et al. [442] compared the observed airglow intensities for many bands with the Brooke et al. Einstein- $A$  values and found generally good agreement for the P- and R-branches, but the Q-branches showed discrepancies. These discrepancies vary considerably depending on the band; a recent check using the 2-0 band in the laboratory spectrum shows satisfactory agreement with the Brooke et al. values for the P-, Q-, and R-branches. The discrepancies [442] are attributed to interactions with the  $A^2\Sigma^+$  state that are not included in the intensity calculation. Work is continuing in order to improve the line strength values.

The line strengths for  $A^2\Sigma^+-X^2\Pi$  bands are from the calculations of Yousefi et al. [450]. This work uses the same methodology [454] as described above for the Meinel bands. A new *ab initio* transition dipole function was calculated and RKR potentials were used in LEVEL to compute  $N$ -dependent transition dipole matrix elements. The Herman-Wallis effect was included in the PGO-PHER intensity calculations but, in contrast to the Meinel bands, was relatively small. The intensities in the line list were compared with a laboratory emission spectrum and with astronomical spectra: satisfactory agreement was obtained.

All line positions and intensities (of  $^{16}\text{OH}$ ) for the Meinel bands and  $A^2\Sigma^+-X^2\Pi$  band have been updated for HITRAN2020, except for hyperfine transitions of the pure rotational transitions. The  $^{18}\text{OH}$  and  $^{16}\text{OD}$  isotopologues remain unchanged.

The air-broadening coefficients applied to all additional OH Meinel band transitions follow the linearly dependent values (from  $N = 1$  to 4) described in HITRAN1996 [10], with a constant value of  $\gamma_{\text{air}} = 0.040 \text{ cm}^{-1}/\text{atm}$  for  $N \geq 5$ . For  $A-X$  transitions, the  $N$ -dependant values from Gillis et al. [455] are used (introduced as part of HITRAN2000 [11]), with a constant value of  $\gamma_{\text{air}} = 0.0526 \text{ cm}^{-1}/\text{atm}$  for  $N \geq 4$ . For typical atmospheric modeling applications, the self-broadening contribution of OH is expected to be negligible; however a default estimated value of  $\gamma_{\text{self}} = 0.30 \text{ cm}^{-1}/\text{atm}$  has been applied for all transitions

to avoid null values. A value of  $n_{\text{air}} = 0.66$  is applied for the temperature dependence of the air-broadened half-widths of all additional lines [10]. A small number of recent broadening measurements have been made for OH broadened by different gases at high temperatures (780–2440 K) [456–458]. However, uncertainty in the temperature dependence means that extrapolation of these values to 296 K is not recommended.

The line list of OH described above was also used to update the HITEMP database [52]. An intensity threshold of  $S = 1.0 \times 10^{-99}$  cm/molecule has been applied to the HITRAN2020 update, but all lines have been added to HITEMP.

#### 2.14. *HF: Hydrogen Fluoride (molecule 14)*

Unchanged.

#### 2.15. *HCl: Hydrogen Chloride (molecule 15)*

Unchanged.

#### 2.16. *HBr: Hydrogen Bromide (molecule 16)*

Unchanged.

#### 2.17. *HI: Hydrogen Iodide (molecule 17)*

Unchanged.

#### 2.18. *ClO: Chlorine Monoxide (molecule 18)*

Unchanged.

#### 2.19. *OCS: Carbonyl Sulfide (molecule 19)*

Carbonyl sulfide (OCS) is the most abundant sulfur-containing gas in the terrestrial atmosphere, with a tropospheric mixing ratio of about 500 ppt [459]. It makes a significant contribution to the formation of stratospheric sulfate aerosols and influences the radiative properties of the Earth’s atmosphere, climate change and stratospheric ozone concentration [460–464]. OCS is present in the atmosphere of Venus [465]. Carbonyl sulfide is released to the atmosphere by

biomass burning, oceans, the oxidation of dimethyl sulfide and carbon disulfide ( $\text{CS}_2$ ), and several anthropogenic sources (coal combustion, aluminum production, and sulfur recovery) [466, 467].

When retrieving OCS abundances from infrared atmospheric spectra measured by the Jet Propulsion Laboratory (JPL) MkIV Fourier transform infrared (FTIR) spectrometer, Toon et al. [468] have identified that several bands of observable intensity were missing from the HITRAN database in the region of the strong  $\nu_3$  fundamental. To mitigate this deficiency, Toon et al. [468] used 709 unassigned lines, spectral parameters of which were inferred empirically from available laboratory data.

In the course of preparing the HITRAN2020 edition, it was recognized (based on the line positions) that many of these “missing” lines were present in the original private line list from Brown and Fayt [469] (briefly explained in Ref. [11]) which formed a substantial bulk of the HITRAN2000 data for the OCS molecule. These particular lines from Brown and Fayt [469] were, however, omitted from HITRAN because of some concerns regarding the accuracy of their intensities. They were however included in the GEISA database [405] and were given vibrational assignments. For HITRAN2020 these new bands for the  $^{16}\text{O}^{12}\text{C}^{32}\text{S}$ ,  $^{16}\text{O}^{12}\text{C}^{34}\text{S}$ ,  $^{16}\text{O}^{13}\text{C}^{32}\text{S}$  isotopologues were therefore based on simultaneous analyses of the lines from Toon et al. [468] and previously unused data from Brown and Fayt [469]. Effectively, the line intensities from Ref. [11] were scaled to the experimental data [468] by factors of 1.1579 and 2.2592 for the 1111–1110 and 0331–0330 bands of the  $^{16}\text{O}^{12}\text{C}^{32}\text{S}$  isotopologue, respectively. Moreover, in the course of analyzing lines from Toon et al. [468], 91 lines of the  $\nu_3$  band of the  $^{16}\text{O}^{13}\text{C}^{34}\text{S}$  isotopologue (band center  $2008.46\text{ cm}^{-1}$ ) were identified, which were not present in Ref. [11], HITRAN, nor GEISA. Therefore, line positions and intensities of these lines have been fit to obtain spectroscopic parameters for this isotopologue. These parameters were used to compute the line positions and intensities of 221 lines up to  $J = 110$ . As a result of this analysis, the lines of the  $^{16}\text{O}^{13}\text{C}^{34}\text{S}$  isotopologue now make their debut in HITRAN. The abundance of  $4.675 \times 10^{-4}$  is calculated for this isotopologue

with  $Q(296\text{K}) = 2546.53$ .

The HITRAN2020 line list of OCS contains 37 461 lines and covers the spectral range from 0.396 to 7821.109  $\text{cm}^{-1}$  with  $J \leq 121$  and with the lower energy up to 2985.102  $\text{cm}^{-1}$ . Uncertainty codes 3 for the line positions and 3 (see Table 2) for the line intensities were used in the case of the new added bands. Figure 25 gives an overview comparison between HITRAN2016 and the new added bands in HITRAN2020 in the 0–8000  $\text{cm}^{-1}$  spectral range.

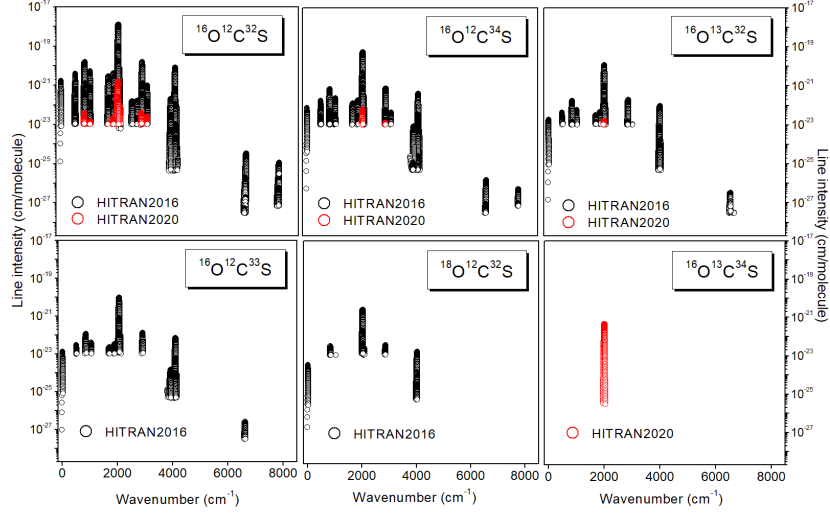


Figure 25: Overview of the line lists of  $^{16}\text{O}^{12}\text{C}^{32}\text{S}$ ,  $^{16}\text{O}^{12}\text{C}^{34}\text{S}$ ,  $^{16}\text{O}^{13}\text{C}^{32}\text{S}$ ,  $^{16}\text{O}^{12}\text{C}^{33}\text{S}$ ,  $^{18}\text{O}^{12}\text{C}^{32}\text{S}$ , and  $^{16}\text{O}^{13}\text{C}^{34}\text{S}$  isotopologues in HITRAN2016 and the new added bands in HITRAN2020 in the 0–8000  $\text{cm}^{-1}$  range.

The He-broadened linewidths of OCS were added to the HITRAN2016 database using the semi-empirical models by Wilzewski et al. [434]. The recent experimental data by Hays et al. [470] (using an E-band chirped pulse spectrometer) along with comparisons to HITRAN, showed that the previous estimated  $\gamma_{\text{He}}$  (for OCS) was approximately half the size of the experimental results. A new semi-empirical model, based on a Padé approximant, has been used to update the He-line broadening parameters for  $J'' \leq 64$ . This work incorporated the

early experimental results from Refs. [471–473] as well as the recent measurements by Hays et al. [470] .

## 2.20. *H<sub>2</sub>CO: Formaldehyde (molecule 20)*

### 2.20.1. *He- and H<sub>2</sub>- broadening parameters*

The He broadening of H<sub>2</sub>CO lines has been measured in the millimeter-wave spectral region in the early work of Nerf [474], and more recently, in the  $2\nu_5$  band by cavity-enhanced absorption spectroscopy [475], as well as two strongest transitions in the  $\nu_6$  band by direct absorption spectroscopy [476]. A Padé approximant has been applied to fit all collected experimental data, and a semi-empirical model has been used to generate  $\gamma_{\text{He}}$  for H<sub>2</sub>CO lines in the database versus the index  $J + 0.2K_a$ . As for H<sub>2</sub> broadening of H<sub>2</sub>CO lines, experiments were made in both the millimeter-wave region [474] and the 9–11  $\mu\text{m}$  region [477]. A good agreement was claimed in comparison with these two experiments indicating no vibrational dependence in these data. A similar approach has been carried out to obtain  $\gamma_{\text{H}_2}$  using the Padé approximant.

### 2.20.2. *Future work*

Formaldehyde has been the subject of a recent MARVEL study (see paper published as part of this issue [478]). This study assembled and validated 16 596 non-redundant transitions from the literature, with a few newly measured as part of the study, giving 5029 empirical energy level determined to high resolution accuracy. These empirical levels were then used to replace the computed energy levels in the ExoMol AITY line list [479] giving 367 779 transitions with empirically-determined wavenumbers of which 183 673 are more intense than the HITRAN cut-off at 296 K. This updated line list will be considered for a future HITRAN upgrade for formaldehyde.

## 2.21. *HOCl: Hypochlorous Acid (molecule 21)*

For typical atmospheric modeling applications, the self-broadening contribution of HOCl is expected to be negligible; however a default estimated value of  $\gamma_{\text{self}} = 0.15 \text{ cm}^{-1}/\text{atm}$  has been applied for all transitions to avoid null values.

## 2.22. $N_2$ : Molecular Nitrogen (molecule 22)

Unchanged.

## 2.23. HCN: Hydrogen Cyanide (molecule 23)

### 2.23.1. $H^{12}CN$

HCN is a product of biomass burning in the Earth’s atmosphere [480] and it is studied as a possible indicator for bacterial lung infection [481]. HCN, and its isomer HNC which is not included in HITRAN, are important astrophysical species. HCN has recently been detected in Pluto’s atmosphere [482] and the atmosphere of exoplanet 55 Cancri e [483]. Isotopologue ratios such as  $H^{12}CN/H^{13}CN$  encode information on the thermal and chemical histories of a variety of solar system materials and provides insights into their origins [484]

For the main isotopologue  $H^{12}C^{14}N$ , the HITRAN entry has been expanded using data from the ExoMol [333] line list due to Barber et al. [485]. This line list is based on the *ab initio* transition intensities of Harris et al. [486] with empirical energy levels from the experiments of Mellau [487]. All lines stronger than  $10^{-30}$  cm/molecule at 296 K and wavenumbers up to  $4001\text{ cm}^{-1}$  not in HITRAN2016 were added. HITRAN2016 contained 58 109 lines; the new release more than doubles this number to 131 031 lines.

A new, significantly improved line list for  $H^{12}C^{14}N$  called “MOMeNT-90” is published as part of this issue [488]. A unique feature of this polyatomic line list comes from the fact that all the line positions, even for the very weak lines that are hardly observable experimentally, were derived from experimental energy levels obtained from the corresponding high-temperature studies [487]. At the same time, this large set of empirical vibrational-rotational energy levels made it possible to improve the fitting procedure used to determine the PES and the nonadiabatic correction used in the variational calculations. The new intensities show many differences from the intensities given in HITRAN2016. The accuracy of the calculated line intensities were demonstrated using a variety of absorption and emission spectra. This line list will form the basis for a future update and is highly recommended for practical usage

### 2.23.2. $H^{13}CN$

The spectrum of  $H^{13}C^{14}N$  at wavenumbers below  $3405\text{ cm}^{-1}$  was included in HITRAN2004 based on the experiments of Maki et al. [489] and Maiwald et al. [490]. Similar to the subsequent updates in HITRAN for the parent isotopologue, we extend the  $H^{13}C^{14}N$  data available to higher wavenumbers based on the use of empirically corrected variational line lists. A new line list was computed using the semi-empirical potential energy surface (PES) and *ab initio* dipole moment surface (DMS) by Makhnev et al. [491]. The update considered wavenumbers up to  $8000\text{ cm}^{-1}$  and limited to transitions which have intensity greater than  $10^{-28}\text{ cm}^2/\text{molecule}$  at 296 K (at 100% abundance) these criteria give a total of 57885 lines. Wavenumbers for the majority of these lines were generated using the empirical energy levels of Hofmann et al. [492] but the transition intensities are the *ab initio* ones. These intensities can be considered fairly reliable based on comparisons with the recent experimental study by Guay et al. [493] which used a free-running, all-fiber dual electro-optic frequency comb system. An overview of the  $H^{13}C^{14}N$  line list in HITRAN2020 is given in Fig. 26.

### 2.23.3. $H_2$ - and He-broadening parameters

There are a number of experimental measurements regarding He-broadening in early works [494–498], however there is generally poor agreement between studies. A critical evaluation has been made to filter selected data, and the rotational distribution of the He-broadening line width ( $\gamma_{He}$ ) is described using a Padé approximant with  $J'' \leq 16$ .

The microwave transient emission technique has been used to study the *l*-doublet transitions of HCN with  $H_2$ -broadening [495, 498]. Later, frequency-stabilized tunable diode laser spectrometers have been used to study the  $H_2$ -broadening line width in the  $\nu_2$  band [496, 499]. More recently, new experimental measurements of  $H_2$ -broadening in the millimeter-wave region have been reported [500]. Comprehensive comparisons with all experimental results exhibit a strong rotational dependence, while they appear to be vibrationally

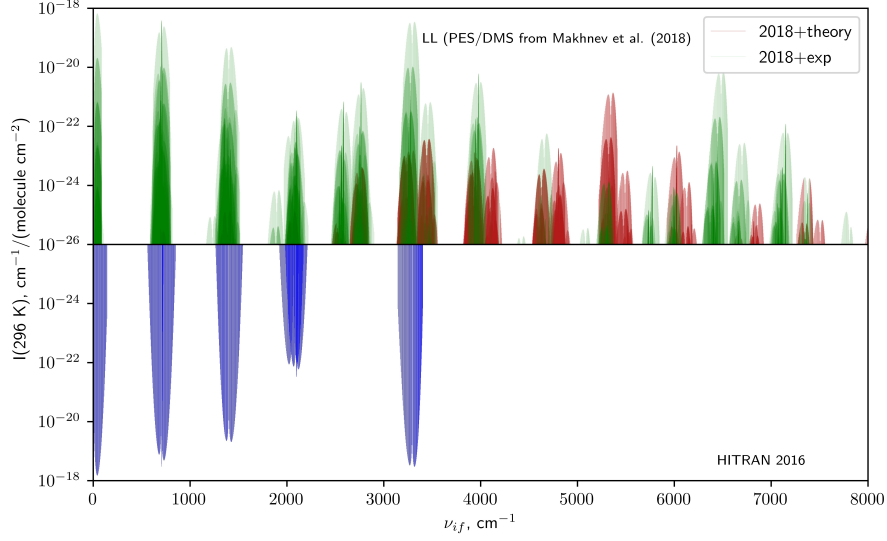


Figure 26: Comparison of the *ab initio* line list from this work and the HITRAN2016 edition for the 0–8000  $\text{cm}^{-1}$  range.

independent. A similar procedure has been used to derive the semi-empirical  $\text{H}_2$ -broadening line width ( $\gamma_{\text{H}_2}$ ) based on the Padé approximant for transitions with  $J'' \leq 31$ .

#### 2.24. $\text{CH}_3\text{Cl}$ : Methyl Chloride (molecule 24)

Unchanged.

#### 2.25. $\text{H}_2\text{O}_2$ : Hydrogen Peroxide (molecule 25)

For the self-broadening half-width (which previously had values of zero), a default estimate value of  $0.3 \text{ cm}^{-1}/\text{atm}$  has now been assigned to all transitions for this molecule.

#### 2.26. $\text{C}_2\text{H}_2$ : Acetylene (molecule 26)

Acetylene is a minor trace gas in the terrestrial atmosphere, primarily originating from combustion sources, and therefore its concentration is highly correlated with carbon monoxide [501]. It is present in the atmospheres of solar



system gas giants and their satellites [502–504]. The acetylene ( $\text{C}_2\text{H}_2$ ) molecule is a prototype system for molecular dynamics with a very rich IR spectra as a consequence of strong couplings between vibrational modes. However, the NIR spectral region in HITRAN had been missing many spectral details.

The global modeling of the  $\text{C}_2\text{H}_2$  spectrum in the frame of the polyad model has been developed at ULB-Brussels [505], and IAO-Tomsk [506, 507]. The approximate relations of the vibrational modes give rise to polyads such that  $P = 5V_1 + 3V_2 + 5V_3 + V_4 + V_5$  (where  $V_i$  are the vibrational normal mode quantum numbers, with  $i = 1 - 5$ ). The vibrational assignments used for  $\text{C}_2\text{H}_2$  in previous editions of HITRAN only indicated the total bending angular momentum,  $|l_4 + l_5|$ . However, as many more bands have been added to HITRAN in recent additions, it has become necessary to separate the bending angular momentum quantum numbers to avoid degeneracy and allow unique identification. For HITRAN2020, the vibrational assignment has been updated for all acetylene transitions of the three isotopologues so that  $V_1, V_2, V_3, V_4, V_5, l_4, l_5, +/ -, u/g$  quantum numbers are now used to identify each vibrational state (with a FORTRAN format of 1X,3I1,4I2,A1,1X,A1).

For HITRAN2016, numerous bands were added in the 13–248  $\text{cm}^{-1}$  and 390–634  $\text{cm}^{-1}$  spectral regions. The last region was supplemented and extended (in the 390–893  $\text{cm}^{-1}$  region) based on the recent  $\Delta P = 1$  work of Jacquemart et al. [508]. This work used a multi-spectrum analysis of FTS measurements and line intensities have been measured for 18 bands (only four of them previously reported). The very good predictability of the theoretical model developed in IAO-Tomsk has been used to include new hot bands in this region as well as to improve line positions and/or intensities of the existing HITRAN2016 bands.

Comparisons to  $\text{N}_2$ -broadened (1 atm) PNNL spectra [242] of  $\text{C}_2\text{H}_2$  for the beginning of the  $\Delta P = 6$  region indicated absorption features of some bands not present in HITRAN. Based on the global model developed in IAO-Tomsk [507], 8 hot bands have been added to HITRAN between 3738 and 3996  $\text{cm}^{-1}$  (see Table 10). Note that under atmospheric pressures, Q-branches of acetylene are affected by line-mixing. This line-mixing is especially the case for the intense

Q-branches of  $^{12}\text{C}_2\text{H}_2$  located at 730, 3881, 3896 and 4090  $\text{cm}^{-1}$ . Using a Voigt line profile for these Q-branches in atmospheric retrievals will lead to systematic residuals due to line-mixing. Studies are in progress to model line-mixing effects for Q-branches of acetylene under atmospheric conditions and will be considered for updates to HITRAN.

Table 10: Hot bands of acetylene included in HITRAN between 3738 and 3996  $\text{cm}^{-1}$ .  $N$  is the number of transitions per band,  $\nu_{\min}$  and  $\nu_{\max}$  are the minimum and maximum wavenumbers (in  $\text{cm}^{-1}$ ), and  $S_{\text{sum}}$  is the sum of line intensities (in  $10^{-20}$   $\text{cm}/\text{molecule}$ ).

Hot band <sup>a</sup>	$N$	$\nu_{\min}$	$\nu_{\max}$	$S_{\text{sum}}$
01031 3-1 – 00010 1 0	263	3744	3969	0.58
00120 2 0 – 00010 1 0	250	3770	3984	0.58
01031 1-1 – 00010 1 0	205	3794	3977	0.36
00120 0 0 – 00010 1 0	101	3817	3975	0.24
00111 1 1 – 00001 0 1	240	3772	3980	0.20
00111 1-1 – 00001 0 1	233	3780	3975	0.16
01022 2 0 – 00001 0 1	220	3756	3963	0.13
01022 2-2 – 00001 0 1	251	3749	3959	0.12

<sup>a</sup>The upper and lower vibrational bands have the format:  
 $V_1, V_2, V_3, V_4, V_5, l_4, l_5$

Lyulin and Campargue [509] collected together the recent experimental studies covering the 5850–6341  $\text{cm}^{-1}$  and 7000–9415  $\text{cm}^{-1}$  spectral regions that used FTS for the stronger bands [510–512] and Cavity Ring Down Spectroscopy (CRDS) for the weaker absorption windows between bands [513–515]. Additional CRDS [516] and FTS [517, 518] studies covered the 5693–5882  $\text{cm}^{-1}$  and 9280–10 740  $\text{cm}^{-1}$  spectral ranges, respectively. Following Lyulin and Campargue [509], these studies have been compiled into an empirical line list for HITRAN. The line list includes numerous  $^{12}\text{C}_2\text{H}_2$  and  $^{12}\text{C}^{13}\text{CH}_2$  bands that have not previously been included in HITRAN. Figure 27 displays the significant number of additional bands that have been included in the NIR for HITRAN2020.

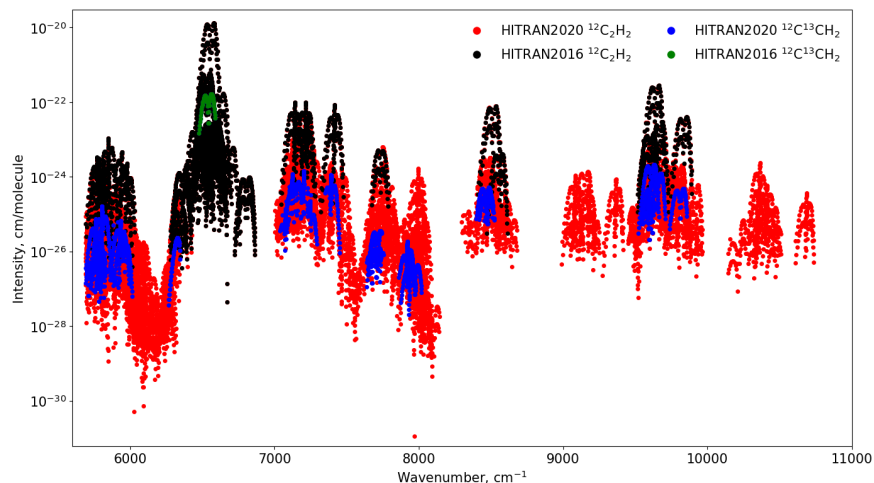


Figure 27: An overview of the NIR bands of  $C_2H_2$  that have been added to HITRAN based on FTS and CRDS measurements [509–518].

As part of the ExoMol project [519], the “aCeTY” line list has been built for  $^{12}C_2H_2$  [520] using the MARVEL acetylene database wherever possible [521]. Comparisons of the aCeTY line list and global model developed in IAO-Tomsk with measurements in the  $\Delta P = 1$  region are presented in Jacquemart et al. [508]. The line lists from aCeTY and the ASD-1000 database [506] are intended for use at high temperature. However further comparisons between models and measurements will be investigated for updates to HITEMP [52].

In addition,  $H_2$ -,  $He$ - and  $CO_2$ -broadening coefficients that were introduced to HITRAN by Wilzewski et al. [434] have been extended to the new transitions for  $C_2H_2$ .

A small number of Einstein- $A$  coefficients and statistical weights have also been corrected for some of the bands of  $C_2H_2$ .

### 2.27. $C_2H_6$ : Ethane (molecule 27)

Ethane ( $C_2H_6$ ) is the most abundant non-methane hydrocarbon (NMHC) in the atmosphere of the outer planets [522] and Titan [523], playing an important role as a tracer of atmospheric chemistry and dynamics. Ethane is also an important constituent of comets and their gaseous envelopes [524]. The relative

abundance of isotopic species of ethane, such as D/H ratio from  $\text{C}_2\text{H}_5\text{D}/\text{C}_2\text{H}_6$ , can carry valuable information about atmospheric formation and chemical evolution. In this work, we have expanded the ethane line list to include two new bands ( $\nu_5$ ,  $\nu_7$ ) of  $^{12}\text{C}_2\text{H}_6$  and the  $\nu_4$ ,  $\nu_{12}$ , and  $2\nu_6$  bands of  $^{12}\text{C}_2\text{H}_5\text{D}$  from recent model predictions validated through a laboratory study.

#### *2.27.1. Region of $\nu_5$ and $\nu_7$ fundamentals (2800 to 3100 $\text{cm}^{-1}$ )*

Until this edition HITRAN contained only strong Q-branch lines of the  $\nu_7$  band in the spectral region around 3.3  $\mu\text{m}$ . Nevertheless, these lines alone are insufficient to correctly interpret atmospheric and planetary spectra and a better high-resolution spectroscopic model is needed. This spectral range is dominated by the CH stretching fundamental of  $\nu_5$  (parallel band) and  $\nu_7$  (degenerate perpendicular band), and the  $\nu_8 + \nu_{11}$  combination band ( $\nu_8$  and  $\nu_{11}$  are the degenerate antisymmetric and symmetric deformations of the two methyl groups, respectively). The characterization of rotational structure in this complex molecule is non-trivial because the  $\nu_7$  band is severely perturbed by overtones and combination states (with a low frequency torsional mode,  $\nu_4$  at 289  $\text{cm}^{-1}$ ) that are in Fermi or Coriolis resonance with  $\nu_7$  [525].

For the HITRAN2020 edition, we expand and advance the  $\nu_7$  band at 3.3  $\mu\text{m}$  based on Refs. [524, 526], add a linelist for the  $\nu_5$  band of ethane at 3.4  $\mu\text{m}$  based on Radeva et al. [527] and add combination bands, including the strong  $\nu_8 + \nu_{11}$  band based on Lattanzi et al. [526].

Relying on a high-resolution FTS spectrum recorded at 229 K in Brussels and line positions measured in a Doppler-limited spectrum recorded at 119 K using a tunable difference-frequency laser spectrometer [528], Lattanzi et al. [526] re-investigated the 2860–3060  $\text{cm}^{-1}$  region of ethane.

This work led to some progress in the understanding of the complex network of interacting vibrational levels occurring in this energy range (see Fig. 2 of [526]). In particular, 572 line positions belonging to  $^{\text{P}}\text{P}$  and  $^{\text{r}}\text{R}$  transitions in the  $\nu_7$  band (maximum  $J = 30$ ),  $^{\text{r}}\text{Q}_0$ ,  $^{\text{P}}\text{P}_1$  and  $^{\text{r}}\text{R}_1$  transitions in the  $\nu_8 + \nu_{11}$  band, and  $^{\text{P}}\text{P}_6$  transitions in the  $\nu_3 + 2\nu_4 + \nu_8$  band were least squares fitted

to a Hamiltonian involving the  $7^1$  degenerate vibrational level and 4 degenerate perturbors, i.e., the  $8^1 11^1$ ,  $3^1 4^2 8^1$ ,  $4^1 11^1 12^1$  and  $3^1 4^3 12^1$  vibrational levels. Although RMS deviations as large as  $0.018 \text{ cm}^{-1}$  were obtained, indicating that the analysis is far from complete, a line list was generated as it could provide an improved description of the  $3.3 \text{ }\mu\text{m}$  region of the ethane spectrum. Positions, relative intensities and lower-state energies of 4969 lines associated with transitions belonging to five perpendicular bands ( $\nu_8 + \nu_{11}$ ,  $\nu_4 + \nu_{11} + \nu_{12}$ ,  $\nu_3 + 3\nu_4 + \nu_{12}$ ,  $\nu_8 + \nu_{11}$  and  $\nu_3 + 2\nu_4 + \nu_8$ ) were calculated between 2900 and  $3071 \text{ cm}^{-1}$ , relying on the model and parameters involved therein and resulting from the least squares analysis. The content of the line list is summarized in Table 8 of [526]. As detailed in [526], incorrectly predicted line positions were recomputed using empirical upper state energies. These altered positions are indicated by the HITRAN error code of 4 (see Table 2), while a conservative error code of 2 was assigned to the remaining predicted positions. The predicted relative line intensities were normalized by inspection of observed and calculated spectra (HITRAN error code = 2).

In order to expand the amount of lines in the  $\nu_7$  band, the lines missing from the line list of Lattanzi et al. [526] were taken from Villanueva et al. [524]. In addition, a complete line list for the  $\nu_5$  band was taken from Radeva et al. [527]. These models of  $\nu_5$  and  $\nu_7$  were generated by characterizing the upper ro-vibrational states using linear progressions of  $J$  and  $K$ . For the ground vibrational state, spectroscopic constants from Pine and Lafferty [525] were used, with specific corrections for some  $J/K$  ladders (see details in Ref. [524]). For the  $\nu_5$  model, the upper state rotational constants were not presented in the literature, therefore they were obtained by fitting experimental data given in Pine and Stone [529] for each  $K$  ladder. For the band intensity of the  $\nu_5$  band, we employed the parameters as reported in Dang-Nhu et al. [530].

The  $\nu_7$  upper-state ro-vibrational structure was derived by fitting to experimental data as presented in Ref. [531], in which cross sections for ethane in the  $3 \text{ }\mu\text{m}$  region at temperatures between 194 and 297 K and total pressures from 0.0689 Torr to 763.48 Torr were reported. Using this dataset we identified

466 lines, which were consolidated with 122 lines reported in Ref. [530] and 66 reported in Ref. [529], ultimately deriving rotational constants for 30  $K$ -ladders of the  $\nu_7$  band of ethane. Our model does provide good results for the selected lines (standard deviation of  $0.005\text{ cm}^{-1}$  for the 654 lines), but because of the numerous perturbations, their validity for higher quanta and weaker spin species is relatively uncertain.

Determining accurate band intensities from experimental data in this highly active spectral region can be complex, in particular for ethane at  $3.3\text{ }\mu\text{m}$ , since multiple fundamental (e.g.  $\nu_7$  and  $\nu_5$ ), combination (e.g.  $\nu_8+\nu_{11}$ ), and hot-bands (e.g.  $\nu_7+\nu_4-\nu_4$ ) overlap at these wavelengths. As reported in Ref. [531], accurate absorption cross sections for ethane at these wavelengths were determined, with an overall uncertainty of 4%. Their cross-sections were calibrated against PNNL spectra [242]. Considering these new absorption cross-sections and taking into account the first torsional hot-band, we derived a band intensity of  $301\text{ cm}^{-2}\text{atm}^{-1}$  for the  $\nu_7$  band [524].

Restricting the model to the lowest  $J/K$  ladders, resulted in a dataset containing 8680 lines (which for HITRAN are partially replaced with data from Ref. [526]) for the  $\nu_7$  band of ethane, and 12 108 lines for the  $\nu_5$  band. The models were further validated and employed to retrieve ethane abundances in comets and Earth’s atmosphere, and to derive upper-limits for ethane on Mars [524, 527].

### 2.27.2. $^{12}\text{CH}_3^{12}\text{CH}_2\text{D}$

Mono-deuterated ethane is the third most abundant isotope of ethane, with a HITRAN abundance of  $9.131\times 10^{-4}$  [56]. The deuterium substitution reduces the symmetry, which results in significantly more transitions being visible in the mid-infrared. It also slightly offsets the bright series of Q-branches around  $2980\text{ cm}^{-1}$ , which are characteristic for  $\text{C}_2\text{H}_6$ , allowing the possibility of remote observations of the D/H ratio in this spectral range. Doney et al. [532] determined line positions and relative intensities of transitions in the C-D (centered around  $2170\text{ cm}^{-1}$ ) and C-H (between  $2850$  and  $3030\text{ cm}^{-1}$ ) stretches, captur-

ing the  $\nu_4$  band ( $2170\text{ cm}^{-1}$ ), the  $2\nu_7$  band ( $2770\text{ cm}^{-1}$ ), as well as a series of bands between 2850 and 3030 ( $2\nu_{14}$ ,  $2\nu_6$ ,  $2\nu_5$ ,  $\nu_1$ ,  $\nu_2$  and  $\nu_{12}$ ). The assignments were made by employing *ab initio* CCSD(T)/ANO 1 calculations. The study was based on spectra recorded at high resolution using a Bruker IFS-125HR equipped with a cryogenic Herriott cell at JPL [533, 534]. For the assignments in Doney et al. [532], spectra were recorded at 85 K, at very low pressures below 0.0022 Torr using an Herriott cell with a pathlength of 20.941 m. The model includes transitions up to  $J'' \leq 22$ ,  $K''_a \leq 10$  and  $K''_c \leq 18$ , with uncertainties of the order of  $\sim 0.05\text{ cm}^{-1}$ . Although the model captures most of the strong transitions, further work is needed to refine the description of weak transitions in the 2850–3300  $\text{cm}^{-1}$  region. No hot bands are included in this line list.

For the update in HITRAN2020, the intensities of the  $\text{C}_2\text{H}_5\text{D}$  transitions have been calibrated against additional experimental spectra recorded using the same setup, but at higher pressures (2.023 and 0.1367 Torr), shorter pathlengths (0.2038 and 0.1526 m), but at intermediate cold and room temperatures (130 and 298 K).

### 2.27.3. Line-shape parameters

For all of the new bands (including deuterated isotopologue) self and  $\text{N}_2$  broadening coefficients and the temperature dependence of the  $\text{N}_2$  broadening coefficients were estimated using the expressions reported by Devi et al. [535, 536] from measurements in the Q-branch of the  $\nu_9$  band near  $822\text{ cm}^{-1}$ . The parameters involved in these expressions were applied from  $K'' = 0$  to  $K_{\text{max}} = 3$  for the broadening coefficients and  $K'' = 0$  to  $K_{\text{max}} = 7$  for their temperature dependence, while those provided for  $K_{\text{max}}$  were used for transitions with  $K'' > K_{\text{max}}$ . The uncertainties for these pressure-induced coefficients are conservatively set (error code = 2) with the warning that the uncertainty is unknown for  $J'' > 31$ . Finally, a constant value of  $-0.004\text{ cm}^{-1}\text{atm}^{-1}$  (error code = 1) was estimated for air pressure induced shifts, from the average of two air-broadening measurements at 296 K for  ${}^{\text{r}}\text{Q}_0$  and  ${}^{\text{p}}\text{Q}_3$  of the  $\nu_7$  band [529]. For pressure-shifts, we consider the  $\text{N}_2$ -broadened pressure-induced shifts

of  $-0.004 \text{ cm}^{-1}\text{atm}^{-1}$  reported in [529] from  $^{\text{r}}\text{Q}_0$  and  $^{\text{p}}\text{Q}_3$ .

For the  $\nu_4$  torsional band at  $35 \mu\text{m}$  region [537], the temperature dependence exponent of the  $\text{N}_2$ -broadened line half-widths,  $n_{\text{N}_2}$ , listed in the HITRAN2016 [15] had a truncation error which removed the integer part when the exponent is greater than 1. This issue has been fixed for HITRAN2020.

### 2.28. $\text{PH}_3$ : Phosphine (molecule 28)

On Earth, phosphine ( $\text{PH}_3$ ) is a trace constituent of the lower troposphere with very low, but highly variable, atmospheric concentrations [538].  $\text{PH}_3$  has also long been observed in the atmospheres of Jupiter and Saturn due to prominent spectral IR features [539] and is used as a tracer for tropospheric dynamics in gas giant planets [540]. While  $\text{PH}_3$  is associated with anaerobic ecosystems of Earth, and notoriously toxic for humans [541], it has also been proposed as a potential biosignature gas in anoxic exoplanets [542].

Recently, a tentative detection of the  $R(0)$  rotational transition in the atmosphere of Venus using mm-wave observations [543] has prompted significant discussion relating to the chemical (and suggested biological) production pathways that can account for the observed concentration. However, a number of followup studies [544–547] have cast substantial doubt on the original detection and conclusions. Nevertheless, these recent works have contributed to a surge of interest in accurate  $\text{PH}_3$  spectroscopic parameters.

The IR spectrum of  $\text{PH}_3$  forms distinct polyad bands due to the approximate relationship of the vibrational modes:  $\nu_1 \approx 2\nu_2 \approx \nu_3 \approx 2\nu_4 \approx \nu_2 + \nu_4$ . For HITRAN2020, the line positions and intensities in the dyad ( $750\text{--}1500 \text{ cm}^{-1}$ ), pentad ( $1750\text{--}2600 \text{ cm}^{-1}$ ) and octad ( $2750\text{--}3650 \text{ cm}^{-1}$ ) spectral regions have been extended or updated, while pure rotational transitions remain unchanged from HITRAN2016 [15].

Kleiner and Devi [548] produced an extensive line list covering the pentad region, based upon the experimental measurements of Refs. [549, 550] that were described in HITRAN2016. The Kleiner and Devi [548] line list consists of 9894 transitions of the  $2\nu_2$ ,  $2\nu_4$ ,  $\nu_2 + \nu_4$ ,  $\nu_1$ ,  $\nu_3$  bands. Line positions were obtained



by fitting 3403 experimental measurements with an Hamiltonian including the interactions within the  $V_2 = 2$ ,  $V_4 = 2$ ,  $V_2 = V_4 = 1$ ,  $V_1 = 1$  and  $V_3 = 1$  upper states (up to  $J = 14$ ) [550], which were combined with empirically determined transition frequencies calculated from accurate ground-state energy levels [551]. Line intensities were based on a fit to 1579 selected transitions [550] with RMS deviations of 7.7%. The methods used for both energy level and intensity fittings are described in Tarrago et al. [552].

The octad region has been analysed by Nikitin et al. [553] between 2733–3660  $\text{cm}^{-1}$  using a global approach. This analysis builds on a previous model for the lower three polyads [554], which was noted to have poor simulation of spectra above 3100  $\text{cm}^{-1}$ . The new model incorporates the empirical line list generated for the octad region (based on Ref. [555]), which was included in HITRAN [14]. The model extended the assignments for the octad region and has been validated against FTS spectra [242, 555, 556] with a quoted RMS deviation of 0.0018  $\text{cm}^{-1}$  and 11% for the positions and intensities, respectively.

Recently, Rey et al. [557] have produced an updated vibration-rotation line list of  $\text{PH}_3$  in several steps. As  $\text{PH}_3$  is a semi-rigid molecule without large amplitude vibrations, the normal mode representation provides an adequate description of the nuclear motions. At the first step, the full nuclear motion Hamiltonian was built in the Eckart-Watson form [558] from the potential energy surface (PES) reported by Nikitin et al. [559] using the reduction techniques described in Rey et al. [560]. For a full account of symmetry, energy levels and transitions were computed by variational method using the irreducible tensor operators following the technique by Rey et al. [561, 562]. At the second step, the *ab initio* PES was empirically optimized to match precisely the four observed fundamental band origins. The line intensities were computed from the *ab initio* dipole moment surface of Nikitin et al. [563]. The RMS deviations for energy levels up to  $J = 20$  between the variational calculations and the empirically-fitted effective Hamiltonian were 0.04, 0.05 and 0.07  $\text{cm}^{-1}$  for the dyad, pentad and octad, respectively. To improve the accuracy of the line positions, additionally we have followed the strategy successfully applied for the

methane line lists [301] that consists in making empirical corrections using a set of experimental vibration-rotation energy levels. Finally, a data set composed of 14 400 energy levels up to the octad ( $J_{\max} = 25$ ) and obtained from previous analyses [553–555] was used to provide empirical corrections for more than 100 000 line positions. The corresponding line list is available via the TheoReTS web site [302]. To determine the preferred line intensities and positions for each spectral region, comparisons have been made to high-resolution FTS spectra recorded at PNNL covering the dyad [564] and pentad [549] regions (resolutions of  $0.0020\text{ cm}^{-1}$  and  $0.0115\text{ cm}^{-1}$ , respectively), along with those obtained from the McMath-Pierce FTS at Kitt Peak [555] for the octad region ( $0.0115\text{ cm}^{-1}$  resolution). Further FTS measurements from PNNL [242], which include all three polyads at lower resolution ( $0.112\text{ cm}^{-1}$ ), have also been used.

For the dyad region, the  $\nu_2$ ,  $\nu_4$  and  $2\nu_2-\nu_2$  bands from HITRAN2016 have been supplemented with the  $\nu_2 + \nu_4-\nu_4$ ,  $\nu_2 + \nu_4-\nu_2$  and  $2\nu_4-\nu_4$  hot bands from Rey et al. [557].

The line list of Kleiner and Devi [548] was intended to be used for updating of the pentad region in HITRAN2016. However, the recent theoretical work of Rey et al. [557] was shown to provide a significant improvement toward the edges of the pentad region as higher rotational levels (i.e.,  $J'' > 14$ ,  $K'' > 12$ ) were not included in the analysis of Kleiner and Devi [548]. Figure 28 demonstrates the significant improvement when compared to PNNL spectra at  $25^\circ\text{C}$  [242]. The positions and intensities of Rey et al. [557] have therefore been adopted for all pentad transitions in HITRAN2020.

In HITRAN2016, the octad region primarily constituted unassigned empirical lines, which restricts the applicable temperature range. The line lists provided by Nikitin et al. [553] and Rey et al. [557] are fully assigned and compared to HITRAN2016 in their ability to reproduce observations. It should be noted that comparisons for the  $3\nu_2$  band are hindered by low signal to noise in the PNNL spectra. High-resolution comparisons demonstrated that the Nikitin et al. [553] list yields the best performance with smallest RMS residuals across the octad region and has been used to update HITRAN. The  $4\nu_2-\nu_2$  hot band

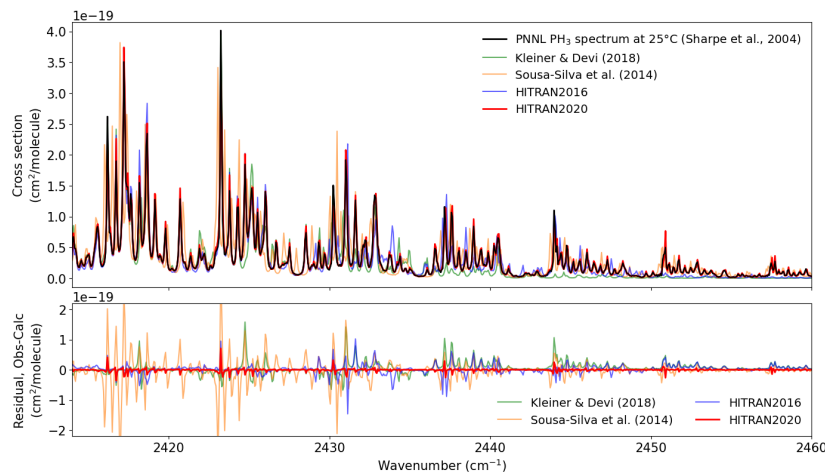


Figure 28: Spectra for the pentad region of  $\text{PH}_3$  compared to the PNNL absorption cross sections at 25°C [242]. The upper panel displays calculated spectra using the HITRAN2020 (see text for details), HITRAN2016 [15], Kleiner and Devi [548] and Sousa-Silva et al. [565] line lists. The lower panel displays the obs-calc residuals, where the observation corresponds to the PNNL spectrum and calculated spectra are identified by the legend (all are shown in the upper panel).

from HITRAN2016 has been retained as these lines were observed in the spectra of Butler et al. [555]. The octad region of the  $\text{PH}_3$  now includes quantum assignments for all transitions.

Sousa-Silva et al. [565] refined an earlier PES [566] to produce the “SAITY” line list covering the spectral range up 10 000  $\text{cm}^{-1}$  and temperatures up to 1500 K. A calculated spectrum for the pentad region is included in the comparisons of Fig. 28. While SAITY is primarily intended for high-temperature simulations, these line predictions can be used to advance the assignment of experimental spectra. Furthermore a MARVEL project is in progress which will allow many of the strong lines in SAITY to be given to experimental accuracy.

There is potential for further empirical improvements to line positions in the dyad, pentad and octad regions. This analysis will be considered for future updates for  $\text{PH}_3$ .

The air-broadening half-widths introduced in HITRAN2008 [13] have been extended to all new transitions and are based on scaled  $\text{N}_2$ -broadening measure-

ments [555, 567–569]. The linear relationship for the temperature dependence exponents of the air-broadening coefficients  $n_{\text{air}} = 0.702 - 0.01J''$  [569, 570] has also been extended to all new transitions. For HITRAN2020, all self-broadening half-widths have been updated with the method described in Nikitin et al. [553] for the octad region, using an empirical function developed for the  $\nu_3$  band [549]. The self-broadening coefficients are given by

$$\gamma_{\text{self}} = 0.1172 - 9.257 \times 10^{-5} [J_m(J_m + 1) + K_m^2] \quad (2)$$

where  $J_m$  and  $K_m$  refer to the maximum values of  $J$  and  $K$ , respectively, for each transition. A minimum value of  $\gamma_{\text{self}} = 0.05 \text{ cm}^{-1}/\text{atm}$  is applied when the predicted values become too small.

Due to the presence of  $\text{PH}_3$  in the atmospheres of Jupiter and Saturn, there have been numerous studies aimed at measuring the  $\text{H}_2$  and  $\text{He}$ -broadening half-widths as well as their temperature dependencies [549, 555, 567, 569–578]. For HITRAN,  $\text{H}_2$ - and  $\text{He}$ -broadening coefficients and temperature dependencies have been introduced for  $\text{PH}_3$ , which will be described in detail in Tan et al. [264].

While updating HITRAN, the Einstein-A coefficients for all  $E$  symmetry transitions have been corrected.

Line-mixing coefficients for phosphine have not been introduced to HITRAN yet, although values are available from experimental [549, 576] and theoretical [578] studies. This will be considered for the future.

#### 2.29. $\text{COF}_2$ : Carbonyl Fluoride (molecule 29)

Unchanged.

#### 2.30. $\text{SF}_6$ : Sulfur Hexafluoride (molecule 30)

Sulfur hexafluoride ( $\text{SF}_6$ ) line lists in the  $\nu_3$  (stretching) and  $\nu_4$  (bending) regions have been largely updated recently thanks to new global analyses of high-resolution infrared spectra [579]. For the main isotopologue,  $^{32}\text{SF}_6$ , these

lists now contain some hot bands. For the minor isotopologues  $^{33}\text{SF}_6$ ,  $^{34}\text{SF}_6$  and  $^{36}\text{SF}_6$  [580], only the  $\nu_3$  fundamental band is included. This amounts to more than 350 000 calculated lines in the SHeCaSDa database (Sulfur Hexafluoride Calculated Spectroscopic Database) [581] which are included in the present HITRAN2020 edition.

Interestingly the amount of lines for this molecule reduce by about a factor of eight, the reason is substantially smaller cutoff in rotational quanta. Indeed, as it is demonstrated in the *ab initio* work [582] from TheoReTs [302] it is an ability to model large amount of hot-bands that is needed to model even room temperature absorption accurately. Nikitin et al. [582] demonstrated that their line list is able to model the PNNL spectra [242] accurately. This line list will be considered for future updates, although it contains billions of lines. Even with the use of “effective” lines proposed in Hargreaves et al. [55] it will likely containing tens of millions of transitions and therefore  $\text{SF}_6$  line list will continue to reside in the supplementary folder of static files.

### 2.31. $\text{H}_2\text{S}$ : Hydrogen Sulfide (molecule 31)

There are no changes to the line positions or intensities of this molecule. However, some recent works offer promising potential for updates in the near future. Recent semi-empirical NIR line lists from Ulenikov et al. [583, 584] could be a potential source for improvements for the intensities of the relevant bands in the future updates.

The line positions throughout the database can be further revised with some recent data including that from the MARVEL analyses [585]. Total of 44 325 measured and assigned transitions were collected in the MARVEL database [585] and a careful analysis of these transitions resulted in 7436 empirical ro-vibrational energy levels up to  $16\,890\text{ cm}^{-1}$ ; these empirical energy levels have already been used to improve the ExoMol line list for  $\text{H}_2\text{S}$  [586]. Self-broadening parameters from Ref. [587] could be used as a source for future updates as well.

The rotational dependence of He-broadening for  $\text{H}_2\text{S}$  lines were studied in the  $\nu_2$  band [588, 589], and in the  $\nu_1$  and  $\nu_3$  band [590]. An optimal set of param-

eters for a model inter-molecular potential that provide the best reproduction of noble gas broadening coefficients for H<sub>2</sub>S lines was reported by Starikov et al. [591]. However, significant discrepancies take place for almost all transitions in the  $\nu_2$  band for H<sub>2</sub>S-He, and in some cases can reach 100%. We excluded the early work of Waschull et al. [588] because of the poor accuracy, and summarized experimental results from Kissel et al. [589] and Sumpf et al. [590]. The broadening coefficients for  $\gamma_{\text{He}}$  decrease strongly with increasing rotational quantum numbers. A Padé approximant has been applied to fit all collected experimental data, and an semi-empirical model has been used to generate  $\gamma_{\text{He}}$  for H<sub>2</sub>S lines in the database versus the index  $J + 0.2K_a$ .

The H<sub>2</sub>-broadening for H<sub>2</sub>S lines has been measured from a pulse-driven diode laser spectrometer [592] in the  $\nu_2$  band and calculated based on the experimental results [593]. Similar fitting procedure from the Padé approximant was applied to the experimental results covering  $J''$  up to 12.

Experimentally determined CO<sub>2</sub> broadening parameters for 39 transitions of H<sub>2</sub>S in the  $\nu_2$  band were presented in [592] with uncertainties about 2%. The semi-empirical method were used to determine the model parameters.

### 2.32. HCOOH: Formic Acid (molecule 32)

Formic acid is one of the most abundant organic acids in the terrestrial atmosphere and is being monitored by different remote sensing instruments, including IASI [594], and ACE [595]. In this edition, a line list for the  $\nu_7$  and  $\nu_9$  fundamentals of HCOOH at 16  $\mu\text{m}$  has been included. All simulations and fits described in this section were performed using PGOPHER [596]. Line positions were computed using the spectroscopic constants previously reported for the ground vibrational state and the strongly interacting  $7^1$  and  $9^1$  vibrational states of the normal isotopologue of formic acid [597]. This corresponds to the inclusion of 53 diagonal parameters and 12 off-diagonal parameters. The  $7^1-0$  and  $9^1-0$  bands are hybrid  $a/b$ -type and  $c$ -type, respectively. Their relative transition moments were determined by performing a fit to the intensities of 2239 isolated peaks (using 3125 transitions) identified in a high resolution ( $0.00096\text{ cm}^{-1}$ )

experimental spectrum of HCOOH (similar to that reported in Ref. [598]) with absorbencies (base-10) ranging from 0.1 to 1; they are  $\mu_a/\mu_b/\mu_c = 1/-1.62/3.45$ . The experimental spectrum, which covered  $400\text{--}1250\text{ cm}^{-1}$  ( $8\text{--}25\text{ }\mu\text{m}$ ) allowed scaling the calculated relative line intensities within the  $16\text{ }\mu\text{m}$  bands to the known spectral line intensities, within the  $9\text{ }\mu\text{m}$  bands (already in HITRAN) [599]. The intensities included in the  $16\text{ }\mu\text{m}$  line list cover seven orders of magnitude [ $2.24 \times 10^{-27}$  to  $2.24 \times 10^{-20}\text{ cm}^{-1}/(\text{molecule cm}^{-2})$ ]. Figure 29 provides a comparison of the experimental and simulated spectra in somewhat randomly chosen regions.

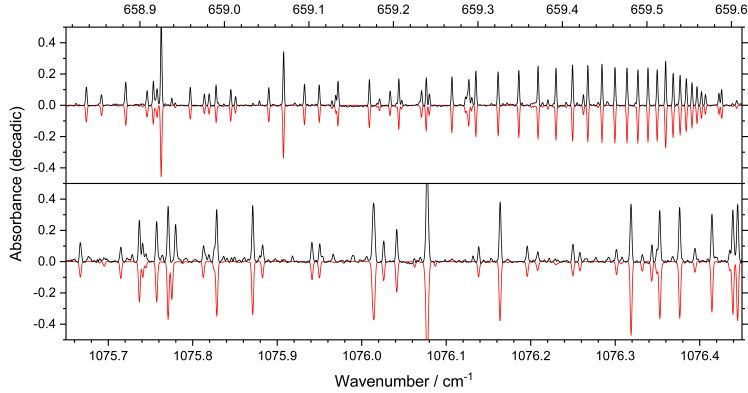


Figure 29: Top panel: Experimental (upward) and simulated (downward) spectra within the  $\nu_9$  fundamental using a Gaussian FWHM of  $0.00171\text{ cm}^{-1}$ . Bottom panel: Experimental (upward) and simulated (downward) spectra within the  $\nu_6$  fundamental using a Gaussian FWHM of  $0.00245\text{ cm}^{-1}$ .

One should take note, that as pointed out by Kochanov et al. [600] that infrared spectra calculated using HITRAN HCOOH data underestimates cross-sections when compared to the PNNL spectra [242] by about 40%. Not surprisingly the new FIR bands introduced here exhibit the same trend because they were scaled based on the HITRAN data for the  $\nu_6$  band. The source of this discrepancy remains unclear. One of the possible explanations could be the lack of hot bands in HITRAN, but it would unlikely to be responsible for a uniform 40% difference across all spectral regions.

2.33. *HO<sub>2</sub>: Hydroperoxyl Radical (molecule 33)*

Unchanged.

2.34. *O: Atomic Oxygen (“molecule” 34)*

Unchanged.

2.35. *ClONO<sub>2</sub>: Chlorine Nitrate (molecule 35)*

Unchanged.

2.36. *NO<sup>+</sup>: Nitric Oxide Cation (molecule 36)*

For typical atmospheric modeling applications, the self-broadening contribution of NO<sup>+</sup> is expected to be negligible; however the previous default value of  $\gamma_{\text{self}} = 0.05 \text{ cm}^{-1}/\text{atm}$  for pure rotational lines has been extended for all transitions to avoid null values.

2.37. *HOBr: Hypobromous Acid (molecule 37)*

For typical atmospheric modeling applications the self-broadening of HOBr is expected to be negligible, however a default estimated value of  $\gamma_{\text{self}} = 0.15 \text{ cm}^{-1}/\text{atm}$  has been applied for all transitions to avoid null values.

2.38. *C<sub>2</sub>H<sub>4</sub>: Ethylene (molecule 38)*

Unchanged. The 3  $\mu\text{m}$  region (C–H stretch) is presently under reinvestigation for both line positions and line intensities thanks to new experimental spectra and to the tensorial formalism developed in Dijon [601]. This line-by-line analysis will result in an upcoming HITRAN update for this molecule. A complete analysis of the 10  $\mu\text{m}$  region for the <sup>13</sup>C<sub>2</sub>H<sub>4</sub> isotopologue is also planned.

2.39. *CH<sub>3</sub>OH: Methanol (molecule 39)*

Unchanged.



2.40.  $\text{CH}_3\text{Br}$ : Methyl Bromide (molecule 40)

Unchanged.

2.41.  $\text{CH}_3\text{CN}$ : Methyl Cyanide (molecule 41)

Unchanged.

The  $\nu_4$  band of methyl cyanide was introduced into HITRAN2008 [13]. The data were based on a multispectrum analysis of this band and a preliminary model of the positions and intensities [602]. A complex model of low-lying vibrational states was recently expanded to include extensive  $\Delta v_4 = 1$  data [603]. These are  $\nu_4$  transition frequencies up to  $J = 61$  and  $K = 13$  along with rotational data up to  $J = 79$  and  $K = 16$ . These new data will allow substantially improving database in this spectral region.

The  $\nu_8$  and  $2\nu_8$  bands are at longer wavelengths. An account on the  $\Delta v_8 = 0$ , 1, and 2 states employing IR and very extensive rotational data was given by Müller et al. [604]. These studies were also mentioned in the HITRAN2016 paper [15]. However, some difficulties in adopting this line list did not allow for inclusion of this band to HITRAN2020, nevertheless we expect to resolve any issues and include it in the forthcoming updates.

2.42.  $\text{CF}_4$ : Carbon Tetrafluoride (molecule 42)

Unchanged.

Recent and ongoing global analyses of carbon tetrafluoride ( $\text{CF}_4$ ) [605] already partly included in the TFMeCaSDa database (TetraFluoro-Methane Calculated Spectroscopic Database) [581] should lead in the near future to further improvements for this molecule (especially concerning hot bands) that will be considered for the next HITRAN update.

Another alternative is the TheoReTs [302] line list calculated with help of *ab initio* methods. Completeness of line lists is essential for appropriate atmospheric retrievals.  $\text{CF}_4$  is heavier than methane and has two low-lying bending frequencies at 440 and 640  $\text{cm}^{-1}$  leading to a huge number of IR-active transitions belonging to the hot bands. A major challenge concerns the modeling

of these hot bands that strongly contribute to the absorption, even at room temperature. It has recently been shown [560] that converged opacity calculations for  $\text{CF}_4$  in the IR using global variational methods requires the same amount of computational effort at room temperature as lighter systems (such as methane) for very elevated temperatures of about 1000 K. The corresponding  $\text{CF}_4$  line list in 0–4000  $\text{cm}^{-1}$  region generated from potential energy and *ab initio* dipole moment surfaces by Rey et al. [560] contained about 2 billion transitions at room temperature. These data are currently too big for the standard HITRAN format but are accessible via TheoReTs [302] information system in a hybrid compressed form. The initially computed full line-by-line lists were partitioned into two sets to accelerate modeling of spectral functions as described in [302, 560] which also demonstrate very good agreement with PNNL database [242]. In the future, this list could be accommodated into HITRAN with the use of “effective” lines proposed in Hargreaves et al. [55].

#### 2.43. $\text{C}_4\text{H}_2$ : Diacetylene (molecule 43)

Unchanged.

#### 2.44. $\text{HC}_3\text{N}$ : Cyanoacetylene (molecule 44)

Cyanoacetylene is a molecule of notable astrochemical importance. It has been detected in a large number of astronomical environments (see Ref. [606] for a list of references), including planetary atmospheres [607], comets [608], and nearby galaxies [609]. Several laboratory works were carried out over the years, exploring mainly the rotational and ro-vibrational spectra of  $\text{HC}_3\text{N}$ . In 2017, a detailed global analysis of this molecule was published [606], which included pure rotational transitions in the ground and some excited vibrational states and ro-vibrational transitions in the window 450–1350  $\text{cm}^{-1}$ , involving all the energy levels lower than 1000  $\text{cm}^{-1}$ . Such analysis has been extended to the far-infrared region below 450  $\text{cm}^{-1}$  and to the stretching region between 2034 and 3360  $\text{cm}^{-1}$ . The newly recorded spectra and the related new global fit are the subjects of a separate paper submitted to this issue. All the experimental

and theoretical details and the treatment of the data are reported in that paper. From this analysis, a new line list of rotational and ro-vibrational transitions has been compiled and introduced in the HITRAN2020 database. The line list reports transition wavenumbers calculated with the best spectroscopic parameters obtained from the global fit. The main advantage of the new line list is the completeness of the data and their consistency, confirmed by the quality of the global fit. For the first time, they include ro-vibrational transitions relative to all seven vibrational modes of HC<sub>3</sub>N up to 3400 cm<sup>-1</sup> (fundamentals, combinations, overtones, and their associated hot-bands) and rotational data in the ground and many vibrational states of all normal modes. The fundamental band  $\nu_7$ , the lowest bending mode at 221.8 cm<sup>-1</sup>, has been detected directly in the far infrared region for the first time. This is important for an accurate derivation of its vibrational energy and therefore for the analysis of many hot bands which originate from it. The global fit also accounts for two anharmonic resonance networks, and their upscale by one quantum of  $\nu_7$ .

It is important to point out that the accuracy of the line positions for the  $\nu_5$  and  $\nu_6$  band systems is at least one order of magnitude better than that reported in the previous line list (although the differences do not exceed 0.001 cm<sup>-1</sup> and in fact for most of the lines are below 0.001 cm<sup>-1</sup>). Very limited extrapolations to  $J$  values higher than the observed ones have been made. With that being said, the intensities of lines in these fundamentals in the new list exceed the intensities in HITRAN2016 (which originate from Ref. [610]). The origins of this discrepancy remain to be determined. Considering that the line list from Ref. [610] is used in Titan studies and no issues were reported in the literature we retain HITRAN2016 parameters in corresponding spectral regions (460-560 cm<sup>-1</sup> and 620-750 cm<sup>-1</sup>). This will be a subject of further investigation.

To make matters even more confusing, the intensities of the  $\nu_1$  fundamental reported in Ref. [608] are a factor of 3 stronger than those in the new line list adapted for HITRAN2020. This also will be a subject of further investigation.

#### 2.45. $H_2$ : Molecular Hydrogen (molecule 45)

The ro-vibrational spectra of molecular hydrogen are relevant for the atmospheres of the giant planets in the solar system and some types of super-Earth exoplanets [611]. Molecular hydrogen was first introduced in HITRAN2012 (line positions, intensities and default value of the broadening parameter [the same for all lines] for the electric quadrupole and dipole lines in  $H_2$  and HD isotopologues, respectively) [14]. In HITRAN2016 [15], the electric quadrupole lines for HD were added and the line-shape parameters for the HT profile (based on experimental spectra) were added for self-perturbed  $H_2$  [165].

In HITRAN2020, a comprehensive dataset of beyond-Voigt line-shape parameters for He-perturbed  $H_2$  lines was added [612]. The dataset is based on *ab initio* quantum-scattering calculations and was validated on highly-accurate CRDS spectra to sub-percent level [612]. It covers a wide temperature range from 20 to 1000 K; the temperature dependencies of all the six line-shape parameters (broadening and shift,  $\gamma_0$  and  $\delta_0$ , speed dependence of broadening and shift,  $\gamma_2$  and  $\delta_2$ , real and imaginary parts of the Dicke parameter,  $\tilde{\nu}_{opt}^r$  and  $\tilde{\nu}_{opt}^i$ ) are represented with the double-power-law (DPL) approximation [118, 119] that recently was adopted in HITRAN [119]. To make the self-perturbed  $H_2$  line-shape parameter datasets [165] consistent with the He-perturbed  $H_2$  dataset [612] and with the DPL format [119], the self-perturbed  $H_2$  dataset, introduced into HITRAN in 2016 [165], was transformed into the DPL format [119].

Recently, it was demonstrated that for high- $J$  levels of  $H_2$  the intensities of the Q-branch lines are considerably influenced by the magnetic dipole contribution [613]. The  $H_2$  line list will be updated in the near future to account for it.

The hydrogen-rich atmospheres are dominated by  $H_2$  and He, but also contain the HD isotopologue whose low abundance is compensated by much larger intensities of dipole lines (compared to quadrupole lines in  $H_2$ ). Therefore a complete dataset for planetary applications should include four systems: He-perturbed  $H_2$ , He-perturbed HD,  $H_2$ -perturbed HD and self-perturbed  $H_2$ . In the near future, we plan to add a comprehensive dataset for the He-perturbed

HD lines (both dipole and quadrupole).

Unlike principal isotopologue HD transitions in HITRAN have only Voigt values which are known to be not efficient for this molecule and rather arbitrary assigned  $0.05 \text{ cm}^{-1}/\text{atm}$  for self- and air-width by default, which however seems to be overestimated approximately by a factor of five when they are compared to laboratory measurements [614]. Recently a new laboratory study of pure rotational transitions has reported the line shape parameters of HD [615], confirming that the HITRAN default values are indeed overestimated. Thus, an immediate update is in near future in favor of the new experimental values, which will include the broadening and frequency shifts of HD by self and  $\text{H}_2$  and their temperature dependences for R(0)–R(3) transitions that are determined through multi-spectrum fitting analysis at temperatures between 100–296 K [616].

#### 2.46. CS: Carbon Monosulfide (molecule 46)

The four most abundant isotopologues of carbon monosulfide ( $^{12}\text{C}^{32}\text{S}$ ,  $^{12}\text{C}^{34}\text{S}$ ,  $^{13}\text{C}^{32}\text{S}$ ,  $^{13}\text{C}^{33}\text{S}$ ) were added to HITRAN2012 [14], with line positions based on lower-state energies provided by the Cologne Database for Molecular Spectroscopy (CDMS) [617] and intensities calculated from Einstein- $A$  coefficients of Chandra et al. [618]. HITRAN includes eight bands for  $^{12}\text{C}^{32}\text{S}$  ( $v'-v'' = 0-0$ ,  $1-1$ ,  $2-2$ ,  $3-3$ ,  $4-4$ ,  $1-0$ ,  $2-1$  and  $2-0$ ), three bands for  $^{12}\text{C}^{34}\text{S}$  and  $^{13}\text{C}^{32}\text{S}$  ( $0-0$ ,  $1-1$  and  $1-0$ ), and two bands for  $^{12}\text{C}^{33}\text{S}$  ( $0-0$  and  $1-1$ ). In addition, CDMS also provides line lists for the  $0-0$  bands of  $^{13}\text{C}^{33}\text{S}$ ,  $^{13}\text{C}^{34}\text{S}$ ,  $^{12}\text{C}^{36}\text{S}$  and  $^{13}\text{C}^{36}\text{S}$ .

Since these data were added to HITRAN, empirically-corrected *ab initio* line lists for the  $X^1\Sigma^+$  electronic ground state of CS has been calculated by Paulose et al. [619] as part of the ExoMol project [333]. Eight isotopologues of CS ( $^{12}\text{C}^{32}\text{S}$ ,  $^{12}\text{C}^{33}\text{S}$ ,  $^{12}\text{C}^{34}\text{S}$ ,  $^{12}\text{C}^{36}\text{S}$ ,  $^{13}\text{C}^{32}\text{S}$ ,  $^{13}\text{C}^{33}\text{S}$ ,  $^{13}\text{C}^{34}\text{S}$ , and  $^{13}\text{C}^{36}\text{S}$ ) were included and cover frequencies up to  $11\,000 \text{ cm}^{-1}$ , with a maximum  $v = 49$  (with maximum  $\Delta v = 9$ ), maximum  $J = 258$  and recommended for use up to 3000 K.

More recently, Hou and Wei [620] have calculated comprehensive empirically-based line positions with *ab initio* intensities for the same eight isotopologues as Ref. [619]. These line lists extend up to  $15\,000\text{ cm}^{-1}$ , with a maximum  $v = 59$  (with maximum  $\Delta v = 12$ ), maximum  $J = 260$  and recommended for use up to  $7500\text{ K}$ .

The  $^{12}\text{C}^{32}\text{S}$  intensities from CDMS [617], ExoMol [619] and Hou and Wei [620] have been compared to bands available in HITRAN [14]. Generally, there is good agreement between all sources for the  $\Delta v = 0$  bands and the 0–0 comparisons are shown in the upper panel of Fig. 30. For the 1–0 band, the intensities of Hou and Wei [620] appear  $\sim 5\%$  weaker than the other studies, whereas for the 2–0 band the intensities of Hou and Wei [620] are  $\sim 50\%$  stronger than HITRAN (the weakest). The differences exhibited for the 2–0 transitions indicate that further validation of the Paulose et al. [619] and Hou and Wei [620] line lists are required. These works will be considered for inclusion into future editions of HITRAN.

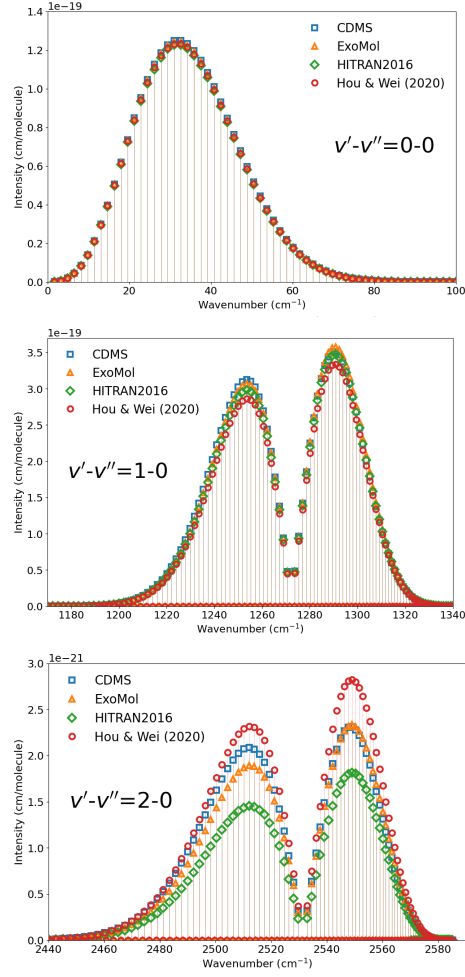


Figure 30: A comparison of the line intensities for the  $v'-v'' = 0-0$ ,  $1-0$  and  $2-0$  bands of  $^{12}\text{C}^{32}\text{S}$  in HITRAN [14] to line intensities in CDMS [617], ExoMol [619] and Hou and Wei [620].

#### 2.47. $\text{SO}_3$ : Sulfur Trioxide (molecule 47)

Unchanged.

#### 2.48. $\text{C}_2\text{N}_2$ : Cyanogen (molecule 48)

Unchanged.

#### 2.49. $\text{COCl}_2$ : Phosgene (molecule 49)

Unchanged.

#### 2.50. $\text{SO}$ : Sulfur Monoxide (molecule 50)

Sulfur monoxide is among sulfur-containing compounds detected on Venus (see for instance Ref. [621]). This molecule has also been detected in the atmospheres of Jupiter’s moon Io [622], and comets [623]. To aid interpretation of the spectra of planetary atmospheres a line list for this molecule was added to HITRAN. The MW line list from the CDMS catalogue [617] and NIR line list of the  $a^1\Delta-X^3\Sigma^-$  (0,0) and (1,1) transitions from Bernath and Bittner [624] were adapted with line positions substituted values based on the fit of data from Ref. [625] and references therein.

#### 2.51. $\text{CH}_3\text{F}$ : Methyl Fluoride (molecule 51)

A line list for methyl fluoride ( $\text{CH}_3\text{F}$ ) is introduced to HITRAN for the first time. This tetrahedral molecule is present in traces in the terrestrial atmosphere and participates in global warming [626]. A line list for the intense  $\nu_6$  band around  $1200\text{ cm}^{-1}$  has now been included in HITRAN, based on the work of Papoušek et al. [627] for line positions, on Ref. [628] for line intensities and self-broadening coefficients, and on the work of Barbouchi Ramani et al. [629] for air-broadening coefficients.

#### 2.52. $\text{GeH}_4$ : Germane (molecule 52)

Germane ( $\text{GeH}_4$ ) is a tetrahedral molecule of interest for the study of the atmospheres of giant planets Jupiter and Saturn. The need for accurate line lists for this molecule has been especially renewed recently by the availability of spectroscopic measurements from the JIRAM (Jovian InfraRed Auroral Mapper) infrared spectrometer aboard NASA’s Juno spacecraft [630]. Germane abundance retrieval in the Jovian atmosphere allows to probe the planet’s troposphere below the ammonia cloud level.



During the past few years, a new experimental and modeling study on this molecule has been undertaken by French (LISA in Créteil, ICB in Dijon) and Belgian (at ULB in Brussels) groups to remeasure high-resolution infrared spectra of the fundamental bands of germane in order to obtain accurate line positions and line intensities. The molecule was studied in natural abundance and effective Hamiltonian and dipole moment parameters were retrieved using the Dijon tensorial formalism and programs [631] for all five isotopologues:  $^{70}\text{GeH}_4$  (21.23 %),  $^{72}\text{GeH}_4$  (27.66 %),  $^{73}\text{GeH}_4$  (7.73 %),  $^{74}\text{GeH}_4$  (35.96 %) and  $^{76}\text{GeH}_4$  (7.44 %). Deuterated species have not been considered in these studies. A first paper was dedicated to the stretching dyad  $\nu_1/\nu_3$  around  $2100\text{ cm}^{-1}$  [632] and a second one to the bending dyad  $\nu_2/\nu_4$  around  $900\text{ cm}^{-1}$  [633].

The retrieved molecular parameters allowed one to produce calculated germane line lists for both regions. These data were first used to setup the GeCaSDa database (Germane Calculated Spectroscopic Database) [581] which can be accessed either directly (<http://vamdc.icb.cnrs.fr>) or through the VAMDC (Virtual Atomic and Molecular Data Centre) portal [634]. It was then decided to introduce germane as a new molecule, number 52, in the HITRAN database for the present edition.

The germane line lists contain line positions and absolute line intensities for approximately 12,200 lines for each of the five isotopologues. These lines pertain to the  $\nu_1$ ,  $\nu_2$ ,  $\nu_3$  and  $\nu_4$  fundamental bands only, in the  $648\text{--}2271\text{ cm}^{-1}$  wavenumber range. The lower intensity threshold for calculations is set to  $10^{-23}\text{ cm}^{-1}/(\text{molecule cm}^{-2})$ , which is a reasonable value avoiding exaggerated extrapolations from the assigned experimental lines.

For completeness, we also mention the work of O. Ulenikov’s group in Tomsk, Russia (see Ref. [635] and references therein), who obtained very similar results.

### 2.53. $\text{CS}_2$ : Carbon Disulfide (molecule 53)

Carbon disulfide ( $\text{CS}_2$ ) has been introduced in the line-by-line part of HITRAN for the first time.  $\text{CS}_2$  is a molecule of interest in atmospheric environmental chemistry, medical diagnostics, and studies of planetary atmospheres. It has

a significant effect on the global atmospheric sulfur budget. The oxidation of carbon disulfide in the atmosphere is a major source of OCS [460–463]. The CS<sub>2</sub> molecule has been detected in comets [636, 637] and in the Jupiter’s atmosphere after its collision with the Shoemaker-Levy 9 comet [638]. The principal sources of CS<sub>2</sub> are industrial and natural processes (volcanic eruptions, evaporation from the oceans, soils, biomass burning, and petroleum refining) [639, 640]. In addition, exposure to CS<sub>2</sub> can cause accelerated atherosclerosis and coronary artery disease [641, 642], and therefore it is essential to monitor its concentrations in relevant production sites.

The HITRAN2020 carbon disulfide line list contains 94 992 transitions of the <sup>12</sup>C<sup>32</sup>S<sub>2</sub>, <sup>32</sup>S<sup>12</sup>C<sup>34</sup>S, <sup>32</sup>S<sup>12</sup>C<sup>33</sup>S, and <sup>13</sup>C<sup>32</sup>S<sub>2</sub> isotopologues in the 1.2–6466.4 cm<sup>−1</sup> spectral range. The line list is described in detail in Ref. [643]; therefore here we only briefly summarize the main characteristics. In the HITRAN2020 edition, the CS<sub>2</sub> molecule was given number “53” to be consistent with the Total Internal Partition Sums (TIPS2017) program [178] (isotopologue ID: <sup>12</sup>C<sup>32</sup>S<sub>2</sub>: 1, <sup>32</sup>S<sup>12</sup>C<sup>34</sup>S: 2, <sup>32</sup>S<sup>12</sup>C<sup>33</sup>S: 3, and <sup>13</sup>C<sup>32</sup>S<sub>2</sub>: 4). Although CS<sub>2</sub> has the same symmetry as CO<sub>2</sub>, the quantum notation that was chosen for this molecule is more in line with that used for other linear molecules, including OCS. In particular, the labeling  $\nu_1\nu_2l_2\nu_3$  of the vibrational states was used (see Ref. [643] for details). The calculations of the line positions and intensities were performed by applying the PGOPHER program [596] using a large set of measured line positions available in the literature, including the most recent high-precision dual-comb laser spectroscopy measurements [644] and transition dipole moments for each measured band. A global least-squares fit of measured line positions to the corresponding spectroscopic parameters for the <sup>12</sup>C<sup>32</sup>S<sub>2</sub>, <sup>32</sup>S<sup>12</sup>C<sup>34</sup>S, <sup>32</sup>S<sup>12</sup>C<sup>33</sup>S, and <sup>13</sup>C<sup>32</sup>S<sub>2</sub> isotopologues was carried out. A unique set of parameters for each lower and upper state was obtained. The maximum rotational angular momentum in the line list was set to  $J = 150$ . In addition, the perturbed line positions of the  $3\nu_3$ ,  $\nu_1+3\nu_3$ , and  $3\nu_1+3\nu_3$  bands of the <sup>12</sup>C<sup>32</sup>S<sub>2</sub> isotopologue and the  $3\nu_3$  band of the <sup>32</sup>S<sup>12</sup>C<sup>34</sup>S isotopologue were replaced by their experimental values from Refs. [645–647]. The calculations of line intensities for 423 bands of the

$^{12}\text{C}^{32}\text{S}_2$ ,  $^{32}\text{S}^{12}\text{C}^{34}\text{S}$ ,  $^{32}\text{S}^{12}\text{C}^{33}\text{S}$ , and  $^{13}\text{C}^{32}\text{S}_2$  isotopologues have been carried out. For vibrational  $\text{CS}_2$  bands known experimentally from the literature, the corresponding transitions of the dipole moments were fitted to the measured line intensities. Different scaling factors were used to correct the line intensities for the carbon disulfide bands not having intensity measurements. In this case, validation and correction of the calculated line intensities have been performed using the PNNL [242] spectrum which covers the 600-6500  $\text{cm}^{-1}$  spectral range. The comparison between the  $\text{CS}_2$  line list (i.e., HITRAN line list) and experimental PNNL spectrum can be found in Fig. 9 and Fig. 10 of Ref. [643]. The overall agreement of the line positions and intensities is fairly good except for the spectral region around of 1535  $\text{cm}^{-1}$ , where there is not enough data to calculate the line parameters for all the hot bands.

The HITRAN line list allowed one to extend the knowledge about the  $\text{CS}_2$  line parameters in the 1–600  $\text{cm}^{-1}$  spectral region dominated by  $\nu_2$  band of  $^{12}\text{C}^{32}\text{S}_2$ . The line intensities of this band were calculated using data from Ref. [648] which may be considered to be imprecise; therefore, new experiments for this band are welcomed. Uncertainty codes for the line positions and the line intensities used in the  $\text{CS}_2$  line list are described in Ref. [643]. A summary of the carbon disulfide line list is given in Table 11.

Table 11: A summary of the carbon disulfide line list in the HITRAN2020 edition.

Isotopologue	Range ( $\text{cm}^{-1}$ )	Number of lines	Number of bands
$^{12}\text{C}^{32}\text{S}_2$	23.6–6466.4	53 770	252
$^{32}\text{S}^{12}\text{C}^{34}\text{S}$	196.7–4542.6	7322	22
$^{32}\text{S}^{12}\text{C}^{33}\text{S}$	611.2–4566.9	3612	12
$^{13}\text{C}^{32}\text{S}_2$	1.2–4425.1	30 288	137
Total		94 992	423

Figure 31 shows an overview of the line lists for the  $^{12}\text{C}^{32}\text{S}_2$ ,  $^{32}\text{S}^{12}\text{C}^{34}\text{S}$ ,  $^{32}\text{S}^{12}\text{C}^{33}\text{S}$ , and  $^{13}\text{C}^{32}\text{S}_2$  isotopologues in the 0–7000  $\text{cm}^{-1}$  region.

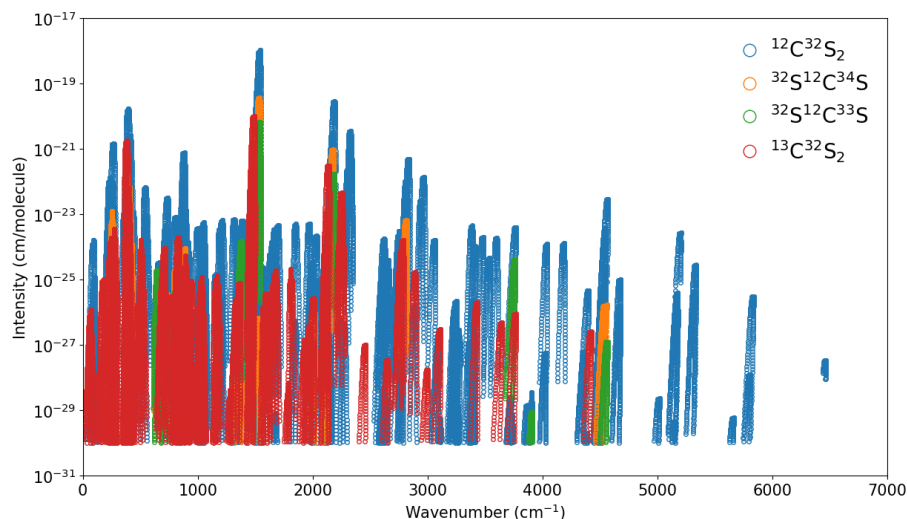


Figure 31: Overview of the line lists of the  $^{12}\text{C}^{32}\text{S}_2$ ,  $^{32}\text{S}^{12}\text{C}^{34}\text{S}$ ,  $^{32}\text{S}^{12}\text{C}^{33}\text{S}$ , and  $^{13}\text{C}^{32}\text{S}_2$  isotopologues in the 0–7000  $\text{cm}^{-1}$  region.

We obtained the air- and self-broadening parameters of  $\text{CS}_2$  and the temperature dependence exponents of the half-widths based on the measured or theoretically calculated data in the literature. To populate these parameters for all the lines of  $\text{CS}_2$ , the available results were fitted using the Padé approximants and these parameters ( $\gamma_{\text{air}}$ ,  $\gamma_{\text{self}}$ , and  $n_{\text{air}}$ ) were predicted for all the lines including the transitions with higher quantum numbers. The pressure shifts of  $\text{CS}_2$  were not yet added to the database because of the lack of the measured data for this parameter.

#### 2.54. $\text{CH}_3\text{I}$ : Methyl Iodide (molecule 54)

Methyl iodide ( $\text{CH}_3\text{I}$ ), a naturally occurring halogenated volatile organic compound, is an important carrier of iodine from the ocean to the atmosphere and plays a crucial role in the chemistry of the atmosphere [649, 650]. In addition, it is used in several industrial and agricultural applications. Examples include use as a methylation reagent in organic synthesis, a fumigant in buildings and soils, and as a pesticide. In nuclear power plants [651], methyl iodide is mainly produced in the containment by the reaction of iodine with organic

coatings of the enclosure under ionizing radiation. In the case of a severe nuclear accident, iodine fission products represent the major part of the released radioactivity and are of deep concern due to the affinity of iodine with the thyroid. It is, therefore, crucial to monitor the release of iodine compounds into the atmosphere as part of nuclear safety and radio-protection. Relevant to all these applications is the capability to install leak detectors as well as to monitor personal exposure limits. Implementation of optical detection schemes is hindered by the lack of accurate spectroscopic models based on high-precision laboratory measurements.

#### 2.54.1. $\nu_6$ band at $11.2\ \mu\text{m}$

A relatively strong  $\nu_6$  band of  $\text{CH}_3\text{I}$  is located at around  $893\ \text{cm}^{-1}$ , coinciding with the  $11\ \mu\text{m}$  transparency window in the atmosphere [20, 185], could be a good candidate for detection of this molecule in atmospheric spectra. Detailed studies concerning the line positions and intensities of the  $\nu_6$  fundamental and interacting  $2\nu_3$  bands were recently carried out [652, 653]. For the computation of the line positions and intensities, the hyperfine structure due to the iodine nuclear quadrupole moment was accounted for explicitly (Fig. 32), together with the vibration-rotation resonances which perturb them.

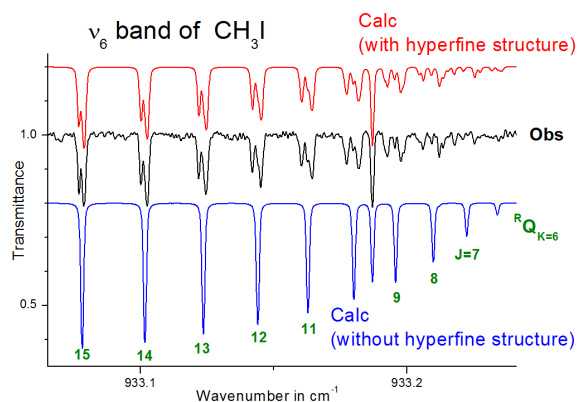


Figure 32: Example of a calculation of methyl iodide transitions with and without accounting for the hyperfine structure.

### 2.54.2. $\nu_4$ band at $3\ \mu\text{m}$

The reported line positions and intensities of the  $\nu_4$  band and the nearby  $\nu_3 + \nu_4 - \nu_3$  hot band are based on a high-precision measurement using optical frequency comb Fourier transform spectroscopy [654]. The details of the mid-IR frequency comb source [655], the home-built fast-scanning Fourier transformer spectrometer (FTS) [656], as well as the auto-balancing detection scheme in the FTS [657] and a Herriot cell are presented elsewhere. The high-resolution spectra were recorded in the region from 2800 to 3160  $\text{cm}^{-1}$  with sampling point spacing of 11 MHz, utilizing the sub-nominal resolution interleaving scheme [658, 659]. The measured spectrum, shown in Fig. 33 (a), contains three main ro-vibrational features: the parallel vibrational overtone and combination bands centered around 2850  $\text{cm}^{-1}$ , the symmetric stretch  $\nu_1$  band centered at 2971  $\text{cm}^{-1}$ , and the asymmetric stretch  $\nu_4$  band centered at 3060  $\text{cm}^{-1}$ . Based on the analysis of these spectra the  $\nu_4$  band and the nearby  $\nu_3 + \nu_4 - \nu_3$  hot band are included in the HITRAN2020 database.

Figure 33(b) shows the measured (black) spectrum of 0.11 mbar of pure  $\text{CH}_3\text{I}$  at 296 K together with the simulations of the  $\nu_4$  band (red) and the  $\nu_3 + \nu_4 - \nu_3$  hot band (blue). Figure 33(c) shows a further zoom in of Fig. 33(b) around a  $Q_K(J)$  sub-branch. The spectra of these two bands were simulated and assigned using PGOPHER [596]. The overall band structure as well as the relative intensities of the individual lines in the simulations agree very well with the experimental data. A least square fit of the assigned transitions to the measured spectrum provided accurate upper state rotational constants of both bands. The hyperfine splittings due to the  $^{127}\text{I}$  iodine nuclear quadrupole moment are observed for transitions with  $J \leq 2K$ . Future work will involve further analysis of the hyperfine splittings and the analysis of the measured  $\nu_1$  band and the parallel vibration bands.

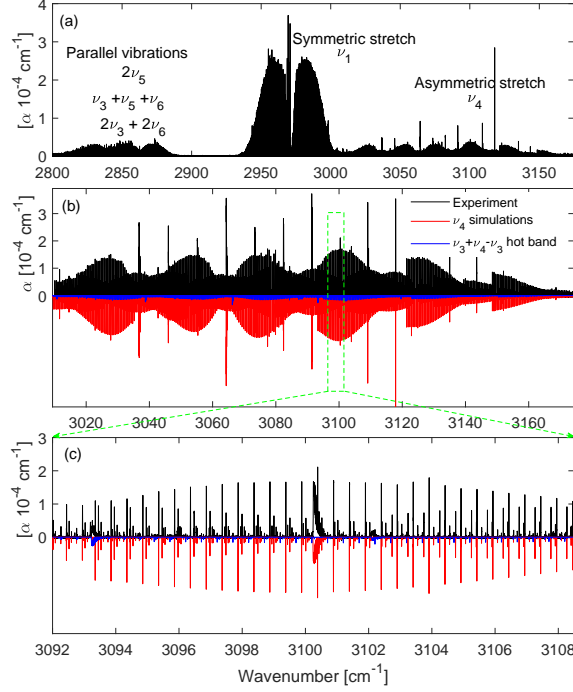


Figure 33: (a) The broadband high-resolution spectrum of pure CH<sub>3</sub>I measured at 0.03 mbar in the range from 2800–3160 cm<sup>-1</sup> using comb-based FTS [654]. (b) The absorption coefficient,  $\alpha$  of the  $\nu_4$  band measured at 0.11 mbar of pure CH<sub>3</sub>I (black) together with the simulations of the  $\nu_4$  band (red) and the  $\nu_3 + \nu_4 - \nu_3$  hot band (blue) obtained using PGOPHER. (c) Zoom in around one of the  $Q_K(J)$  sub-branches of the  $\nu_4$  band.

For self- and air-broadening parameters for all transitions are based on recent studies by Raddaoui et al. [626, 660]. The values are based on FT-spectra analysis for the  $\nu_6$  band proposed a set of smoothed empirical parameters to calculate widths up to  $J = 80$ . Empirical parameters are fitted through the  $K$ -rotational dependencies observed for transitions having same lower  $J$  value. The rotational  $J$ - and  $K$ -dependencies calculated by this model reproduced the measurements (around 1000) with a sub-percent average discrepancy and one standard deviation of around 7% both for self- and air-broadening coefficients. The smoothed parameters of Table 4 from Ref. [626] and Table 5 from Ref. [660] for self- and air-broadening coefficients respectively have been used to generate broadening coefficients at 296 K for all CH<sub>3</sub>I transitions. Error code of 5 (see

Table 2) has been used for both self- and air-broadening coefficients.

Default values for temperature dependence (fixed to 0.75) of air-broadening coefficients and air-pressure shift coefficients (fixed to  $-0.001 \text{ cm}^{-1}/\text{atm}$ ) have been used for all  $\text{CH}_3\text{I}$  transitions. There are no line shifts and temperature dependence parameters for this molecule available in the literature. For atmospheric applications, a study of the temperature dependence of the line-shape parameters of  $\text{CH}_3\text{I}$  (190–300 K) will be required.

#### 2.55. $\text{NF}_3$ : Nitrogen Trifluoride (molecule 55)

The nitrogen trifluoride ( $\text{NF}_3$ ) line list is presented in the HITRAN database for the first time. This line list includes more than 40 cold and 680 hot sub-bands and covers the spectral range up to  $2200 \text{ cm}^{-1}$ .  $\text{NF}_3$  is known as an anthropogenic greenhouse gas with a high global warming potential of about 17 000 [661–663]. The concentration of  $\text{NF}_3$  has been increasing in the Earth’s atmosphere during the past decade [664, 665] because this gas is widely used in the semiconductor industry. The  $\text{NF}_3$  molecule is semirigid, belonging to  $\text{C}_{3v}$  point group; the symmetry properties and selection rules are quite similar to those of other symmetric tops included in the previous HITRAN2016 release like  $\text{PH}_3$  or  $\text{CH}_3\text{D}$ , for which the reader can find detailed discussions in Ref. [666] (and references therein). However, nitrogen trifluoride has lower vibrational modes and smaller rotational constants leading to a much more congested infrared spectra, which leads to complicated line-by-line analyses using a purely empirical approach. This is particularly true for line intensity determination because of numerous overlapping hot bands even at room temperature. The HITRAN2020 version includes the global *combined* line list of Egorov et al. [667], which was based on large-scale variational calculations with *ab initio* potential energy (PES) and dipole moment surfaces (DMS) constructed at the CCSD(T)/CVQZ and CCSD(T)/AVQZ levels of the theory. The effective Hamiltonian of  $\text{NF}_3$  was then obtained by the six-order contact transformation approach using the MOL\_CT computational code [212, 668] from the *ab initio*



PES. The effective polyad model included six groups of the vibrational states: from ground up to icosad. The *ab initio* parameters of the effective model were refined using the MIRS computational code [669, 670] and experimental transitions of  $\text{NF}_3$  existing in the literature. In particular, the experimental line positions from the following works were used for the fine tuning of the energy levels:  $\nu_4(\text{E})$  [671];  $\nu_2(\text{A}_1)$ ,  $\nu_2 + \nu_4(\text{E})$ , and  $2\nu_2(\text{A}_1)$  [672];  $2\nu_4(\text{A}_1, \text{E})$  [673];  $\nu_1(\text{E})$  [674];  $\nu_3(\text{E})$  [675];  $\nu_1 + \nu_4(\text{E})$  [676, 677];  $2\nu_3(\text{A}_1, \text{E})$  and  $\nu_1 + \nu_3(\text{E})$  [678];  $\nu_2 + \nu_3(\text{E})$ ,  $2\nu_1(\text{A}_1)$  and  $\nu_1 + \nu_2 + \nu_4(\text{E})$  [679]. The empirical parameters of the ground state were taken from Ref. [673] where the “loop-method” was applied to determine the K-dependent parameters ( $C_0$ ,  $D_K$ ,  $H_K$  etc.) by combining the experimental pure rotational transitions with those from the ground state combination differences. All  $\text{NF}_3$  line intensities were calculated variationally from the pure *ab initio* DMS and are available in the TheoReTS web site (<http://theorets.univ-reims.fr>; <http://theorets.tsu.ru>). The first experimental studies of  $\text{NF}_3$  integrated cross sections with a medium spectral resolution were conducted in Ref. [680] and then revisited in Ref. [661]. The present  $\text{NF}_3$  line list has been validated in detail in the work of Egorov et al. [667] by comparison with the PNNL absorption coefficients [242] above 600  $\text{cm}^{-1}$ . The line positions and intensities in the region of the  $2\nu_3(\text{A}_1, \text{E})$  and  $\nu_1 + \nu_3(\text{E})$  bands were additionally validated using low-temperature (196 K) Fourier spectra in Ref. [681]. The  $\text{NF}_3$  line list is now provided in the HITRAN database with the averaged values of air- and self-broadened half-widths ( $\gamma_{\text{air}} = 0.1 \text{ cm}^{-1}\text{atm}^{-1}$ ,  $\gamma_{\text{self}} = 0.5 \text{ cm}^{-1}\text{atm}^{-1}$ ) as well as the temperature dependence exponent ( $n_{\text{air}} = 0.55$ ). The total internal partition sum  $Q_{\text{tot}}(\text{T} = 296 \text{ K}) = 346\,346.82$ . It is worth mentioning that only the principal isotopologue ( $^{14}\text{NF}_3$ ) is included at this time with the abundance of 0.9964. The error codes (explained in Table 2) for all *ab initio* line intensities were set to 4, to 3 for the line positions of the corrected to the experiment bands, and to 2 for the *ab initio* line positions of all other bands.

### 3. Absorption cross-sections

#### 3.1. IR cross-sections

The comprehensive update of the infrared absorption cross-sections carried out for HITRAN2016 [682] dramatically extended the number of compounds represented in this section to almost 300. For HITRAN2020 some additional updates are introduced and are described below.

##### 3.1.1. Halogenated species of atmospheric interest

Four high-spectral-resolution absorption cross-section datasets of the halogenated species trichlorofluoromethane ( $\text{CCl}_3\text{F}$  a.k.a. CFC-11), 1,1-dichloro-1-fluoroethane ( $\text{CH}_3\text{CCl}_2\text{F}$  a.k.a. HCFC-141b), sulfur hexafluoride ( $\text{SF}_6$ ), and carbon tetrafluoride ( $\text{CF}_4$  a.k.a. CFC-14) have been added to HITRAN2020 (see Table 12). Covering a wide range of atmospherically relevant pressures and temperatures, these datasets are intended for use by the atmospheric remote-sensing community, particularly for the interpretation of measurements by atmospheric infrared limb sounders such as the ACE-FTS (Atmospheric Chemistry Experiment–Fourier transform spectrometer) [683]. CFC-11 was one of the first chlorofluorocarbons (CFCs) developed in the 1930s as inexpensive, reliable, safe and non-toxic refrigerants for domestic use. Its applications ranged from refrigerators and air conditioners to propellants in spray cans and blowing agents in foam production. As the use of CFCs became widespread, their atmospheric concentrations steadily rose. However, the discovery that they were destroying stratospheric ozone led to the signing of the 1987 Montreal Protocol. Designed to protect the Earth’s ozone layer, the Protocol mandated the phasing out of CFC production. Although phased out, CFC-11 is still emitted into the atmosphere from existing “banks” (e.g., old refrigerators and air conditioners containing CFCs), but overall its atmospheric abundance is now decreasing. It was recently discovered that China began illegally emitting CFC-11 from around 2013 [684, 685], although these illegal emissions had largely been curbed by 2019 [686, 687]. Hydrochlorofluorocarbons (HCFCs) were initially adopted

as ‘transitional’ CFC replacements because of their shorter atmospheric lifetimes on account of their more efficient reaction with OH in the troposphere, and their reduced stratospheric ozone depletion potentials. With the worldwide CFC phase out achieved under the terms of the Montreal Protocol, the focus has now shifted to HCFCs themselves, with a final phase out currently scheduled for 2030 for developed countries and 2040 in the developing world. HCFC-141b is primarily used as a foam blowing agent, a solvent in electronics, and for precision cleaning applications. Like other HCFCs, its atmospheric abundance continues to increase. Both  $\text{CF}_4$  and  $\text{SF}_6$  belong to the class of source gases known as F-gases, with fluorine as the only halogen attached to either carbon, sulfur, or nitrogen. These gases are not ozone-depleting and are not regulated by the Montreal Protocol. They both have small natural sources; degassing of the Earth’s crust sustains an atmospheric background of 34.7 ppt for  $\text{CF}_4$  [688] and up to 0.01 ppt for  $\text{SF}_6$  [689]. However, anthropogenic emissions of these species now dominate. As these species are potent greenhouse gases with very long atmospheric lifetimes, they fall within the remit of the Kyoto Protocol.  $\text{CF}_4$  and  $\text{SF}_6$  have leaked into the atmosphere from a number of industrial applications;  $\text{CF}_4$  from the production of aluminium and the manufacture of microchips in the semiconductor industry, and  $\text{SF}_6$  as an insulating medium in high-voltage electrical equipment, in particular in electricity distribution systems, magnesium production, and semi-conductor manufacturing. Due to their very long atmospheric lifetimes,  $\text{SF}_6$  and  $\text{CF}_4$  in the stratosphere are useful tracers for age of air. Remote-sensing measurements of both species have the potential to investigate changes in the Brewer–Dobson circulation due to climate change.

Table 12: Absorption cross sections added to HITRAN2020 for remote sensing of the terrestrial atmosphere.

Molecule	Temperature range (K)	Pressure range (Torr)	Number of P,T sets	Spectral range ( $\text{cm}^{-1}$ )
$\text{CCl}_3\text{F}$ (CFC-11)	192 – 293	7.5 – 760	30	710 – 1290
$\text{CH}_3\text{CCl}_2\text{F}$ (HCFC-141b)	188 – 295	7.5 – 761	30	705 – 1280
$\text{SF}_6$	189 – 294	7.5 – 751	37	780 – 1100
$\text{CF}_4$ (CFC-14)	190 – 296	7.5 – 760	34	1190 – 1336

*3.1.1.1. Trichlorofluoromethane ( $\text{CCl}_3\text{F}$ , CFC-11).* The CFC-11 cross section dataset in previous HITRAN compilations was provided by Varanasi et al. [11, 690] and has been used extensively for remote-sensing applications. For HITRAN2020, this has been replaced by a new dataset from Harrison [691], determined from spectra recorded using a high-resolution FTS (Bruker IFS 125HR) and a 26-cm-pathlength cell at spectral resolutions between 0.01 and 0.03  $\text{cm}^{-1}$  (see Table 12). This new dataset resolves a number of issues with the Varanasi data, namely a more accurately calibrated wavenumber scale, more consistent integrated band intensities, improved signal-to-noise, no channel fringing, and a wider range of pressures and temperatures. The Varanasi dataset is now available in the HITRAN alternate folder.

*3.1.1.2. 1,1-Dichloro-1-fluoroethane ( $\text{CH}_3\text{CCl}_2\text{F}$ , HCFC-141b).* The HITRAN2016 compilation included three 760-Torr- $\text{N}_2$ -broadened HCFC-141b cross sections (278, 298, and 323 K) at 0.112  $\text{cm}^{-1}$  spectral resolution, and seven cross sections (223, 233, 243, 253, 263, 273, and 283 K) for pure HCFC-141b at 0.02  $\text{cm}^{-1}$  resolution [692]. However, these do not account for air-broadening below 760 Torr, so are not the most appropriate for use in remote sensing of the Earth’s atmosphere. HITRAN2020 now includes air-broadened HCFC-141b cross sections [693] over a range of pressures and temperatures appropriate for atmospheric conditions (Table 12); these are derived from spectra recorded at spectral resolutions between 0.01 and 0.03  $\text{cm}^{-1}$  using a high-resolution FTS (Bruker IFS 125HR) and a 26-cm-pathlength cell.

*3.1.1.3. Sulfur hexafluoride ( $SF_6$ ).* Although line parameters for the strong  $\nu_3$  band of  $^{32}SF_6$  at  $948.1\text{ cm}^{-1}$  can be found in HITRAN, they are relegated to a supplemental folder because line parameters for the underlying hot bands, which contribute about half of the total absorption under stratospheric conditions, are not included. It has always been recommended that HITRAN users make use of absorption cross sections for remote sensing purposes; in previous compilations this has meant using the dataset derived from measurements by Varanasi et al. [11, 694]. For HITRAN2020, this dataset has been replaced by a new one from Harrison [695], which covers a wider range of pressures and temperatures, notably at the low-pressure end, has a more accurately calibrated wavenumber scale, with improved signal-to-noise, more consistent integrated band intensities, and no channel fringes. This new dataset has been determined from spectra of pure and air-broadened  $SF_6$  recorded at spectral resolutions between  $0.002$  and  $0.03\text{ cm}^{-1}$  using a high-resolution FTS (Bruker IFS 125HR) and a 26-cm-pathlength cell. The previous dataset is now available in the HITRAN alternate folder.

*3.1.1.4. Carbon tetrafluoride ( $CF_4$ , CFC-14).* In previous compilations, the IR absorption cross sections of  $CF_4$  available for remote sensing were derived from measurements by Varanasi et al. [11, 696]. Their use was recommended instead of the HITRAN  $CF_4$  line parameters for the  $\nu_3$  band at  $\sim 1283.2\text{ cm}^{-1}$ , which are relegated to a supplemental folder because the underlying hot bands are missing. For HITRAN2020, this cross-section dataset has been replaced by a new one from Harrison [697], determined from spectra of pure and air-broadened  $CF_4$  recorded at spectral resolutions between  $0.0018$  and  $0.03\text{ cm}^{-1}$  using a high-resolution FTS (Bruker IFS 125HR) and 5-cm- and 26-cm-pathlength sample cells. The new dataset covers a wider range of pressures and temperatures, notably at the low-pressure end, and corrects problems with the under-resolved low-pressure measurements. Furthermore, it has a more accurately calibrated wavenumber scale, more consistent integrated band intensities, and improved signal-to-noise. The previous Varanasi dataset is now available in the HITRAN

alternate folder.

### *3.1.2. Planetary-relevant broadening and high temperatures*

The vast majority of absorption cross-sections in HITRAN2016 were measurements of pure gases (or samples broadened by air or N<sub>2</sub>). To extend the applicability of the HITRAN database to planetary environments, many line-by-line molecules in HITRAN now contain collisional broadening parameters for H<sub>2</sub>, He, CO<sub>2</sub> and H<sub>2</sub>O (see Section 2). This allows the HITRAN line lists to be applied in radiative transfer calculations of planetary atmospheres. Similarly, absorption cross-sections broadened by planetary-relevant species (H<sub>2</sub>, He, CO<sub>2</sub>, N<sub>2</sub>) and covering appropriate temperatures (including higher temperatures applicable to exoplanets) are also being added to HITRAN. In HITRAN2020 some of the first “planetary” cross-sections have been included, but a larger update of relevant cross-sections is planned in the near future.

The lower atmosphere of Titan predominantly consists of N<sub>2</sub> (~94.2%) and CH<sub>4</sub> (~5.6%) with a small H<sub>2</sub> contribution (0.1%) and other carbon-rich compounds [698]. Therefore, the N<sub>2</sub>-broadened absorption cross-sections already contained in HITRAN can be applied to the study of Titan. These will be supplemented with N<sub>2</sub>-broadened absorption cross-sections of many hydrocarbon compounds recorded with experimental conditions (pressure, composition and temperature) chosen to represent those found in Titan’s atmosphere. These compounds include: ethane [699], propylene [700], propane [701], n-butane [702], isobutane [703–705], neopentane [706], and benzene [707, 708].

For outer planet and exoplanetary atmospheres, the dominant constituents are typically H<sub>2</sub> and He. Again, many measurements have been recorded with experimental conditions (pressure, composition and temperature) applicable to the outer planets. These compounds include: ethane [699, 709], propane [710–713], isobutane [703–705], and benzene [707, 708]. Absorption cross-sections broadened by H<sub>2</sub> and He will be added to HITRAN2020 as an update.

The absorption cross-sections in HITRAN are typically recorded at room temperatures (and below) as appropriate for the terrestrial atmosphere. Ab-

sorption cross-sections of spectroscopically-challenging compounds are predicted to be abundant (with respect to the terrestrial atmosphere) in planetary atmospheres at elevated temperatures. A series of FTIR measurements have been recorded at high-temperatures (up to 1100 K) using a tube cell and furnace for ethane [714], propane [715], propylene [716, 717], 1-butene [718], methanol [719] and larger compounds [720]. Further high-temperature (up to 1600 K) absorption cross sections have been measured of hydrocarbons [721, 722], alcohols [723] and aldehydes [724] using a rapid-tuning broad scan external cavity quantum cascade laser in conjunction with shock tube facilities. Therefore to increase the applicability of the HITRAN data to planetary environments, absorption cross-sections at higher temperatures will be added to HITRAN2020 as an update.

### *3.2. UV cross-sections*

#### *3.2.1. $O_3$ :*

A new UV cross-section database for ozone (referred to as DLR-O3-2020), which straddles the peak of the Hartley band and covers the spectral range 28 000–42 000  $\text{cm}^{-1}$  (357–238 nm) and temperature range 193–293 K was generated within the framework of the ESA project SEOM-IAS, ESA/AO/1-7566/13/I-BG. A detailed publication is in preparation [725]. The database was tested for analysis of OMI observations and found to be satisfactory [726].

FTS transmittance measurements were performed using a Bruker IFS 125 HR high resolution spectrometer in combination with a coolable 22.15-cm-long single-pass cell. Measurements of absorption spectra were performed under sealed-off conditions. Ozone was prepared from  $O_2$  in a silent discharge and purified and handled applying procedures similar to those given in [217]. Because decomposition of ozone was negligible at low temperatures, number densities could be derived from absolute pressure measurements. Absorption cross-sections span a large dynamic range from  $3 \times 10^{-22}$ – $10^{-17}$   $\text{cm}^2/\text{molec}$ , requiring pressure measurements over the range 0.1–30 mbar. In total 191 spectra were

measured. The transmittance spectra are given with an uncalibrated wavenumber scale which is justified by the low-resolution nature of the O<sub>3</sub> spectra. It was confirmed that, due to this smooth spectral dependence, the cross-sections do not depend markedly on the air pressure. Consequently, the total pressure dependence of the cross-sections was neglected.

A multi-spectrum fitting approach as described in [216] was applied for each of the 6 temperatures in the range 193–293 K. Above 35 000 cm<sup>-1</sup> the original spectral resolution of 3.3 cm<sup>-1</sup> was decreased to ca. 7.7 cm<sup>-1</sup> by Gaussian smoothing. Uncertainties for each spectral point were propagated from the noise in the transmittance spectra.

Polynomials of first- (>37 000 cm<sup>-1</sup>) and second-order (<37 000 cm<sup>-1</sup>) in temperature (in K) were then fitted to the absorption cross sections for each spectral point. This fit reveals systematic errors and reduces the statistical uncertainty. Absorption cross-sections were calculated from the polynomials at temperatures (193, 213, 233, 253, 273, 293 K) near the measurement conditions and are given in the database. The relative systematic uncertainties in the DLR-O3-2020 absorption cross-sections are 0.3%.

This is the first work where a large wavelength range relevant for ozone remote sensing was measured entirely with the FTS technique and a single spectrometer. We find differences of relative absorption cross-sections between the DLR-O3-2020 data with those from older references and inconsistencies among previous data on the order of few percent, which can be attributed to radiometric problems in the grating instruments. This result is supported by the good agreement of relative absorption cross sections with UV FTS measurements in the range 310–350 nm by the Bremen spectroscopy group [727]. The high quality of the DLR-O3-2020 data can be seen by the good agreement with recent high-accuracy, room temperature ozone cross-sections, which include the 254 nm value recommended by Hodges et al. [728]  $u_r = 0.31\%$  (DLR-O3-2020 data



0.64(35)% below) and the laser-based measurement at 325.126 nm of Janssen et al. [729]  $u_r = 0.09\%$  (DLR-O3-2020 data 0.94(31)% below). We note that as described in [728], choice of the cross-section at 254 nm constitutes the spectroscopic anchor point for SI-traceable measurements of ozone mole fraction in the lower atmosphere. These observations are ubiquitous and are based on an international network of ground-level standard reference photometers (SRPs) operating at 254 nm that are dedicated to environmental monitoring. Currently, these instruments use the outdated cross-section value reported by Hearn et al. [730], which has a value that is about 1.2% greater and sixfold more uncertain than that recommended by Hodges et al. [728]. We note that there will be a globally coordinated change to the new cross-section value lasting 3 to 5 years, with a target change date of January 1, 2024. For physically consistent comparisons with ozone mixing ratios provided by ground-based SRPs to be based on the updated cross-section at 254 nm, future satellite retrievals of ozone abundance that use the DLR-O3-2020 data may be multiplied by 1.0064. Nevertheless, there remains some debate whether this scaling factor can be uniformly applied to the DLR-O3-2020 cross-section data at all wavelengths. At the moment, a broadband correction of this form will be left to the discretion of the user.

The measurement database, calculated absorption cross sections with statistical uncertainties and polynomials can be downloaded from [731].

### 3.2.2. $SO_2$ :

Starting with HITRAN2008 edition [13] UV cross-sections of  $SO_2$  from Refs. [732, 733] were used in the database. While being of excellent quality they cover only relatively high (by terrestrial atmosphere standards) temperature range of 298–358 K. A new UV database in the spectral range 23 000–36 000  $cm^{-1}$  (435–278 nm) and the temperature range 193–293 K was generated within the framework of the ESA project SEOM-IAS, ESA/AO/1-7566/13/I-BG. A detailed publication is in preparation [734].

FTS transmittance measurements were performed using a Bruker IFS 125 HR high resolution spectrometer in combination with a 22.15 cm coolable single pass cell with a maximum optical path difference of 0.3 cm. Measurements of absorption spectra were performed under sealed-off conditions. SO<sub>2</sub> was supplied by Linde with a specified purity of 99.98%.

Since SO<sub>2</sub> is stable number densities could be derived from absolute pressure measurements. The absorption cross sections have a large dynamic range from  $10^{-24}$ – $10^{-18}$  cm<sup>2</sup>/molec, requiring a pressure range from 1.0–1000 mbar. In total 87 spectra were measured. A calibration factor of 1.000003905 was applied, deduced from the calibration factor of a CH<sub>4</sub> measurement around 6000 cm<sup>-1</sup> with a correction accounting for the different input aperture diameter.

A multi-spectrum fitting approach as described in [216] was applied for each of the 6 temperatures in the range 193–293 K. Uncertainties in the baseline were reduced by fixing the absorption cross sections in the ranges <23 500 cm<sup>-1</sup> and 24 000–24 400 cm<sup>-1</sup> to zero. Uncertainties for each spectral point were propagated from the noise in the transmittance spectra.

In contrast to ozone SO<sub>2</sub> showed high resolution features with widths down to the Doppler limit. An error free absorption cross sections database would require air broadened measurements with sub-Doppler instrumental resolution. To avoid self broadening SO<sub>2</sub> pressures must be below 10 mbar which in turn requires multi-reflection cell measurements. In principle this could have been done but would have exceeded the resources by far. Thus, it was decided to measure pure SO<sub>2</sub> up to 1000 mbar with a moderate resolution of 1.7 cm<sup>-1</sup>. In order to assess the systematic errors associated with this approach Doppler limited measurements have been carried out as well as self broadened measurements with sufficient instrumental resolution to have monochromatic spectra (not provided here). The impact under conditions relevant to the TROPOMI

instrument was found to be small within the requirements. The total column error was  $<2\%$  for all atmospheric scenarios with  $\text{SO}_2$  columns up to 2000 DU.

Polynomials of second-order in temperature (in K) were then fitted to the absorption cross sections for each spectral point in the range  $25\,000\text{--}36\,000\text{ cm}^{-1}$  (400–278 nm). This fit reveals systematic errors and improves the statistical uncertainty. Indeed, a fourth-order offset polynomial had to be fitted for the 213 K absorption cross sections in the range  $25\,000\text{--}30\,900\text{ cm}^{-1}$  to reduce the residuals of the temperature dependence fit. The statistical errors of the absorption cross sections were propagated into the polynomial coefficients errors and are used together with the  $\chi^2$  of the polynomial fit to calculate absorption cross sections at about measurement temperatures.

The new data overcome some problems with the data sets used so far. The data from Hermans and Vandaele [732, 733] are applied for high atmospheric  $\text{SO}_2$  load in the spectral region 360–390 nm ( $27\,800\text{--}25\,640\text{ cm}^{-1}$ ) and are extrapolated to lower temperature since measurements covered only 298–358 K. In the regions for lower volcanic (325–335 nm,  $30\,770\text{--}29\,850\text{ cm}^{-1}$ ) and background (312–326 nm,  $32\,050\text{--}30\,675\text{ cm}^{-1}$ )  $\text{SO}_2$  the data from Bogumil et al. [735] are used for atmospheric retrieval. These data have an inconsistency between 203 and 223 K in the temperature dependence of the absorption cross sections. Applying the new absorption cross section data would yield maximum  $\text{SO}_2$  column changes of 5% with respect to the Hermans/Vandaele data and 16% with respect to the Bogumil et al. data.

The measurement database, calculated (semi-empirical) absorption cross sections with statistical uncertainties and polynomials can be downloaded from [736]. The cross-sections from this work were added to the HITRAN2020 database.

## 4. Collision-Induced Absorption

### 4.1. Description of 2019 update

Collision-induced absorption (CIA) is the process of absorption of light by pairs of colliding molecules, due to the dipole moment induced by interactions between the colliding molecules. That is, CIA is an additional source of absorption, not just broadening of the existing monomer absorption lines. However, often CIA will lead to absorption in the same spectral regions as monomer absorption, leading to a broad feature underneath sharp absorption lines. The contribution of this continuum absorption is especially important for forbidden transitions, where monomer transitions are weak, or conversely if the absorption lines are saturated, such that it becomes difficult to extract information from their intensity. In the far infrared CIA contributes appreciably to the heat balance of planetary atmospheres due to absorption of outgoing blackbody radiation. In the terrestrial atmosphere, CIA by  $\text{N}_2$  and  $\text{O}_2$  molecules is important for the calibration or remote sensing [303, 737–742], and in exoplanetary atmospheres  $\text{O}_2$ - $\text{O}_2$  collision absorption is an important target as a possible biomarker [743]. Collision-induced absorption involving  $\text{N}_2$  and  $\text{CO}_2$  molecules is important in the atmospheres of Titan and Venus, respectively, whereas collision partners such as He,  $\text{H}_2$  and  $\text{CH}_4$  are important in gas giants and brown dwarfs [744]. Collision-induced absorption by  $\text{CH}_4$ ,  $\text{CO}_2$ , and  $\text{H}_2$  was suggested to affect the modeling of Venusian and Martian atmospheres in the early stages of geological history [745, 746].

HITRAN has a section devoted to collision-induced absorption, which was introduced in 2012 [747]. This section has recently been updated [748]. The temperature and spectral ranges for the bands included for each collisional pair can be found in Table 13. The main updates involved the roto-translational and vibrational bands of  $\text{N}_2$ - $\text{N}_2$ ,  $\text{CO}_2$ - $\text{CO}_2$ , the roto-translational band of  $\text{CO}_2$ - $\text{H}_2$ , collisions involving helium atoms,  $\text{H}_2$ - $\text{H}_2$  at low temperatures, and electronic transitions in  $\text{O}_2$ - $\text{O}_2$  and  $\text{O}_2$ - $\text{N}_2$ . The database now contains CIA for  $\text{N}_2$ - $\text{N}_2$ ,  $\text{N}_2$ - $\text{H}_2$ ,  $\text{N}_2$ - $\text{CH}_4$ ,  $\text{N}_2$ - $\text{H}_2\text{O}$ ,  $\text{N}_2$ - $\text{O}_2$ ,  $\text{O}_2$ - $\text{O}_2$ ,  $\text{O}_2$ - $\text{CO}_2$ ,  $\text{CO}_2$ - $\text{CO}_2$ ,  $\text{H}_2$ - $\text{H}_2$ ,  $\text{H}_2$ -He,  $\text{H}_2$ -

CH<sub>4</sub>, H<sub>2</sub>-H, H-He, CH<sub>4</sub>-CH<sub>4</sub>, CH<sub>4</sub>-CO<sub>2</sub>, CH<sub>4</sub>-He, and CH<sub>4</sub>-Ar collision pairs. Instructions for accessing the CIA section of the HITRAN database can be found on the HITRAN website ([www.hitran.org/cia](http://www.hitran.org/cia)). A set of supplementary files is available in the “Alternate folder” which contain data that are not recommended in general but do have a clear advantage over the recommended data, such as extended temperature ranges, account for spin statistics, or are constructed to be consistent with a particular line list. Further updates of the CIA data are forthcoming, as described below.

Table 13: Summary of the different bands available in the HITRAN CIA section, including Supplementary folders for all collisional systems.

System	Folder	Spectral range (cm <sup>-1</sup> )	T range (K)	# of sets	Ref.
H <sub>2</sub> -H <sub>2</sub>	Main	20-10 000	200-3000	113	[749]
	Alternate	0-2400	40-400	120	[750]
H <sub>2</sub> -He	Main	20-20 000	200-9900	334	[751]
H <sub>2</sub> -H	Main	100-10 000	1000-2500	4	[752]
He-H	Main	50-11 000	1500-10 000	10	[753]
H <sub>2</sub> -CH <sub>4</sub>	Main	0-1946	40-400	10	[754]
N <sub>2</sub> -He	Main	1-1000	300	1	[755]
CO <sub>2</sub> -He	Main	0-1000	300	1	[755]
CO <sub>2</sub> -Ar	Main	0-300	200-400	21	[756]
CH <sub>4</sub> -He	Main	1-1000	40-350	10	[757]
CH <sub>4</sub> -Ar	Alternate	1-697	70-296	5	[758]
CH <sub>4</sub> -CH <sub>4</sub>	Alternate	0-990	200-800	7	[759]
CO <sub>2</sub> -H <sub>2</sub>	Main	0-2000	200-350	4	[746]
CO <sub>2</sub> -CH <sub>4</sub>	Main	1-2000	200-350	4	[746]
CO <sub>2</sub> -CO <sub>2</sub>	Main	1-750	200-800	10	[760]
		1000-1800	200-350	6	[761]
		1000-1800	200-350	6	[762]
		2510-2850	221-297	3	[763]

*Continued on next page*

Table 13 – *Continued from previous page*

System	Folder	Spectral range (cm <sup>-1</sup> )	T range (K)	# of sets	Ref.	
N <sub>2</sub> –H <sub>2</sub>	Main	2850–3250	298	1	[763]	
		0–1886	40–400	10	[764]	
		0–450	70–200	14	[765]	
N <sub>2</sub> –N <sub>2</sub>	Main	0–550	210–300	10	[765]	
		0–650	310–400	10	[765]	
		1850–3000	301–363	5	[766]	
		2000–2698	228–272	5	[767]	
	Alternate	4300–5000	200–330	14	[740]	
		30–300	78–129	4	[768]	
	Main	1150–1950	193–353	15	[769]	
		7450–8491	296	1	[770]	
	O <sub>2</sub> –O <sub>2</sub>	Main	9091–9596	293	1	[771]
			10 512–11 228	293	1	[772]
12 600–13 839			296	1	[773]	
14 206–14 898			293	1	[774]	
15 290–16 664			203–287	4	[775]	
16 700–29 800			203–293	5	[775]	
Alternate			1300–1850	193–356	7	[776, 777]
			7583–8183	206–346	15	[771]
9060–9960			206–346	15	[771]	
10 525–11 125			206–346	15	[771]	
12 804–13 402			206–346	15	[771]	
14 296–14 806			206–346	15	[771]	
Main		1300–1850	193–356	7	[776, 777]	
	1850–3000	301–363	5	[766, 778]		
	2000–2698	228–272	5	[767, 778]		
	7450–8488	293	1	[770]		

*Continued on next page*

Table 13 – *Continued from previous page*

System	Folder	Spectral range (cm <sup>-1</sup> )	T range (K)	# of sets	Ref.
N <sub>2</sub> –Air	Alternate	12 600–13 840	296	1	[773]
		7583–8183	206–346	15	[771]
		12 804–13 402	206–346	15	[771]
	Main	1850–3000	301–363	5	[766, 778]
		2000–2698	228–272	5	[767, 778]
O <sub>2</sub> –Air	Main	4300–5000	200–330	14	[740]
		1300–1850	193–356	7	[776, 777]
		7450–8480	250–296	3	[770]
		9091–9596	293	1	[771]
		10 512–11 228	293	1	[772]
	Alternate	12 600–13 839	300	1	[773]
		12 990–13 220	298	1	[318]
		7583–8183	206–346	15	[771]
		9060–9960	206–346	15	[771]
		10 525–11 125	206–346	15	[771]
		12 802–13 402	206–346	15	[771]
		14 206–14 806	206–346	15	[771]
		1930–2830	250–350	11	[779]
N <sub>2</sub> –H <sub>2</sub> O	Main	1930–2830	250–350	11	[779]
N <sub>2</sub> –CH <sub>4</sub>	Alternate	0–1379	40–400	10	[780]
O <sub>2</sub> –CO <sub>2</sub>	Main	12 600–13 839	200–300	1	[781]

#### 4.2. Post-2019 updates and prospects for the future

#### 4.3. N<sub>2</sub>–N<sub>2</sub> rototranslational band

In the Karman et al. [748] effort, the Main folder rototranslational spectra for N<sub>2</sub>–N<sub>2</sub> were updated with the results of quantum mechanical lineshape

calculations from Karman et al. [782]. Also, the results of experimental measurements from Sung et al. [768] were provided in the Alternate folder. In the current edition, we updated the Main folder  $\text{N}_2\text{--N}_2$  CIA spectra with the slightly refined results of the semiclassical trajectory-based simulation performed in Chistikov et al. [765] at 34 temperatures between 70 and 400 K.

Basically, the trajectory-based approach developed in Ref. [765] relies on assumption that the collisional dynamics, as well as the interaction with the electromagnetic field, can be considered within the classical framework. On the one hand, the use of classical approximation allows then extension of this approach to the molecular systems, for which quantum consideration is presently unfeasible. On the other hand, immediately produced classical spectral profiles do not conform to the detailed balance principle [783], which is responsible for the striking asymmetry of the experimentally observed profiles. It is widely believed that this major defect of the classical approach can be approximately corrected through the use of the so-called desymmetrization procedure [783, 784]. The latter, however, is not unambiguously defined (e.g., discussion in Ref. [784]). The use of a semiempirically scaled variant of Egelstaff's procedure described by Frommhold [783] instead of the Schofield's procedure [785] adopted in Ref. [765] improved the agreement with the low-temperature measurements reported in Sung et al. [768].

Figure 34 shows the results of the theoretical calculations for the  $\text{N}_2\text{--N}_2$  rototranslational band and experimental measurements [768] at two representative temperatures. It is seen that, at least in the vicinity of the absorption peak, the trajectory-based results [765] refined with the use of Egelstaff's procedure demonstrate an improvement compared to the previous results of Karman et al. [782]. For the temperatures 78.3, 89.3, 109.6, and 129.0 K, the measured data at the peak exceed the Karman et al. [782] calculations by 18, 13, 12, and 10%, respectively. In contrast, the trajectory-based spectra underestimate that measured by 5, 3, 3, and 2%, respectively. Such a deviation, at least for temperatures in excess of 80 K, is not significant given a reported  $\pm 3\%$  uncertainty in the measured absorption. The measurements at 78 K appear to be suffering



from the systematic non-zero offset, therefore the discrepancy with theoretical results should be interpreted with caution. In the far wing, longward of 150  $\text{cm}^{-1}$ , irrespective of the temperature, neither of the calculations demonstrate perfect overall agreement. We have to note, however, that at 109.6 and 129.0 K the Karman et al. [782] calculations have an edge as far as the band wing is concerned.

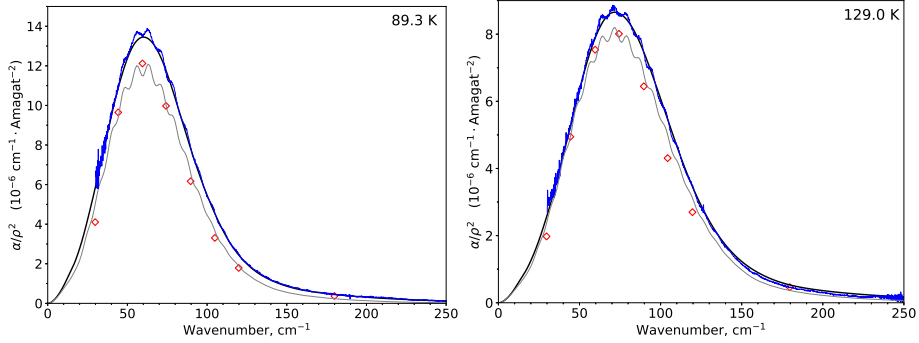


Figure 34:  $\text{N}_2\text{--N}_2$  collision-induced absorption spectra at two temperatures. The black curves indicate results from the trajectory-based calculation [765], the blue curves denote the experimental measurements [768], the red diamonds denote the results from the quantum-mechanical calculation [782], and the grey curves denote Borysow model spectra [786]. (For interpretation of the references to color in this figure legend, the reader is referred to the web version of this article.)

At millimeter wavelength range, Serov et al. [787] have recently shown that trajectory-based spectra issued from Chistikov et al. [765], as well as Borysow et al. model [786], are in good agreement with new resonator spectrometer measurements from 105 to 200 GHz and the results of previous experimental studies, e.g., Meshkov et al. [788]. The  $\text{N}_2\text{--N}_2$  data provided in the previous effort [748] were found to significantly underestimate absorption in the 105-200 GHz range due to the choice of interpolating procedure, which is imperative to simulate continuous frequency dependence since the calculations in Karman et al. [782] were carried out on a rare frequency grid.

#### 4.4. $\text{O}_2$ fundamental in $\text{O}_2\text{--N}_2$ , $\text{O}_2\text{--O}_2$ and $\text{O}_2\text{--Air}$

In the Richard et al. [747] effort, the  $\text{O}_2$  fundamental band  $\text{O}_2\text{--O}_2$  data were adopted from Baranov et al. [766]. These Main folder data remained unchanged

in the 2019 update [748]. Here, we include the data for the O<sub>2</sub> fundamental in O<sub>2</sub>–N<sub>2</sub> and O<sub>2</sub>–Air, which weren’t previously provided, and extend the data in the O<sub>2</sub>–O<sub>2</sub> Alternate folder as described below.

Laboratory measurements of the absorption by pure O<sub>2</sub> and O<sub>2</sub>–N<sub>2</sub> mixtures most recently have been reported in Thibault et al. [776], Orlando et al. [777], and Mate et al. [789]. The data from Mate et al. [789] will be retrieved from authors and considered for future inclusion in the database. Thibault et al. [776] and Orlando et al. [777] performed comprehensive FTIR studies at 193–293 K with 0.5 cm<sup>−1</sup> resolution and at 225–356 K with 1.0 cm<sup>−1</sup> resolution, respectively. Both sets of measurements for O<sub>2</sub>–O<sub>2</sub> were validated against the Baranov et al. [766] data. As seen in Fig. 35, Orlando et al. [777] data contain the most noise but extend to higher temperatures than those reported in Thibault et al. [776]. The absorption data from Thibault et al. [776] at 193–293 K and Orlando et al. [777] at 356 K converted to the HITRAN format are available in Main folder O<sub>2</sub>–N<sub>2</sub> and Alternate folder O<sub>2</sub>–O<sub>2</sub>. The Orlando et al. [777] data at 356 K was cast to the same frequency grid as was used in Thibault et al. [776] through cubic spline interpolation.

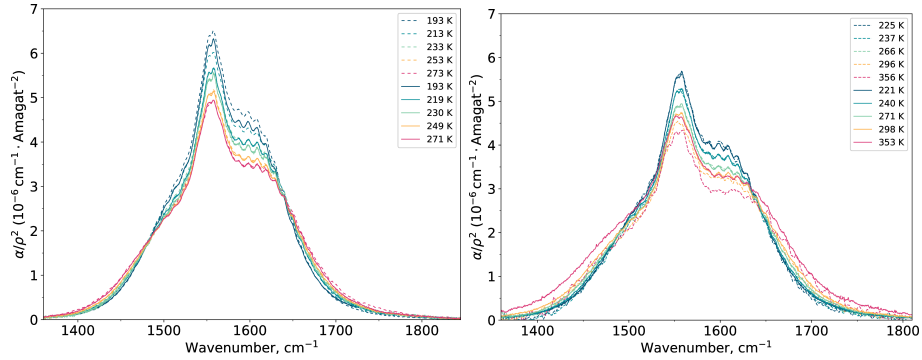


Figure 35: Overview of O<sub>2</sub>–O<sub>2</sub> data in the O<sub>2</sub> fundamental. Solid lines refer to the Baranov et al. [766] data, dashed lines refer to the Thibault et al. [776] data in the left panel and the Orlando et al. [777] data in the right panel, respectively.

Following the concept introduced in the HITRAN2016 update [15], we provided O<sub>2</sub>–Air data useful for applications for the Earth’s atmosphere. The data for O<sub>2</sub>–Air was represented as a sum of O<sub>2</sub>–O<sub>2</sub> and O<sub>2</sub>–N<sub>2</sub> continua taken with

79% and 21% weights corresponding to the oxygen and nitrogen abundances in the atmosphere. For consistency's sake, the  $\text{O}_2$ –Air cross-sections for each temperature are calculated based on the  $\text{O}_2$ – $\text{O}_2$  and  $\text{O}_2$ – $\text{N}_2$  data from the same source. Thibault et al. [776] data at 193–293 K and on Orlando et al. data at 356 K were taken to estimate the  $\text{O}_2$ –Air cross-sections. In order to reduce the noise, the Orlando et al. [777] data were smoothed using a simple moving average routine with the window size of  $15 \text{ cm}^{-1}$ . Figure 36 demonstrates that  $\text{O}_2$ –Air absorption data, despite being compiled from two sources, exhibit consistent temperature dependence.

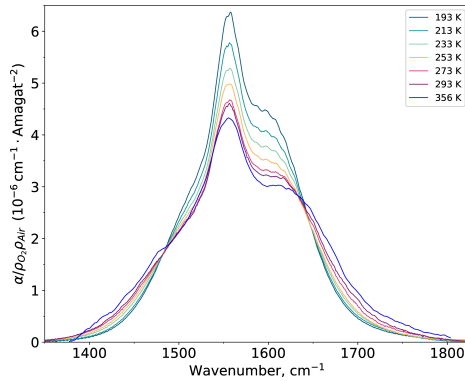


Figure 36: Overview of  $\text{O}_2$ –Air data. The data for 193–293K and 356K are derived from the Thibault et al. [776] and Orlando et al. [777] measurements, respectively.

#### 4.5. $\text{CO}_2$ –Ar rototranslational band

Argon is known to be the third most abundant gas in the Earth’s atmosphere, at 0.934 volume percents. It is more than twice as abundant as water vapor, and more than 20 times as abundant as carbon dioxide. Although largely inert in absorption, argon is capable of modifying radiative properties of other molecular species by virtue of weak intermolecular perturbation.

We include the  $\text{CO}_2$ –Ar rototranslational spectra issued from the trajectory-based simulation carried out in Ref. [756]. In these calculations, an array of up to 20 million classical trajectories was rendered through the solution of dynamical equations in Hamilton form in the laboratory frame of reference. The ensemble-averaged autocorrelation function of the induced dipole moment is ob-

tained from these simulations, and its Fourier transform yields the absorption spectrum. The contributions to CIA profile from the free/quasibound and true bound states were calculated separately using the same computational approach. The trajectory-based calculations were performed using *ab initio* potential energy and induced dipole surfaces obtained with the coupled-cluster (CCSD(T)) method.

The absorption spectra at millimeter wavelengths in the CO<sub>2</sub>–Ar mixtures have been recorded with a resonator spectrometer as is described in detail in Odintsova et al. [756]. These spectra were measured in a 105–240 GHz range at 297.3 K. An excellent agreement between reported experimental data and calculated profiles was achieved. In an earlier study, Oparin et al. [790] examined the CO<sub>2</sub>–Ar RT band using classical trajectories method and simplified potential energy and induced dipole surfaces. A thorough comparison of the data from Ref. [790] with the results of the recent trajectory-based simulation in Odintsova et al. [756] showed good agreement of both sets of calculated CIA spectra over the entire range of CO<sub>2</sub>–Ar RT band including the millimeter wavelength range. However, we consider the data from Ref. [756], which are based on *ab initio* potential energy and induced dipole surfaces, to be somewhat more precise. Moreover, the Odintsova et al. [756] data cover wider temperature range compared to the Oparin et al. data [790].

Overall, HITRAN CIA tabulates 21 spectra for CO<sub>2</sub>–Ar RT band from 200 K to 400 K with 10 K step. The temperature variation in the CO<sub>2</sub>–Ar RT bandshape is shown in Fig. 37. The contribution from true bound states manifests itself as a secondary peak in the 3–7 cm<sup>−1</sup> interval, which becomes more pronounced at lower temperatures.

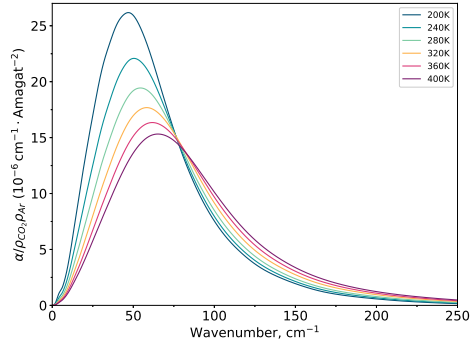


Figure 37: The temperature variation of the CO<sub>2</sub>–Ar CIA RT bandshape in the 200–400 K range.

#### 4.6. Outlook for the future

The CIA section of the HITRAN database underwent a substantial update in 2019 [748] featuring improvements to the existing data, extension of temperature and spectral ranges, and addition of new collisional pairs. Nevertheless, there is a growing demand to further improve and extend CIA data in HITRAN. This update represents a small revision of the CIA section. For the next update of the CIA section, data from a number of recent papers will be evaluated, such as measurements and semiempirical models of CO<sub>2</sub>–H<sub>2</sub> within RT band [745, 791, 792] and (1-0) band of H<sub>2</sub> [793] and CH<sub>4</sub>–CO<sub>2</sub> within RT band [745, 791, 792], results of trajectory-based simulation of CH<sub>4</sub>–N<sub>2</sub> RT band [794], measurements of  $a^1\Delta_g(\nu = 1) \leftarrow X^3\Sigma_g^-(\nu = 0)$  O<sub>2</sub>–CO<sub>2</sub> [795] and  $a^1\Delta_g \leftarrow X^3\Sigma_g^-$  O<sub>2</sub>–O<sub>2</sub> [796] CIA bands.

### 5. Aerosol refractive indices

HITRAN2020 contains refractive indices in the visible, infrared, and millimeter spectral ranges of many types of materials which make up cloud, aerosol particles, and planetary surfaces. The indices apply to materials found in the Earth’s atmosphere and surface, and candidate exoplanet atmospheres. Knowing the real and imaginary indices of particles, as a function of wavelength, and the particle size distribution of cloud or aerosol particles, one can calculate

the extinction, scattering, and absorptive properties of the atmospheric particles [797]. These particle optical depths add to gas optical depths, which in combination, determine the wavelength dependent total optical depths of an atmosphere. The interpretation of remote-sensing retrievals of gaseous species is limited frequently by how well one can separate gaseous opacity from that of clouds and aerosols. Clouds and aerosols also take part in chemical reactions in both the liquid and solid phases, with heterogeneous chemistry on Polar Stratospheric Clouds (PSCs) being a particularly important example [798]. Table 14 lists the HITRAN2020 indices. The listing is comprised of main and supplementary data sets. Several of the supplementary datasets are older, correspond to a limited number of wavelengths, or are not complete, e.g., just the imaginary component is tabulated. Several of the supplementary datasets are for similar materials in the main set and can be used to compare indices from different laboratories. Table 14 begins with the venerable set of indices compiled at the Air Force Cambridge Research Laboratory in 1987 [799], which includes a wide variety of materials: Water, ice, sodium chloride, sea salt, water-soluble aerosol, ammonium sulfate, carbonaceous aerosol, volcanic dust, sulfuric acid, meteoric dust, quartz, hematite, and sand. Table 14 then lists indices of supercooled water, ice at various temperatures, materials which comprise PSC particles, Saharan dust, volcanic ash, secondary organic aerosol (SOA), brown carbon, biomass fire particles, flame particles, surface minerals, Titan tholins, and candidate exoplanet atmospheric particulates.

Table 14: Refractive indices included in HITRAN2020.

	Measurement	
Compound	Specifics	Reference
Water, ice, sodium chloride, sea salt, water soluble aerosol, ammonium sulfate, carbonaceous aerosol, volcanic dust, sulfuric acid, meteoric dust,		

*Continued on next page*

Table14 – *Continued from previous page*

Compound	Measurement	Reference
	Specifics	
quartz, hematite, sand	Room temperature, 0.2–40 $\mu\text{m}$	[799]
Water	27°C, 10–5000 $\text{cm}^{-1}$	[800]
Supercooled water	238 – 269 K, 1100 – 4500 $\text{cm}^{-1}$	[801]
Ice	266 K, 0.04 $\mu\text{m}$ – 2 m	[802]
Ice	130 – 210 K, 800 – 4000 $\text{cm}^{-1}$	[803]
Sulfuric acid ( $\text{H}_2\text{SO}_4/\text{H}_2\text{O}$ )	215 K, 499–6996 $\text{cm}^{-1}$	[804]
Sulfuric acid ( $\text{H}_2\text{SO}_4/\text{H}_2\text{O}$ )	273 – 298 K, 400 – 7500 $\text{cm}^{-1}$	[805]
Nitric acid ( $\text{HNO}_3$ )	223 – 293 K, 450 – 6500 $\text{cm}^{-1}$	[806]
Ternary Solution ( $\text{H}_2\text{SO}_4/\text{H}_2\text{O}/\text{HNO}_3$ )	203 – 293 K, 450 – 6500 $\text{cm}^{-1}$	[806]
NAD	160–190 K, 700–4700 $\text{cm}^{-1}$	[807]
NAT	160 K, 711–4004 $\text{cm}^{-1}$	[808]
Amorphous nitric acid (NAM, NAD, NAT)	153 K, 482–7000 $\text{cm}^{-1}$	[809]
NAM	179 K, 482–6002 $\text{cm}^{-1}$	[809]
NAD	184 K, 482–6981 $\text{cm}^{-1}$	[809]
aNAT	181 K, 482–6989 $\text{cm}^{-1}$	[809]
bNAT	196 K, 482–6364 $\text{cm}^{-1}$	[809]
Saharan dust	0.30 – 0.95 $\mu\text{m}$	[810]
Volcanic ash	0.45 – 25 $\mu\text{m}$	[811]
Volcanic ash	690 – 32500 $\text{cm}^{-1}$	[812]
SOA	0.23 – 1.2 $\mu\text{m}$	[813]
SOA	0.23 – 1.2 $\mu\text{m}$	[814]
Organic acids (Oxalic, malonic, succinic, pinonic, pyruvic, phthalic)	0.25 – 1.1 $\mu\text{m}$	[815]
Brown carbon	0.2 – 1.2 $\mu\text{m}$	[816]
Burning vegetation	525–5000 $\text{cm}^{-1}$	[817]
Burning vegetation	0.35 – 1.5 $\mu\text{m}$	[818]
Carbon flame	0.4 – 0.7 $\mu\text{m}$ , 25 – 600°C	[819]

*Continued on next page*

Table14 – *Continued from previous page*

Compound	Measurement	Reference
	Specifics	
Flame soot	0.2 – 38 $\mu\text{m}$	[820]
Minerals (clay, illite, kaolin, montmorillonite)	2.5 – 200 $\mu\text{m}$	[821]
Minerals (granite, montmorillonite)	5 – 40 $\mu\text{m}$	[822]
Titan tholins	0.02 – 920 $\mu\text{m}$	[823]
Titan tholins	0.2 – 1 $\mu\text{m}$	[824]
Titan tholins	2.5 – 25 $\mu\text{m}$	[825]
KCl	0.22 – 166 $\mu\text{m}$	[821]
ZnS	0.22 – 166 $\mu\text{m}$	[821]
SiO <sub>2</sub> (amorphous)	6.6 - 487 $\mu\text{m}$ , 10 – 300 K	[826]
SiO <sub>2</sub> (crystalline)	6.25 $\mu\text{m}$ – 10 $\mu\text{m}$ , 300 – 928 K	[827]
Al <sub>2</sub> O <sub>3</sub>	7.8 – 200 $\mu\text{m}$	[828]
FeO	0.2 – 500 $\mu\text{m}$	[829]
CaTiO <sub>3</sub> (Perovskite)	2.0 – 500 $\mu\text{m}$	[830]
Fe <sub>2</sub> O <sub>3</sub>	0.1 – 1000 $\mu\text{m}$	[831]
Fe <sub>2</sub> SiO <sub>4</sub> (Fayalite)	0.4 – 10 $\mu\text{m}$	[832]
Fe <sub>2</sub> SiO <sub>4</sub> (Fayalite)	2 $\mu\text{m}$ – 10 $\mu\text{m}$	[833]
MgAl <sub>2</sub> O <sub>4</sub> (annealed)	1.6 – 6825 $\mu\text{m}$	[834]
MgAl <sub>2</sub> O <sub>4</sub> (natural)	2.0 $\mu\text{m}$ – 10 $\mu\text{m}$	[834]
Mg <sub>2</sub> SiO <sub>4</sub>	0.19 – 948 $\mu\text{m}$	[835]
MgSiO <sub>3</sub>	0.2 - 500 $\mu\text{m}$	[835]
TiO <sub>2</sub> (Rutile)	0.47 – 36.2 $\mu\text{m}$	[836]
TiO <sub>2</sub> (Anatase)	2.0 – 5843 $\mu\text{m}$	[836]
TiO <sub>2</sub> (Brookite)	2.0 – 5843 $\mu\text{m}$	[837]
Supplementary		
Water and Ice	0.67 – 2.5 $\mu\text{m}$ , imaginary	[838]
Saharan Dust	0.35 -0.65 $\mu\text{m}$	[839]

*Continued on next page*



Table14 – *Continued from previous page*

Compound	Measurement	Reference
	Specifics	
SOA	0.375 and 0.632 nm, various radical sources	[840]
SOA	0.532 nm, various cases	[841]
Diesel Soot	0.45 – 10 $\mu\text{m}$	[821]
Sulfuric acid ( $\text{H}_2\text{SO}_4/\text{H}_2\text{O}$ )	200–300 K, 825–4700 $\text{cm}^{-1}$	[842]
Sulfuric acid ( $\text{H}_2\text{SO}_4/\text{H}_2\text{O}$ )	183– 293 K, 2 – 23 $\mu\text{m}$	[843]
Nitric acid ( $\text{H}_2\text{SO}_4/\text{HNO}_3$ )	213–293 K, 2 – 23 $\mu\text{m}$	[843]
Sulfuric acid ( $\text{H}_2\text{SO}_4/\text{H}_2\text{O}$ )	Room temperature, 75 and 90% $\text{H}_2\text{SO}_4$	[844]
Nitric acid ( $\text{H}_2\text{SO}_4/\text{HNO}_3$ )	220 K, 754–4700 $\text{cm}^{-1}$	[845]
Nitric acid ( $\text{H}_2\text{SO}_4/\text{HNO}_3$ )	Room temperature, 2 – 40 $\mu\text{m}$	[846]
Sulfuric and Nitric acids	Room temperature, 6 – 11 $\mu\text{m}$	[847]
Titan organic haze	0.525 $\mu\text{m}$	[848]

As discussed in the Bohren and Huffman [849] text on light scattering and Mie calculations, the complex refractive index  $m$  is a function of wavelength, with real  $m_{real}$  and imaginary  $m_{imag}$  components.

$$m = m_{real} + im_{imag} \quad (3)$$

A plane light wave of wavelength  $\lambda$  is attenuated along the propagation  $x$  axis according to

$$E = E_0 \exp(-2\pi m_{imag} x / \lambda) \exp(i2\pi m_{real} x / \lambda - i2\pi ct / \lambda) \quad (4)$$

with time  $t$  and the speed of light  $c$ . The imaginary refractive index  $m_{imag}$  therefore determines the amount of light absorption in a medium, attenuating the light intensity by  $\exp(-4\pi m_{imag} x / \lambda)$  along a path of distance  $x$ .

Exoplanet atmosphere particles are produced at a variety of temperatures from 700 K (e.g., ZnS) to 1725 K (e.g.,  $\text{SiO}_2$ ). HITRAN2020 includes most of the

condensates tabulated by Wakeford and Sing [850], who studied hot Jupiter exoplanet atmospheres. Dr. Harrold Mutschke of the Friedrich Schiller University Jena kindly provided the exoplanet indices to HITRAN. Additional exoplanet material indices not listed in Table 14 are accessible from the extensive Jena web site (<http://www.astro.uni-jena.de/Laboratory/OCDB/index.html>). New indices in HITRAN2020 include the secondary organic aerosol (SOA) indices of Liu et al. [813], [814] and Dingle et al. [840], volcanic ash indices of Deguine [812], and additional indices of Titan tholins (Imanaka et al. [825]). While primary organic aerosols are emitted into the troposphere directly by the biosphere, SOA is produced by a series of gas-phase organic chemistry reactions. The Liu et al. [813], [814] indices (from 0.23 to 1.2  $\mu\text{m}$ ) and the Dingle et al. [840] indices (at 532 and 1064 nm) correspond to several sets of indices, each of which corresponds to a specific set of hydrocarbon, hydroxyl radical sources, and NO initial laboratory conditions. SOA comprises an important fraction of tropospheric aerosols. An example of the new volcanic ash indices is presented in Fig. 5.1, which displays the volcanic ash indices of Deguine et al. [812]. Due to the impact upon civil aviation by the Icelandic Eyjafjallajökull eruption in 2010, there is interest in the optical properties of dust emissions from active volcanoes. Figure 38 displays the indices for six volcanoes, including Eyjafjallajökull. There is a sizable difference (by a factor of 1.5) in the imaginary indices near 10.6  $\mu\text{m}$  for the Etna (Italy) and Grímsvötn (Iceland) volcanoes, and thus for the same particle size distribution, a sizable difference in the extinction spectra (a factor of 1.6 at 10.6  $\mu\text{m}$ ).

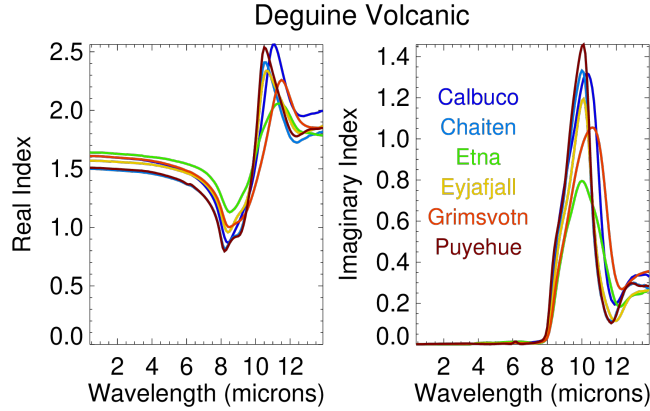


Figure 38: Variations in the real and imaginary indices in volcanic samples from six volcanoes [812].

HITRAN2020 extends the HITRAN-RI program [851] that resides on the HITRAN website, by including a version of the program written in Python. HITRAN-RI is also written in the IDL (Interactive Design Language) and FORTRAN 90 programming languages, and all three versions apply the Bohren-Huffman [849] Mie code. The FORTRAN 90 version has been changed to read in ASCII files for compilation ease purposes. All programs and subdirectories are bundled together in a single tar file. In all three versions of the program, the user edits the directory pathnames in the `directory.dat` ASCII file, specifying the subdirectories that have the input data sets and the output subdirectory to which files are written to. One then examines the `indices.dat` ASCII file to determine which material to work with. The editing of the `work.dat` file just requires simply replacing integers and floating-point numbers with new values. The wavelength range, and the particle size distribution, are also specified in the `work.dat` file. The use of the `.dat` files allows the user to specify the HITRAN-RI calculations without having to modify the source code. The HITRAN-RI program then calculates optical property spectra of extinction, scattering, absorption, single scattering albedo, and the asymmetry parameter. The IDL version of HITRAN-RI generates output postscript and NetCDF files of the input in-

dices, particle size distribution, and wavelength dependent optical properties. As an instructional aid, test cases can be run. PDF versions of the original reference papers are contained in a subdirectory, while the refractive indices are stored in subdirectories in ASCII and NetCDF formats. The user can edit the `work.dat` file to instruct the program to read in user-specified refractive indices and/or the particle size distribution. Since all of the source code is fully accessible, HITRAN-RI can be modified as desired by the user.

## 6. Global data and software

### 6.1. Database structure and interface

The software providing an online interface to the HITRAN database at <https://hitran.org>, *HITRANonline*, has undergone a series of improvements and minor modifications since its release in 2015 [50]. In addition to bug-fixes and security patches, the entire code base was ported to Python 3 in 2019, using Django 2 as its web framework. At the same time the web server was configured to use the HTTPS protocol for secure communication with client computers. Errors in the HDF-5 output format were corrected and compatibility with the major web browsers on both Windows and Unix-like operating systems improved.

To access the database, *HITRANonline* requires users to register for an account by providing a name and using a valid email address. An ongoing inconvenience has been the large number of automated bots signing up fake accounts with the website that consequently required removal. This has been mitigated by the introduction of a question on the registration page which is found to be difficult to parse by a bot but intended to be easy for humans to answer correctly. The question is currently “1 + two”; for the avoidance of doubt, the correct answer to this question is “3” or “three”.

A number of video tutorials (<https://hitran.org/videos/>) have been created to guide users through the main aspects of the database and demonstrate how to navigate the website and make queries in different formats. These tu-

torials have proven to be very helpful to new users and on aggregate they have been watched over 8200 times so far.

Recently, a new automated referencing system has been developed and implemented as part of the HITRAN project to provide consistent, accurate and detailed bibliographies for every source of data in the HITRAN database. Administrators using this system can obtain the complete bibliographic entry for the article they wish to cite by entering only its unique digital object identifier (DOI). The referencing program, which is available as open source software, is described by Skinner et al. [852]. It provides a convenient, customizable bibliographic system to allow database administrators to implement bibliographies in their database systems more efficiently and with fewer human errors.

## 6.2. *HAPI2*

The first generation of HITRAN Application Programming Interface (HAPI) [51] has proven to be a convenient tool for acquiring and working with HITRAN data. The HAPI library provided a means of downloading and filtering the spectroscopic transitions for molecules provided by the *HITRANonline* [50] web server, using a range of partition sums and spectral line parameters. A significant feature of HAPI was the ability to calculate absorption coefficients based on the line-by-line spectroscopic parameters. For more detailed description of this software library, we refer readers to the dedicated paper [51] and corresponding user manual available online (<https://hitran.org/hapi>).

Although the first generation of HAPI allows users to build new functions, it does not have the functionality to make use the whole range of spectroscopic data currently available in the HITRAN database. For instance, the first version of the REST-API used by HAPI only allowed line-by-line data to be downloaded. For this reason, an extended version of HAPI (with greater functionality) is provided as part of HITRAN2020. This extended version, named “HAPI2”, includes all the functionality of HAPI but with a new Python library and has been designed to be backward-compatible. To take advantage of the more advanced features in the “second generation” extension library, users will

be required to upgrade to HAPI2.



Figure 39: Sample JSON response for the REST API query requesting molecule information, with an additional restriction imposed on the HITRAN ID value. The JSON fields contain the information on the molecule entry with the id=1 (water vapor).

One main feature of HAPI2 will be the ability to consider more objects available for downloading. This essentially means users will now be able to access the vast library of absorption cross-sections, CIA and more. This was achieved by revisiting the HITRAN server's REST API. A new version is able to access the information for a number of entities available in HITRAN. Among these entities are molecule information, reference sources, line-by-line transitions, monomer and collision-induced absorption cross-sections and metadata on line parameters. An example of the REST API query for the water molecule and corresponding JSON response are shown in Fig. 39. Users should note that, in order to be able to query the new REST API, a valid API key is required in the request. An API key is a unique string identifier, which can be generated

in the HITRAN*online* user profile by pressing the button “generate API key”, as shown in Fig. 40.

**HITRANonline**

Home Data Access Documentation Conferences

User Profile for John Doe

To update your profile, please edit the following fields.  
The fields in **bold text** are required.

Title:

**First Name:**  *i.e. given name, prénom*

Middle Initials:

**Last Name:**  *i.e. surname, family name, nom*

Affiliation:  *e.g. University, institute, company or agency*

Email address:  (email)

API Key:

Figure 40: An API key is required to make use of the full querying capabilities of HAPI2. Users can generate a personal API key from their HITRAN*online* user profile at [www.hitran.org](http://www.hitran.org) by clicking “Generate API key”. The resulting API key will be displayed in the location indicated in the screenshot.

Secondly, for applications that require numerous transitions to be considered in absorption coefficient calculations (such as at high-temperatures), the speed of calculation is of paramount importance. Although the first generation of HAPI [51] contained some Numpy-based optimizations [853] it lacked the means for fast cross-section computation. In HAPI2, efficient coding for HT and SDV profiles [73, 854, 855] that makes use of the “Just-in-time” compilation approach, has provided a significant speed increase for computations.

In addition, among the prominent features of HAPI2 is accounting for the full line-mixing. Following the work of Hashemi et al. [161], the latest versions (starting from v1.1) of HAPI [51] can account for line-mixing effects through the implementation of the first-order Rosenkranz line-mixing parameters  $Y$  [230] into the Hartmann-Tran profile for the  $\text{CO}_2$  molecule. Despite the advantages of the first-order approach (e.g., reduced number of collisional quantities and fast computations of the profiles), it fails to model the absorption for regions where

lines are dense and strongly affected by line-mixing, such as CO<sub>2</sub> Q-branches. The HAPI2 extension includes the Python version of the line-mixing code by Lamouroux et al. [166] with the account of the corrections made by Hashemi et al. [161]. Despite the structure of the Python version, it has essentially the same structure as the FORTRAN version [166] (and references therein), the major difference is that the database files are no longer provided. They will be constructed from the code locally by the users, as a preliminary step of the first CO<sub>2</sub> line-mixing calculation. If the files were already built, this step will not be executed by the code, except if it is explicitly asked by the user.

As was the case for HAPI [51], the HAPI2 extension stores the downloaded files locally. Thus, the final prominent feature of HAPI2 is the ability to make use of the fast and flexible relational database on these local files. This gives users the ability to perform data mining on the stored sets of molecules, references, line parameters, and cross-sections, including user-supplied data sets. The data scheme used in this relational engine is an extension of the relational scheme constructed by Hill et al. [49]. In the HAPI2 implementation, this scheme was created using the SQLAlchemy (<https://www.sqlalchemy.org/>) library which provides back-ends for many existing database management systems such as SQLite, MySQL, PostgreSQL, and more. HAPI2 uses SQLite as the default database back-end. The back-ends in HAPI2 use the Object Relational Mapping (ORM) technique to connect with the low-level database. Some of the data filtering is available through the REST API on the server side (e.g., setting the wavenumber range for transitions and specifying the set of isotopologues). Nevertheless, the full capability of the data filtering can be done locally by the means of the standard SQLAlchemy ORM methods.

The HAPI2 extension is currently available on the Github repository (<https://github.com/hitranonline/hapi2>) as well as in the Python Package Index. More complete description of the HAPI2 extension library will be described in a separate paper.



### 6.3. HAPIEST

The HITRAN Application Programming Interface and Efficient Spectroscopic Tools (HAPIEST) is a joint project which started in the Fall of 2017 as a collaboration between the HITRAN team and the State University of New York at Oswego. The purpose of HAPIEST is to simplify usage of HAPI to work efficiently with *HITRANonline* and to allow users who are not familiar with Python to access the spectroscopic data offered by HITRAN.

HAPIEST provides a cross-platform graphical user interface that gives access to the basic features of HAPI (such as data fetching and filtering ), as well as calculating and plotting spectral functions (absorption coefficients, and transmittance, absorption, and radiance spectra). Moreover, HAPIEST provides access to most of the controls that are involved in spectral filtering and simulation, and is distributed both as binary and source code. The most recent version of the source code can be found on Github (<https://github.com/hitranonline/hapiest>), as well as the most recent binary versions (<https://github.com/hitranonline/hapiest/releases>).

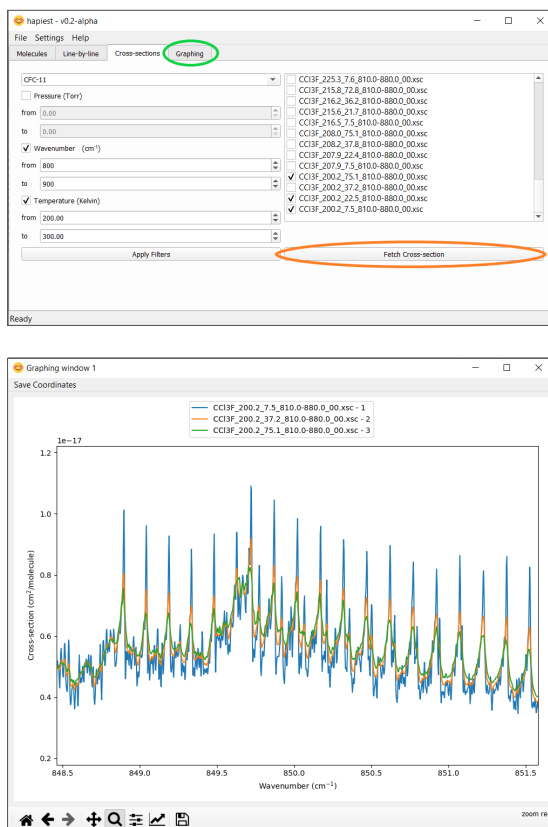


Figure 41: Screenshots of the graphical user interface of HAPIEST. The upper window displays the tab where absorption cross-section spectra from HITRAN*online* can be queried and filtered, then downloaded using the “Fetch cross-section” button (circled orange). In this example, three absorption cross-sections of CFC-11 ( $\text{CCl}_3\text{F}$ ) with different pressures have been selected by filtering the available CFC-11 absorption cross-sections between 800–900  $\text{cm}^{-1}$  and 200–300 K. Clicking the “Graphing” tab (circled green) allows users to create a plot of their chosen cross-section spectra. The same three CFC-11 cross-sections have been plotted in the lower window using the graphing functionality of HAPIEST. Here, users are able to adjust their plot using the tools on the lower left of the window (such as by zooming to compare spectral regions) and the results can be saved.

Using the HAPI and HAPI2 libraries, HAPIEST can retrieve the spectroscopic line-by-line data for any molecule or isotopologue in HITRAN. There are currently three functionalities provided in HAPIEST for line-by-line data: viewing, graphing, and data selection. The “view” feature allows line-by-line data to be viewed in a spreadsheet-like widget. This feature automatically paginates tables to save on system resources, but this page-length can be changed

in the user-configurable settings. One major feature of HAPIEST is the graphing capability. HAPIEST is able to display the line-by-line data in graphical form by calculating absorption coefficients, as well as absorption, transmittance, and radiance spectra, with a variety of instrumental functions and line profiles. As part of the HAPIEST functionality, users are able to filter (e.g., by vibrational band) and plot results separately. When bands are plotted, HAPIEST creates a legend for band graphs which will display upper and lower quanta of each band. In addition, the absorption cross-section data can also be downloaded from the HITRAN*Online* web server and plotted by HAPIEST. Multiple absorption cross-sections can be plotted on the same axes and compared, as shown in Fig. 41 for three different temperature-pressure sets of CFC-11.

#### 6.4. Total Internal Partition Sums (TIPS)

Total internal partition sums (TIPS) are calculated for all new isotopologues ( $^{33}\text{S}^{16}\text{O}_2$ ,  $^{16}\text{O}^{32}\text{S}^{18}\text{O}$ ,  $^{15}\text{N}^{16}\text{O}_2$ ,  $^{16}\text{O}^{13}\text{C}^{34}\text{S}$ ,  $^{12}\text{C}_2\text{H}_5\text{D}$ ) and molecules ( $\text{SO}$ ,  $\text{CH}_3\text{F}$ ,  $\text{GeH}_4$ ,  $\text{CS}_2$ ,  $\text{CH}_3\text{I}$ ,  $\text{NF}_3$ ) that have been introduced to the database for HITRAN2020 and were not included as part of TIPS2017 [178]. In addition, partition sums of ozone have been revised to eliminate discrepancies noted in Birk et al. [198]. The TIPS are calculated in one-degree intervals from 1 K until the convergence of each partition sum (which is different for each molecule) and will be provided as an update to TIPS2017, which was used for all isotopologues in the previous edition of HITRAN [15]. The full TIPS for each new isotopologue and molecule will be made available through the HITRAN*Online* website (<https://hitran.org/docs/iso-meta/>) where the corresponding partition sum at 296 K,  $Q(296\text{ K})$ , is provided.

## 7. Conclusions and Future work

This article introduces and details the improvements and expansion of the new HITRAN2020 database release with respect to its predecessor, HITRAN2016 [15]. These improvements include the increased quality of reference spectral parameters, expansions of spectral and dynamic ranges, and new parametrizations

and capabilities. The addition of new molecules and isotopologues or new collisional complexes is justified and explained. Non-Voigt line shapes continue to be expanded in the database. In this edition, important atmospheric absorbers that include CO<sub>2</sub>, N<sub>2</sub>O and CO, now have not only Voigt but also speed-dependent Voigt parameters (for both air and self broadening) for every transition of these molecules in the database. This way, the capabilities of HITRAN are enhanced, and also the implementation by the users is simplified. In addition, many molecules now have line-shape parameters due to ambient water vapor pressure provided for all transitions. There are also substantially more molecules with parameters associated with the pressure of “planetary” gases: H<sub>2</sub>, He and CO<sub>2</sub>. Experimental cross-sections, aerosols, and collision induced absorption datasets have also been revised and extended.

Additionally, HITRAN continues to evolve in terms of structure and scope. This evolution includes expanded capabilities and documentation for the online server and restructuring and optimization of HAPI, which now also has a GUI.

The compilation is free and can be accessed through [www.hitran.org](http://www.hitran.org).

### *7.1. Future work*

#### *7.1.1. Double-power-law (DPL) representation of the temperature dependencies of the line-shape parameters*

Recently, a new scheme of representing the temperature dependencies of the line-shape parameters was adopted in HITRAN [119]. The approach approximates the temperature dependencies with double-power-law (DPL) function [118]. The scheme adopted in HITRAN [119] is very general and applicable also to beyond-Voigt cases. It should be noted, however, that for many molecular systems, not all the collisional effects are important at the considered accuracy level and, for a given experimental temperature range, a simple single-power law suffices. In such cases, either a single-power law and a smaller number of line-shape parameters will be stored in HITRAN or the full DPL parametrization will be adopted but some of the coefficients will be set to zero.

	Coefficient 1	Coefficient 2	Exponent 1	Exponent 2
$\gamma_0(T)$	$g_0$	$g'_0$	$n$	$n'$
$\delta_0(T)$	$d_0$	$d'_0$	$m$	$m'$
$\gamma_2(T)$	$g_2$	$g'_2$	$j$	$j'$
$\delta_2(T)$	$d_2$	$d'_2$	$k$	$k'$
$\tilde{\nu}_{opt}^r(T)$	$r$	$r'$	$p$	$p'$
$\tilde{\nu}_{opt}^i(T)$	$i$	$i'$	$q$	$q'$

Table 15: A list of the 24 coefficients that define the DPL parametrization for all the six line-shape parameters: pressure broadening and shift ( $\gamma_0$  and  $\delta_0$ ), speed dependence of pressure broadening and shift ( $\gamma_2$  and  $\delta_2$ ), real and imaginary parts of the complex Dicke parameter ( $\tilde{\nu}_{opt}^r$  and  $\tilde{\nu}_{opt}^i$ ).

In the most general case, the DPL parametrization involves 24 coefficients, i.e., four DPL coefficients per each of the six line-shape parameters, see Table 15. The explicit formulas for the DPL temperature dependencies are following [119]:

$$\begin{aligned}
\gamma_0(T) &= g_0(T_{\text{ref}}/T)^n + g'_0(T_{\text{ref}}/T)^{n'}, \\
\delta_0(T) &= d_0(T_{\text{ref}}/T)^m + d'_0(T_{\text{ref}}/T)^{m'}, \\
\gamma_2(T) &= g_2(T_{\text{ref}}/T)^j + g'_2(T_{\text{ref}}/T)^{j'}, \\
\delta_2(T) &= d_2(T_{\text{ref}}/T)^k + d'_2(T_{\text{ref}}/T)^{k'}, \\
\tilde{\nu}_{opt}^r(T) &= r(T_{\text{ref}}/T)^p + r'(T_{\text{ref}}/T)^{p'}, \\
\tilde{\nu}_{opt}^i(T) &= i(T_{\text{ref}}/T)^q + i'(T_{\text{ref}}/T)^{q'},
\end{aligned} \tag{5}$$

where  $T_{\text{ref}} = 296$  K.

The DPL parametrization replaces the four temperature ranges (4TR) representation introduced in 2016 [165]. It was shown in Ref. [119] that the DPL parametrization requires fewer parameters, gives better accuracy and is more self-consistent than 4TR. In HITRAN2020, the full structure of the DPL parametrization is populated for the cases of self- and He-perturbed  $\text{H}_2$  lines.

### 7.1.2. Water-vapor continuum

In the last 50 years, HITRAN has made enormous progress toward being a complete source for all atmospheric absorption parameters. Nevertheless, it has not yet expanded to include continuum absorption by water vapor. This gap in

the database will be filled in forthcoming updates to HITRAN2020.

Absorption and emission by the water-vapor continuum play an important role in radiative processes in the terrestrial atmosphere and have an appreciable impact on weather and the climate of the Earth [856–858]. There is still uncertainty with respect to the physical phenomena behind either the self (interactions of water vapor with other water vapor molecules) or the foreign (interaction of water vapor with dry air molecules) continuum, with bound dimers, quasi-stable dimers, and monomer far wings possibly contributing to the total absorption. Theoretical analysis has not yet been able to disentangle the relative contributions of these phenomena as a function of wavenumber and temperature. This is still the subject of an active debate (e.g., see reviews [859, 860]).

The next version of HITRAN will include the updated and well documented MT\_CKD water-vapor continuum model (Mlawer-Tobin-Clough-Kneizys-Davies) [857], which is widely used in atmospheric radiative-transfer codes. The MT\_CKD model is based on a combination of analyses of field measurements, lab measurements, and semi-empirical model calculations and is a descendant of the CKD continuum model (Clough-Kneizys-Davies) [861] developed in the 1980s. The goal of these models is to provide a representation of smoothly varying water-vapor absorption that, once added to the absorption due to water vapor lines (cut off at  $25\text{ cm}^{-1}$  from line center), best agrees with high-quality observations and theoretical calculations of the total water-vapor absorption. In many spectral regions, observations from different studies provide conflicting information on the strength of the water-vapor continuum, and a judgment must be made as to which source should provide the basis for the coefficients in MT\_CKD. The overall perspective in developing the MT\_CKD water-vapor continuum is consistent with that of HITRAN – regular updates to the spectroscopic parameters in order to agree with studies considered to be most accurate.

The importance of the water-vapor continuum and aforementioned discrepancies have sparked a number of new laboratory measurements in different spectral regions [859, 862–876]. While many of these experiments show a decent level

of consistency with MT\_CKD (see discussion in Ref. [869], for instance) they nevertheless have warranted revisions to the model. For example, MT\_CKD recently incorporated the results of numerous lab measurements in near-infrared windows by the group of Campargue at Grenoble, which provided water-vapor continuum absorption coefficients with stated uncertainties lower than had previously been reported in these regions. In some windows, these continuum values disagreed by more than an order of magnitude with previous measurements (see, for instance, the recent review [877]). These improvements to the MT\_CKD self and foreign continua due to the measurements in Grenoble [869–874, 876] have made a noticeable positive impact on the retrievals of carbon dioxide with the OCO-2 mission [314]. Uncertainties still remain, however. The “BPS” water-vapor continuum model [878] has different absorption coefficients than MT\_CKD in certain near-infrared windows and other regions, leading to different results in the atmosphere.

Other recent updates to MT\_CKD include the far-infrared foreign continuum, which was modified based on an analysis of field campaign observations [121]. Subsequent studies [879, 880] have provided validation for these far-infrared absorption coefficients. The most recent revision was MT\_CKD\_3.5, which improved the continuum in the microwave (self and foreign) and far-infrared (self) based on analyses of field and lab experiments (see, e.g., Ref. [881]). Ongoing analyses are expected to lead to improvements in the MT\_CKD model in the infrared window (self and possibly foreign) and water vapor  $\nu_2$  band (foreign).

## 8. Acknowledgements

The global COVID-19 pandemic has impacted the working conditions and lives of everyone involved in the production of HITRAN2020. In recognition of the difficult conditions of the previous year, we would like to extend our sincere gratitude to all researchers and collaborators who have been able to contribute to this edition.

Development of the HITRAN2020 database and associated tools was supported through the NASA grants NNX17AI78G, NNX16AG51G and 80NSSC20K0962.

We gratefully acknowledge the many researchers who provided data, experimental and/or theoretical: Ad van der Avoird, Yury Baranov, Chris Benner, Yury Borkov, Christian Boulet, Daniil Chistikov, Malathy Devi, Randika Dondangodage, Anna Dudaryonok, Samuel Gordon, Gerrit Groenenboom, Magnus Gustafsson, Adrian Hjältén, Shuiming Hu, Christof Janssen, Aleksandra Kyuberis, Julien Lamouroux, Nina Lavrentieva, Daniel Lisak, Anwen Liu, Sergei Lokshtanov, Marie-Alién Martin-Drumel, Harrold Mutschke, Laurence Régalia, Shanelle Samuels, Mary-Ann Smith, Alexander M. Solodov, Alexander A. Solodov, Ryan Thalman, Mikhail Tretyakov, Yixin Wang, Edward H. Wishnow, Wim van der Zande, Rainer Volkamer, Shanshan Yu, Nikolai Zobov.

Those who provided independent validations are also acknowledged: Matthew Alvarado, Juyeson Bak, Natasha Batalha, Chris Boone, Ryan Cole, Sergio DeSouza-Machado, Xiong Liu, Emile Medvedev, Clayton Mulvihill, Fabiano Oyafuso, Erwan Pannier, Vivienne Payne, Olivier Pirali, Greg Rieker, Keith Shine, Clara Sousa-Silva, Kang Sun, Boris Voronin.

The researches from the V.E. Zuev Institute of Atmospheric Optics of Siberian Branch of Russian Academy of Sciences were supported by the Ministry of Science and Higher Education of the Russian Federation. The work of Tomsk group on ozone spectroscopy was supported by the Russian Science Foundation RNF grant no. 19-12-00171. GSMA Reims and LiPhy Grenoble acknowledge support from the French-Russian collaboration program LIA CNRS “SAMIA”. AGC, TF, and RT received support from the ELTE Institutional Excellence Program (TKP2020-IKA-05) and from NKFIH (K119658). OLP and JT received support from the UK Natural Environment Research Council under grants NE/N001508/1 and the European Research Council under ERC Advanced Investigator grant 8838302



## References

- [1] R. McClatchey, W. Benedict, S. Clough, D. Burch, R. Calfee, K. Fox, L. Rothman, J. Garing, AFCRL Atmospheric Absorption Line Parameters Compilation, Environmental Research Papers 434 (1973) 1–86.
- [2] L. S. Rothman, R. A. McClatchey, Updating of the AFCRL atmospheric absorption line parameters compilation, Applied Optics 15 (1976) 2616–2617.
- [3] L. S. Rothman, Update of the AFGL atmospheric absorption line parameters compilation, Applied Optics 17 (1978) 3517–3518.
- [4] L. S. Rothman, S. A. Clough, R. A. McClatchey, L. G. Young, D. E. Snider, A. Goldman, AFGL trace gas compilation, Applied Optics 17 (1978) 507.
- [5] L. S. Rothman, A. Goldman, J. R. Gillis, R. H. Tipping, L. R. Brown, J. S. Margolis, A. G. Maki, L. D. Young, AFGL trace gas compilation: 1980 version, Applied Optics 20 (1981) 1323–8.
- [6] L. S. Rothman, R. R. Gamache, A. Barbe, A. Goldman, J. R. Gillis, L. R. Brown, R. A. Toth, J. M. Flaud, C. Camy-Peyret, AFGL atmospheric absorption line parameters compilation: 1982 edition, Applied Optics 22 (1983) 2247–56.
- [7] L. S. Rothman, A. Goldman, J. R. Gillis, R. R. Gamache, H. M. Pickett, R. L. Poynter, N. Husson, A. Chedin, AFGL trace gas compilation: 1982 version, Applied Optics 22 (1983) 1616–1627.
- [8] L. S. Rothman, R. R. Gamache, A. Goldman, L. R. Brown, R. A. Toth, H. M. Pickett, R. L. Poynter, J. M. Flaud, C. Camy-Peyret, A. Barbe, N. Husson, C. P. Rinsland, M. A. H. Smith, The HITRAN database: 1986 edition, Applied Optics 26 (1987) 4058–4097.

- [9] L. Rothman, R. Gamache, R. Tipping, C. Rinsland, M. Smith, D. Benner, V. Devi, J.-M. Flaud, C. Camy-Peyret, A. Perrin, A. Goldman, S. Massie, L. Brown, R. Toth, The HITRAN molecular database: Editions of 1991 and 1992, *Journal of Quantitative Spectroscopy and Radiative Transfer* 48 (1992) 469–507.
- [10] L. S. Rothman, C. P. Rinsland, A. Goldman, S. T. Massie, D. P. Edwards, J.-M. Flaud, A. Perrin, C. Camy-Peyret, V. Dana, J. Y. Mandin, J. Schroeder, A. McCann, R. R. Gamache, R. B. Wattson, K. Yoshino, K. Chance, K. Jucks, L. R. Brown, V. Nemtchinov, P. Varanasi, The HITRAN Molecular Spectroscopic Database and HAWKS (HITRAN Atmospheric Workstation): 1996 Edition, *Journal of Quantitative Spectroscopy and Radiative Transfer* 60 (1998) 665–710.
- [11] L. S. Rothman, A. Barbe, D. C. Benner, L. R. Brown, C. Camy-Peyret, M. R. Carleer, K. Chance, C. Clerbaux, V. Dana, V. M. Devi, A. Fayt, J.-M. Flaud, R. R. Gamache, A. Goldman, D. Jacquemart, K. W. Jucks, W. J. Lafferty, J.-Y. Mandin, S. T. Massie, V. Nemtchinov, D. A. Newnham, A. Perrin, C. P. Rinsland, J. Schroeder, K. M. Smith, M. A. H. Smith, K. Tang, R. A. Toth, J. Vander Auwera, P. Varanasi, K. Yoshino, The HITRAN molecular spectroscopic database: Edition of 2000 including updates through 2001, *Journal of Quantitative Spectroscopy and Radiative Transfer* 82 (2003) 5–44.
- [12] L. S. Rothman, D. Jacquemart, A. Barbe, D. Chris Benner, M. Birk, L. R. Brown, M. R. Carleer, C. Chackerian, K. Chance, L. H. Coudert, V. Dana, V. M. Devi, J.-M. Flaud, R. R. Gamache, A. Goldman, J.-M. Hartmann, K. W. Jucks, A. G. Maki, J.-Y. Mandin, S. T. Massie, J. Orphal, A. Perrin, C. P. Rinsland, M. A. H. Smith, J. Tennyson, R. N. Tolchenov, R. A. Toth, J. Vander Auwera, P. Varanasi, G. Wagner, The HITRAN 2004 molecular spectroscopic database, *Journal of Quantitative Spectroscopy and Radiative Transfer* 96 (2005) 139–204.

- [13] L. S. Rothman, I. E. Gordon, A. Barbe, D. C. Benner, P. F. Bernath, M. Birk, V. Boudon, L. R. Brown, A. Campargue, J.-P. Champion, K. Chance, L. H. Coudert, V. Dana, V. M. Devi, S. Fally, J.-M. Flaud, R. R. Gamache, A. Goldman, D. Jacquemart, I. Kleiner, N. Lacome, W. J. Lafferty, J.-Y. Mandin, S. T. Massie, S. N. Mikhailenko, C. E. Miller, N. Moazzen-Ahmadi, O. V. Naumenko, A. V. Nikitin, J. Orphal, V. I. Perevalov, A. Perrin, A. Predoi-Cross, C. P. Rinsland, M. Rotger, M. Šimečková, M. A. H. Smith, K. Sung, S. A. Tashkun, J. Tennyson, R. A. Toth, A. C. Vandaele, J. Vander Auwera, The HITRAN 2008 molecular spectroscopic database, *Journal of Quantitative Spectroscopy and Radiative Transfer* 110 (2009) 533–572.
- [14] L. Rothman, I. Gordon, Y. Babikov, A. Barbe, D. Chris Benner, P. Bernath, M. Birk, L. Bizzocchi, V. Boudon, L. Brown, A. Campargue, K. Chance, E. Cohen, L. Coudert, V. Devi, B. Drouin, A. Fayt, J.-M. Flaud, R. Gamache, J. Harrison, J.-M. Hartmann, C. Hill, J. Hodges, D. Jacquemart, A. Jolly, J. Lamouroux, R. Le Roy, G. Li, D. Long, O. Lyulin, C. Mackie, S. Massie, S. Mikhailenko, H. Müller, O. Naumenko, A. Nikitin, J. Orphal, V. Perevalov, A. Perrin, E. Polovtseva, C. Richard, M. Smith, E. Starikova, K. Sung, S. Tashkun, J. Tennyson, G. Toon, V. Tyuterev, G. Wagner, The HITRAN2012 molecular spectroscopic database, *Journal of Quantitative Spectroscopy and Radiative Transfer* 130 (2013) 4–50.
- [15] I. E. Gordon, L. S. Rothman, C. Hill, R. V. Kochanov, Y. Tan, P. F. Bernath, M. Birk, V. Boudon, A. Campargue, K. V. Chance, B. J. Drouin, J. M. Flaud, R. R. Gamache, J. T. Hodges, D. Jacquemart, V. I. Perevalov, A. Perrin, K. P. Shine, M. A. H. Smith, J. Tennyson, G. C. Toon, H. Tran, V. G. Tyuterev, A. Barbe, A. G. Császár, V. M. Devi, T. Furtenbacher, J. J. Harrison, J. M. Hartmann, A. Jolly, T. J. Johnson, T. Karman, I. Kleiner, A. A. Kyuberis, J. Loos, O. M. Lyulin, S. T. Massie, S. N. Mikhailenko, N. Moazzen-Ahmadi, H. S. P. Müller, O. V. Naumenko,

- A. V. Nikitin, O. L. Polyansky, M. Rey, M. Rotger, S. W. Sharpe, K. Sung, E. Starikova, S. A. Tashkun, J. Vander Auwera, G. Wagner, J. Wilzewski, P. Wcisło, S. Yu, E. J. Zak, The HITRAN2016 molecular spectroscopic database, *Journal of Quantitative Spectroscopy and Radiative Transfer* 203 (2017) 3–69.
- [16] D. Crisp, R. Atlas, F.-M. Breon, L. Brown, J. Burrows, P. Ciais, B. Connor, S. Doney, I. Fung, D. Jacob, C. Miller, D. O'Brien, S. Pawson, J. Randerson, P. Rayner, R. Salawitch, S. Sander, B. Sen, G. Stephens, P. Tans, G. Toon, P. Wennberg, S. Wofsy, Y. Yung, Z. Kuang, B. Chudasama, G. Sprague, B. Weiss, R. Pollock, D. Kenyon, S. Schroll, The Orbiting Carbon Observatory (OCO) mission, *Advances in Space Research* 34 (2004) 700–709.
- [17] A. Eldering, T. E. Taylor, C. W. O'Dell, R. Pavlick, The OCO-3 mission: measurement objectives and expected performance based on 1 year of simulated data, *Atmospheric Measurement Techniques* 12 (2019) 2341–2370.
- [18] R. Beer, TES on the Aura Mission: Scientific objectives, measurements, and analysis overview, *IEEE Transactions on Geoscience and Remote Sensing* 44 (2006) 1102–1105.
- [19] A. Kuze, H. Suto, M. Nakajima, T. Hamazaki, Thermal and near infrared sensor for carbon observation Fourier-transform spectrometer on the Greenhouse Gases Observing Satellite for greenhouse gases monitoring, *Applied Optics* 48 (2009) 6716.
- [20] P. F. Bernath, Atmospheric chemistry experiment (ACE): Mission overview, *Geophysical Research Letters* 32 (2005) L15S01.
- [21] J. Veefkind, I. Aben, K. McMullan, H. Förster, J. de Vries, G. Otter, J. Claas, H. Eskes, J. de Haan, Q. Kleipool, M. van Weele, O. Hasekamp, R. Hoogeveen, J. Landgraf, R. Snel, P. Tol, P. Ingmann, R. Voors,

- B. Kruizinga, R. Vink, H. Visser, P. Levelt, TROPOMI on the ESA Sentinel-5 Precursor: A GMES mission for global observations of the atmospheric composition for climate, air quality and ozone layer applications, *Remote Sensing of Environment* 120 (2012) 70–83.
- [22] J. Kim, U. Jeong, M.-H. Ahn, J. H. Kim, R. J. Park, H. Lee, C. H. Song, Y.-S. Choi, K.-H. Lee, J.-M. Yoo, M.-J. Jeong, S. K. Park, K.-M. Lee, C.-K. Song, S.-W. Kim, Y. J. Kim, S.-W. Kim, M. Kim, S. Go, X. Liu, K. Chance, C. Chan Miller, J. Al-Saadi, B. Veihelmann, P. K. Bhartia, O. Torres, G. G. Abad, D. P. Haffner, D. H. Ko, S. H. Lee, J.-H. Woo, H. Chong, S. S. Park, D. Nicks, W. J. Choi, K.-J. Moon, A. Cho, J. Yoon, S.-k. Kim, H. Hong, K. Lee, H. Lee, S. Lee, M. Choi, P. Veefkind, P. F. Levelt, D. P. Edwards, M. Kang, M. Eo, J. Bak, K. Baek, H.-A. Kwon, J. Yang, J. Park, K. M. Han, B.-R. Kim, H.-W. Shin, H. Choi, E. Lee, J. Chong, Y. Cha, J.-H. Koo, H. Irie, S. Hayashida, Y. Kasai, Y. Kanaya, C. Liu, J. Lin, J. H. Crawford, G. R. Carmichael, M. J. Newchurch, B. L. Lefer, J. R. Herman, R. J. Swap, A. K. H. Lau, T. P. Kurosu, G. Jaross, B. Ahlers, M. Dobber, C. T. McElroy, Y. Choi, New Era of Air Quality Monitoring from Space: Geostationary Environment Monitoring Spectrometer (GEMS), *Bulletin of the American Meteorological Society* 101 (2020) E1–E22.
- [23] L. Palchetti, H. Brindley, R. Bantges, S. A. Buehler, C. Camy-Peyret, B. Carli, U. Cortesi, S. Del Bianco, G. Di Natale, B. M. Dinelli, D. Feldman, X. L. Huang, L. C.-Labonnote, Q. Libois, T. Maestri, M. G. Mlynchzak, J. E. Murray, H. Oetjen, M. Ridolfi, M. Riese, J. Russell, R. Saunders, C. Serio, FORUM: Unique Far-Infrared Satellite Observations to Better Understand How Earth Radiates Energy to Space, *Bulletin of the American Meteorological Society* 101 (2020) E2030–E2046.
- [24] P. Zoogman, X. Liu, R. Suleiman, W. Pennington, D. Flittner, J. Al-Saadi, B. Hilton, D. Nicks, M. Newchurch, J. Carr, S. Janz, M. Andraschko, A. Arola, B. Baker, B. Canova, C. Chan Miller, R. Cohen,

- J. Davis, M. Dussault, D. Edwards, J. Fishman, A. Ghulam, G. González Abad, M. Grutter, J. Herman, J. Houck, D. Jacob, J. Joiner, B. Kerridge, J. Kim, N. Krotkov, L. Lamsal, C. Li, A. Lindfors, R. Martin, C. McElroy, C. McLinden, V. Natraj, D. Neil, C. Nowlan, E. O’Sullivan, P. Palmer, R. Pierce, M. Pippin, A. Saiz-Lopez, R. Spurr, J. Szykman, O. Torres, J. Veefkind, B. Veihelmann, H. Wang, J. Wang, K. Chance, Tropospheric emissions: Monitoring of pollution (TEMPO), *Journal of Quantitative Spectroscopy and Radiative Transfer* 186 (2017) 17–39.
- [25] S. C. Wofsy, S. Hamburg, MethaneSAT - A New Observing Platform For High Resolution Measurements Of Methane and Carbon Dioxide, in: AGU Fall Meeting Abstracts, volume 2019, 2019, pp. A53F–02.
- [26] M. W. Shephard, S. A. Clough, V. H. Payne, W. L. Smith, S. Kireev, K. E. Cady-Pereira, Performance of the line-by-line radiative transfer model (LBLRTM) for temperature and species retrievals: IASI case studies from JAIVEx, *Atmospheric Chemistry and Physics* 9 (2009) 7397–7417.
- [27] A. Berk, F. Hawes, Validation of MODTRAN<sup>®</sup>6 and its line-by-line algorithm, *Journal of Quantitative Spectroscopy and Radiative Transfer* 203 (2017) 542–556.
- [28] D. Edwards, GENLN2: A General Line-by-line Atmospheric Transmittance and Radiance Model. Version 3.0 Description and Users Guide. NCAR Technical Note NCAR/TN-367+STR, Technical Report, National Center for Atmospheric Research, 1992. URL: <http://opensky.ucar.edu/islandora/object/technotes:134>. doi:10.5065/D6W37T86.
- [29] A. Dudhia, The Reference Forward Model (RFM), *Journal of Quantitative Spectroscopy and Radiative Transfer* 186 (2017) 243–253.
- [30] S. A. Buehler, P. Eriksson, T. Kuhn, A. von Engeln, C. Verdes, ARTS, the atmospheric radiative transfer simulator, *Journal of Quantitative Spectroscopy and Radiative Transfer* 91 (2005) 65–93.

- [31] F. Schreier, S. Gimeno García, P. Hedelt, M. Hess, J. Mendrok, M. Vasquez, J. Xu, GARLIC — A general purpose atmospheric radiative transfer line-by-line infrared-microwave code: Implementation and evaluation, *Journal of Quantitative Spectroscopy and Radiative Transfer* 137 (2014) 29–50.
- [32] S. Desouza-Machado, L. Larrabee Strow, H. Motteler, S. Hannon, kCARTA: a fast pseudo line-by-line radiative transfer algorithm with analytic Jacobians, fluxes, nonlocal thermodynamic equilibrium, and scattering for the infrared, *Atmospheric Measurement Techniques* 13 (2020) 323–339.
- [33] R. J. Spurr, VLIDORT: A linearized pseudo-spherical vector discrete ordinate radiative transfer code for forward model and retrieval studies in multilayer multiple scattering media, *Journal of Quantitative Spectroscopy and Radiative Transfer* 102 (2006) 316–342.
- [34] P. G. J. Irwin, N. A. Teanby, R. de Kok, L. N. Fletcher, C. J. A. Howett, C. C. C. Tsang, C. F. Wilson, S. B. Calcutt, C. A. Nixon, P. D. Parrish, The NEMESIS planetary atmosphere radiative transfer and retrieval tool, *Journal of Quantitative Spectroscopy and Radiative Transfer* 109 (2008) 1136–1150.
- [35] P. Mollière, J. P. Wardenier, R. van Boekel, T. Henning, K. Molaverdikhani, I. A. G. Snellen, petitRADTRANS: A Python radiative transfer package for exoplanet characterization and retrieval, *Astronomy & Astrophysics* 627 (2019) A67.
- [36] G. L. Villanueva, M. D. Smith, S. Protopapa, S. Faggi, A. M. Mandell, Planetary Spectrum Generator: An accurate online radiative transfer suite for atmospheres, comets, small bodies and exoplanets, *Journal of Quantitative Spectroscopy and Radiative Transfer* 217 (2018) 86–104.
- [37] E. M. Kempton, R. Lupu, A. Owusu-Asare, P. Slough, B. Cale, Exotransmit: An open-source code for calculating transmission spectra for

exoplanet atmospheres of varied composition, *Publications of the Astronomical Society of the Pacific* 129 (2017) 044402.

- [38] S. L. Grimm, M. Malik, D. Kitzmann, A. Guzmán-Mesa, H. J. Hoeijmakers, C. Fisher, J. M. Mendonça, S. N. Yurchenko, J. Tennyson, F. Alesina, N. Buchschacher, J. Burnier, D. Segransan, R. L. Kurucz, K. Heng, HELIOS-K 2.0 Opacity Calculator and Open-source Opacity Database for Exoplanetary Atmospheres, *arXiv e-prints* (2021) arXiv:2101.02005.
- [39] D. V. Titov, H. Svedhem, D. McCoy, J. P. Lebreton, S. Barabash, J. L. Bertaux, P. Drossart, V. Formisano, B. Haesler, O. I. Korabev, W. Markiewicz, D. Neveance, M. Petzold, G. Piccioni, T. L. Zhang, F. W. Taylor, E. Lellouch, D. Koschny, O. Witasse, M. Warhaut, A. Acomazzo, J. Rodrigues-Cannabal, J. Fabrega, T. Schirmann, A. Clochet, M. Coradini, Venus Express: Scientific goals, instrumentation, and scenario of the mission, *Cosmic Research* 44 (2006) 334–348.
- [40] L. Trompet, Y. Geunes, T. Ooms, A. Mahieux, V. Wilquet, S. Chamberlain, S. Robert, I. R. Thomas, S. Erard, B. Cecconi, P. Le Sidaner, A. C. Vandaele, Description, accessibility and usage of SOIR/Venus Express atmospheric profiles of Venus distributed in VESPA (Virtual European Solar and Planetary Access), *Planetary and Space Science* 150 (2018) 60–64.
- [41] O. Korabev, F. Montmessin, A. Trokhimovskiy, A. A. Fedorova, A. V. Shakun, A. V. Grigoriev, B. E. Moshkin, N. I. Ignatiev, F. Forget, F. Lefèvre, K. Anufreychik, I. Dzuban, Y. S. Ivanov, Y. K. Kalinnikov, T. O. Kozlova, A. Kungurov, V. Makarov, F. Martynovich, I. Maslov, D. Merzlyakov, P. P. Moiseev, Y. Nikolskiy, A. Patrakeev, D. Patsaev, A. Santos-Skripko, O. Sazonov, N. Semena, A. Semenov, V. Shashkin, A. Sidorov, A. V. Stepanov, I. Stupin, D. Timonin, A. Y. Titov, A. Viktorov, A. Zharkov, F. Altieri, G. Arnold, D. A. Belyaev, J. L. Bertaux, D. S. Betsis, N. Duxbury, T. Encrenaz, T. Fouchet, J. C. Gérard,



- D. Grassi, S. Guerlet, P. Hartogh, Y. Kasaba, I. Khatuntsev, V. A. Krasnopolsky, R. O. Kuzmin, E. Lellouch, M. A. Lopez-Valverde, M. Luginin, A. Määttänen, E. Marcq, J. Martin Torres, A. S. Medvedev, E. Millour, K. S. Olsen, M. R. Patel, C. Quantin-Nataf, A. V. Rodin, V. I. Shematovich, I. Thomas, N. Thomas, L. Vazquez, M. Vincendon, V. Wilquet, C. F. Wilson, L. V. Zasova, L. M. Zelenyi, M. P. Zorzano, The Atmospheric Chemistry Suite (ACS) of Three Spectrometers for the ExoMars 2016 Trace Gas Orbiter, *Space Science Reviews* 214 (2018) 29.
- [42] K. Olsen, C. Boone, G. Toon, F. Montmessin, A. Fedorova, O. Korabiev, A. Trokhimovskiy, Validation of the HITRAN 2016 and GEISA 2015 line lists using ACE-FTS solar occultation observations, *Journal of Quantitative Spectroscopy and Radiative Transfer* 236 (2019) 106590.
- [43] L. D. Jaffe, L. M. Herrell, Cassini/Huygens science instruments, spacecraft, and mission, *Journal of Spacecraft and Rockets* 34 (1997) 509–521.
- [44] A. Tsiaras, I. P. Waldmann, M. Rocchetto, R. Varley, G. Morello, M. Damiano, G. Tinetti, A New Approach to Analyzing HST Spatial Scans: The Transmission Spectrum of HD 209458 b, *Astrophysical Journal* 832 (2016) 202.
- [45] J.-L. Baudino, P. Mollière, O. Venot, P. Tremblin, B. Bézard, P.-O. Lagage, Toward the Analysis of JWST Exoplanet Spectra: Identifying Troublesome Model Parameters, *Astrophysical Journal* 850 (2017) 150.
- [46] G. Tinetti, P. Drossart, P. Eccleston, P. Hartogh, A. Heske, J. Leconte, G. Micela, M. Ollivier, G. Pilbratt, L. Puig, D. Turrini, B. Vandenbussche, P. Wolkenberg, J. P. Beaulieu, L. A. Buchave, M. Ferus, M. Griffin, M. Guedel, K. Justtanont, P. O. Lagage, P. Machado, G. Malaguti, M. Min, H. U. Nørgaard-Nielsen, M. Rataj, T. Ray, I. Ribas, M. Swain, R. Szabo, S. Werner, J. Barstow, M. Burleigh, J. Cho, V. C. du Foresto, A. Coustenis, L. Decin, T. Encrenaz, M. Galand, M. Gillon, R. Helled,

J. C. Morales, A. G. Muñoz, A. Moneti, I. Pagano, E. Pascale, G. Piccioni, D. Pinfield, S. Sarkar, F. Selsis, J. Tennyson, A. Triaud, O. Venot, I. Waldmann, D. Waltham, G. Wright, J. Amiaux, J. L. Auguères, M. Berthé, N. Bezawada, G. Bishop, N. Bowles, D. Coffey, J. Colomé, M. Crook, P. E. Crouzet, V. Da Peppo, I. E. Sanz, M. Focardi, M. Frericks, T. Hunt, R. Kohley, K. Middleton, G. Morgante, R. Ottensamer, E. Pace, C. Pearson, R. Stamper, K. Symonds, M. Rengel, E. Renotte, P. Ade, L. Affer, C. Alard, N. Allard, F. Altieri, Y. André, C. Arena, I. Argyriou, A. Aylward, C. Baccani, G. Bakos, M. Banaszkiewicz, M. Barlow, V. Batista, G. Bellucci, S. Benatti, P. Bernardi, B. Bézard, M. Blecka, E. Bolmont, B. Bonfond, R. Bonito, A. S. Bonomo, J. R. Brucato, A. S. Brun, I. Bryson, W. Bujwan, S. Casewell, B. Charnay, C. C. Pestellini, G. Chen, A. Ciaravella, R. Claudi, R. Clédassou, M. Damasso, M. Damiano, C. Danielski, P. Deroo, A. M. Di Giorgio, C. Dominik, V. Doublier, S. Doyle, R. Doyon, B. Drummond, B. Duong, S. Eales, B. Edwards, M. Farina, E. Flacomio, L. Fletcher, F. Forget, S. Fossey, M. Fränz, Y. Fujii, Á. García-Piquer, W. Gear, H. Geoffray, J. C. Gérard, L. Gesa, H. Gomez, R. Graczyk, C. Griffith, D. Grodent, M. G. Guarcello, J. Gustin, K. Hamano, P. Hargrave, Y. Hello, K. Heng, E. Herrero, A. Hornstrup, B. Hubert, S. Ida, M. Ikoma, N. Iro, P. Irwin, C. Jarchow, J. Jaubert, H. Jones, Q. Julien, S. Kameda, F. Kerschbaum, P. Kervella, T. Koskinen, M. Krijger, N. Krupp, M. Lafarga, F. Landini, E. Lellouch, G. Leto, A. Luntzer, T. Rank-Lüftinger, A. Maggio, J. Maldonado, J. P. Maillard, U. Mall, J. B. Marquette, S. Mathis, P. Maxted, T. Matsuo, A. Medvedev, Y. Miguel, V. Minier, G. Morello, A. Mura, N. Narita, V. Nascimbeni, N. Nguyen Tong, V. Noce, F. Oliva, E. Palle, P. Palmer, M. Pancrazzi, A. Papageorgiou, V. Parmentier, M. Perger, A. Petralia, S. Pezzuto, R. Pierrehumbert, I. Pillitteri, G. Piotto, G. Pisano, L. Prisinzano, A. Radioti, J. M. Réess, L. Rezac, M. Rocchetto, A. Rosich, N. Sanna, A. Santerne, G. Savini, G. Scandariato, B. Sicardy, C. Sierra, G. Sindoni, K. Skup, I. Snellen, M. Sobiecki, L. Soret, A. Sozzetti,

- A. Stiepen, A. Strugarek, J. Taylor, W. Taylor, L. Terenzi, M. Tessenyi, A. Tsiaras, C. Tucker, D. Valencia, G. Vasisht, A. Vazan, F. Vilardell, S. Vinatier, S. Viti, R. Waters, P. Wawer, A. Wawrzaszek, A. Whitworth, Y. L. Yung, S. N. Yurchenko, M. R. Z. Osorio, R. Zellem, T. Zingales, F. Zwart, A chemical survey of exoplanets with ARIEL, *Experimental Astronomy* 46 (2018) 135–209.
- [47] J. L. Bertaux, R. Lallement, S. Ferron, C. Boonne, R. Bodichon, TAPAS, a web-based service of atmospheric transmission computation for astronomy, *Astronomy & Astrophysics* 564 (2014) 46.
- [48] Y. Tan, R. V. Kochanov, L. S. Rothman, I. E. Gordon, Introduction of water-vapor broadening parameters and their temperature-dependent exponents into the HITRAN database: Part I—CO<sub>2</sub>, N<sub>2</sub>O, CO, CH<sub>4</sub>, O<sub>2</sub>, NH<sub>3</sub>, and H<sub>2</sub>S, *Journal of Geophysical Research (Atmospheres)* 124 (2019) 11,580–11,594.
- [49] C. Hill, I. E. Gordon, L. S. Rothman, J. Tennyson, A new relational database structure and online interface for the HITRAN database, *Journal of Quantitative Spectroscopy and Radiative Transfer* 130 (2013) 51–61.
- [50] C. Hill, I. E. Gordon, R. V. Kochanov, L. Barrett, J. S. Wilzewski, L. S. Rothman, HITRANonline: An online interface and the flexible representation of spectroscopic data in the HITRAN database, *Journal of Quantitative Spectroscopy and Radiative Transfer* 177 (2016) 4–14.
- [51] R. V. Kochanov, I. E. Gordon, L. S. Rothman, P. Wcisło, C. Hill, J. S. Wilzewski, HITRAN Application Programming Interface (HAPI): A comprehensive approach to working with spectroscopic data, *Journal of Quantitative Spectroscopy and Radiative Transfer* 177 (2016) 15–30.
- [52] L. S. Rothman, I. E. Gordon, R. J. Barber, H. Dothe, R. R. Gamache, A. Goldman, V. I. Perevalov, S. A. Tashkun, J. Tennyson, HITEMP, the high-temperature molecular spectroscopic database, *Journal of Quantitative Spectroscopy and Radiative Transfer* 111 (2010) 2139–2150.

- [53] L. S. Rothman, R. B. Wattson, R. Gamache, J. W. Schroeder, A. McCann, HITRAN HAWKS and HITEMP: high-temperature molecular database, in: J. C. Dainty (Ed.), *Atmospheric Propagation and Remote Sensing IV*, volume 2471 of *Society of Photo-Optical Instrumentation Engineers (SPIE) Conference Series*, 1995, pp. 105–111. doi:10.1117/12.211919.
- [54] R. J. Hargreaves, I. E. Gordon, L. S. Rothman, S. A. Tashkun, V. I. Perevalov, A. A. Lukashetskaya, S. N. Yurchenko, J. Tennyson, H. S. P. Müller, Spectroscopic line parameters of NO, NO<sub>2</sub>, and N<sub>2</sub>O for the HITEMP database, *Journal of Quantitative Spectroscopy and Radiative Transfer* 232 (2019) 35–53.
- [55] R. J. Hargreaves, I. E. Gordon, M. Rey, A. V. Nikitin, V. G. Tyuterev, R. V. Kochanov, L. S. Rothman, An Accurate, Extensive, and Practical Line List of Methane for the HITEMP Database, *Astrophysical Journal Supplement Series* 247 (2020) 55.
- [56] P. De Bièvre, M. Gallet, N. E. Holden, I. L. Barnes, Isotopic Abundances and Atomic Weights of the Elements, *Journal of Physical and Chemical Reference Data* 13 (1984) 809–891.
- [57] T. Furtenbacher, A. G. Császár, J. Tennyson, MARVEL: measured active rotational-vibrational energy levels, *Journal of Molecular Spectroscopy* 245 (2007) 115–125.
- [58] T. Furtenbacher, A. G. Császár, MARVEL: measured active rotational-vibrational energy levels. II. Algorithmic improvements, *Journal of Quantitative Spectroscopy and Radiative Transfer* 113 (2012) 929–935.
- [59] J. Tennyson, P. F. Bernath, L. R. Brown, A. Campargue, A. G. Császár, L. Daumont, R. R. Gamache, J. T. Hodges, O. V. Naumenko, O. L. Polyansky, L. S. Rothman, A. C. Vandaele, N. F. Zobov, A database of water transitions from experiment and theory (IUPAC technical report), *Pure Applied Chemistry* 86 (2014) 71–83.

- [60] R. A. Toth, Linelist of water vapor parameters from 500 to 8000  $\text{cm}^{-1}$ , 2009. URL: <https://mark4sun.jpl.nasa.gov/h2o.html>.
- [61] L. Brown, R. Toth, M. Dulick, Empirical line parameters of  $\text{H}_2^{16}\text{O}$  near 0.94  $\mu\text{m}$ : positions, intensities and air-broadening coefficients, *Journal of Molecular Spectroscopy* 212 (2002) 57–82.
- [62] R. Tolchenov, J. Tennyson, Water Line Parameters from Refitted Spectra constrained by empirical upper state levels: study of the 9500 – 14500  $\text{cm}^{-1}$  region, *Journal of Quantitative Spectroscopy and Radiative Transfer* 109 (2008) 559–568.
- [63] R. Tolchenov, O. Naumenko, N. Zobov, S. Shirin, O. Polyansky, J. Tennyson, M. Carleer, P.-F. Coheur, S. Fally, A. Jenouvrier, A. Vandaele, Water vapour line assignments in the 9250 – 26 000  $\text{cm}^{-1}$  frequency range, *Journal of Molecular Spectroscopy* 233 (2005) 68–76.
- [64] G. Wagner, M. Birk, Water line intensities in the 1  $\mu\text{m}$  region, 2013.
- [65] J. Loos, M. Birk, G. Wagner, Measurement of positions, intensities and self-broadening line shape parameters of  $\text{H}_2\text{O}$  lines in the spectral ranges 1850–2280  $\text{cm}^{-1}$  and 2390–4000  $\text{cm}^{-1}$ , *Journal of Quantitative Spectroscopy and Radiative Transfer* 203 (2017) 119–132. HITRAN2016 Special Issue.
- [66] D. Lisak, D. Havey, J. T. Hodges, Spectroscopic line parameters of water vapor for rotation-vibration transitions near 7180  $\text{cm}^{-1}$ , *Physical Review A* 79 (2009) 52507.
- [67] S. Mikhailenko, S. Kassı, L. Wang, A. Campargue, The absorption spectrum of water in the 1.25  $\mu\text{m}$  transparency window (7408–7920  $\text{cm}^{-1}$ ), *Journal of Molecular Spectroscopy* 269 (2011) 92–103.
- [68] O. Leshchishina, S. Mikhailenko, D. Mondelain, S. Kassı, A. Campargue, Crds of water vapor at 0.1 torr between 6886 and 7406  $\text{cm}^{-1}$ , *Journal of Quantitative Spectroscopy and Radiative Transfer* 113 (2012) 2155–2166.

- [69] L. Regalia, C. Oudot, S. Mikhailenko, L. Wang, X. Thomas, A. Jenouvrier, P. V. der Heyden, Water vapor line parameters from 6450 to 9400  $\text{cm}^{-1}$ , *Journal of Quantitative Spectroscopy and Radiative Transfer* 136 (2014) 119–136.
- [70] A. Campargue, S. Mikhailenko, B. Lohan, E. Karlovets, D. Mondelain, S. Kass, The absorption spectrum of water vapor in the 1.25  $\mu\text{m}$  atmospheric window (7911–8337  $\text{cm}^{-1}$ ), *Journal of Quantitative Spectroscopy and Radiative Transfer* 157 (2015) 135–152.
- [71] V.T. Sironneau AND J.T. Hodges, Line shapes, positions and intensities of water transitions near 1.28  $\mu\text{m}$ , *Journal of Quantitative Spectroscopy and Radiative Transfer* 152 (2015) 1–15.
- [72] I. E. Gordon, L. S. Rothman, R. R. Gamache, D. Jacquemart, C. Boone, P. F. Bernath, M. W. Shephard, J. S. Delamere, S. a. Clough, Current updates of the water-vapor line list in HITRAN: A new “Diet” for air-broadened half-widths, *Journal of Quantitative Spectroscopy and Radiative Transfer* 108 (2007) 389–402.
- [73] N. H. Ngo, D. Lisak, H. Tran, J. -M. Hartmann, An isolated line-shape model to go beyond the Voigt profile in spectroscopic databases and radiative transfer codes, *Journal of Quantitative Spectroscopy and Radiative Transfer* 129 (2013) 89–100.
- [74] J. Tennyson, P. F. Bernath, A. Campargue, A. G. Császár, L. Daumont, R. R. Gamache, J. T. Hodges, D. Lisak, O. V. Naumenko, L. S. Rothman, H. Tran, N. F. Zobov, J. Buldyreva, C. D. Boone, M. D. D. Vizia, L. Gianfrani, J.-M. Hartmann, R. McPheat, D. Weidmann, J. Murray, N. H. Ngo, O. L. Polyansky, Recommended isolated-line profile for representing high-resolution spectroscopic transitions (IUPAC technical report), *Pure and Applied Chemistry* 86 (2014) 1931–1943.
- [75] A. D. Baker, C. H. Blake, A. Reiners, The IAG Solar Flux Atlas: Telluric

Correction with a Semiempirical Model, *Astrophysical Journal Supplement Series* 247 (2020) 24.

- [76] E. K. Conway, A. A. Kyuberis, O. L. Polyansky, J. Tennyson, N. Zobov, A highly accurate *ab initio* dipole moment surface for the ground electronic state of water vapour for spectra extending into the ultraviolet, *Journal Chemical Physics* 149 (2018) 084307.
- [77] P. Zoogman, X. Liu, R. M. Suleiman, W. F. Pennington, D. E. Flittner, J. A. Al-Saadi, B. B. Hilton, D. K. Nicks, M. J. Newchurch, J. L. Carr, S. J. Janz, M. R. Andraschko, A. Arola, B. D. Baker, B. P. Canova, C. C. Miller, R. C. Cohen, J. E. Davis, M. E. Dussault, D. P. Edwards, J. Fishman, A. Ghulam, G. G. Abad, M. Grutter, J. R. Herman, J. Houck, D. J. Jacob, J. Joiner, B. J. Kerridge, J. Kim, N. A. Krotkov, L. Lamsal, C. Li, A. Lindfors, R. V. Martin, C. T. McElroy, C. McLinden, V. Natraj, D. O. Neil, C. R. Nowlan, E. J. O’Sullivan, P. I. Palmer, R. B. Pierce, M. R. Pippin, A. Saiz-Lopez, R. J. D. Spurr, J. J. Szykman, O. Torres, J. P. Veefkind, B. Veihelmann, H. Wang, J. Wang, K. Chance, Tropospheric emissions: Monitoring of pollution (TEMPO), *Journal of Quantitative Spectroscopy and Radiative Transfer* 186 (2017) 17–39.
- [78] Gonzalo Gonzalez Abad et al., Five decades observing Earth’s atmospheric trace gases using ultraviolet and visible backscatter solar radiation from space, *Journal of Quantitative Spectroscopy and Radiative Transfer* 238 (2019) 106478.
- [79] H. Wang, A. H. Souri, G. González Abad, X. Liu, K. Chance, Ozone Monitoring Instrument (OMI) Total Column Water Vapor version 4 validation and applications, *Atmospheric Measurements Techniques* 12 (2019) 5183–5199.
- [80] H. Wang, X. Liu, K. Chance, G. G. Abad, C. C. Miller, Water vapor retrieval from OMI visible spectra, *Atmospheric Measurements Techniques* 7 (2014) 1901–1913.

- [81] J. Lampel, D. Pöhler, O. L. Polyansky, A. A. Kyuberis, N. F. Zobov, J. Tennyson, L. Lodi, U. Friß, Y. Wang, S. Beirle, U. Platt, T. Wagner, Detection of water vapour absorption around 363 nm in measured atmospheric absorption spectra and its effect on DOAS evaluations, *Atmospheric Chemistry and Physics* 17 (2017) 1271–1295.
- [82] O. L. Polyansky, A. A. Kyuberis, N. F. Zobov, J. Tennyson, S. N. Yurchenko, L. Lodi, ExoMol molecular line lists XXX: a complete high-accuracy line list for water, *Monthly Notices Royal Astronomical Society* 480 (2018) 2597–2608.
- [83] L. Lodi, J. Tennyson, O. L. Polyansky, A global, high accuracy ab initio dipole moment surface for the electronic ground state of the water molecule, *Journal Chemical Physics* 135 (2011) 034113.
- [84] E. K. Conway, I. E. Gordon, A. A. Kyuberis, O. L. Polyansky, J. Tennyson, N. F. Zobov, Calculated line lists for  $\text{H}_2^{16}\text{O}$  and  $\text{H}_2^{18}\text{O}$  with extensive comparisons to theoretical and experimental sources including the HITRAN2016 database, *Journal of Quantitative Spectroscopy and Radiative Transfer* 241 (2020) 106711.
- [85] E. K. Conway, I. E. Gordon, J. Tennyson, O. L. Polyansky, S. N. Yurchenko, K. Chance, A semi-empirical potential energy surface and line list for  $\text{H}_2^{16}\text{O}$  extending into the near-ultraviolet, *Atmospheric Chemistry and Physics* 20 (2020) 10015–10027.
- [86] J. Lampel, D. Pöhler, J. Tschritter, U. Friß, U. Platt, On the relative absorption strengths of water vapour in the blue wavelength range, *Atmospheric Measurement Techniques* 8 (2015) 4329–4346.
- [87] E. M. Wilson, J. C. Wenger, D. S. Venables, Upper limits for absorption by water vapor in the near-UV, *Journal of Quantitative Spectroscopy and Radiative Transfer* 170 (2016) 194–199.



- [88] J. Du, L. Huang, Q. Min, L. Zhu, The influence of water vapor absorption in the 290–350 nm region on solar radiance: Laboratory studies and model simulation, *Geophysical Research Letters* 40 (2013) 4788–4792.
- [89] L. Pei, Q. Min, Y. Du, Z. Wang, B. Yin, K. Yang, P. Disterhoft, T. Pongetti, L. Zhu, Water Vapor Near-UV Absorption: Laboratory Spectrum, Field Evidence, and Atmospheric Impacts, *Journal Geophysical Research (Atmospheres)* 124 (2019) 14310–14324.
- [90] S. Mikhailenko, S. Kassi, D. Mondelain, A. Campargue, Water vapor absorption between 5690 and 8340  $\text{cm}^{-1}$ : Accurate empirical line centers and validation tests of calculated line intensities, *Journal of Quantitative Spectroscopy and Radiative Transfer* 245 (2020) 106840.
- [91] I. I. Bubukina, O. L. Polyansky, N. F. Zobov, S. N. Yurchenko, Optimized semiempirical potential energy surface for  $\text{H}_2^{16}\text{O}$  up to 26 000  $\text{cm}^{-1}$ , *Optics Spectroscopy* 110 (2011) 160–166.
- [92] I. I. Mizus, A. A. Kyuberis, N. F. Zobov, V. Y. Makhnev, O. L. Polyansky, J. Tennyson, High accuracy water potential energy surface for the calculation of infrared spectra, *Philosophical Transactions of the Royal Society of London A* 376 (2018) 20170149.
- [93] A. G. Császár, T. Furtenbacher, Spectroscopic networks, *Journal of Molecular Spectroscopy* 266 (2011) 99–103.
- [94] R. Tóbiás, T. Furtenbacher, I. Simkó, A. G. Császár, M. L. Diouf, F. M. J. Cozijn, J. M. A. Staa, E. J. Salumbides, W. Ubachs, Spectroscopic-network-assisted precision spectroscopy and its application to water, *Nature Communications* 11 (2020) 1708.
- [95] T. Furtenbacher, R. Tóbiás, J. Tennyson, O. L. Polyansky, A. G. Császár, W2020: A database of validated rovibrational experimental transitions and empirical energy levels of  $\text{H}_2^{16}\text{O}$ , *Journal Physical Chemical Reference Data* 49 (2020) 033101.

- [96] T. Furtenbacher, R. Tóbiás, J. Tennyson, O. L. Polyansky, A. A. Kyuberis, R. I. Ovsyannikov, N. F. Zobov, A. G. Császár, The W2020 database of validated rovibrational experimental transitions and empirical energy levels of water isotopologues. II.  $\text{H}_2^{17}\text{O}$  and  $\text{H}_2^{18}\text{O}$  with an update to  $\text{H}_2^{16}\text{O}$ , *Journal of Physical and Chemical Reference Data* 49 (2020) 043103.
- [97] E. K. Conway, I. E. Gordon, O. L. Polyansky, J. Tennyson, Determination of approximate quantum labels based on projections of the total angular momentum on the molecule-fixed axis, *Journal of Quantitative Spectroscopy and Radiative Transfer* (2021). This issue.
- [98] G. Hose, H. S. Taylor, Quantum kolmogorov-arnol'd-moser-like theorem: Fundamentals of localization in quantum theory, *Physical Review Letters* 51 (1983) 947–950.
- [99] J. Tennyson, M. A. Kostin, P. Barletta, G. J. Harris, O. L. Polyansky, J. Ramanlal, N. F. Zobov, DVR3D: a program suite for the calculation of rotation-vibration spectra of triatomic molecules, *Computer Physics Communications* 163 (2004) 85–116.
- [100] J. W. Harder, J. W. Brault, Atmospheric measurements of water vapor in the 442-nm region, *Journal of Geophysical Research: Atmospheres* 102 (1997) 6245–6252.
- [101] J. Loos, M. Birk, G. Wagner, Measurement of air-broadening line shape parameters and temperature dependence parameters of  $\text{H}_2\text{O}$  lines in the spectral ranges 1850-2280  $\text{cm}^{-1}$  and 239-4000  $\text{cm}^{-1}$ , *Journal of Quantitative Spectroscopy and Radiative Transfer* 203 (2017) 103–118. HITRAN2016 Special Issue.
- [102] M. Birk, G. Wagner, J. Loos, D. Mondelain, A. Campargue, ESA SEOM-IAS – Spectroscopic parameters database 2.3  $\mu\text{m}$  region, Technical Report, Scientific Exploitation of Operational Missions - Improved Atmospheric Spectroscopy Databases, 2017. URL: <https://doi.org/10.5281/zenodo.1009125>. doi:10.5281/zenodo.1009126.

- [103] M. Birk, G. Wagner, J. Loos, L. Lodi, O. L. Polyansky, A. A. Kyuberis, N. F. Zobov, J. Tennyson, Accurate line intensities for water transitions in the infrared: Comparison of theory and experiment, *Journal of Quantitative Spectroscopy and Radiative Transfer* 203 (2017) 88–102. HITRAN2016 Special Issue.
- [104] E. K. Conway, I. E. Gordon, O. L. Polyansky, J. Tennyson, Use of the complete basis set limit for computing highly accurate ab initio dipole moments, *Journal of Chemical Physics* 152 (2020) 024105.
- [105] R. A. Toth, K. Sung, L. R. Brown, H<sub>2</sub><sup>16</sup>O line strengths revisited:  $\nu_2$  and  $2\nu_2-\nu_2$  at 6  $\mu\text{m}$ , *Journal of Molecular Spectroscopy* 265 (2011) 59 – 68.
- [106] A. Campargue, S. Kass, A. Yachmenev, A. A. Kyuberis, J. Küpper, S. N. Yurchenko, Observation of electric-quadrupole infrared transitions in water vapor, *Physical Review Research* 2 (2020) 023091.
- [107] A. Campargue, A. M. Solodov, A. A. Solodov, A. Yachmenev, S. N. Yurchenko, Detection of electric-quadrupole transitions in water vapour near 5.4 and 2.5  $\mu\text{m}$ , *Physical Chemistry Chemical Physics* 22 (2020) 12476–12481.
- [108] S. N. Yurchenko, W. Thiel, P. Jensen, Theoretical ROVibrational Energies (TROVE): A robust numerical approach to the calculation of rovibrational energies for polyatomic molecules, *Journal of Molecular Spectroscopy* 245 (2007) 126–140.
- [109] A. Owens, A. Yachmenev, Richmol: A general variational approach for rovibrational molecular dynamics in external electric fields, *Journal of Chemical Physics* 148 (2018) 124102.
- [110] C. Borger, S. Beirle, S. Dörner, H. Sihler, T. Wagner, Total column water vapour retrieval from S-5P/TROPOMI in the visible blue spectral range, *Atmospheric Measurement Techniques* 13 (2020) 2751–2783.

- [111] W. Livingston, L. Wallace, An atlas of the solar spectrum in the infrared from 1850 to 9000  $\text{cm}^{-1}$  (1.1 to 5.4 micrometer), NSO Technical Report, Tucson: National Solar Observatory, National Optical Astronomy Observatory, 1991 -1 (2003).
- [112] M. Tanaka, O. Naumenko, J. W. Brault, J. Tennyson, Fourier transform absorption spectra of  $\text{H}_2^{18}\text{O}$  and  $\text{H}_2^{17}\text{O}$  in the  $3\nu+\delta$  and  $4\nu$  polyad region, Journal of Molecular Spectroscopy 234 (2005) 1–9.
- [113] S. Mikhailenko, V. Serdyukov, L. Sinitsa, Study of  $\text{H}_2^{16}\text{O}$  and  $\text{H}_2^{18}\text{O}$  absorption in the 16 460–17 200  $\text{cm}^{-1}$  range using LED-based Fourier transform spectroscopy, Journal of Quantitative Spectroscopy and Radiative Transfer 217 (2018) 170 – 177.
- [114] L. Lodi, J. Tennyson, Line lists for  $\text{H}_2^{18}\text{O}$  and  $\text{H}_2^{17}\text{O}$  based on empirically-adjusted line positions and *ab initio* intensities, Journal of Quantitative Spectroscopy and Radiative Transfer 113 (2012) 850–858.
- [115] O. L. Polyansky, A. A. Kyuberis, L. Lodi, J. Tennyson, R. I. Ovsyannikov, N. Zobov, ExoMol molecular line lists XIX: high accuracy computed line lists for  $\text{H}_2^{17}\text{O}$  and  $\text{H}_2^{18}\text{O}$ , Monthly Notices Royal Astronomical Society 466 (2017) 1363–1371.
- [116] S. Mikhailenko, V. Serdyukov, L. Sinitsa, LED-based Fourier transform spectroscopy of  $\text{H}_2^{18}\text{O}$  in the 15 000–16 000  $\text{cm}^{-1}$  range, Journal of Quantitative Spectroscopy and Radiative Transfer 156 (2015) 36–46.
- [117] A. A. Kyuberis, N. F. Zobov, O. V. Naumenko, B. A. Voronin, O. L. Polyansky, L. Lodi, A. Liu, S.-M. Hu, J. Tennyson, Room temperature line lists for deuterated water, Journal of Quantitative Spectroscopy and Radiative Transfer 203 (2017) 175–185.
- [118] R. R. Gamache, B. Vispoel, On the temperature dependence of half-widths and line shifts for molecular transitions in the microwave and in-

- frared regions, *Journal of Quantitative Spectroscopy and Radiative Transfer* 217 (2018) 440 – 452.
- [119] N. Stolarczyk, F. Thibault, H. Cybulski, H. Jóźwiak, G. Kowzan, B. Vispoel, I.E. Gordon, L.S. Rothman, R.R. Gamache, P. Wcisło, Evaluation of different parameterizations of temperature dependences of the line-shape parameters based on *ab initio* calculations: Case study for the HITRAN database, *Journal of Quantitative Spectroscopy and Radiative Transfer* 240 (2020) 106676.
  - [120] R. R. Gamache, J.-M. Hartmann, An intercomparison of measured pressure-broadening and pressure-shifting parameters of water vapor, *Canadian Journal of Chemistry* 82 (2004) 1013–1027.
  - [121] E. J. Mlawer, D. D. Turner, S. N. Paine, L. Palchetti, G. Bianchini, V. H. Payne, K. E. Cady-Pereira, R. L. Pernak, M. J. Alvarado, D. Gombos, J. S. Delamere, M. G. Mlynczak, J. C. Mast, Analysis of Water Vapor Absorption in the Far-Infrared and Submillimeter Regions Using Surface Radiometric Measurements From Extremely Dry Locations, *Journal of Geophysical Research: Atmospheres* 124 (2019) 8134–8160.
  - [122] B. Vispoel, J. H. Cavalcanti, R. R. Gamache, Modified complex Robert-Bonamy calculations of line shape parameters and their temperature dependence for water vapor in collision with N<sub>2</sub>, *Journal of Quantitative Spectroscopy and Radiative Transfer* 228 (2019) 79–89.
  - [123] R. R. Gamache, M. Farese, C. L. Renaud, A spectral line list for water isotopologues in the 1100–4100 cm<sup>−1</sup> region for application to CO<sub>2</sub>-rich planetary atmospheres, *Journal of Molecular Spectroscopy* 326 (2016) 144–150.
  - [124] V. Malathy Devi, D. C. Benner, K. Sung, T. J. Crawford, R. R. Gamache, C. L. Renaud, M. A. H. Smith, A. W. Mantz, G. L. Villanueva, Line parameters for CO<sub>2</sub>- and self-broadening in the  $\nu_1$  band of HD<sup>16</sup>O, *Journal of Quantitative Spectroscopy and Radiative Transfer* 203 (2017) 133–157.

- [125] V. Malathy Devi, D. C. Benner, K. Sung, T. J. Crawford, R. R. Gamache, C. L. Renaud, M. A. H. Smith, A. W. Mantz, G. L. Villanueva, Line parameters for CO<sub>2</sub>- and self-broadening in the  $\nu_3$  band of HD<sup>16</sup>O, *Journal of Quantitative Spectroscopy and Radiative Transfer* 203 (2017) 158–174.
- [126] R. R. Gamache, J.-M. Hartmann, Collisional parameters of H<sub>2</sub>O lines: effects of vibration, *Journal of Quantitative Spectroscopy and Radiative Transfer* 83 (2004) 119–147.
- [127] D. Jacquemart, R. R. Gamache, L. S. Rothman, Semi-empirical calculation of air-broadened half-widths and air pressure-induced frequency shifts of water-vapor absorption lines, *Journal of Quantitative Spectroscopy and Radiative Transfer* 96 (2005) 205–239.
- [128] R. R. Gamache, J. Lamouroux, Predicting accurate line-shape parameters for CO<sub>2</sub> transitions, *Journal of Quantitative Spectroscopy and Radiative Transfer* 130 (2013) 158–171. HITRAN2012 special issue.
- [129] R. R. Gamache, B. Vispoel, C. L. Renaud, K. Cleghorn, L. Hartmann, Vibrational dependence, temperature dependence, and prediction of line shape parameters for the H<sub>2</sub>O-H<sub>2</sub> collision system, *Icarus* 326 (2019) 186–196.
- [130] B. Vispoel, J. H. Cavalcanti, E. T. Paige, R. R. Gamache, Vibrational dependence, temperature dependence, and prediction of line shape parameters for the H<sub>2</sub>O-N<sub>2</sub> collision system, *Journal of Quantitative Spectroscopy and Radiative Transfer* 253 (2020) 107030.
- [131] G. Wagner, M. Birk, In Preparation, 2021.
- [132] M. Birk, G. Wagner, J. Loos, D. Mondelain, C. Alain, ESA SEOM-IAS – Measurement database 2.3  $\mu$ m region, *Zenodo* (2017).
- [133] C. E. Miller, L. R. Brown, R. A. Toth, D. C. Benner, V. M. Devi, Spectroscopic challenges for high accuracy retrievals of atmospheric CO<sub>2</sub> and

the Orbiting Carbon Observatory (OCO) experiment, *Comptes Rendus Physique* 6 (2005) 876–887.

- [134] E. V. Karlovets, I. E. Gordon, L. S. Rothman, R. Hashemi, R. J. Hargreaves, G. Toon, A. Campargue, V. I. Perevalov, S. N. Yurchenko, The updated line lists of carbon dioxide for the HITRAN2020 spectroscopic database, *Journal of Quantitative Spectroscopy and Radiative Transfer* In Preparation (2021).
- [135] S. A. Tashkun, V. I. Perevalov, R. R. Gamache, J. Lamouroux, CDSD-296, high resolution carbon dioxide spectroscopic databank: Version for atmospheric applications, *Journal of Quantitative Spectroscopy and Radiative Transfer* 152 (2015) 45–73.
- [136] O. L. Polyansky, K. Bielska, M. Ghysels, L. Lodi, N. F. Zobov, J. T. Hodges, J. Tennyson, High accuracy CO<sub>2</sub> line intensities determined from theory and experiment, *Phys. Rev. Lett.* 114 (2015) 243001.
- [137] E. J. Zak, O. L. Polyanski, L. Lodi, N. F. Zobov, S. A. Tashkun, V. I. Perevalov, A room temperature CO<sub>2</sub> line list with *ab initio* computed intensities, *Journal of Quantitative Spectroscopy and Radiative Transfer* 177 (2016) 31–42.
- [138] E. J. Zak, J. Tennyson, O. L. Polyansky, L. Lodi, N. F. Zobov, S. A. Tashkun, V. I. Perevalov, Room temperature line lists for CO<sub>2</sub> symmetric isotopologues with *ab initio* computed intensities, *Journal of Quantitative Spectroscopy and Radiative Transfer* 189 (2017) 267–280.
- [139] E. J. Zak, J. Tennyson, O. L. Polyansky, L. Lodi, N. F. Zobov, S. A. Tashkun, V. I. Perevalov, Room temperature linelists for CO<sub>2</sub> asymmetric isotopologues with *ab initio* computed intensities, *Journal of Quantitative Spectroscopy and Radiative Transfer* 203 (2017) 265–281.
- [140] S. A. Tashkun, V. I. Perevalov, R. R. Gamache, J. Lamouroux, CDSD-296, high-resolution carbon dioxide spectroscopic databank: An update,

- Journal of Quantitative Spectroscopy and Radiative Transfer 228 (2019) 124–131.
- [141] S. N. Yurchenko, T. M. Mellor, R. S. Freedman, J. Tennyson, ExoMol line lists - XXXIX. Ro-vibrational molecular line list for CO<sub>2</sub>, Monthly Notices of the Royal Astronomical Society 496 (2020) 5282–5291.
  - [142] X. Huang, D. W. Schwenke, R. S. Freedman, T. J. Lee, Ames-2016 line lists for 13 isotopologues of CO<sub>2</sub>: Updates, consistency, and remaining issues, Journal of Quantitative Spectroscopy and Radiative Transfer 203 (2017) 224–241.
  - [143] E. V. Karlovets, S. Kass, A. Campargue, High sensitivity CRDS of CO<sub>2</sub> in the 1.18  $\mu$ m transparency window. Validation tests of current spectroscopic databases, Journal of Quantitative Spectroscopy and Radiative Transfer 247 (2020) 106942.
  - [144] V. I. Perevalov, S. A. Tashkun, CDSD-296 (Carbon Dioxide Spectroscopic Databank): Updated and Enlarged Version for Atmospheric Applications, in: 10th Biennial HITRAN Conference, 2008, p. 7. doi:10.5281/zenodo.17520.
  - [145] G. C. Toon, CO<sub>2</sub> Spectroscopy Evaluation: 670 to 7000 cm<sup>-1</sup>, 2020. URL: <https://mark4sun.jpl.nasa.gov/presentation.html>, reports and Presentations for the HITRAN meeting, Jun 2020, Jet Propulsion Laboratory, California Institute of Technology.
  - [146] G. C. Toon, CO<sub>2</sub> Spectroscopy Evaluation: 670 to 7000 cm<sup>-1</sup>, 2018. URL: <https://mark4sun.jpl.nasa.gov/presentation.html>, reports and Presentations for the ACE STM, Oct 2018, Jet Propulsion Laboratory, California Institute of Technology.
  - [147] J. J. Butler, X. J. Xiong, X. Gu, Measuring atmospheric carbon dioxide from space with the Orbiting Carbon Observatory-2 (OCO-2), in: J. J.



- Butler, X. J. Xiong, X. Gu (Eds.), *Earth Observing Systems XX*, volume 9607 of *Society of Photo-Optical Instrumentation Engineers (SPIE) Conference Series*, 2015, p. E2. doi:10.1117/12.2187291.
- [148] P. Čermák, E. V. Karlovets, D. Mondelain, S. Kassi, V. I. Perevalov, A. Campargue, High sensitivity CRDS of CO<sub>2</sub> in the 1.74  $\mu\text{m}$  transparency window. A validation test for the spectroscopic databases, *Journal of Quantitative Spectroscopy and Radiative Transfer* 207 (2018) 95–103.
- [149] E. V. Karlovets, P. Čermák, D. Mondelain, S. Kassi, A. Campargue, S. A. Tashkun, V. I. Perevalov, Analysis and theoretical modeling of the <sup>18</sup>O enriched carbon dioxide spectrum by CRDS near 1.74  $\mu\text{m}$ , *Journal of Quantitative Spectroscopy and Radiative Transfer* 217 (2018) 73–85.
- [150] E. V. Karlovets, A. D. Sidorenko, P. Čermák, D. Mondelain, S. Kassi, V. I. Perevalov, A. Campargue, The <sup>13</sup>CO<sub>2</sub> absorption spectrum by CRDS near 1.74  $\mu\text{m}$ , *Journal of Molecular Spectroscopy* 354 (2018) 54–59.
- [151] H. Fleurbaey, H. Yi, E. M. Adkins, A. J. Fleisher, J. T. Hodges, Cavity ring-down spectroscopy of CO<sub>2</sub> near  $\lambda = 2.06 \mu\text{m}$ : Accurate transition intensities for the Orbiting Carbon Observatory-2 (OCO-2) “strong band”, *Journal of Quantitative Spectroscopy and Radiative Transfer* 252 (2020) 107104.
- [152] D. A. Long, Z. D. Reed, A. J. Fleisher, J. Mendonca, S. Roche, J. T. Hodges, High-Accuracy Near-Infrared Carbon Dioxide Intensity Measurements to Support Remote Sensing, *Geophysical Research Letters* 47 (2020) e2019GL086344.
- [153] M. Birk, C. Röske, G. Wagner, High accuracy CO<sub>2</sub> Fourier transform measurements in the range 6000–7000  $\text{cm}^{-1}$ , *Journal of Quantitative Spectroscopy and Radiative Transfer* submitted to HITRAN2020 special issue (2021).

- [154] M. Birk, C. Röske, G. Wagner, Measurement and line parameter database CO<sub>2</sub> 6000-7000 cm<sup>-1</sup>, Zenodo (2021).
- [155] J. F. Campbell, B. Lin, J. Dobler, S. Pal, K. Davis, M. D. Obland, W. Erxleben, D. McGregor, C. O'Dell, E. Bell, B. Weir, T. Fan, S. Kooi, I. Gordon, A. Corbett, R. Kochanov, Field Evaluation of Column CO<sub>2</sub> Retrievals From Intensity-Modulated Continuous-Wave Differential Absorption Lidar Measurements During the ACT-America Campaign, *Earth and Space Science* 7 (2020) e2019EA000847.
- [156] A. Trokhimovskiy, V. Perevalov, O. Korablev, A. A. Fedorova, K. S. Olsen, J. L. Bertaux, A. Patrakeeve, A. Shakun, F. Montmessin, F. Lefèvre, A. Lukashevskaya, First observation of the magnetic dipole CO<sub>2</sub> absorption band at 3.3  $\mu$ m in the atmosphere of Mars by the ExoMars Trace Gas Orbiter ACS instrument, *Astronomy & Astrophysics* 639 (2020) A142.
- [157] V. I. Perevalov, A. Y. Trokhimovskiy, A. A. Lukashevskaya, O. I. Korablev, A. Fedorova, F. Montmessin, Magnetic dipole and electric quadrupole absorption in carbon dioxide, *Journal of Quantitative Spectroscopy and Radiative Transfer* 259 (2021) 107408.
- [158] Y. G. Borkov, A. M. Solodov, A. A. Solodov, V. I. Perevalov, Line intensities of the 01111-00001 magnetic dipole absorption band of <sup>12</sup>C<sup>16</sup>O<sub>2</sub>: Laboratory measurements, *Journal of Molecular Spectroscopy* 376 (2021) 111418.
- [159] Z. Majcherova, P. Macko, D. Romanini, V. I. Perevalov, S. A. Tashkun, J. L. Teffo, A. Campargue, High-sensitivity CW-cavity ringdown spectroscopy of <sup>12</sup>CO<sub>2</sub> near 1.5  $\mu$ m, *Journal of Molecular Spectroscopy* 230 (2005) 1–21.
- [160] H. Fleurbaey, R. Grilli, D. Mondelain, S. Kassi, A. Yachmenev, S. N. Yurchenko, A. Campargue, Electric-quadrupole and magnetic-dipole contributions to the  $\nu_2 + \nu_3$  band of carbon dioxide near 3.3  $\mu$ m, *Journal of Quantitative Spectroscopy and Radiative Transfer* (2021) 107558.

- [161] R. Hashemi, I. E. Gordon, H. Tran, R. V. Kochanov, E. V. Karlovets, Y. Tan, J. Lamouroux, N. H. Ngo, L. S. Rothman, Revising the line-shape parameters for air- and self-broadened CO<sub>2</sub> lines toward a sub-percent accuracy level, *Journal of Quantitative Spectroscopy and Radiative Transfer* 256 (2020) 107283.
- [162] W. Voigt, Über das gesetz intensitätsverteilung innerhalb der linien eines gas spektrums., *Sitzber. Bayr Akad. München Ber.* 603 (1912) 18.
- [163] A. S. Pine, Line shape asymmetries in Ar-broadened HF ( $\nu = 1-0$ ) in the Dicke-narrowing regime, *Journal of Chemical Physics* 101 (1994) 3444–3452.
- [164] H. M. Pickett, Effects of velocity averaging on the shapes of absorption lines, *Journal of Chemical Physics* 73 (1980) 6090–6094.
- [165] P. Wcisło, I.E. Gordon, H. Tran, Y. Tan, S.-M. Hu, A. Campargue, S. Kassi and D. Romanini, C. Hill, R.V. Kochanov, L.S. Rothman, The implementation of non-Voigt line profiles in the HITRAN database: H<sub>2</sub> case study, *Journal of Quantitative Spectroscopy and Radiative Transfer* 177 (2016) 75–91.
- [166] J. Lamouroux, L. Régalia, X. Thomas, J. Vander Auwera, R. R. Gamache, J. M. Hartmann, CO<sub>2</sub> line-mixing database and software update and its tests in the 2.1  $\mu\text{m}$  and 4.3  $\mu\text{m}$  regions, *Journal of Quantitative Spectroscopy and Radiative Transfer* 151 (2015) 88–96.
- [167] D.A. Long and S. Wójtewicz and C.E. Miller and J.T. Hodges, Frequency-agile, rapid scanning cavity ring-down spectroscopy (FARS-CRDS) measurements of the 30012–00001 near-infrared carbon dioxide band, *Journal of Quantitative Spectroscopy and Radiative Transfer* 161 (2015) 35 – 40.
- [168] D. A. Long, K. Bielska, D. Lisak, Daniel D. K. Havey, M. Okumura, C. E. Miller, J. T. Hodges, The air-broadened, near-infrared CO<sub>2</sub> line-shape in

- the spectrally isolated regime: Evidence of simultaneous Dicke narrowing and speed dependence, *Journal of Chemical Physics* 135 (2011) 064308.
- [169] T. Q. Bui, D. A. Long, A. Cygan, V. T. Sironneau, D. W. Hogan, P. M. Rupasinghe, R. Ciuryło, D. Lisak, M. Okumura, Observations of Dicke narrowing and speed dependence in air-broadened CO<sub>2</sub> line-shapes near 2.06  $\mu\text{m}$ , *Journal of Chemical Physics* 141 (2014) 174301.
- [170] M. V. Devi, D. C. Benner, K. Sung L. R. Brown, T. J. Crawford, C. E. Miller, B. J. Drouin, V. H. Payne, S. Yu, M. A. H. Smith, A. W. Mantz, R. R. Gamache, Line parameters including temperature dependences of self- and air-broadened line-shapes of <sup>12</sup>C<sup>16</sup>O<sub>2</sub>: 1.6  $\mu\text{m}$  region, *Journal of Quantitative Spectroscopy and Radiative Transfer* 177 (2016) 117–144.
- [171] R. Hashemi, H. Rozario, A. Ibrahim, A. Predoi-Cross, line-shape study of the carbon dioxide laser band I, *Canadian Journal of Physics* 91 (2013) 924–936.
- [172] A. Predoi-Cross, W. Liu, C. Holladay, A. Unni, I. Schofield, A. McKellar, D. Hurtmans, Line profile study of transitions in the 30012–00001 and 30013–00001 bands of carbon dioxide perturbed by air, *Journal of Molecular Spectroscopy* 246 (2007) 98–112.
- [173] J.-M. Hartmann, A simple empirical model for the collisional spectral shift of air-broadened CO<sub>2</sub> lines, *Journal of Quantitative Spectroscopy and Radiative Transfer* 110 (2009) 2019–2026.
- [174] H. Nguyen, N. Ngo, H. Tran, Line-shape parameters and their temperature dependence predicted from molecular dynamics simulations for O<sub>2</sub>- and air-broadened CO<sub>2</sub> lines, *Journal of Quantitative Spectroscopy and Radiative Transfer* 242 (2020) 106729.
- [175] E. M. Adkins, D.A. Long and J.T. Hodges, Air-broadening in near-infrared carbon dioxide line-shapes: quantifying contributions from O<sub>2</sub>,

- N<sub>2</sub> and Ar, *Journal of Quantitative Spectroscopy and Radiative Transfer*, submitted to HITRAN2020 special issue (2021).
- [176] A. Predoi-Cross, A. Unni, W. Liu, I. Schofield, C. Holladay, A. McKellar, D. Hurtmans, Line-shape parameters measurement and computations for self-broadened carbon dioxide transitions in the 30012–00001 and 30013–00001 bands, line mixing, and speed dependence, *Journal of Molecular Spectroscopy* 245 (2007) 34–51.
  - [177] L. Daneshvar, T. Földes, J. Buldyreva, J. Vander Auwera, Infrared absorption by pure CO<sub>2</sub> near 3340 cm<sup>−1</sup>: Measurements and analysis of collisional coefficients and line mixing effects at subatmospheric pressures, *Journal of Quantitative Spectroscopy and Radiative Transfer* 149 (2014) 258–274.
  - [178] R. R. Gamache, C. Roller, E. Lopes, I. E. Gordon, L. S. Rothman, O. L. Polyansky, N. F. Zobov, A. A. Kyuberis, J. Tennyson, S. N. Yurchenko, A. G. Császár, T. Furtenbacher, X. Huang, D. W. Schwenke, T. J. Lee, B. J. Drouin, S. A. Tashkun, V. I. Perevalov, R. V. Kochanov, Total internal partition sums for 166 isotopologues of 51 molecules important in planetary atmospheres: Application to HITRAN2016 and beyond, *Journal of Quantitative Spectroscopy and Radiative Transfer* 203 (2017) 70–87.
  - [179] R. Hashemi, CO<sub>2</sub> absorption coefficients (ABSCO) tables for the 4700 to 5100 cm<sup>−1</sup> region using Voigt profile accounting for the line mixing, 2020. URL: <https://doi.org/10.5281/zenodo.4126999>. doi:10.5281/zenodo.4126999.
  - [180] L. Rosenmann, J.-M. Hartmann, M.-Y. Perrin, J. Taine, Accurate calculated tabulations of IR and Raman CO<sub>2</sub> line broadening by CO<sub>2</sub>, H<sub>2</sub>O, N<sub>2</sub>, O<sub>2</sub> in the 300–2400 K temperature range, *Applied Optics* 27 (1988) 3902–3907.
  - [181] L. Rosenmann, M. Y. Perrin, J. M. Hartmann, J. Taine, Diode-laser measurements and calculations of CO<sub>2</sub>-line-broadening by H<sub>2</sub>O from 416 to

- 805K and by N<sub>2</sub> from 296 to 803 K., *Journal of Quantitative Spectroscopy and Radiative Transfer* 40 (1988) 569–576.
- [182] K. Sung, L. R. Brown, R. A. Toth, T. J. Crawford, Fourier transform infrared spectroscopy measurements of H<sub>2</sub>O-broadened half-widths of CO<sub>2</sub> at 4.3  $\mu$ m, *Canadian Journal of Physics* 87 (2009) 469–484.
  - [183] C. J. Wallace, C. Jeon, C. N. Anderson, D. K. Havey, H<sub>2</sub>O broadening of a CO<sub>2</sub> line and its nearest neighbors near 6360 cm<sup>-1</sup>, *Journal of Physical Chemistry A* 115 (2011) 13804–13810.
  - [184] T. Delahaye, X. Landsheere, E. Pangui, F. Huet, J. M. Hartmann, H. Tran, Broadening of CO<sub>2</sub> lines in the 4.3  $\mu$ m region by H<sub>2</sub>O, *Journal of Molecular Spectroscopy* 326 (2016) 17–20.
  - [185] C. Clerbaux, A. Boynard, L. Clarisse, M. George, J. Hadji-Lazaro, H. Herbin, D. Hurtmans, M. Pommier, A. Razavi, S. Turquety, C. Wespes, P. F. Coheur, Monitoring of atmospheric composition using the thermal infrared IASI/MetOp sounder, *Atmospheric Chemistry and Physics* 9 (2009) 6041–6054.
  - [186] E. Hilsenrath, W. Attmannspacher, A. Bass, W. Evans, R. Hagemeyer, R. A. Barnes, W. Komhyr, K. Mauersberger, J. Mentall, M. Proffitt, D. Robbins, S. Taylor, A. Torres, E. Weinstock, Results from the balloon ozone intercomparison campaign (BOIC), *Journal of Geophysical Research* 91 (1986) 13137.
  - [187] I. Murata, K. Sato, S. Okano, Y. Tomikawa, Measurements of stratospheric ozone with a balloon-borne optical ozone sensor, *International Journal of Remote Sensing* 30 (2009) 3961–3966.
  - [188] D. Hubert, J. C. Lambert, T. Verhoelst, J. Granville, A. Keppens, J. L. Baray, A. E. Bourassa, U. Cortesi, D. A. Degenstein, L. Froidevaux, S. Godin-Beekmann, K. W. Hoppel, B. J. Johnson, E. Kyrölä, T. Leblanc, G. Lichtenberg, M. Marchand, C. T. McElroy, D. Murtagh, H. Nakane,

- T. Portafaix, R. Querel, J. M. Russell, J. Salvador, H. G. Smit, K. Stebel, W. Steinbrecht, K. B. Strawbridge, R. Stübi, D. P. Swart, G. Taha, D. W. Tarasick, A. M. Thompson, J. Urban, J. A. Van Gijsel, R. Van Malderen, P. Von Der Gathen, K. A. Walker, E. Wolfram, J. M. Zawodny, Ground-based assessment of the bias and long-term stability of 14 limb and occultation ozone profile data records, *Atmospheric Measurement Techniques* 9 (2016) 2497–2534.
- [189] A. Barbe, S. Mikhailenko, E. Starikova, M. R. De Backer, V. G. Tyuterev, D. Mondelain, S. Kassi, A. Campargue, C. Janssen, S. Tashkun, R. Kochanov, R. Gamache, J. Orphal, Ozone spectroscopy in the electronic ground state: High-resolution spectra analyses and update of line parameters since 2003, *Journal of Quantitative Spectroscopy and Radiative Transfer* 130 (2013) 172–190.
- [190] G. Toon, Evaluation of HITRAN 2016 O<sub>3</sub> linelist, (private communication), 2017. URL: [https://mark4sun.jpl.nasa.gov/report/o3\\_spectroscopy\\_evaluation\\_20170930.compressed.pdf](https://mark4sun.jpl.nasa.gov/report/o3_spectroscopy_evaluation_20170930.compressed.pdf).
- [191] M. Birk, G. Wagner, J. M. Flaud, Experimental Linestrengths of Far-Infrared Pure Rotational Transitions of Ozone, *Journal of Molecular Spectroscopy* 163 (1994) 245–261.
- [192] Y. L. Babikov, S. N. Mikhailenko, A. Barbe, V. G. Tyuterev, S&MPO - An information system for ozone spectroscopy on the WEB, *Journal of Quantitative Spectroscopy and Radiative Transfer* 145 (2014) 169–196.
- [193] B. J. Drouin, T. J. Crawford, S. Yu, Validation of ozone intensities at 10  $\mu$ m with THz spectrometry, *Journal of Quantitative Spectroscopy and Radiative Transfer* 203 (2017) 282–292.
- [194] C. Janssen, C. Boursier, H. Elandaloussi, P. Jeseck, D. Koshelev, C. Marie-Jeanne, P. Rouillé, D. Jacquemart, F. Thibout, M. Vaudescal-Escudier, Y. Té, Multi-spectral investigation of ozone: Part I. Setup & uncertainty

- p>budget,
- Journal of Quantitative Spectroscopy and Radiative Transfer*
- (2021). This issue.
- [195] D. Jacquemart, C. Boursier, H. Elandaloussi, P. Jeseck, Y. Té, C. Janssen, Multi-spectral investigation of ozone: Part II. Line intensities at 5  $\mu\text{m}$  and 10  $\mu\text{m}$  at one percent accuracy, *Journal of Quantitative Spectroscopy and Radiative Transfer* (2021). This issue.
- [196] G. Wagner, M. Birk, J.-M. Flaud, In Preparation, 2021.
- [197] J. M. Flaud, R. Bacis, The ozone molecule: infrared and microwave spectroscopy, *Spectrochimica Acta Part A: Molecular Spectroscopy* 54 (1998) 3–16.
- [198] M. Birk, G. Wagner, I. E. Gordon, B. J. Drouin, Ozone intensities in the rotational bands, *Journal of Quantitative Spectroscopy and Radiative Transfer* 226 (2019) 60–65.
- [199] V. G. Tyuterev, A. Barbe, D. Jacquemart, C. Janssen, S. N. Mikhailenko, E. N. Starikova, *Ab initio* predictions and laboratory validation for consistent ozone intensities in the MW, 10 and 5  $\mu\text{m}$  ranges, *Journal of Chemical Physics* 150 (2019) 184303.
- [200] V. Tyuterev, A. Barbe, M. S., S. E., B. Yu., Towards the intensity consistency of the ozone bands in the infrared range: ab initio corrections to the S&MPO database, *Journal of Quantitative Spectroscopy and Radiative Transfer* In Preparation (2021).
- [201] A. Barbe, S. Mikhailenko, E. Starikova, V. Tyuterev, Ozone FTS spectra in the infrared range revisited, *Journal of Quantitative Spectroscopy and Radiative Transfer* In Preparation (2021).
- [202] A. Barbe, E. Starikova, M.-R. De Backer, High resolution infrared spectra of the  $^{16}\text{O}^{16}\text{O}^{17}\text{O}$  and the  $^{16}\text{O}^{17}\text{O}^{16}\text{O}$  ozone isotopic species. The 5 and 10 micron spectral ranges revisited, *Journal of Quantitative Spectroscopy and Radiative Transfer* 203 (2017) 293–299.



- [203] A. Barbe, E. Starikova, M. R. De Backer, V. G. Tyuterev, Analyses of infrared FT spectra of asymmetric ozone isotopologue  $^{16}\text{O}^{16}\text{O}^{18}\text{O}$  in the range  $950\text{--}3850\text{ cm}^{-1}$ , *Journal of Quantitative Spectroscopy and Radiative Transfer* 218 (2018) 231–247.
- [204] G. Guillon, P. Honvault, R. Kochanov, V. Tyuterev, First-Principles Computed Rate Constant for the  $\text{O}+\text{O}_2$  Isotopic Exchange Reaction Now Matches Experiment, *The Journal of Physical Chemistry Letters* 9 (2018) 1931–1936.
- [205] C. H. Yuen, D. Lapierre, F. Gatti, V. Kokoouline, V. G. Tyuterev, The Role of Ozone Vibrational Resonances in the Isotope Exchange Reaction  $16\text{O}16\text{O} + 18\text{O} \rightarrow 18\text{O}16\text{O} + 16\text{O}$ : The Time-Dependent Picture, *Journal of Physical Chemistry A* 123 (2019) 7733–7743.
- [206] V. Kokoouline, D. Lapierre, A. Alijah, V. Tyuterev, Localized and delocalized bound states of the main isotopologue  $48\text{O}3$  and of  $18\text{O}$ -enriched  $50\text{O}3$  isotopomers of the ozone molecule near the dissociation threshold, *Physical Chemistry Chemical Physics (Incorporating Faraday Transactions)* 22 (2020) 15885–15899.
- [207] S. Vasilchenko, A. Barbe, E. Starikova, S. Kassi, D. Mondelain, A. Campargue, V. Tyuterev, Detection and assignment of ozone bands near 95% of the dissociation threshold: Ultrasensitive experiments for probing potential energy function and vibrational dynamics, *Physical Review A* 102 (2020) 052804.
- [208] V. G. Tyuterev, R. V. Kochanov, S. A. Tashkun, F. Holka, P. G. Szalay, New analytical model for the ozone electronic ground state potential surface and accurate ab initio vibrational predictions at high energy range, *Journal of Chemical Physics* 139 (2013) 134307–134307.
- [209] V. G. Tyuterev, R. V. Kochanov, S. A. Tashkun, Accurate ab initio dipole moment surfaces of ozone: First principle intensity predictions for

- rotationally resolved spectra in a large range of overtone and combination bands, *Journal of Chemical Physics* 146 (2017) 064304.
- [210] K. M. Mack, J. S. Muentner, Stark and Zeeman properties of ozone from molecular beam spectroscopy, *Journal of Chemical Physics* 66 (1977) 5278–5283.
- [211] S. Mikhailenko, A. Barbe, High resolution infrared spectrum of  $^{16}\text{O}_3$ : The 3600–4300  $\text{cm}^{-1}$  range reinvestigated, *Journal of Quantitative Spectroscopy and Radiative Transfer* 244 (2020) 106823.
- [212] V. G. Tyuterev, S. A. Tashkun, H. Seghir, High-order contact transformations: general algorithm, computer implementation, and triatomic tests, in: L. N. Sinita, S. N. Mikhailenko (Eds.), 14th Symposium on High-Resolution Molecular Spectroscopy, volume 5311 of *Society of Photo-Optical Instrumentation Engineers (SPIE) Conference Series*, 2004, pp. 164–175. doi:10.1117/12.545641.
- [213] S. N. Mikhailenko, V. G. Tyuterev, V. I. Starikov, K. K. Albert, B. P. Winnewisser, M. Winnewisser, G. Mellau, C. Camy-Peyret, R. Lanquetin, J. M. Flaud, J. W. Brault, Water Spectra in the Region 4200–6250  $\text{cm}^{-1}$ , Extended Analysis of  $\nu_1 + \nu_2$ ,  $\nu_2 + \nu_3$ , and  $3\nu_2$  Bands and Confirmation of Highly Excited States from Flame Spectra and from Atmospheric Long-Path Observations, *Journal of Molecular Spectroscopy* 213 (2002) 91–121.
- [214] M. Heyart, A. Perrin, J.-M. Flaud, C. Camy-Peyret, C. Rinsland, M. Smith, V. Malathy Devi, The  $\nu_1$  and  $\nu_3$  bands of  $^{16}\text{O}^{17}\text{O}^{16}\text{O}$  line positions and intensities, *Journal of Molecular Spectroscopy* 156 (1992) 210–216.
- [215] A. Perrin, J. M. Flaud, F. Keller, M. A. H. Smith, C. P. Rinsland, V. M. Devi, D. C. Benner, T. M. Stephen, A. Goldman, The  $\nu_1 + \nu_3$  Bands of the  $^{16}\text{O}^{17}\text{O}^{16}\text{O}$  and  $^{16}\text{O}^{16}\text{O}^{17}\text{O}$  Isotopomers of Ozone, *Journal of Molecular Spectroscopy* 207 (2001) 54–59.

- [216] G. Wagner, M. Birk, New infrared spectroscopic database for bromine nitrate, *Journal of Molecular Spectroscopy* 326 (2016) 95–105.
- [217] G. Wagner, M. Birk, F. Schreier, J. M. Flaud, Spectroscopic database for ozone in the fundamental spectral regions, *Journal of Geophysical Research (Atmospheres)* 107 (2002) 4626.
- [218] M. Birk, G. Wagner, A. Barbe, M.-R. De Backer, M. Rotger, J.-M. Flaud, ESA SEOM-IAS - Measurement and line parameter database O<sub>3</sub> MIR region, Zenodo (2021).
- [219] M. Minissale, T. Zanon-Willette, P. Jeseck, C. Boursier, C. Janssen, First pressure shift measurement of ozone molecular lines at 9.54  $\mu\text{m}$  using a tunable quantum cascade laser, *Journal of Molecular Spectroscopy* 348 (2018) 103–113.
- [220] D. Jacquemart, O. Polyansky, V. Maknev, J. Tennyson, Synthesis of *ab initio* and effective Hamiltonian line lists for ozone, *Journal of Quantitative Spectroscopy and Radiative Transfer* (2021). This issue.
- [221] O. L. Polyansky, N. F. Zobov, I. I. Mizus, A. A. Kyuberis, L. Lodi, J. Tennyson, Potential energy surface, dipole moment surface and the intensity calculations for the 10  $\mu\text{m}$ , 5  $\mu\text{m}$  and 3  $\mu\text{m}$  bands of ozone, *Journal of Quantitative Spectroscopy and Radiative Transfer* 210 (2018) 127–135.
- [222] J. M. Flaud, G. Wagner, M. Birk, C. Camy-Peyret, C. Claveau, M. R. de Backer-Barilly, A. Barbe, C. Piccolo, Ozone absorption around 10  $\mu\text{m}$ , *Journal of Geophysical Research (Atmospheres)* 108 (2003) 4269.
- [223] J. M. Flaud, Effective Hamiltonian calculation at 10  $\mu\text{m}$ , 2019. Private communication.
- [224] G. C. Toon, Ozone Spectroscopy Evaluation, 2020. URL: [https://mark4sun.jpl.nasa.gov/report/O3\\_Spectroscopy\\_Eval\\_2020\\_11\\_30.pdf](https://mark4sun.jpl.nasa.gov/report/O3_Spectroscopy_Eval_2020_11_30.pdf), report, Jet Propulsion Laboratory, California Institute of Technology.

- [225] H. M. Pickett, R. L. Poynter, E. A. Cohen, M. L. Delitsky, J. C. Pearson, H. S. P. Müller, Submillimeter, millimeter and microwave spectral line catalog., *Journal of Quantitative Spectroscopy and Radiative Transfer* 60 (1998) 883–890.
- [226] E. M. Adkins, D. A. Long, A. J. Fleisher, J. T. Hodges, Near-infrared cavity ring-down spectroscopy measurements of nitrous oxide in the (4200) $\leftarrow$ (0000) and (5000) $\leftarrow$ (0000) bands, *Journal of Quantitative Spectroscopy and Radiative Transfer* 262 (2021) 107527.
- [227] R. A. Toth, Linelist of N<sub>2</sub>O parameters from 500 to 7500 cm<sup>-1</sup>, JPL online, <https://mark4sun.jpl.nasa.gov/n2o.html> (2004).
- [228] L. Daumont, J. Vander Auwera, J.-L. Teffo, V. I. Perevalov, S. A. Tashkun, Line intensity measurements in <sup>14</sup>N<sub>2</sub><sup>16</sup>O and their treatment using the effective dipole moment approach II. The 5400–11 000 cm<sup>-1</sup> region, *Journal of Quantitative Spectroscopy and Radiative Transfer* 104 (2007) 342–356.
- [229] C. D. Boone, P. F. Bernath, D. Cok, S. C. Jones, J. Steffen, Version 4 retrievals for the atmospheric chemistry experiment Fourier transform spectrometer (ACE-FTS) and imagers, *Journal of Quantitative Spectroscopy and Radiative Transfer* 247 (2020) 106939.
- [230] P. Rosenkranz, Shape of the 5 mm oxygen band in the atmosphere, *IEEE Transactions on Antennas and Propagation* 23 (1975) 498–506.
- [231] R. Hashemi, I. E. Gordon, J. T. Hodges, D. A. Long, E. M. Adkins, M. Birk, A. Predoi-Cross, L. S. Rothman, Improvement of the spectroscopic parameters of the air- and self-broadened N<sub>2</sub>O and CO lines, toward HITRAN2020, *Journal of Quantitative Spectroscopy and Radiative Transfer*. In Preparation (2021).
- [232] N. Lacome, A. Levy, G. Guelachvili, Fourier transform measurement of

- self-, N<sub>2</sub>-, and O<sub>2</sub>-broadening of N<sub>2</sub>O lines: Temperature dependence of linewidths, *Applied Optics* 23 (1984) 425–435.
- [233] R. A. Toth, Line strengths (900–3600 cm<sup>-1</sup>), self-broadened linewidths, and frequency shifts (1800–2360 cm<sup>-1</sup>) of N<sub>2</sub>O, *Applied Optics* 32 (1993) 7326–7365.
- [234] V. Nemtchinov, C. Sun, Prasad Varanasi, Measurements of line intensities and line widths in the  $\nu_3$ -fundamental band of nitrous oxide at atmospheric temperatures, *Journal of Quantitative Spectroscopy and Radiative Transfer* 83 (2004) 267–284.
- [235] R. A. Toth, N<sub>2</sub>- and air-broadened linewidths and frequency-shifts of N<sub>2</sub>O, *Journal of Quantitative Spectroscopy and Radiative Transfer* 66 (2000) 285–304.
- [236] E. M. Adkins, MATS: Multi-spectrum Analysis Tool for Spectroscopy, NIST online, <https://pages.nist.gov/MATS/> (2020).
- [237] V. Werwein, J. Brunzendorf, A. Serdyukov, O. Werhahn, V. Ebert, First measurements of nitrous oxide self-broadening and self-shift coefficients in the 0002-0000 band at 2.26  $\mu\text{m}$  using high resolution Fourier transform spectroscopy, *Journal of Molecular Spectroscopy* 323 (2016) 28–42. *Atmospheric Spectroscopy*.
- [238] J. Loos, M. Birk, G. Wagner, Pressure broadening, -shift, speed dependence and line mixing in the  $\nu_3$  rovibrational band of N<sub>2</sub>O, *Journal of Quantitative Spectroscopy and Radiative Transfer* 151 (2015) 300–309.
- [239] T. Odintsova, E. Fasci, S. Gravina, L. Gianfrani, A. Castrillo, Optical feedback laser absorption spectroscopy of N<sub>2</sub>O at 2  $\mu\text{m}$ , *Journal of Quantitative Spectroscopy and Radiative Transfer* 254 (2020) 107190.
- [240] B. Gentry, L. L. Strow, Line mixing in a N<sub>2</sub>-broadened CO<sub>2</sub> Q branch observed with a tunable diode laser, *Journal of Chemical Physics* 86 (1987) 5722–5730.

- [241] S. A. Tashkun, V. I. Perevalov, N. N. Lavrentieva, NOSD-1000, the high-temperature nitrous oxide spectroscopic databank, *Journal of Quantitative Spectroscopy and Radiative Transfer* 177 (2016) 43–48.
- [242] S. W. Sharpe, T. J. Johnson, R. L. Sams, P. M. Chu, G. C. Rhoderick, P. A. Johnson, Gas-Phase Databases for Quantitative Infrared Spectroscopy, *Applied Spectroscopy* 58 (2004) 1452–1461.
- [243] S. A. Tashkun, V. I. Perevalov, E. V. Karlovets, S. Kass, A. Campargue, High sensitivity cavity ring down spectroscopy of  $\text{N}_2\text{O}$  near  $1.22\ \mu\text{m}$ : (II)  $^{14}\text{N}_2^{16}\text{O}$  line intensity modeling and global fit of  $^{14}\text{N}_2^{18}\text{O}$  line positions, *Journal of Quantitative Spectroscopy and Radiative Transfer* 176 (2016) 62–69.
- [244] R. A. Toth, Line Positions and Strengths of  $\text{N}_2\text{O}$  between 3515 and 7800  $\text{cm}^{-1}$ , *Journal of Molecular Spectroscopy* 197 (1999) 158–187.
- [245] E. Karlovets, S. Kass, S. Tashkun, A. Campargue, The absorption spectrum of nitrous oxide between 8325 and 8622  $\text{cm}^{-1}$ , *Journal of Quantitative Spectroscopy and Radiative Transfer* 262 (2021) 107508.
- [246] A. W. Liu, S. Kass, P. Malara, D. Romanini, V. I. Perevalov, S. A. Tashkun, S. M. Hu, A. Campargue, High sensitivity CW-cavity ring down spectroscopy of  $\text{N}_2\text{O}$  near  $1.5\ \mu\text{m}$  (I), *Journal of Molecular Spectroscopy* 244 (2007) 33–47.
- [247] A. W. Liu, S. Kass, V. I. Perevalov, S. A. Tashkun, A. Campargue, High sensitivity CW-Cavity Ring Down Spectroscopy of  $\text{N}_2\text{O}$  near  $1.5\ \mu\text{m}$  (II), *Journal of Molecular Spectroscopy* 244 (2007) 48–62.
- [248] Y. Lu, D. Mondelain, A. W. Liu, V. I. Perevalov, S. Kass, A. Campargue, High sensitivity CW-Cavity Ring Down Spectroscopy of  $\text{N}_2\text{O}$  between 6950 and 7653  $\text{cm}^{-1}$  ( $1.44\text{--}1.31\ \mu\text{m}$ ): I. Line positions, *Journal of Quantitative Spectroscopy and Radiative Transfer* 113 (2012) 749–762.

- [249] E. V. Karlovets, Y. Lu, D. Mondelain, S. Kassi, A. Campargue, S. A. Tashkun, V. I. Perevalov, High sensitivity CW-Cavity Ring Down Spectroscopy of  $\text{N}_2\text{O}$  between 6950 and 7653  $\text{cm}^{-1}$  (1.44-1.31  $\mu\text{m}$ ): II. Line intensities, *Journal of Quantitative Spectroscopy and Radiative Transfer* 117 (2013) 81–87.
- [250] E. V. Karlovets, A. Campargue, S. Kassi, V. I. Perevalov, S. A. Tashkun, High sensitivity Cavity Ring Down Spectroscopy of  $\text{N}_2\text{O}$  near 1.22  $\mu\text{m}$ : (I) Rovibrational assignments and band-by-band analysis, *Journal of Quantitative Spectroscopy and Radiative Transfer* 169 (2016) 36–48.
- [251] T. Bertin, D. Mondelain, E. Karlovets, S. Kassi, V. Perevalov, A. Campargue, High sensitivity cavity ring down spectroscopy of  $\text{N}_2\text{O}$  near 1.74  $\mu\text{m}$ , *Journal of Quantitative Spectroscopy and Radiative Transfer* 229 (2019) 40–49.
- [252] A. W. Liu, S. Kassi, V. I. Perevalov, S. A. Tashkun, A. Campargue, High sensitivity CW-Cavity Ring Down Spectroscopy of  $\text{N}_2\text{O}$  near 1.28  $\mu\text{m}$ , *Journal of Molecular Spectroscopy* 267 (2011) 191–199.
- [253] A. W. Liu, S. Kassi, V. I. Perevalov, S. M. Hu, A. Campargue, High sensitivity CW-cavity ring down spectroscopy of  $\text{N}_2\text{O}$  near 1.5  $\mu\text{m}$  (III), *Journal of Molecular Spectroscopy* 254 (2009) 20–27.
- [254] A. W. Liu, C. L. Hu, J. Wang, V. I. Perevalov, S. M. Hu, Cavity ring-down spectroscopy of  $^{15}\text{N}$  enriched  $\text{N}_2\text{O}$  near 1.56  $\mu\text{m}$ , *Journal of Quantitative Spectroscopy and Radiative Transfer* 232 (2019) 1–9.
- [255] G. Li, I. E. Gordon, L. S. Rothman, Y. Tan, S.-M. Hu, S. Kassi, A. Campargue, E. S. Medvedev, Rovibrational Line Lists for Nine Isotopologues of the CO Molecule in the  $X^1\Sigma^+$  Ground Electronic State, *Astrophysical Journal Supplement Series* 216 (2015) 15.
- [256] V. M. Devi, D. C. Benner, K. Sung, T. J. Crawford, G. Li, R. R. Gamache, M. A. H. Smith, I. E. Gordon, A. W. Mantz, Positions, intensities and

- line shape parameters for the  $1\leftarrow 0$  bands of CO isotopologues, *Journal of Quantitative Spectroscopy and Radiative Transfer* 218 (2018) 203–230.
- [257] S. Wójtewicz, K. Stec, P. Masłowski, A. Cygan, D. Lisak, R. Trawiński, R. Ciuryło, Low pressure line-shape study of self-broadened CO transitions in the  $(3\leftarrow 0)$  band, *Journal of Quantitative Spectroscopy and Radiative Transfer* 130 (2013) 191–200.
- [258] A. Cygan, P. Wcisło, S. Wójtewicz, G. Kowzan, M. Zaborowski, D. Charczun, K. Bielska, R. S. Trawiński, R. Ciuryło, P. Masłowski, D. Lisak, High-accuracy and wide dynamic range frequency-based dispersion spectroscopy in an optical cavity, *Optics Express* 27 (2019) 21810.
- [259] Y. G. Borkov, A. M. Solodov, A. A. Solodov, T. M. Petrova, E. V. Karlovets, V. I. Perevalov, Fourier transform CO spectra near  $1.6\ \mu\text{m}$ , *Journal of Quantitative Spectroscopy and Radiative Transfer* 253 (2020) 107064.
- [260] Y. G. Borkov, A. M. Solodov, T. M. Petrova, A. A. Solodo, E. V. Karlovets, V. I. Perevalov, Fourier transforms CO spectra near  $1.19\ \mu\text{m}$ , *Journal of Quantitative Spectroscopy and Radiative Transfer* 242 (2020) 106790.
- [261] B. Bordet, S. Kassi, A. Campargue, Line parameters of the  $4\leftarrow 0$  band of carbon monoxide by high sensitivity cavity ring down spectroscopy near  $1.2\ \mu\text{m}$ , *Journal of Quantitative Spectroscopy and Radiative Transfer* 260 (2021) 107453.
- [262] P. Hochstaffl, F. Schreier, M. Birk, G. Wagner, D. G. Feist, J. Notholt, R. Sussmann, Y. Té, Impact of molecular spectroscopy on carbon monoxide abundances from TROPOMI, *Remote Sensing* 12 (2020) 3486.
- [263] P. Hochstaffl, F. Schreier, Impact of molecular spectroscopy on carbon monoxide abundances from SCIAMACHY, *Remote Sensing* 12 (2020) 1084.



- [264] Y. Tan, S. Samuels, R. J. Hargreaves, R. Hashemi, I. E. Gordon, H<sub>2</sub>, He, and CO<sub>2</sub> line-broadening coefficients, and temperature-dependence exponents for the HITRAN database. Part II: CO<sub>2</sub>, N<sub>2</sub>O, CO, OCS, H<sub>2</sub>CO, HCN, PH<sub>3</sub> and H<sub>2</sub>S, *Journal of Quantitative Spectroscopy and Radiative Transfer*. In Preparation (2021).
- [265] L. Régalia-Jarlot, X. Thomas, P. von der Heyden, A. Barbe, Pressure-broadened line widths and pressure-induced line shifts coefficients of the (1–0) and (2–0) bands of <sup>12</sup>C<sup>16</sup>O, *Journal of Quantitative Spectroscopy and Radiative Transfer* 91 (2005) 121–131.
- [266] P. Varanasi, Measurement of line widths of CO of planetary interest at low temperatures, *Journal of Quantitative Spectroscopy and Radiative Transfer* 15 (1975) 191–196.
- [267] K. Sung, P. Varanasi, Intensities, collision-broadened half-widths, and collision-induced line shifts in the second overtone band of <sup>12</sup>C<sup>16</sup>O, *Journal of Quantitative Spectroscopy and Radiative Transfer* 83 (2004) 445–458.
- [268] V. Malathy Devi, D. Chris Benner, M. A. H. Smith, A. W. Mantz, K. Sung, L. R. Brown, A. Predoi-Cross, Spectral line parameters including temperature dependences of self- and air-broadening in the 2←0 band of CO at 2.3 μm, *Journal of Quantitative Spectroscopy and Radiative Transfer* 113 (2012) 1013–1033.
- [269] V. Malathy Devi, D. Chris Benner, M. A. H. Smith, A. W. Mantz, K. Sung, L. R. Brown, Spectral line parameters including temperature dependences of air-broadening for the 2 ← 0 bands of <sup>13</sup>C<sup>16</sup>O and <sup>12</sup>C<sup>18</sup>O at 2.3 μm, *Journal of Molecular Spectroscopy* 276 (2012) 33–48.
- [270] N. Ngo, X. Landsheere, E. Pangui, S. Morales, H. Tran, J.-M. Hartmann, Self-broadening and -shifting of very intense lines of the 1←0 band of <sup>12</sup>C<sup>16</sup>O, *Journal of Quantitative Spectroscopy and Radiative Transfer* 149 (2014) 285–290.

- [271] V. Malathy Devi, A. Predoi-Cross, D. Chris Benner, M. A. H. Smith, C. P. Rinsland, A. W. Mantz, Self- and H<sub>2</sub>-broadened width and shift coefficients in the 2 $\leftarrow$ 0 band of <sup>12</sup>C<sup>16</sup>O: revisited, *Journal of Molecular Spectroscopy* 228 (2004) 580–592.
- [272] K. Esteki, A. Predoi-Cross, C. Povey, S. Ivanov, A. Ghoufi, F. Thibault, M. A. H. Smith, Room temperature self- and H<sub>2</sub>-broadened line parameters of carbon monoxide in the first overtone band: Theoretical and revised experimental results, *Journal of Quantitative Spectroscopy and Radiative Transfer* 203 (2017) 309–324.
- [273] A. Predoi-Cross, J. P. Bouanich, D. C. Benner, A. D. May, J. R. Drummond, Broadening, shifting, and line asymmetries in the 2 $\leftarrow$  band of CO and CO-N<sub>2</sub>: Experimental results and theoretical calculations, *Journal of Chemical Physics* 113 (2000) 158–168.
- [274] A. Predoi-Cross, C. Hnatovsky, K. Strong, J. R. Drummond, D. Chris Benner, Temperature dependence of self- and N<sub>2</sub>-broadening and pressure-induced shifts in the 3 $\leftarrow$ 0 band of CO, *Journal of Molecular Structure* 695-696 (2004) 269–286.
- [275] K. Sung, P. Varanasi, Hydrogen-broadened half-widths and hydrogen-induced line shifts of <sup>12</sup>C<sup>16</sup>O relevant to the Jovian atmospheric spectra, *Journal of Quantitative Spectroscopy and Radiative Transfer* 85 (2004) 165–182.
- [276] P. M. Sinclair, P. Duggan, R. Berman, J. R. Drummond, A. D. May, Line Broadening in the Fundamental Band of CO in CO-He and CO-Ar Mixtures, *Journal of Molecular Spectroscopy* 191 (1998) 258–264.
- [277] A. W. Mantz, V. Malathy Devi, D. Chris Benner, M. A. H. Smith, A. Predoi-Cross, M. Dulick, A multispectrum analysis of widths and shifts in the 2010-2260 cm<sup>-1</sup> region of <sup>12</sup>C<sup>16</sup>O broadened by Helium at temperatures between 80 and 297 K, *Journal of Molecular Structure* 742 (2005) 99–110.

- [278] A. Predoi-Cross, K. Esteki, H. Rozario, H. Naseri, S. Latif, F. Thibault, V. Malathy Devi, M. Smith, A. Mantz, Theoretical and revisited experimentally retrieved He-broadened line parameters of carbon monoxide in the fundamental band, *Journal of Quantitative Spectroscopy and Radiative Transfer* 184 (2016) 322–340.
- [279] C. Luo, R. Wehr, J. R. Drummond, A. D. May, F. Thibault, J. Boissoles, J. M. Launay, C. Boulet, J.-P. Bouanich, and J.-M. Hartmann, Shifting and broadening in the fundamental band of CO highly diluted in He and Ar: A comparison with theory, *Journal of Chemical Physics* 115 (2001) 2198–2206.
- [280] F. Thibault, J. Boissoles, R. L. Doucen, R. Farrenq, M. Morillon-Chapey, C. Boulet, Line-by-line measurements of interference parameters for the 0–1 and 0–2 bands of CO in He, and comparison with coupled-states calculations, *Journal of Chemical Physics* 97 (1992) 4623–4632.
- [281] R. Hashemi, A. Predoi-Cross, A. Dudaryonok, N. Lavrentieva, A. Vandaele, J. Vander Auwera, CO<sub>2</sub> pressure broadening and shift coefficients for the 2–0 band of <sup>12</sup>C<sup>16</sup>O, *Journal of Molecular Spectroscopy* 326 (2016) 60–72. *New Visions of Spectroscopic Databases, Volume I*.
- [282] T. Y. Chesnokova, M. V. Makarova, A. V. Chentsov, V. S. Kostsov, A. V. Poberovskii, V. I. Zakharov, N. V. Rokotyan, Estimation of the impact of differences in the CH<sub>4</sub> absorption line parameters on the accuracy of methane atmospheric total column retrievals from ground-based FTIR spectra, *Journal of Quantitative Spectroscopy and Radiative Transfer* 254 (2020) 107187.
- [283] A. Rodina, A. Nikitin, X. Thomas, L. Manceron, L. Daumont, M. Rey, K. Sung, S. Tashkun, V. Tyuterev, Improved line list of <sup>12</sup>CH<sub>4</sub> in the 3760–4100 cm<sup>−1</sup> region, *Journal of Quantitative Spectroscopy and Radiative Transfer* 225 (2019) 351–362.

- [284] A. Lorente, T. Borsdorff, A. Butz, O. Hasekamp, J. aan de Brugh, A. Schneider, L. Wu, F. Hase, R. Kivi, D. Wunch, D. F. Pollard, K. Shiomi, N. M. Deutscher, V. A. Velazco, C. M. Roehl, P. O. Wennberg, T. Warneke, J. Landgraf, Methane retrieved from TROPOMI: improvement of the data product and validation of the first 2 years of measurements, *Atmospheric Measurement Techniques* 14 (2021) 665–684.
- [285] A. Nikitin, A. Protasevich, M. Rey, V. Serdyukov, L. Sinitsa, A. Lugovskoy, V. Tyuterev, Improved line list of  $^{12}\text{CH}_4$  in the 8850–9180  $\text{cm}^{-1}$  region, *Journal of Quantitative Spectroscopy and Radiative Transfer* 239 (2019) 106646.
- [286] P. A. Kocheril, C. R. Markus, A. M. Esposito, A. W. Schrader, T. S. Dieter, B. J. McCall, Extended sub-Doppler resolution spectroscopy of the  $\nu_3$  band of methane, *Journal of Quantitative Spectroscopy and Radiative Transfer* 215 (2018) 9–12.
- [287] R. Gotti, M. Prevedelli, S. Kassi, M. Marangoni, D. Romanini, Feed-forward coherent link from a comb to a diode laser: Application to widely tunable cavity ring-down spectroscopy, *Journal of Chemical Physics* 148 (2018) 054202.
- [288] M. Kiseleva, J. Mandon, S. Persijn, F. Harren, Accurate measurements of line strengths and air-broadening coefficients in methane around 1.66  $\mu\text{m}$  using cavity ring down spectroscopy, *Journal of Quantitative Spectroscopy and Radiative Transfer* 224 (2019) 9–17.
- [289] L. Yang, H. Lin, M. Plimmer, X. Feng, J. Zhang, Lineshape test on overlapped transitions (R9F1, R9F2) of the  $2\nu_3$  band of  $^{12}\text{CH}_4$  by frequency-stabilized cavity ring-down spectroscopy, *Journal of Quantitative Spectroscopy and Radiative Transfer* 210 (2018) 82–90.
- [290] M. Ghysels, D. Mondelain, S. Kassi, A. Nikitin, M. Rey, A. Campargue, The methane absorption spectrum near 1.73  $\mu\text{m}$  (5695–5850  $\text{cm}^{-1}$ ): Em-

- pirical line lists at 80 K and 296 K and rovibrational assignments, *Journal of Quantitative Spectroscopy and Radiative Transfer* 213 (2018) 169–177.
- [291] E. Starikova, K. Sung, A. V. Nikitin, M. Rey, Assignment and modeling of the  $^{13}\text{CH}_4$  cold absorption spectrum in the  $5471\text{--}5852\text{ cm}^{-1}$  spectral range, *Journal of Quantitative Spectroscopy and Radiative Transfer* 235 (2019) 278–286.
- [292] B. Panda, S. Maithani, M. Pradhan, High-resolution investigation of temperature and pressure-induced spectroscopic parameters of  $^{13}\text{C}$ -isotopomer of  $\text{CH}_4$  in the  $\nu_4$  band using cavity ring-down spectroscopy, *Chemical Physics* 535 (2020) 110769.
- [293] A. Campargue, E. Karlovets, E. Starikova, A. Sidorenko, D. Mondelain, The absorption spectrum of  $^{13}\text{CH}_4$  in the  $1.58\text{ }\mu\text{m}$  transparency window ( $6147\text{--}6653\text{ cm}^{-1}$ ), *Journal of Quantitative Spectroscopy and Radiative Transfer* 244 (2020) 106842.
- [294] L. Yang, H. Lin, M. Plimmer, X.-J. Feng, Y.-J. Ma, J.-T. Luo, J.-F. Luo, J.-T. Zhang, Measurement of the spectral line positions in the  $2\nu_3\text{ R}(6)$  manifold of methane, *Journal of Quantitative Spectroscopy and Radiative Transfer* 245 (2020) 106888.
- [295] A. Foltynowicz, L. Rutkowski, I. Silander, A. C. Johansson, V. Silva de Oliveira, O. Axner, G. Soboń, T. Martynkien, P. Mergo, K. K. Lehmann, Measurement and assignment of double-resonance transitions to the  $8900\text{--}9100\text{ cm}^{-1}$  levels of methane, *Physical Review A* 103 (2021) 022810.
- [296] M. Konefał, M. Ghysels, D. Mondelain, S. Kass, A. Campargue, The absorption spectrum of  $^{13}\text{CH}_4$  at 80 K and 296 K near  $1.73\text{ }\mu\text{m}$ , *Journal of Molecular Spectroscopy* 351 (2018) 14–20.
- [297] A. Nikitin, X. Thomas, L. Daumont, M. Rey, K. Sung, G. Toon, M. Smith, A. Mantz, A. Protasevich, S. Tashkun, V. Tyuterev, Assignment and mod-

- elling of  $^{12}\text{CH}_4$  spectra in the 5550–5695, 5718–5725 and 5792–5814  $\text{cm}^{-1}$  regions, *Journal of Quantitative Spectroscopy and Radiative Transfer* 219 (2018) 323–332.
- [298] M. Koshelev, I. Vilkov, O. Egorov, A. Nikitin, M. Rey, High-sensitivity measurements of  $^{12}\text{CH}_3\text{D}$  pure rotational lines in ground and excited vibrational states in the subTHz region, *Journal of Quantitative Spectroscopy and Radiative Transfer* 242 (2020) 106781.
- [299] C. Bray, A. Cuisset, F. Hindle, R. Bocquet, G. Mouret, B. J. Drouin,  $^{12}\text{CH}_3\text{D}$  photomixing spectroscopy up to 2.5THz: New set of rotational and dipole parameters, first THz self-broadening measurements, *Journal of Quantitative Spectroscopy and Radiative Transfer* 189 (2017) 198–205.
- [300] C. Bray, A. Cuisset, F. Hindle, R. Bocquet, G. Mouret, B. J. Drouin, Corrigendum to ‘CH3D photomixing spectroscopy up to 2.5 THz: new set of rotational and dipole parameters, first THz self-broadening measurements’ (*Journal of Quantitative Spectroscopy and Radiative Transfer* (2017) 189 (198–205), (S0022407316306719), (10.1016/j.jqsrt.2016.11.011)), 2020. doi:10.1016/j.jqsrt.2019.106758.
- [301] M. Rey, A. V. Nikitin, V. G. Tyuterev, Accurate Theoretical Methane Line Lists in the Infrared up to 3000 K and Quasi-continuum Absorption/Emission Modeling for Astrophysical Applications, *Astrophysical Journal* 847 (2017) 105.
- [302] M. Rey, A. V. Nikitin, Y. L. Babikov, V. G. Tyuterev, TheoReTS - An information system for theoretical spectra based on variational predictions from molecular potential energy and dipole moment surfaces, *Journal of Molecular Spectroscopy* 327 (2016) 138–158.
- [303] I. E. Gordon, S. Kass, A. Campargue, G. C. Toon, First identification of the  $a^1\Delta_g-X^3\Sigma_g^-$  electric quadrupole transitions of oxygen in solar and laboratory spectra, *Journal of Quantitative Spectroscopy and Radiative Transfer* 111 (2010) 1174–1183.

- [304] D. Wunch, G. C. Toon, J.-F. L. Blavier, R. A. Washenfelder, J. Notholt, B. J. Connor, D. W. T. Griffith, V. Sherlock, P. O. Wennberg, The Total Carbon Column Observing Network, *Philosophical Transactions of the Royal Society A: Mathematical, Physical and Engineering Sciences* 369 (2011) 2087–2112.
- [305] K. Sun, I. E. Gordon, C. E. Sioris, X. Liu, K. Chance, S. C. Wofsy, Reevaluating the Use of  $\text{O}_2$   $\text{a}^1\Delta_g$  Band in Spaceborne Remote Sensing of Greenhouse Gases, *Geophysical Research Letters* 45 (2018) 5779–5787.
- [306] F. Pasternak, L. Georges, V. Pascal, P. Bernard, The Microcarb instrument, in: N. Karafolas, B. Cugny, Z. Sodnik (Eds.), *International Conference on Space Optics — ICSO 2016*, volume 10562, SPIE, 2017, p. 258. URL: <https://spiedigitallibrary.org/conference-proceedings-of-spie/10562/2296225/The-microcarb-instrument/10.1117/12.2296225.full>. doi:10.1117/12.2296225.
- [307] A. Mishra, T. Balasubramanian, B. Shetty, Generalized electric quadrupole branch linestrengths for the infrared atmospheric oxygen bands, *Journal of Quantitative Spectroscopy and Radiative Transfer* 112 (2011) 2303–2309.
- [308] M. Konefal, S. Kassi, D. Mondelain, A. Campargue, High sensitivity spectroscopy of the  $\text{O}_2$  band at  $1.27\ \mu\text{m}$ : (I) pure  $\text{O}_2$  line parameters above  $7920\ \text{cm}^{-1}$ , *Journal of Quantitative Spectroscopy and Radiative Transfer* 241 (2020) 106653.
- [309] D. D. Tran, H. Tran, S. Vasilchenko, S. Kassi, A. Campargue, D. Mondelain, High sensitivity spectroscopy of the  $\text{O}_2$  band at  $1.27\ \mu\text{m}$ : (II) air-broadened line profile parameters, *Journal of Quantitative Spectroscopy & Radiative Transfer* 240 (2020) 106673.
- [310] J. Mendonca, K. Strong, D. Wunch, G. C. Toon, D. A. Long, J. T. Hodges, V. T. Sironneau, J. E. Franklin, Using a speed-dependent Voigt line

- shape to retrieve O<sub>2</sub>; from Total Carbon Column Observing Network solar spectra to improve measurements of XCO<sub>2</sub>, *Atmospheric Measurement Techniques* 12 (2019) 35–50.
- [311] T. K. Balasubramanian, V. P. Bellary, Intensity distribution in the rotational structure of  $^1\Delta\text{-}^3\Sigma$  and  $^1\Pi\text{-}^3\Sigma$  transitions in diatomic molecules, *Acta Physica Hungarica* 63 (1988) 249.
- [312] S. Yu, B. J. Drouin, C. E. Miller, High resolution spectral analysis of oxygen. IV. Energy levels, partition sums, band constants, RKR potentials, Franck-Condon factors involving the  $X^3\Sigma^-_g$ ,  $a^1\Delta_g$  and  $b^1\Sigma^+_g$  states, *Journal of Chemical Physics* 141 (2014).
- [313] J. M. Hobbs, B. J. Drouin, F. Oyafuso, V. H. Payne, M. R. Gunson, J. McDuffie, E. J. Mlawer, Spectroscopic uncertainty impacts on OCO-2/3 retrievals of XCO<sub>2</sub>, *Journal of Quantitative Spectroscopy and Radiative Transfer* 257 (2020).
- [314] V. H. Payne, B. J. Drouin, F. Oyafuso, L. Kuai, B. M. Fisher, K. Sung, D. Nemchick, T. J. Crawford, M. Smyth, D. Crisp, E. Adkins, J. T. Hodges, D. A. Long, E. J. Mlawer, A. Merrelli, E. Lunny, C. W. O’Dell, Absorption coefficient (ABSCO) tables for the Orbiting Carbon Observatories: Version 5.1, *Journal of Quantitative Spectroscopy and Radiative Transfer* 255 (2020) 107217.
- [315] E. M. Lunny, High-resolution Photoacoustic Spectroscopy of the Oxygen A-band, Ph.D. thesis, California Institute of Technology, 2020. URL: <https://resolver.caltech.edu/CaltechTHESIS:06082020-132244698>. doi:10.7907/qxcm-4909.
- [316] D. J. Robichaud, J. T. Hodges, L. R. Brown, D. Lisak, P. Maslowski, L. Y. Yeung, M. Okumura, C. E. Miller, Experimental intensity and lineshape parameters of the oxygen A-band using frequency-stabilized cavity ring-down spectroscopy, *Journal of Molecular Spectroscopy* 248 (2008) 1–13.



- [317] D. A. Long, D. K. Havey, M. Okumura, C. E. Miller, J. T. Hodges, O<sub>2</sub> A-band line parameters to support atmospheric remote sensing, *Journal of Quantitative Spectroscopy and Radiative Transfer* 111 (2010) 2021–2036.
- [318] B. J. Drouin, D. C. Benner, L. R. Brown, M. J. Cich, T. J. Crawford, V. M. Devi, A. Guillaume, J. T. Hodges, E. J. Mlawer, D. J. Robichaud, F. Oyafuso, V. H. Payne, K. Sung, E. H. Wishnow, S. Yu, Multispectrum analysis of the oxygen A-band, *Journal of Quantitative Spectroscopy and Radiative Transfer* 186 (2017) 118–138.
- [319] V. H. Payne, B. J. Drouin, F. Oyafuso, L. Kuai, B. M. Fisher, K. Sung, D. Nemchick, T. J. Crawford, M. Smyth, D. Crisp, E. Adkins, J. T. Hodges, D. A. Long, E. J. Mlawer, A. Merrelli, E. Lunny, C. W. O'Dell, Corrigendum to “Absorption coefficient (ABSCO) tables for the Orbiting Carbon Observatories: Version 5.1” [*J. Quant. Spectrosc. Radiat. Transf.* 255 (2020) 107217], *Journal of Quantitative Spectroscopy and Radiative Transfer* 257 (2020).
- [320] J. Domysławska, S. Wójtewicz, P. Masłowski, A. Cygan, K. Bielska, R. S. Trawiński, R. Ciuryło, D. Lisak, Spectral line shapes and frequencies of the molecular oxygen B-band R-branch transitions, *Journal of Quantitative Spectroscopy and Radiative Transfer* 155 (2015) 22–31.
- [321] J. Domysławska, S. Wójtewicz, P. Masłowski, A. Cygan, K. Bielska, R. S. Trawiński, R. Ciuryło, D. Lisak, A new approach to spectral line shapes of the weak oxygen transitions for atmospheric applications, *Journal of Quantitative Spectroscopy and Radiative Transfer* 169 (2016) 111–121.
- [322] K. Sung, E. H. Wishnow, T. J. Crawford, D. Nemchick, B. J. Drouin, G. C. Toon, S. Yu, V. H. Payne, J. H. Jiang, FTS measurements of O<sub>2</sub> collision-induced absorption in the 565–700 nm region using a high pressure gas absorption cell, *Journal of Quantitative Spectroscopy and Radiative Transfer* 235 (2019) 232–243.

- [323] G. Fanjoux, G. Millot, R. Saint-Loup, R. Chaux, L. Rosenmann, Coherent anti-Stokes Raman spectroscopy study of collisional broadening in the O<sub>2</sub>-H<sub>2</sub>O Q-branch, *Journal of Chemical Physics* 101 (1994) 1061–1071.
- [324] E. M. Vess, C. J. Wallace, H. M. Campbell, V. E. Awadalla, J. T. Hodges, D. A. Long, D. K. Havey, Measurement of H<sub>2</sub>O Broadening of O<sub>2</sub> A-Band Transitions and Implications for Atmospheric Remote Sensing, *Journal of Physical Chemistry A* 116 (2012) 4069–4073.
- [325] B. J. Drouin, V. Payne, F. Oyafuso, K. Sung, E. Mlawer, Pressure broadening of oxygen by water, *Journal of Quantitative Spectroscopy and Radiative Transfer* 133 (2014) 190–198.
- [326] M. A. Koshelev, I. N. Vilkov, M. Y. Tretyakov, Pressure broadening of oxygen fine structure lines by water, *Journal of Quantitative Spectroscopy and Radiative Transfer* 154 (2015) 24–27.
- [327] T. Delahaye, X. Landsheere, E. Pangui, F. Huet, J. M. Hartmann, H. Tran, Measurements of H<sub>2</sub>O-broadening coefficients of O<sub>2</sub> A-band lines, *Journal of Quantitative Spectroscopy and Radiative Transfer* 184 (2016) 316–321.
- [328] M. Koshelev, I. Vilkov, D. Makarov, M. Tretyakov, P. Rosenkranz, Speed-dependent broadening of the O<sub>2</sub> fine-structure lines, *Journal of Quantitative Spectroscopy and Radiative Transfer* 264 (2021) 107546.
- [329] P. J. Crutzen, The Role of NO and NO<sub>2</sub> in the Chemistry of the Troposphere and Stratosphere, *Annual Review of Earth and Planetary Sciences* 7 (1979) 443.
- [330] J. A. Logan, Nitrogen oxides in the troposphere: Global and regional budgets, *Journal of Geophysical Research* 88 (1983) 10,785–10,807.
- [331] J. L. Gardner, B. Funke, M. G. Mlynczak, M. López-Puertas, F. J. Martin-Torres, J. M. Russell, S. M. Miller, R. D. Sharma, J. R. Winick, Compar-

- ison of nighttime nitric oxide 5.3  $\mu\text{m}$  emissions in the thermosphere measured by MIPAS and SABER, *Journal of Geophysical Research (Space Physics)* 112 (2007) A10301.
- [332] A. Wong, S. N. Yurchenko, P. Bernath, H. S. P. Müller, S. McConkey, J. Tennyson, ExoMol line list - XXI. Nitric Oxide (NO), *Monthly Notices of the Royal Astronomical Society* 470 (2017) 882–897.
  - [333] J. Tennyson, S. N. Yurchenko, ExoMol: molecular line lists for exoplanet and other atmospheres, *Monthly Notices of the Royal Astronomical Society* 425 (2012) 21–33.
  - [334] S. N. Yurchenko, L. Lodi, J. Tennyson, A. V. Stolyarov, DUO: A general program for calculating spectra of diatomic molecules, *Computer Physics Communications* 202 (2016) 262–275.
  - [335] H. S. P. Müller, K. Kobayashi, K. Takahashi, K. Tomaru, F. Matsushima, Terahertz spectroscopy of  $\text{N}^{18}\text{O}$  and isotopic invariant fit of several nitric oxide isotopologs, *Journal of Molecular Spectroscopy* 310 (2015) 92–98.
  - [336] M. N. Spencer, C. Chackerian, L. P. Giver, L. R. Brown, The Nitric Oxide Fundamental Band: Frequency and Shape Parameters for Rovibrational Lines, *Journal of Molecular Spectroscopy* 165 (1994) 506–524.
  - [337] J. M. Hartmann, C. Boulet, Line shape parameters for HF in a bath of argon as a test of classical path models, *Journal of Chemical Physics* 113 (2000) 9000–9010.
  - [338] K. Heinrich, T. Fritsch, P. Hering, M. Mürtz, Infrared laser-spectroscopic analysis of  $^{14}\text{NO}$  and  $^{15}\text{NO}$  in human breath, *Applied Physics B: Lasers and Optics* 95 (2009) 281–286.
  - [339] Q. Qu, B. Cooper, S. N. Yurchenko, J. Tennyson, A spectroscopic model for the low-lying electronic states of NO, *Journal of Chemical Physics* 154 (2021) 074112.

- [340] Q. Qu, S. N. Yurchenko, J. Tennyson, ExoMol molecular line lists – XLII: Rovibronic molecular line list for the low-lying states of NO, *Monthly Notices of the Royal Astronomical Society* (2021).
- [341] S. A. Carn, V. E. Fioletov, C. A. McLinden, C. Li, N. A. Krotkov, A decade of global volcanic SO<sub>2</sub> emissions measured from space, *Scientific Reports* 7 (2017) 1–12.
- [342] C. K. Lin, R. T. Lin, P. C. Chen, P. Wang, N. De Marcellis-Warin, C. Zigler, D. C. Christiani, A global perspective on sulfur oxide controls in coal-fired power plants and cardiovascular disease, *Scientific Reports* 8 (2018) 2611.
- [343] A. C. Vandaele, O. Korablev, D. Belyaev, S. Chamberlain, D. Evdokimova, T. Encrenaz, L. Esposito, K. L. Jessup, F. Lefèvre, S. Limaye, A. Mahieux, E. Marcq, F. P. Mills, F. Montmessin, C. D. Parkinson, S. Robert, T. Roman, B. Sandor, A. Stolzenbach, C. Wilson, V. Wilquet, Sulfur dioxide in the Venus atmosphere: I. Vertical distribution and variability, *Icarus* 295 (2017) 16–33.
- [344] T. Encrenaz, T. K. Greathouse, M. J. Richter, J. H. Lacy, T. Fouchet, B. Bézard, F. Lefèvre, F. Forget, S. K. Atreya, A stringent upper limit to SO<sub>2</sub> in the Martian atmosphere, *Astronomy & Astrophysics* 530 (2011) 37.
- [345] V. A. Krasnopolsky, Search for methane and upper limits to ethane and SO<sub>2</sub> on Mars, *Icarus* 217 (2012) 144–152.
- [346] K. Loftus, R. D. Wordsworth, C. V. Morley, Sulfate Aerosol Hazes and SO<sub>2</sub> Gas as Constraints on Rocky Exoplanets’ Surface Liquid Water, *Astrophysical Journal* 887 (2019) 231.
- [347] X. Huang, D. W. Schwenke, T. J. Lee, Quantitative validation of Ames IR intensity and new line lists for <sup>32/33/34</sup>S<sup>16</sup>O<sub>2</sub>, <sup>32</sup>S<sup>18</sup>O<sub>2</sub> and <sup>16</sup>O<sup>32</sup>S<sup>18</sup>O,

- Journal of Quantitative Spectroscopy and Radiative Transfer 225 (2019) 327–336.
- [348] O. V. Naumenko, V.-M. Horneman,  $^{32}\text{S}^{16}\text{O}_2$  line list, 2019. Private communication.
  - [349] R. Tóbiás, T. Furtenbacher, A. G. Császár, O. V. Naumenko, J. Tennyson, J.-M. Flaud, P. Kumar, B. Poirier, Critical evaluation of measured rotational-vibrational transitions of four sulphur isotopologues of  $\text{S}^{16}\text{O}_2$ , Journal of Quantitative Spectroscopy and Radiative Transfer 208 (2018) 152–163.
  - [350] X. Huang, D. W. Schwenke, T. J. Lee, Highly accurate potential energy surface, dipole moment surface, rovibrational energy levels, and infrared line list for  $^{32}\text{S}^{16}\text{O}_2$  up to  $8000\text{ cm}^{-1}$ , Journal of Chemical Physics 140 (2014) 114311.
  - [351] X. Huang, D. W. Schwenke, T. J. Lee, Empirical infrared line lists for five  $\text{SO}_2$  isotopologues:  $^{32/33/34/36}\text{S}^{16}\text{O}_2$  and  $^{32}\text{S}^{18}\text{O}_2$ , Journal of Molecular Spectroscopy 311 (2015) 19–24.
  - [352] X. Huang, D. W. Schwenke, T. J. Lee, Ames  $^{32}\text{S}^{16}\text{O}^{18}\text{O}$  line list for high-resolution experimental IR analysis, Journal of Molecular Spectroscopy 330 (2016) 101–111.
  - [353] X. Huang, D. W. Schwenke, T. J. Lee, Isotopologue consistency of semi-empirically computed infrared line lists and further improvement for rare isotopologues:  $\text{CO}_2$  and  $\text{SO}_2$  case studies, Journal of Quantitative Spectroscopy and Radiative Transfer 230 (2019) 222–246.
  - [354] X. Huang, D. W. Schwenke, T. J. Lee, Exploring the limits of the Data-Model-Theory synergy: “Hot” MW transitions for rovibrational IR studies, Journal of Molecular Structure 1217 (2020) 128260.
  - [355] D. S. Underwood, J. Tennyson, S. N. Yurchenko, X. Huang, D. W. Schwenke, T. J. Lee, S. Clausen, A. Fateev, ExoMol molecular line lists

- XIV. The rotation-vibration spectrum of hot SO<sub>2</sub>, Monthly Notices of the Royal Astronomical Society 459 (2016) 3890–3899.
- [356] O. Ulenikov, E. Bekhtereva, V.-M. Horneman, S. Alanko, O. Gromova, High resolution study of the  $3\nu_1$  band of SO<sub>2</sub>, Journal of Molecular Spectroscopy 255 (2009) 111–121.
- [357] O. Ulenikov, E. Bekhtereva, S. Alanko, V. Horneman, O. Gromova, C. Leroy, On the high resolution spectroscopy and intramolecular potential function of SO<sub>2</sub>, Journal of Molecular Spectroscopy 257 (2009) 137–156.
- [358] O. Ulenikov, E. Bekhtereva, O. Gromova, S. Alanko, V.-M. Horneman, C. Leroy, Analysis of highly excited ‘hot’ bands in the SO<sub>2</sub> molecule:  $\nu_2 + 3\nu_3 - \nu_2$  and  $2\nu_1 + \nu_2 + \nu_3 - \nu_2$ , Molecular Physics 108 (2010) 1253–1261.
- [359] O. Ulenikov, O. Gromova, E. Bekhtereva, I. Bolotova, C. Leroy, V.-M. Horneman, S. Alanko, High resolution study of the  $\nu_1 + 2\nu_2 - \nu_2$  and  $2\nu_2 + \nu_3 - \nu_2$  “hot” bands and ro-vibrational re-analysis of the  $\nu_1 + \nu_2 / \nu_2 + \nu_3 / 3\nu_2$  polyad of the <sup>32</sup>SO<sub>2</sub> molecule, Journal of Quantitative Spectroscopy and Radiative Transfer 112 (2011) 486–512.
- [360] O. Ulenikov, O. Gromova, E. Bekhtereva, I. Bolotova, I. Konov, V.-M. Horneman, C. Leroy, High resolution analysis of the SO<sub>2</sub> spectrum in the 2600–2900 cm<sup>−1</sup> region:  $2\nu_3$ ,  $\nu_2 + 2\nu_3 - \nu_2$  and  $2\nu_1 + \nu_2$  bands, Journal of Quantitative Spectroscopy and Radiative Transfer 113 (2012) 500–517.
- [361] O. Ulenikov, G. Onopenko, O. Gromova, E. Bekhtereva, V.-M. Horneman, Re-analysis of the (100), (001), and (020) rotational structure of SO<sub>2</sub> on the basis of high resolution FTIR spectra, Journal of Quantitative Spectroscopy and Radiative Transfer 130 (2013) 220–232.
- [362] O. Ulenikov, O. Gromova, E. Bekhtereva, A. Belova, S. Bauerecker, C. Maul, C. Sydow, V.-M. Horneman, High resolution analysis of the

- (111) vibrational state of SO<sub>2</sub>, Journal of Quantitative Spectroscopy and Radiative Transfer 144 (2014) 1–10.
- [363] O. Ulenikov, E. Bekhtereva, O. Gromova, K. Berezkin, V. Horneman, C. Sydow, C. Maul, S. Bauerecker, First high resolution analysis of the  $3\nu_2$  and  $3\nu_2 - \nu_2$  bands of  $^{32}\text{S}^{16}\text{O}_2$ , Journal of Quantitative Spectroscopy and Radiative Transfer 202 (2017) 1–5.
- [364] T. Blake, J.-M. Flaud, W. Lafferty, First analysis of the rotationally-resolved  $\nu_2$  and  $2\nu_2 - \nu_2$  bands of sulfur dioxide,  $^{33}\text{S}^{16}\text{O}_2$ , Journal of Molecular Spectroscopy 333 (2017) 19–22.
- [365] J.-M. Flaud, T. Blake, W. Lafferty, First high-resolution analysis of the  $\nu_1$ ,  $\nu_3$  and  $\nu_1 + \nu_3$  bands of sulphur dioxide  $^{33}\text{S}^{16}\text{O}_2$ , Molecular Physics 115 (2017) 447–453.
- [366] O. Ulenikov, O. Gromova, E. Bekhtereva, A. Fomchenko, C. Sydow, S. Bauerecker, First high resolution analysis of the  $3\nu_1$  band of  $^{34}\text{S}^{16}\text{O}_2$ , Journal of Molecular Spectroscopy 319 (2016) 50–54.
- [367] O. Ulenikov, E. Bekhtereva, O. Gromova, T. Buttersack, C. Sydow, S. Bauerecker, High resolution FTIR study of  $^{34}\text{S}^{16}\text{O}_2$ : The bands  $2\nu_1$ ,  $\nu_1 + \nu_3$ ,  $\nu_1 + \nu_2 + \nu_3 - \nu_2$  and  $\nu_1 + \nu_2 + \nu_3$ , Journal of Quantitative Spectroscopy and Radiative Transfer 169 (2016) 49–57.
- [368] O. Ulenikov, O. Gromova, E. Bekhtereva, Y. Krivchikova, E. Sklyarova, T. Buttersack, C. Sydow, S. Bauerecker, High resolution FTIR study of  $^{34}\text{S}^{16}\text{O}_2$ : The bands  $2\nu_3$ ,  $2\nu_1 + \nu_2$  and  $2\nu_1 + \nu_2 - \nu_2$ , Journal of Molecular Spectroscopy 318 (2015) 26–33.
- [369] O. Ulenikov, E. Bekhtereva, O. Gromova, T. Buttersack, C. Sydow, S. Bauerecker, High resolution FTIR study of  $^{34}\text{S}^{16}\text{O}_2$ : Re-analysis of the bands  $\nu_1 + \nu_2$ ,  $\nu_2 + \nu_3$ , and first analysis of the hot band  $2\nu_2 + \nu_3 - \nu_2$ , Journal of Molecular Spectroscopy 319 (2016) 17–25.

- [370] O. Ulenikov, E. Bekhtereva, Y. Krivchikova, V. Zamotaeva, T. Buttersack, C. Sydow, S. Bauerecker, Study of the high resolution spectrum of  $^{32}\text{S}^{16}\text{O}^{18}\text{O}$ : The  $\nu_1$  and  $\nu_3$  bands, *Journal of Quantitative Spectroscopy and Radiative Transfer* 168 (2016) 29–39.
- [371] O. Ulenikov, E. Bekhtereva, O. Gromova, V. Zamotaeva, S. Kuznetsov, C. Sydow, S. Bauerecker, High resolution study of the rotational structure of doubly excited vibrational states of  $^{32}\text{S}^{16}\text{O}^{18}\text{O}$ : The first analysis of the  $2\nu_1$ ,  $\nu_1 + \nu_3$ , and  $2\nu_3$  bands, *Journal of Quantitative Spectroscopy and Radiative Transfer* 189 (2017) 344–350.
- [372] O. N. Ulenikov, O. V. Gromova, E. S. Bekhtereva, A. G. Ziatkova, E. A. Sklyarova, S. I. Kuznetsov, C. Sydow, S. Bauerecker, First rotational analysis of the (111) and (021) vibrational state of  $\text{S}^{16}\text{O}^{18}\text{O}$  from the “hot”  $\nu_1 + \nu_2 + \nu_3 - \nu_2$  and  $2\nu_2 + \nu_3 - \nu_2$  bands, *Journal of Quantitative Spectroscopy and Radiative Transfer* 202 (2017) 98–103.
- [373] O. N. Ulenikov, E. S. Bekhtereva, O. V. Gromova, V. M. Horneman, C. Sydow, S. Bauerecker, High resolution FTIR spectroscopy of sulfur dioxide in the 1550-1950  $\text{cm}^{-1}$  region: First analysis of the  $\nu_1 + \nu_2 / \nu_2 + \nu_3$  bands of  $^{32}\text{S}^{16}\text{O}^{18}\text{O}$  and experimental line intensities of ro-vibrational transitions in the  $\nu_1 + \nu_2 / \nu_2 + \nu_3$  bands of  $^{32}\text{S}^{16}\text{O}_2$ ,  $^{34}\text{S}^{16}\text{O}_2$ ,  $^{32}\text{S}^{18}\text{O}_2$  and  $^{32}\text{S}^{16}\text{O}^{18}\text{O}$ , *Journal of Quantitative Spectroscopy and Radiative Transfer* 203 (2017) 377–391.
- [374] F. Gueye, L. Manceron, A. Perrin, F. K. Tchana, J. Demaison, First far-infrared high-resolution analysis of the  $\nu_2$  band of sulphur dioxide  $^{32}\text{S}^{16}\text{O}^{18}\text{O}$  and  $^{32}\text{S}^{18}\text{O}_2$ , *Molecular Physics* 114 (2016) 2769–2776.
- [375] H. S. Müller, Online EH(CDMS) model data for the  $^{34}\text{S}^{16}\text{O}_2$  isotopologue, 2008. URL: <https://cdms.astro.uni-koeln.de/classic/predictions/daten/S02/34S02/s34.par>.
- [376] J.-M. Flaud, Private email communications, 2018.



- [377] W. Lafferty, J.-M. Flaud, E. H. A. Ngom, R. Sams,  $^{34}\text{S}^{16}\text{O}_2$ : High-resolution analysis of the (030), (101), (111), (002) and (201) vibrational states; determination of equilibrium rotational constants for sulfur dioxide and anharmonic vibrational constants, *Journal of Molecular Spectroscopy* 253 (2009) 51–54.
- [378] I. A. Vasilenko, O. V. Naumenko, V.-M. Horneman, Expert List of Absorption Lines of the  $\text{SO}_2$  Molecule in the 2000-3000  $\text{cm}^{-1}$  Spectral Region, *Atmospheric and Oceanic Optics* 33 (2020) 443–448.
- [379] O. V. Naumenko, I. A. Vasilenko, V.-M. Horneman, High-resolution FTIR spectrum of  $\text{SO}_2$  molecule in the region of the  $2\nu_1 + \nu_3$  band, *The Twenty-sixth Colloquium on High Resolution Molecular Spectroscopy Book of abstracts* (2019) 74.
- [380] Y. G. Borkov, O. M. Lyulin, T. M. Petrova, A. M. Solodov, A. A. Solodov, V. M. Deichuli, V. I. Perevalov,  $\text{CO}_2$ -broadening and shift coefficients of sulfur dioxide near 4  $\mu\text{m}$ , *Journal of Quantitative Spectroscopy and Radiative Transfer* 225 (2019) 119–124.
- [381] Y. Tan, R. V. Kochanov, L. S. Rothman, I. E. Gordon, The broadening coefficients of  $\text{SO}_2$ , in: *Towards HITRAN 2016*, 2016, p. 2. doi:10.5281/zenodo.163447.
- [382] R. J. Hargreaves, P. F. Bernath, J. Bailey, M. Dulick, Empirical Line Lists and Absorption Cross Sections for Methane at High Temperatures, *Astrophysical Journal* 813 (2015) 12.
- [383] G. C. M. Vinken, K. F. Boersma, J. D. Maasakkers, M. Adon, R. V. Martin, Worldwide biogenic soil  $\text{NO}_x$  emissions inferred from OMI  $\text{NO}_2$  observations, *Atmospheric Chemistry & Physics* 14 (2014) 10363–10381.
- [384] S. C. Anenberg, D. K. Henze, V. Tinney, P. L. Kinney, W. Raich, N. Fann, C. S. Malley, H. Roman, L. Lamsal, B. Duncan, R. V. Martin, A. van Donkelaar, M. Brauer, R. Doherty, J. E. Jonson, Y. Davila, K. Sudo, J. C.

- Kuylensstierna, Estimates of the global burden of ambient PM<sub>2.5</sub>, ozone, and NO<sub>2</sub> on asthma incidence and emergency room visits, *Environmental Health Perspectives* 126 (2018) 107004.
- [385] J. D. Lee, W. S. Drysdale, D. P. Finch, S. E. Wilde, P. I. Palmer, UK surface NO<sub>2</sub> levels dropped by 42% during the COVID-19 lockdown: impact on surface O<sub>3</sub>, *Atmospheric Chemistry & Physics* 20 (2020) 15743–15759.
- [386] A. A. Lukashevskaya, N. N. Lavrentieva, A. C. Dudaryonok, V. I. Perevalov, NDSD-1000: High-resolution, high-temperature Nitrogen Dioxide Spectroscopic Databank, *Journal of Quantitative Spectroscopy and Radiative Transfer* 184 (2016) 205–217.
- [387] A. A. Lukashevskaya, N. N. Lavrentieva, A. S. Dudaryonok, V. I. Perevalov, Corrected version of the NDSD-1000 databank, *Journal of Quantitative Spectroscopy and Radiative Transfer* 202 (2017) 37–37.
- [388] A. Perrin, S. Kassi, A. Campargue, First high-resolution analysis of the  $4\nu_1 + \nu_3$  band of nitrogen dioxide near 1.5  $\mu\text{m}$ , *Journal of Quantitative Spectroscopy and Radiative Transfer* 111 (2010) 2246–2255.
- [389] O. V. Naumenko, A. A. Lukashevskaya, S. Kassi, S. Bégurier, A. Campargue, The  $\nu_1 + 3\nu_3$  absorption band of nitrogen dioxide ( $^{14}\text{N}^{16}\text{O}_2$ ) by CRDS near 6000  $\text{cm}^{-1}$ , *Journal of Quantitative Spectroscopy and Radiative Transfer* 232 (2019) 146–151.
- [390] A. A. Lukashevskaya, O. V. Naumenko, D. Mondelain, S. Kassi, A. Campargue, High sensitivity cavity ring down spectroscopy of the  $3\nu_1 + 3\nu_2 + \nu_3$  band of NO<sub>2</sub> near 7587  $\text{cm}^{-1}$ , *Journal of Quantitative Spectroscopy and Radiative Transfer* 177 (2016) 225–233.
- [391] A. A. Lukashevskaya, O. V. Naumenko, S. Kassi, A. Campargue, First detection and analysis of the  $3\nu_1 + \nu_2 + \nu_3$  band of NO<sub>2</sub> by CRDS near 6156  $\text{cm}^{-1}$ , *Journal of Molecular Spectroscopy* 338 (2017) 91–96.

- [392] A. A. Lukashevskaya, S. Kassi, A. Campargue, V. I. Perevalov, High sensitivity cavity ring down spectroscopy of the  $4\nu_3$  band of  $\text{NO}_2$  near  $1.59\ \mu\text{m}$ , *Journal of Quantitative Spectroscopy and Radiative Transfer* 202 (2017) 302–307.
- [393] A. A. Lukashevskaya, S. Kassi, A. Campargue, V. I. Perevalov, High sensitivity Cavity Ring Down Spectroscopy of the  $2\nu_1 + 3\nu_2 + \nu_3$  band of  $\text{NO}_2$  near  $1.57\ \mu\text{m}$ , *Journal of Quantitative Spectroscopy and Radiative Transfer* 200 (2017) 17–24.
- [394] A. A. Lukashevskaya, D. Mondelain, A. Campargue, V. I. Perevalov, High sensitivity cavity ring down spectroscopy of the  $\nu_1 + 4\nu_3$  band of  $\text{NO}_2$  near  $1.34\ \mu\text{m}$ , *Journal of Quantitative Spectroscopy and Radiative Transfer* 219 (2018) 393–398.
- [395] A. A. Lukashevskaya, O. V. Naumenko, A. Perrin, D. Mondelain, S. Kassi, A. Campargue, High sensitivity cavity ring down spectroscopy of  $\text{NO}_2$  between  $7760$  and  $7917\ \text{cm}^{-1}$ , *Journal of Quantitative Spectroscopy and Radiative Transfer* 130 (2013) 249–259.
- [396] D. Mondelain, A. Perrin, S. Kassi, A. Campargue, First high-resolution analysis of the  $5\nu_3$  band of nitrogen dioxide near  $1.3\ \mu\text{m}$ , *Journal of Quantitative Spectroscopy and Radiative Transfer* 113 (2012) 1058–1065.
- [397] A. D. Bykov, N. N. Lavrentieva, L. N. Sinitsa, Semi-empiric approach to the calculation of  $\text{H}_2\text{O}$  and  $\text{CO}_2$  line broadening and shifting, *Molecular Physics* 102 (2004) 1653–1658.
- [398] A. S. Dudaryonok, N. N. Lavrentieva, M. Q., The average energy difference method for calculation of line broadening of asymmetric tops, *Atmospheric and Oceanic Optics* 28 (2015) 503–509.
- [399] V. Dana, J. Y. Mandin, M. Y. Allout, A. Perrin, L. Régalia, A. Barbe, J. J. Plateaux, X. Thomas, Broadening parameters of  $\text{NO}_2$  lines in the  $3.4$

- $\mu\text{m}$  spectral region., *Journal of Quantitative Spectroscopy and Radiative Transfer* 57 (1997) 445–457.
- [400] D. C. Benner, T. A. Blake, L. R. Brown, V. Malathy Devi, M. A. H. Smith, R. A. Toth, Air-broadening parameters in the  $\nu_3$  band of  $^{14}\text{N}^{16}\text{O}_2$  using a multispectrum fitting technique, *Journal of Molecular Spectroscopy* 228 (2004) 593–619.
  - [401] A. Perrin, L. Manceron, J.-M. Flaud, F. Kwabia-Tchana, R. Armante, P. Roy, D. Doizi, The new nitrogen dioxide ( $\text{NO}_2$ ) linelist in the GEISA database and first identification of the  $\nu_1+2\nu_3-\nu_3$  band of  $^{14}\text{N}^{16}\text{O}_2$ , *Journal of Molecular Spectroscopy* 376 (2021) 111394.
  - [402] J. Orphal, A. Perrin, J. M. Flaud, M. Smirnov, S. Himmelmann, S. Voigt, J. P. Burrows, New High-Resolution Analysis of the  $\nu_3$  Band of the  $^{15}\text{N}^{16}\text{O}_2$  Isotopomer of Nitrogen Dioxide by Fourier Transform Spectroscopy, *Journal of Molecular Spectroscopy* 204 (2000) 72–79.
  - [403] A. Perrin, G. Toon, J. Orphal, Detection of atmospheric  $^{15}\text{NO}_2$  in the  $\nu_3$  spectral region ( $6.3\ \mu\text{m}$ ), *Journal of Quantitative Spectroscopy and Radiative Transfer* 154 (2015) 91–97.
  - [404] A. Perrin, J. M. Flaud, C. Camy-Peyret, A. M. Vasserot, G. Guelachvili, A. Goldman, F. J. Murcray, R. D. Blatherwick, The  $\nu_1$ ,  $2\nu_2$ , and  $\nu_3$  interacting bands of  $^{14}\text{N}^{16}\text{O}_2$ : Line positions and intensities, *Journal of Molecular Spectroscopy* 154 (1992) 391–406.
  - [405] N. Jacquinet-Husson, R. Armante, N. A. Scott, A. Chédin, L. Crépeau, C. Boutammine, A. Bouhdaoui, C. Crevoisier, V. Capelle, C. Boone, N. Poulet-Crovisier, A. Barbe, D. Chris Benner, V. Boudon, L. R. Brown, J. Buldyreva, A. Campargue, L. H. Coudert, V. M. Devi, M. J. Down, B. J. Drouin, A. Fayt, C. Fittschen, J. M. Flaud, R. R. Gamache, J. J. Harrison, C. Hill, Ø. Hodnebrog, S. M. Hu, D. Jacquemart, A. Jolly, E. Jiménez, N. N. Lavrentieva, A. W. Liu, L. Lodi, O. M. Lyulin, S. T.

- Massie, S. Mikhailenko, H. S. P. Müller, O. V. Naumenko, A. Nikitin, C. J. Nielsen, J. Orphal, V. I. Perevalov, A. Perrin, E. Polovtseva, A. Predoi-Cross, M. Rotger, A. A. Ruth, S. S. Yu, K. Sung, S. A. Tashkun, J. Tennyson, V. G. Tyuterev, J. Vander Auwera, B. A. Voronin, A. Makie, The 2015 edition of the GEISA spectroscopic database, *Journal of Molecular Spectroscopy* 327 (2016) 31–72.
- [406] J. W. Erisman, M. A. Sutton, J. Galloway, Z. Klimont, W. Winiwarter, How a century of ammonia synthesis changed the world, *Nature Geoscience* 1 (2008) 636–639.
- [407] V. P. Aneja, W. H. Schlesinger, Q. Li, A. Nahas, W. H. Battye, Characterization of the Global Sources of Atmospheric Ammonia from Agricultural Soils, *Journal of Geophysical Research: Atmospheres* 125 (2020) e31684.
- [408] E. Lutsch, K. Strong, D. B. A. Jones, I. Ortega, J. W. Hannigan, E. Dammers, M. W. Shephard, E. Morris, K. Murphy, M. J. Evans, M. Parrington, S. Whitburn, M. Van Damme, L. Clarisse, P.-F. Coheur, C. Clerbaux, B. Croft, R. V. Martin, J. R. Pierce, J. A. Fisher, Unprecedented Atmospheric Ammonia Concentrations Detected in the High Arctic From the 2017 Canadian Wildfires, *Journal of Geophysical Research: Atmospheres* 124 (2019) 8178–8202.
- [409] M. Van Damme, L. Clarisse, S. Whitburn, J. Hadji-Lazaro, D. Hurtmans, C. Clerbaux, P.-F. Coheur, Industrial and agricultural ammonia point sources exposed, *Nature* 564 (2018) 99–103.
- [410] B. Tournadre, P. Chelin, M. Ray, J. Cuesta, R. D. Kutzner, X. Landsheere, A. Fortems-Cheiney, J.-M. Flaud, F. Hase, T. Blumenstock, J. Orphal, C. Viatte, C. Camy-Peyret, Atmospheric ammonia ( $\text{NH}_3$ ) over the Paris megacity: 9 years of total column observations from ground-based infrared remote sensing, *Atmospheric Measurement Techniques* 13 (2020) 3923–3937.

- [411] E. Dammers, C. A. McLinden, D. Griffin, M. W. Shephard, S. Van Der Graaf, E. Lutsch, M. Schaap, Y. Gainairu-Matz, V. Fioletov, M. Van Damme, S. Whitburn, L. Clarisse, K. Cady-Pereira, C. Clerbaux, P. F. Coheur, J. W. Erisman,  $\text{NH}_3$  emissions from large point sources derived from CrIS and IASI satellite observations, *Atmospheric Chemistry and Physics* 19 (2019) 12 261–12 293.
- [412] L. Clarisse, M. Van Damme, W. Gardner, P. F. Coheur, C. Clerbaux, S. Whitburn, J. Hadji-Lazaro, D. Hurtmans, Atmospheric ammonia ( $\text{NH}_3$ ) emanations from Lake Natron’s saline mudflats, *Scientific Reports* 9 (2019) 4441.
- [413] T. Guillot, D. J. Stevenson, S. K. Atreya, S. J. Bolton, H. N. Becker, Storms and the Depletion of Ammonia in Jupiter: I. Microphysics of “Mushballs”, *Journal of Geophysical Research: Planets* 125 (2020) e06403.
- [414] T. Guillot, C. Li, S. J. Bolton, S. T. Brown, A. P. Ingersoll, M. A. Janssen, S. M. Levin, J. I. Lunine, G. S. Orton, P. G. Steffes, D. J. Stevenson, Storms and the Depletion of Ammonia in Jupiter: II. Explaining the Juno Observations, *Journal of Geophysical Research: Planets* 125 (2020) e06404.
- [415] J. I. Canty, P. W. Lucas, S. N. Yurchenko, J. Tennyson, S. K. Leggett, C. G. Tinney, H. R. A. Jones, B. Burningham, D. J. Pinfield, R. L. Smart, Methane and ammonia in the near-infrared spectra of late-T dwarfs, *Monthly Notices of the Royal Astronomical Society* 450 (2015) 454–480.
- [416] R. J. MacDonald, N. Madhusudhan, HD 209458b in new light: evidence of nitrogen chemistry, patchy clouds and sub-solar water, *Monthly Notices of the Royal Astronomical Society* 469 (2017) 1979–1996.
- [417] P. A. Coles, R. I. Ovsyannikov, O. L. Polyansky, S. N. Yurchenko, J. Tennyson, Improved potential energy surface and spectral assignments for am-

- monia in the near-infrared region, *Journal of Quantitative Spectroscopy and Radiative Transfer* 219 (2018) 199–212.
- [418] P. A. Coles, S. N. Yurchenko, J. Tennyson, ExoMol molecular line lists - XXXV. A rotation-vibration line list for hot ammonia, *Monthly Notices of the Royal Astronomical Society* 490 (2019) 4638–4647.
  - [419] S. N. Yurchenko, R. J. Barber, J. Tennyson, A variationally computed hot line list for  $\text{NH}_3$ , *Monthly Notices of the Royal Astronomical Society* 413 (2011) 1828–1834.
  - [420] T. Furtenbacher, P. A. Coles, J. Tennyson, S. N. Yurchenko, S. Yu, B. Drouin, R. Tóbiás, A. G. Császár, Empirical rovibrational energy levels of ammonia up to  $7500\text{ cm}^{-1}$ , *Journal of Quantitative Spectroscopy and Radiative Transfer* 251 (2020) 107027.
  - [421] C. A. Beale, R. J. Hargreaves, P. Coles, J. Tennyson, P. F. Bernath, Infrared absorption spectra of hot ammonia, *Journal of Quantitative Spectroscopy and Radiative Transfer* 203 (2017) 410–416.
  - [422] C. A. Beale, R. J. Hargreaves, P. Coles, J. Tennyson, P. F. Bernath, Erratum to “Infrared absorption spectra of hot ammonia” [*J Quant Spectrosc Radiat Transf* 203 (2017) 410–416], *Journal of Quantitative Spectroscopy and Radiative Transfer* 245 (2020) 106870.
  - [423] C. A. Beale, A. Wong, P. Bernath, Infrared transmission spectra of hot ammonia in the  $4800\text{--}9000\text{ cm}^{-1}$  region, *Journal of Quantitative Spectroscopy and Radiative Transfer* 246 (2020) 106911.
  - [424] P. Cacciani, P. Čermák, S. Béguier, A. Campargue, The absorption spectrum of ammonia between  $5650\text{ and }6350\text{ cm}^{-1}$ , *Journal of Quantitative Spectroscopy and Radiative Transfer* 258 (2021) 107334.
  - [425] J. Vander Auwera, T. Vanfleteren, Line positions and intensities in the  $7400\text{--}8600\text{ cm}^{-1}$  region of the ammonia spectrum, *Journal of Quantitative Spectroscopy and Radiative Transfer* 116 (2018) 3621–3630.

- [426] K. Sung, S. Yu, J. Pearson, O. Pirali, F. Kwabia Tchana, L. Manceron, Far-infrared  $^{14}\text{NH}_3$  line positions and intensities measured with a FT-IR and AILES beamline, Synchrotron SOLEIL, *Journal of Molecular Spectroscopy* 327 (2016) 1–20.
- [427] K. Sung, L. R. Brown, X. Huang, D. W. Schwenke, T. J. Lee, S. L. Coy, K. K. Lehmann, Extended line positions, intensities, empirical lower state energies and quantum assignments of  $\text{NH}_3$  from 6300 to 7000  $\text{cm}^{-1}$ , *Journal of Quantitative Spectroscopy and Radiative Transfer* 113 (2012) 1066–1083.
- [428] E. J. Barton, S. N. Yurchenko, J. Tennyson, S. Béguier, A. Campargue, A near infrared line list for  $\text{NH}_3$ : Analysis of a Kitt Peak spectrum after 35 years, *Journal of Molecular Spectroscopy* 325 (2016) 7–12.
- [429] N. F. Zobov, T. Bertin, J. Vander Auwera, S. Civis, A. Knizek, M. Ferus, R. I. Ovsyannikov, V. Y. Makhnev, J. Tennyson, O. L. Polyansky, The spectrum of ammonia near 0.793  $\mu\text{m}$ , *Journal of Quantitative Spectroscopy and Radiative Transfer* (2021). This issue.
- [430] N. F. Zobov, P. A. Coles, R. I. Ovsyannikov, A. A. Kyuberis, R. J. Hargreaves, P. F. Bernath, J. Tennyson, S. N. Yurchenko, O. L. Polyansky, Analysis of the red and green optical absorption spectrum of gas phase ammonia, *Journal of Quantitative Spectroscopy and Radiative Transfer* 209 (2018) 224–231.
- [431] P. G. J. Irwin, N. Bowles, A. S. Braude, R. Garland, S. Calcutt, P. A. Coles, S. N. Yurchenko, J. Tennyson, Analysis of gaseous ammonia ( $\text{NH}_3$ ) absorption in the visible spectrum of Jupiter - Update, *Icarus* 321 (2019) 572–582.
- [432] S. N. Yurchenko, A theoretical room-temperature line list for  $^{15}\text{NH}_3$ , *Journal of Quantitative Spectroscopy and Radiative Transfer* 152 (2015) 28–36.



- [433] V. Nemtchinov, Measurements of line intensities and half-widths in the 10- $\mu\text{m}$  bands of  $^{14}\text{NH}_3$ , *Journal of Quantitative Spectroscopy and Radiative Transfer* 83 (2004) 243–265.
- [434] J. S. Wilzewski, I. E. Gordon, R. V. Kochanov, C. Hill, L. S. Rothman,  $\text{H}_2$ , He, and  $\text{CO}_2$  line-broadening coefficients, pressure shifts and temperature-dependence exponents for the HITRAN database. Part 1:  $\text{SO}_2$ ,  $\text{NH}_3$ , HF, HCl, OCS and  $\text{C}_2\text{H}_2$ , *Journal of Quantitative Spectroscopy and Radiative Transfer* 168 (2016) 193–206.
- [435] F. M. Skinner, R. J. Hargreaves, I. E. Gordon, Modeling Planetary Opacities with HITRAN and HAPI: Test case of Ammonia Microwave Absorption Spectra Under Jovian Condition, in: *AGU Fall Meeting Abstracts*, 2020, pp. A076–08.
- [436] E. Mills, J. Corby, A. Clements, N. Butterfield, P. Jones, M. Cunningham, J. Ott, A centimeter-wave study of methanol and ammonia isotopologues in Sgr B2 (N): physical and chemical differentiation between two hot cores, *Astrophysical Journal* 869 (2018) 121.
- [437] E. Canè, G. Di Lonardo, L. Fusina, F. Tamassia, A. Predoi-Cross, The  $\nu_2 = 1$ , 2 and  $\nu_4 = 1$  bending states of  $^{15}\text{NH}_3$  and their analysis at experimental accuracy, *Journal of Chemical Physics* 150 (2019) 194301.
- [438] E. Canè, G. D. Lonardo, L. Fusina, F. Tamassia, A. Predoi-Cross, Spectroscopic characterization of the  $\nu_2 = 3$  and  $\nu_2 = \nu_4 = 1$  states for  $^{15}\text{NH}_3$  from high resolution infrared spectra, *Journal of Quantitative Spectroscopy and Radiative Transfer* 250 (2020) 106987.
- [439] J. C. Pearson, S. Yu, O. Pirali, Modeling the spectrum of the  $2\nu_2$  and  $\nu_4$  states of ammonia to experimental accuracy, *Journal of Chemical Physics* 145 (2016) 124301.
- [440] J. Pearson, S. Yu, J. Pearson, K. Sung, B. Drouin, O. Pirali, Extended measurements and an experimental accuracy effective hamiltonian model

- for the  $3\nu_2$  and  $\nu_4 + \nu_2$  states of ammonia, *Journal of Molecular Spectroscopy* 353 (2018) 60–66.
- [441] H. M. Pickett, B. J. Drouin, T. Canty, R. J. Salawitch, R. A. Fuller, V. S. Perun, N. J. Livesey, J. W. Waters, R. A. Stachnik, S. P. Sander, W. A. Traub, K. W. Jucks, K. Minschwaner, Validation of Aura Microwave Limb Sounder OH and HO<sub>2</sub> measurements, *Journal of Geophysical Research: Atmospheres* 113 (2008) D16S30.
- [442] S. Noll, H. Winkler, O. Goussev, B. Proxauf, OH level populations and accuracies of Einstein-A coefficients from hundreds of measured lines, *Atmospheric Chemistry and Physics* 20 (2020) 5269–5292.
- [443] R. Cheung, K. Fai Li, S. Wang, T. J. Pongetti, R. P. Cageao, S. P. Sander, Y. L. Yung, Atmospheric hydroxyl radical (OH) abundances from ground-based ultraviolet solar spectra: an improved retrieval method, *Applied Optics* 47 (2008) 6277.
- [444] M. Asplund, N. Grevesse, A. J. Sauval, C. Allende Prieto, D. Kiselman, Line formation in solar granulation. IV. [O I], O I and OH lines and the photospheric O abundance, *Astronomy & Astrophysics* 417 (2004) 751–768.
- [445] J. R. Goicoechea, C. Joblin, A. Contursi, O. Berné, J. Cernicharo, M. Gerin, J. Le Bourlot, E. A. Bergin, T. A. Bell, M. Röllig, OH emission from warm and dense gas in the Orion Bar PDR, *Astronomy & Astrophysics* 530 (2011) L16.
- [446] J. P. Maillard, J. Chauville, A. W. Mantz, High-resolution emission spectrum of OH in an oxyacetylene flame from 3.7 to 0.9  $\mu\text{m}$ , *Journal of Molecular Spectroscopy* 63 (1976) 120–141.
- [447] C. M. Western, PGOPHER: A program for simulating rotational, vibrational and electronic spectra, *Journal of Quantitative Spectroscopy and Radiative Transfer* 186 (2017) 221–242.

- [448] J. S. A. Brooke, P. F. Bernath, C. M. Western, C. Sneden, M. Afşar, G. Li, I. E. Gordon, Line strengths of rovibrational and rotational transitions in the  $X^2\Pi$  ground state of OH, *Journal of Quantitative Spectroscopy and Radiative Transfer* 168 (2016) 142–157.
- [449] P. F. Bernath, R. Colin, Revised molecular constants and term values for the  $X^2\Pi$  and  $B^2\Sigma^+$  states of OH, *Journal of Molecular Spectroscopy* 257 (2009) 20–23.
- [450] M. Yousefi, P. F. Bernath, J. Hodges, T. Masseron, A new line list for the  $A^2\Sigma^+-X^2\Pi$  electronic transition of OH, *Journal of Quantitative Spectroscopy and Radiative Transfer* 217 (2018) 416–424.
- [451] G. Stark, J. W. Brault, M. C. Abrams, Fourier-transform spectra of the  $A^2\Sigma^+-X^2\Pi$   $\Delta v = 0$  bands of OH and OD, *Journal of the Optical Society of America B Optical Physics* 11 (1994) 3–32.
- [452] A. Fast, J. E. Furneaux, S. A. Meek, Precision spectra of  $A^2\Sigma^+$ ,  $v' = 0 \leftarrow X^2\Pi_{3/2}$ ,  $v'' = 0$ ,  $J'' = 3/2$  transitions in  $^{16}\text{OH}$  and  $^{16}\text{OD}$ , *Physical Review A* 98 (2018) 052511.
- [453] R. J. Le Roy, LEVEL: A computer program for solving the radial Schrödinger equation for bound and quasibound levels, *Journal of Quantitative Spectroscopy and Radiative Transfer* 186 (2017) 167–178.
- [454] P. F. Bernath, MoLLIST: Molecular Line Lists, Intensities and Spectra, *Journal of Quantitative Spectroscopy and Radiative Transfer* 240 (2020) 106687.
- [455] J. R. Gillis, A. Goldman, G. Stark, C. P. Rinsland, Line parameters for the  $A^2\Sigma^+-X^2\Pi$  bands of OH, *Journal of Quantitative Spectroscopy and Radiative Transfer* 68 (2001) 225–230.
- [456] S. M. Hwang, J. N. Kojima, Q.-V. Nguyen, M. J. Rabinowitz, Measurement of collision broadening of the  $p_1(5)$  line of (0,0) band of oh  $a^2\sigma^+ \leftarrow$

- $x^2\pi$  transition at high temperatures, *Journal of Quantitative Spectroscopy and Radiative Transfer* 109 (2008) 2715–2724.
- [457] J. J. Girard, R. Choudhary, R. K. Hanson, Collisional-induced broadening and shift parameters of OH with Ar and N<sub>2</sub> near 308.6 nm, measured at T = 1300–2000 K and P = 20–100 atm, *Journal of Quantitative Spectroscopy and Radiative Transfer* 221 (2018) 194–201.
- [458] J. J. Girard, S. Clees, R. K. Hanson, Collisional broadening and shift of five OH  $A^2\Sigma^+ \leftarrow X^2\Pi$  (0-0) transitions in the Q<sub>1</sub>-branch, by H<sub>2</sub>O, O<sub>2</sub>, CO<sub>2</sub>, N<sub>2</sub> and Ar, at 1220 K, *Journal of Quantitative Spectroscopy and Radiative Transfer* 240 (2020) 106681.
- [459] S. Kremser, L. W. Thomason, M. von Hobe, M. Hermann, T. Deshler, C. Timmreck, M. Toohey, A. Stenke, J. P. Schwarz, R. Weigel, S. Fueglistaler, F. J. Prata, J.-P. Vernier, H. Schlager, J. E. Barnes, J.-C. Antuña-Marrero, D. Fairlie, M. Palm, E. Mahieu, J. Notholt, M. Rex, C. Bingen, F. Vanhellemont, A. Bourassa, J. M. C. Plane, D. Klocke, S. A. Carn, L. Clarisse, T. Trickl, R. Neely, A. D. James, L. Rieger, J. C. Wilson, B. Meland, Stratospheric aerosol—Observations, processes, and impact on climate, *Reviews of Geophysics* 54 (2016) 278–335.
- [460] D. J. Hofmann, Increase in the stratospheric background sulfuric acid aerosol mass in the past 10 years, *Science* 248 (1990) 996–1000.
- [461] M. Chin, D. D. Davis, A reanalysis of carbonyl sulfide as a source of stratospheric background sulfur aerosol, *Journal of Geophysical Research: Atmospheres* 100 (1995) 8993–9005.
- [462] S. J. Taubman, J. F. Kasting, Carbonyl sulfide: No remedy for global warming, *Geophysical Research Letters* 22 (1995) 803–805.
- [463] A. R. Bandy, D. C. Thornton, J. E. Johnson, Carbon disulfide measurements in the atmosphere of the western North Atlantic and the north-

- western South Atlantic Oceans, *Journal of Geophysical Research: Atmospheres* 98 (1993) 23 449–23 457.
- [464] C. Brühl, J. Lelieveld, P. J. Crutzen, H. Tost, The role of carbonyl sulphide as a source of stratospheric sulphate aerosol and its impact on climate, *Atmospheric Chemistry and Physics* 12 (2012) 1239–1253.
- [465] V. A. Krasnopolsky, High-resolution spectroscopy of Venus: Detection of OCS, upper limit to H<sub>2</sub>S, and latitudinal variations of CO and HF in the upper cloud layer, *Icarus* 197 (2008) 377–385.
- [466] J. E. Campbell, M. E. Whelan, U. Seibt, S. J. Smith, J. A. Berry, T. W. Hilton, Atmospheric carbonyl sulfide sources from anthropogenic activity: Implications for carbon cycle constraints, *Geophysical Research Letters* 42 (2015) 3004–3010.
- [467] A. J. Kettle, U. Kuhn, M. von Hobe, J. Kesselmeier, M. O. Andreae, Global budget of atmospheric carbonyl sulfide: Temporal and spatial variations of the dominant sources and sinks, *Journal of Geophysical Research :Atmospheres* 107 (2002) 4658.
- [468] G. C. Toon, J.-F. L. Blavier, K. Sung, Atmospheric carbonyl sulfide (OCS) measured remotely by FTIR solar absorption spectrometry, *Atmospheric Chemistry and Physics* 18 (2018) 1923–1944.
- [469] L. Brown, A. Fayt, 1997. L.R. Brown, A. Fayt, Private Communication.
- [470] B. M. Hays, T. Guillaume, T. S. Hearne, I. R. Cooke, D. Gupta, O. Abdelkader Khedaoui, S. D. Le Picard, I. R. Sims, Design and performance of an E-band chirped pulse spectrometer for kinetics applications: OCS - He pressure broadening, *Journal of Quantitative Spectroscopy and Radiative Transfer* 250 (2020) 107001.
- [471] H. Mäder, J. Ekkers, W. Hoke, W. H. Flygare, A  $\pi$ ,  $\tau$ ,  $\pi/2$  type pulse sequence method for the determination of  $T_1$  in rotational transitions, *Journal of Chemical Physics* 62 (1975) 4380–4387.

- [472] I. C. Story, V. I. Metchnik, R. W. Parsons, The measurement of the widths and pressure-induced shifts of microwave spectra lines, *Journal of Physics B Atomic Molecular Physics* 4 (1971) 593–608.
- [473] M. Broquier, A. Picard-Bersellini, B. J. Whitaker, S. Green, Rotational inelastic cross sections for OCS-Ar, OCS-He, OCS-H<sub>2</sub> collisions - A comparison between theory and experiment, *Journal of Chemical Physics* 84 (1986) 2104–2107.
- [474] R. B. Nurf, Pressure broadening and shift in the millimeter-wave spectrum of formaldehyde, *Journal of Molecular Spectroscopy* 58 (1975) 451–473.
- [475] H. R. Barry, L. Corner, G. Hancock, R. Peverall, T. L. Ranson, G. A. D. Ritchie, Measurements of pressure broadening coefficients of selected transitions in the 2<sub>7</sub>5 band of formaldehyde, *Physical Chemistry Chemical Physics (Incorporating Faraday Transactions)* 5 (2003) 3106.
- [476] L. Wang, T. R. Sharples, Intrapulse quantum cascade laser spectroscopy: pressure induced line broadening and shifting in the  $\nu_6$  band of formaldehyde, *Applied Physics B: Lasers and Optics* 108 (2012) 427–435.
- [477] S. Nadler, D. C. Reuter, S. J. Daunt, Tunable diode laser measurements of formaldehyde foreign-gas broadening parameters and line strengths in the 9–11  $\mu\text{m}$  region, *Applied Optics* 26 (1987) 1641–1646.
- [478] A. R. Al-Derzi, S. N. Yurchenko, J. Tennyson, M. Melosso, N. Jiang, C. Puzzarini, L. Dore, T. Furtenbacher, R. Tobias, A. G. Császár, MARVEL analysis of the measured high-resolution spectra of formaldehyde, *Journal of Quantitative Spectroscopy and Radiative Transfer* 266 (2021) 107563.
- [479] A. F. Al-Refaie, S. N. Yurchenko, A. Yachmenev, J. Tennyson, ExoMol line lists - VIII: A variationally computed line list for hot formaldehyde, *Monthly Notices of the Royal Astronomical Society* 448 (2015) 1704–1714.

- [480] D. Hot, R. L. Pedersen, W. Weng, Y. Zhang, M. Alden, Z. Li, Spatially and temporally resolved IR-DFWM measurement of HCN released from gasification of biomass pellets, *Proceedings of the Combustion Institute* 37 (2019) 1337–1344.
- [481] M. Azhar, J. Mandon, A. Neerincx, Z. Liu, J. Mink, P. Merkus, S. Cristescu, F. Harren, A widely tunable, near-infrared laser-based trace gas sensor for hydrogen cyanide (HCN) detection in exhaled breath, *Applied Physics B* 123 (2017) 1–7.
- [482] E. Lellouch, M. Gurwell, B. Butler, T. Fouchet, P. Lavvas, D. Strobel, B. Sicardy, A. Mouillet, R. Moreno, D. Bockelée-Morvan, et al., Detection of CO and HCN in Pluto’s atmosphere with ALMA, *Icarus* 286 (2017) 289–307.
- [483] A. Tsiaras, M. Rocchetto, I. P. Waldmann, O. Venot, R. Varley, G. Morello, M. Damiano, G. Tinetti, E. J. Barton, S. N. Yurchenko, J. Tennyson, Detection of an Atmosphere Around the Super-Earth 55 Cancri e, *Astrophysical Journal* 820 (2016) 99.
- [484] M. Cordiner, M. Palmer, M. de Val-Borro, S. Charnley, L. Paganini, G. Villanueva, D. Bockelée-Morvan, N. Biver, A. Remijan, Y.-J. Kuan, et al., ALMA autocorrelation spectroscopy of comets: the HCN/H<sup>13</sup>CN ratio in C/2012 S1 (ISON), *Astrophysical Journal Letters* 870 (2019) L26.
- [485] R. J. Barber, J. K. Strange, C. Hill, O. L. Polyansky, G. C. Mellau, S. N. Yurchenko, J. Tennyson, ExoMol line lists – III. An improved hot rotation-vibration line list for HCN and HNC, *Monthly Notices of the Royal Astronomical Society* 437 (2014) 1828–1835.
- [486] G. J. Harris, O. L. Polyansky, J. Tennyson, Opacity data for HCN and HNC from a new *ab initio* linelist, *Astrophysical Journal* 578 (2002) 657–663.

- [487] G. C. Mellau, Complete experimental rovibrational eigenenergies of HCN up to  $6880\text{ cm}^{-1}$  above the ground state, *Journal of Chemical Physics* 134 (2011) 234303.
- [488] G. C. Mellau, V. Y. Makhnev, I. E. Gordon, N. F. Zobov, J. Tennyson, O. Polyansky, An experimentally-accurate and complete room-temperature infrared HCN line-list for the HITRAN database, *Journal of Quantitative Spectroscopy and Radiative Transfer In Preparation* (2021).
- [489] A. Maki, G. C. Mellau, S. Klee, M. Winnewisser, W. Quapp, High-temperature infrared measurements in the region of the bending fundamental of  $\text{H}^{12}\text{C}^{14}\text{N}$ ,  $\text{H}^{12}\text{C}^{15}\text{N}$ , and  $\text{H}^{13}\text{C}^{14}\text{N}$ , *Journal of Molecular Spectroscopy* 202 (2000) 67–82.
- [490] F. Maiwald, F. Lewen, V. Ahrens, M. Beaky, R. Gendriesch, A. Koroliev, A. Negirev, D. Paveljev, B. Vowinkel, G. Winnewisser, Pure rotational spectrum of hcn in the terahertz region: use of a new planar schottky diode multiplier, *Journal of Molecular Spectroscopy* 1 (2000) 166–168.
- [491] V. Y. Makhnev, A. A. Kyuberis, O. L. Polyansky, I. I. Mizus, J. Tennyson, N. F. Zobov, A new spectroscopically-determined potential energy surface and *ab initio* dipole moment surface for high accuracy HCN intensity calculations, *Journal of Molecular Spectroscopy* 353 (2018) 40–53.
- [492] J. P. Hofmann, B. Eifert, G. C. Mellau, Near infrared emission spectrum of  $\text{H}^{13}\text{CN}$ , *Journal of Molecular Spectroscopy* 262 (2010) 75–81.
- [493] P. Guay, J. Genest, A. J. Fleisher, Precision spectroscopy of  $\text{H}^{13}\text{CN}$  using a free-running, all-fiber dual electro-optic frequency comb system, *Optics Letters* 43 (2018) 1407–1410.
- [494] J. B. Cohen, E. B. Wilson, Rotational energy transfer in pure HCN and in HCN-rare gas mixtures by microwave double resonance and pressure broadening, *Journal of Chemical Physics* 58 (1973) 442–455.



- [495] S. C. Mehrotra, H. Mäder, J. P. M. de Vreede, H. A. Dijkerman, *J*-dependence of self-, H<sub>2</sub>- and He-broadened linewidth parameters for *l*-type doublet transitions in the bending vibrational state (01<sup>1</sup>0) of HCN, *Chemical Physics* 93 (1985) 115–125.
- [496] V. Lemaire, A. Babay, B. Lemoine, F. Rohart, J. P. Bouanich, Self- and Foreign-Gas-Broadening and Shifting of Lines in the  $\nu_2$  Band of HCN, *Journal of Molecular Spectroscopy* 177 (1996) 40–45.
- [497] J. F. D’Eu, B. Lemoine, F. Rohart, Infrared HCN Lineshapes as a Test of Galatry and Speed-Dependent Voigt Profiles, *Journal of Molecular Spectroscopy* 212 (2002) 96–110.
- [498] M. Charrón, T. G. Anderson, J. I. Steinfeld, Measurements of  $T_2$  in excited vibrational states of HCN, *Journal of Chemical Physics* 73 (1980) 1494–1497.
- [499] V. Landrain, G. Blanquet, M. Lepère, J. Walrand, J.-P. Bouanich, Diode-Laser Measurements of H<sub>2</sub>-Broadening Coefficients in the  $\nu_2$  Band of HCN, *Journal of Molecular Spectroscopy* 182 (1997) 184–188.
- [500] F. Rohart, L. Nguyen, J. Buldyreva, J. M. Colmont, G. Wlodarczak, Line-shapes of the 172 and 602 GHz rotational transitions of HC<sup>15</sup>N, *Journal of Molecular Spectroscopy* 246 (2007) 213–227.
- [501] Y. Xiao, D. J. Jacob, S. Turquety, Atmospheric acetylene and its relationship with CO as an indicator of air mass age, *Journal of Geophysical Research* 112 (2007) D12305.
- [502] C. A. Nixon, R. K. Achterberg, P. N. Romani, M. Allen, X. Zhang, N. A. Teanby, P. G. J. Irwin, F. M. Flasar, Abundances of Jupiter’s trace hydrocarbons from Voyager and Cassini, *Planetary and Space Science* 58 (2010) 1667–1680.

- [503] G. S. Orton, D. K. Aitken, C. Smith, P. F. Roche, J. Caldwell, R. Snyder, The spectra of Uranus and Neptune at 8-14 and 17-23  $\mu\text{m}$ , *Icarus* 70 (1987) 1–12.
- [504] B. M. Dinelli, M. López Puertas, F. Fabiano, A. Adriani, M. L. Moriconi, B. Funke, M. García-Comas, F. Oliva, E. D’Aversa, G. Filacchione, Climatology of  $\text{CH}_4$ ,  $\text{HCN}$  and  $\text{C}_2\text{H}_2$  in Titan’s upper atmosphere from Cassini/VIMS observations, *Icarus* 331 (2019) 83–97.
- [505] B. Amyay, A. Fayt, M. Herman, J. Vander Auwera, Vibration-rotation spectroscopic database on acetylene,  $\tilde{X}^1 \Sigma_g^+$  ( $^{12}\text{C}_2\text{H}_2$ ), *Journal of Physical and Chemical Reference Data* 45 (2016) 023103.
- [506] O. M. Lyulin, V. I. Perevalov, ASD-1000: High-resolution, high-temperature acetylene spectroscopic databank, *Journal of Quantitative Spectroscopy and Radiative Transfer* 201 (2017) 94–103.
- [507] O. M. Lyulin, V. I. Perevalov, Global modeling of vibration-rotation spectra of the acetylene molecule, *Journal of Quantitative Spectroscopy and Radiative Transfer* 177 (2016) 59–74.
- [508] D. Jacquemart, P. Soulard, O. M. Lyulin, Recommended acetylene  $^{12}\text{C}_2\text{H}_2$  line list in 13.6  $\mu\text{m}$  spectral region: New measurements and global modeling, *Journal of Quantitative Spectroscopy and Radiative Transfer* 258 (2021) 107200.
- [509] O. M. Lyulin, A. Campargue, An empirical spectroscopic database for acetylene in the regions of 5850–6341  $\text{cm}^{-1}$  and 7000–9415  $\text{cm}^{-1}$ , *Journal of Quantitative Spectroscopy and Radiative Transfer* 203 (2017) 461–471.
- [510] O. M. Lyulin, J. Vander Auwera, A. Campargue, The Fourier transform absorption spectrum of acetylene between 7000 and 7500  $\text{cm}^{-1}$ , *Journal of Quantitative Spectroscopy and Radiative Transfer* 160 (2015) 85–93.

- [511] O. M. Lyulin, J. Vander Auwera, A. Campargue, The Fourier transform absorption spectrum of acetylene between 8280 and 8700  $\text{cm}^{-1}$ , *Journal of Quantitative Spectroscopy and Radiative Transfer* 177 (2016) 234–240.
- [512] S. Béguier, O. M. Lyulin, S. M. Hu, A. Campargue, Line intensity measurements for acetylene between 8980 and 9420  $\text{cm}^{-1}$ , *Journal of Quantitative Spectroscopy and Radiative Transfer* 189 (2017) 417–420.
- [513] O. M. Lyulin, A. Campargue, D. Mondelain, S. Kass, The absorption spectrum of acetylene by CRDS between 7244 and 7918  $\text{cm}^{-1}$ , *Journal of Quantitative Spectroscopy and Radiative Transfer* 130 (2013) 327–334.
- [514] O. M. Lyulin, D. Mondelain, S. Béguier, S. Kass, J. Vander Auwera, A. Campargue, High-sensitivity CRDS absorption spectroscopy of acetylene between 5851 and 6341  $\text{cm}^{-1}$ , *Molecular Physics* 112 (2014) 2433–2444.
- [515] S. Kass, O. M. Lyulin, S. Béguier, A. Campargue, New assignments and a rare peculiarity in the high sensitivity CRDS spectrum of acetylene near 8000  $\text{cm}^{-1}$ , *Journal of Molecular Spectroscopy* 326 (2016) 106–114.
- [516] O. Lyulin, S. Vasilchenko, D. Mondelain, A. Campargue, The CRDS spectrum of acetylene near 1.73  $\mu\text{m}$ , *Journal of Quantitative Spectroscopy and Radiative Transfer* 234 (2019) 147–158.
- [517] O. M. Lyulin, A. Campargue, The absorption spectrum of acetylene near 1  $\mu\text{m}$  (9280–10 740  $\text{cm}^{-1}$ ) (II): Line intensities, *Journal of Quantitative Spectroscopy and Radiative Transfer* 215 (2018) 51–58.
- [518] O. M. Lyulin, S. Béguier, S. M. Hu, A. Campargue, The absorption spectrum of acetylene near 1  $\mu\text{m}$  (9280–10740  $\text{cm}^{-1}$ ) (I): Line positions, *Journal of Quantitative Spectroscopy and Radiative Transfer* 208 (2018) 179–187.
- [519] J. Tennyson, S. N. Yurchenko, A. F. Al-Refaie, E. J. Barton, K. L. Chubb, P. A. Coles, S. Diamantopoulou, M. N. Gorman, C. Hill, A. Z. Lam,

- L. Lodi, L. K. McKemmish, Y. Na, A. Owens, O. L. Polyansky, T. Rivlin, C. Sousa-Silva, D. S. Underwood, A. Yachmenev, E. Zak, The ExoMol database: Molecular line lists for exoplanet and other hot atmospheres, *Journal of Molecular Spectroscopy* 327 (2016) 73–94.
- [520] K. L. Chubb, J. Tennyson, S. N. Yurchenko, ExoMol molecular line lists - XXXVII. Spectra of acetylene, *Monthly Notices of the Royal Astronomical Society* 493 (2020) 1531–1545.
- [521] K. L. Chubb, M. Joseph, J. Franklin, N. Choudhury, T. Furtenbacher, A. G. Császár, G. Gaspard, P. Oguoko, A. Kelly, S. N. Yurchenko, J. Tennyson, C. Sousa-Silva, MARVEL analysis of the measured high-resolution rovibrational spectra of  $C_2H_2$ , *Journal of Quantitative Spectroscopy and Radiative Transfer* 204 (2018) 42–55.
- [522] P. V. Sada, G. H. McCabe, G. L. Bjoraker, D. E. Jennings, D. C. Reuter,  $^{13}C$ -Ethane in the Atmospheres of Jupiter and Saturn, *Astrophysical Journal* 472 (1996) 903–907.
- [523] F. M. Flasar, R. K. Achterberg, B. J. Conrath, P. J. Gierasch, V. G. Kunde, C. A. Nixon, G. L. Bjoraker, D. E. Jennings, P. N. Romani, A. A. Simon-Miller, B. Bézard, A. Coustenis, P. G. J. Irwin, N. A. Teanby, J. Brasunas, J. C. Pearl, M. E. Segura, R. C. Carlson, A. Mamoutkine, P. J. Schinder, A. Barucci, R. Courtin, T. Fouchet, D. Gautier, E. Lellouch, A. Marten, R. Prangé, S. Vinatier, D. F. Strobel, S. B. Calcutt, P. L. Read, F. W. Taylor, N. Bowles, R. E. Samuelson, G. S. Orton, L. J. Spilker, T. C. Owen, J. R. Spencer, M. R. Showalter, C. Ferrari, M. M. Abbas, F. Raulin, S. Edgington, P. Ade, E. H. Wishnow, Titan’s atmospheric temperatures, winds, and composition, *Science* 308 (2005) 975–978.
- [524] G. L. Villanueva, M. J. Mumma, K. Magee-Sauer, Ethane in planetary and cometary atmospheres: Transmittance and fluorescence models of the  $\nu_7$  band at 3.3  $\mu m$ , *Journal of Geophysical Research* 116 (2011) 1–23.

- [525] A. S. Pine, W. J. Lafferty, Torsional Splittings and Assignments of the Doppler-Limited Spectrum of Ethane in the C-H Stretching Region, *Journal of Research of the National Bureau of Standards* 83 (1982) 1–20.
- [526] F. Lattanzi, C. Di Lauro, J. Vander Auwera, Toward the understanding of the high resolution infrared spectrum of  $\text{C}_2\text{H}_6$  near  $3.3\ \mu\text{m}$ , *Journal of Molecular Spectroscopy* 267 (2011) 71–79.
- [527] Y. L. Radeva, M. J. Mumma, G. L. Villanueva, M. F. A’Hearn, A Newly Developed Fluorescence Model for  $\text{C}_2\text{H}_6\ \nu_5$  and Application to Cometary Spectra Acquired with NIRSPEC at Keck II, *The Astrophysical Journal* 729 (2011) 135.
- [528] A. S. Pine, W. J. Lafferty, Torsional splittings and assignments of the Doppler-limited spectrum of ethane in the C–H stretching region, *Journal of Research of the National Bureau of Standards* 87 (1982) 237–256.
- [529] A. S. Pine, S. C. Stone, Torsional tunneling and  $A_1$ – $A_2$  splittings and air broadening of the  ${}^rQ_0$  and  ${}^pQ_3$  subbranches of the  $\nu_7$  band of ethane, *Journal of Molecular Spectroscopy* 175 (1995) 21–30.
- [530] M. Dang-Nhu, A. S. Pine, W. J. Lafferty, Intensities in the  $\nu_5$ ,  $\nu_7$ , and  $\nu_8+\nu_{11}$  bands of ethane ( $\text{C-12}\text{H}_6$ ), *Canadian Journal of Physics* 62 (1984) 512.
- [531] J. J. Harrison, N. D. C. Allen, P. F. Bernath, Infrared absorption cross sections for ethane ( $\text{C}_2\text{H}_6$ ) in the 3  $\mu\text{m}$  region, *Journal of Quantitative Spectroscopy and Radiative Transfer* 111 (2010) 357.
- [532] K. D. Doney, V. Kofman, G. Villanueva, K. Sung, A new model of monodeuterated ethane ( $\text{C}_2\text{H}_5\text{D}$ ) spectrum: Enabling sensitive constraints on the D/H in ethane emission in comets, *Journal of Quantitative Spectroscopy and Radiative Transfer* 255 (2020) 107225.
- [533] K. Sung, A. W. Mantz, M. A. H. Smith, L. R. Brown, T. J. Crawford, V. M. Devi, D. C. Benner, Cryogenic absorption cells operating inside a

- Bruker IFS-125HR: First results for  $^{13}\text{CH}_4$  at  $7\ \mu\text{m}$ , *Journal of Molecular Spectroscopy* 262 (2010) 122–134.
- [534] A. W. Mantz, K. Sung, L. R. Brown, T. J. Crawford, M. A. H. Smith, V. Malathy Devi, D. Chris Benner, A cryogenic Herriott cell vacuum-coupled to a Bruker IFS-125HR, *Journal of Molecular Spectroscopy* 304 (2014) 12–24.
- [535] V. M. Devi, C. P. Rinsland, D. C. Benner, R. L. Sams, T. A. Blake, Multispectrum analysis of the  $\nu_9$  band of  $^{12}\text{C}_2\text{H}_6$ : Positions, intensities, self- and  $\text{N}_2$ -broadened half-width coefficients, *Journal of Quantitative Spectroscopy and Radiative Transfer* 111 (2010) 1234–1251.
- [536] V. Malathy Devi, D. Chris Benner, C. Rinsland, M. Smith, R. Sams, T. Blake, J.-M. Flaud, K. Sung, L. Brown, A. Mantz, Multispectrum measurements of spectral line parameters including temperature dependences of  $\text{N}_2$ - and self-broadened half-width coefficients in the region of the  $\nu_9$  band of  $^{12}\text{C}_2\text{H}_6$ , *Journal of Quantitative Spectroscopy and Radiative Transfer* 111 (2010) 2481–2504.
- [537] N. Moazzen-Ahmadi, J. Norooz Oliaee, I. Ozier, E. H. Wishnow, K. Sung, T. J. Crawford, L. R. Brown, V. M. Devi, An intensity study of the torsional bands of ethane at  $35\ \mu\text{m}$ , *Journal of Quantitative Spectroscopy and Radiative Transfer* 151 (2015) 123–132.
- [538] M. A. Pasek, J. M. Sampson, Z. Atlas, Redox chemistry in the phosphorus biogeochemical cycle, *Proceedings of the National Academy of Science* 111 (2014) 15468–15473.
- [539] H. P. Larson, R. R. Treffers, U. Fink, Phosphine in Jupiter’s atmosphere: the evidence from high-altitude observations at 5 micrometers, *Astrophysical Journal* 211 (1977) 972–979.
- [540] L. N. Fletcher, G. S. Orton, N. A. Teanby, P. G. J. Irwin, Phosphine on Jupiter and Saturn from Cassini/CIRS, *Icarus* 202 (2009) 543–564.

- [541] J. L. Burgess, D. J. Burgess, Phosphine exposure from a methamphetamine laboratory investigation, *Journal of Toxicology: Clinical Toxicology* 39 (2001) 165–168.
- [542] C. Sousa-Silva, S. Seager, S. Ranjan, J. J. Petkowski, Z. Zhan, R. Hu, W. Bains, Phosphine as a Biosignature Gas in Exoplanet Atmospheres, *Astrobiology* 20 (2020) 235–268.
- [543] J. S. Greaves, A. M. S. Richards, W. Bains, P. B. Rimmer, H. Sagawa, D. L. Clements, S. Seager, J. J. Petkowski, C. Sousa-Silva, S. Ranjan, E. Drabek-Maunder, H. J. Fraser, A. Cartwright, I. Mueller-Wodarg, Z. Zhan, P. Friberg, I. Coulson, E. Lee, J. Hoge, Phosphine gas in the cloud decks of Venus, *Nature Astronomy* (2020).
- [544] G. Villanueva, M. Cordiner, P. Irwin, I. de Pater, B. Butler, M. Gurwell, S. Milam, C. Nixon, S. Luszcz-Cook, C. Wilson, V. Kofman, G. Liuzzi, S. Faggi, T. Fauchez, M. Lippi, R. Cosentino, A. Thelen, A. Moullet, P. Hartogh, E. Molter, S. Charnley, G. Arney, A. Mandell, N. Biver, A. Vandaele, K. de Kleer, R. Kopparapu, No phosphine in the atmosphere of Venus, *arXiv e-prints* (2020) arXiv:2010.14305.
- [545] T. Encrenaz, T. K. Greathouse, E. Marcq, T. Widemann, B. Bézard, T. Fouchet, R. Giles, H. Sagawa, J. Greaves, C. Sousa-Silva, A stringent upper limit of the  $\text{PH}_3$  abundance at the cloud top of Venus, *Astronomy & Astrophysics* 643 (2020) L5.
- [546] I. A. G. Snellen, L. Guzman-Ramirez, M. R. Hogerheijde, A. P. S. Hygate, F. F. S. van der Tak, Re-analysis of the 267 GHz ALMA observations of Venus, No statistically significant detection of phosphine, *Astronomy & Astrophysics* 644 (2020) L2.
- [547] L. Trompet, S. Robert, A. Mahieux, F. Schmidt, J. Erwin, A. C. Vandaele, Phosphine in Venus’ atmosphere: Detection attempts and upper limits above the cloud top assessed from the SOIR/VEx spectra, *Astronomy & Astrophysics* 645 (2021) L4.

- [548] I. Kleiner, V. M. Devi, PH<sub>3</sub> line list, 2018.
- [549] V. M. Devi, D. C. Benner, I. Kleiner, R. L. Sams, L. N. Fletcher, Line shape parameters of PH<sub>3</sub> transitions in the Pentad near 4-5  $\mu\text{m}$ : Self-broadened widths, shifts, line mixing and speed dependence, *Journal of Molecular Spectroscopy* 302 (2014) 17–33.
- [550] V. M. Devi, I. Kleiner, R. L. Sams, L. R. Brown, D. C. Benner, L. N. Fletcher, Line positions and intensities of the phosphine (PH<sub>3</sub>) Pentad near 4.5  $\mu\text{m}$ , *Journal of Molecular Spectroscopy* 298 (2014) 11–23.
- [551] L. Fusina, M. Carlotti, The far-infrared spectrum and spectroscopic parameters of PH<sub>3</sub> in the ground state, *Journal of Molecular Spectroscopy* 130 (1988) 371–381.
- [552] G. Tarrago, N. Lacome, A. Lévy, G. Guelachvili, B. Bézard, P. Drossart, Phosphine spectrum at 4-5  $\mu\text{m}$ : Analysis and line-by-line simulation of  $2\nu_2$ ,  $\nu_2 + \nu_4$ ,  $2\nu_4$ ,  $\nu_1$ , and  $\nu_3$  bands, *Journal of Molecular Spectroscopy* 154 (1992) 30–42.
- [553] A. V. Nikitin, Y. A. Ivanova, M. Rey, S. A. Tashkun, G. C. Toon, K. Sung, V. G. Tyuterev, Analysis of PH<sub>3</sub> spectra in the Octad range 2733–3660  $\text{cm}^{-1}$ , *Journal of Quantitative Spectroscopy and Radiative Transfer* 203 (2017) 472–479.
- [554] A. V. Nikitin, J. P. Champion, R. A. H. Butler, L. R. Brown, I. Kleiner, Global modeling of the lower three polyads of PH<sub>3</sub>: Preliminary results, *Journal of Molecular Spectroscopy* 256 (2009) 4–16.
- [555] R. A. H. Butler, L. Sagui, I. Kleiner, L. R. Brown, The absorption spectrum of phosphine (PH<sub>3</sub>) between 2.8 and 3.7  $\mu\text{m}$ : Line positions, intensities, and assignments, *Journal of Molecular Spectroscopy* 238 (2006) 178–192.
- [556] L. Wang, P. Chen, G.-S. Cheng, Y. Ding, S.-M. Hu, Absorption line intensities of phosphine in the regions 1950–2480  $\text{cm}^{-1}$  and 3280–3580  $\text{cm}^{-1}$



- studied by Fourier-transform spectroscopy, *Spectroscopy and Spectral Analysis* 25 (2005) 1221–1226.
- [557] M. Rey, A. V. Nikitin, V. G. Tyuterev, TheoReTS line list of PH<sub>3</sub>, 2020.
- [558] J. K. G. Watson, Simplification of the molecular vibration-rotation Hamiltonian, *Molecular Physics* 15 (1968) 479–490.
- [559] A. V. Nikitin, F. Holka, V. G. Tyuterev, J. Fremont, Vibration energy levels of the PH<sub>3</sub>, PH<sub>2</sub>D, and PHD<sub>2</sub> molecules calculated from high order potential energy surface, *Journal of Chemical Physics* 130 (2009) 244312–244312.
- [560] M. Rey, I. S. Chizhmakova, A. V. Nikitin, V. G. Tyuterev, Understanding global infrared opacity and hot bands of greenhouse molecules with low vibrational modes from first-principles calculations: the case of CF<sub>4</sub>, *Physical Chemistry Chemical Physics (Incorporating Faraday Transactions)* 20 (2018) 21008–21033.
- [561] M. Rey, A. V. Nikitin, V. G. Tyuterev, Ab initio ro-vibrational Hamiltonian in irreducible tensor formalism: a method for computing energy levels from potential energy surfaces for symmetric-top molecules, *Molecular Physics* 108 (2010) 2121–2135.
- [562] M. Rey, A. V. Nikitin, V. G. Tyuterev, Accurate first-principles calculations for <sup>12</sup>CH<sub>3</sub>D infrared spectra from isotopic and symmetry transformations, *Journal of Chemical Physics* 141 (2014) 044316.
- [563] A. V. Nikitin, M. Rey, V. G. Tyuterev, High order dipole moment surfaces of PH<sub>3</sub> and ab initio intensity predictions in the Octad range, *Journal of Molecular Spectroscopy* 305 (2014) 40–47.
- [564] L. R. Brown, R. L. Sams, I. Kleiner, C. Cottaz, L. Sagui, Line Intensities of the Phosphine Dyad at 10  $\mu$ m, *Journal of Molecular Spectroscopy* 215 (2002) 178–203.

- [565] C. Sousa-Silva, A. F. Al-Refaie, J. Tennyson, S. N. Yurchenko, ExoMol line lists - VII. The rotation-vibration spectrum of phosphine up to 1500 K, *Monthly Notices of the Royal Astronomical Society* 446 (2015) 2337–2347.
- [566] C. Sousa-Silva, S. N. Yurchenko, J. Tennyson, A computed room temperature line list for phosphine, *Journal of Molecular Spectroscopy* 288 (2013) 28–37.
- [567] J.-P. Bouanich, J. Walrand, G. Blanquet, N<sub>2</sub>-broadening coefficients in the  $\nu_2$  and  $\nu_4$  bands of PH<sub>3</sub>, *Journal of Molecular Spectroscopy* 232 (2005) 40–46.
- [568] J.-P. Bouanich, G. Blanquet, N<sub>2</sub>-broadening coefficients in the  $\nu_2$  and  $\nu_4$  bands of PH<sub>3</sub> at low temperature, *Journal of Molecular Spectroscopy* 241 (2007) 186–191.
- [569] J.-P. Bouanich, J. Salem, H. Aroui, J. Walrand, G. Blanquet, H<sub>2</sub>-broadening coefficients in the  $\nu_2$  and  $\nu_4$  bands of PH<sub>3</sub>, *Journal of Quantitative Spectroscopy and Radiative Transfer* 84 (2004) 195–205.
- [570] J. Salem, J.-P. Bouanich, J. Walrand, H. Aroui, G. Blanquet, Hydrogen line broadening in the  $\nu_2$  and  $\nu_4$  bands of phosphine at low temperature, *Journal of Molecular Spectroscopy* 228 (2004) 23–30.
- [571] H. M. Pickett, R. L. Poynter, E. A. Cohen, Pressure broadening of phosphine by hydrogen and helium, *Journal of Quantitative Spectroscopy and Radiative Transfer* 26 (1981) 197.
- [572] M. Sergent-Rozey, Nguyen-van-Thanh, I. Rossi, N. Lacome, A. Levy, Collisional broadening and line intensities in the pure rotational spectrum of PH<sub>3</sub>, *Journal of Molecular Spectroscopy* 131 (1988) 66–76.
- [573] A. Levy, N. Lacome, G. Tarrago, Hydrogen- and Helium-Broadening of Phosphine Lines, *Journal of Molecular Spectroscopy* 157 (1993) 172–181.

- [574] A. Levy, N. Lacome, G. Tarrago, Temperature Dependence of Collision-Broadened Lines of Phosphine, *Journal of Molecular Spectroscopy* 166 (1994) 20–31.
- [575] J. Salem, J.-P. Bouanich, J. Walrand, H. Aroui, G. Blanquet, Helium- and argon-broadening coefficients of phosphine lines in the  $\nu_2$  and  $\nu_4$  bands, *Journal of Molecular Spectroscopy* 232 (2005) 247–254.
- [576] J. Salem, G. Blanquet, M. Lepère, H. Aroui,  $H_2$  line mixing coefficients in the  $\nu_2$  and  $\nu_4$  bands of  $PH_3$ , *Journal of Molecular Spectroscopy* 297 (2014) 58–61.
- [577] E. J. Barton, C. Hill, M. Czurylo, H. Y. Li, A. Hyslop, S. N. Yurchenko, J. Tennyson, The ExoMol pressure broadening diet:  $H_2$  and He line-broadening parameters, *Journal of Quantitative Spectroscopy and Radiative Transfer* 203 (2017) 490–495.
- [578] C. Boulet, Q. Ma, Line shape parameters of  $PH_3$  transitions: Theoretical studies of self-broadened widths and line mixing effects, *Journal of Chemical Physics* 152 (2020) 214305.
- [579] M. Faye, V. Boudon, M. Loëte, P. Roy, L. Manceron, The high overtone and combination levels of  $SF_6$  revisited at Doppler-limited resolution: A global effective rovibrational model for highly excited vibrational states, *Journal of Quantitative Spectroscopy and Radiative Transfer* 190 (2017) 38–47.
- [580] M. Faye, L. Manceron, P. Roy, V. Boudon, M. Loëte, First high resolution analysis of the  $\nu_3$  band of the  $^{36}SF_6$  isotopologue, *Journal of Molecular Spectroscopy* 346 (2018) 23–26.
- [581] C. Richard and V. Boudon and M. Rotger, Calculated spectroscopic databases for the VAMDC portal: New molecules and improvements, *Journal of Quantitative Spectroscopy and Radiative Transfer* 251 (2020) 107096.

- [582] A. V. Nikitin, M. Rey, I. S. Chizhmakova, V. G. Tyuterev, First Full-Dimensional Potential Energy and Dipole Moment Surfaces of SF<sub>6</sub>, *J. Phys. Chem* 2020 (2020) 7023.
- [583] O. N. Ulenikov, E. S. Bekhtereva, O. V. Gromova, N. I. Raspopova, A. S. Belova, C. Maul, C. Sydow, S. Bauerecker, Experimental line strengths of the  $5\nu_2$  band of H<sub>2</sub><sup>32</sup>S in comparison with the results of “variational” calculation and HITRAN database, *Journal of Quantitative Spectroscopy and Radiative Transfer* 243 (2020).
- [584] O. N. Ulenikov, E. S. Bekhtereva, O. V. Gromova, F. Zhang, N. I. Raspopova, C. Sydow, S. Bauerecker, Ro-vibrational analysis of the first hexad of hydrogen sulfide: Line position and strength analysis of the  $4\nu_2$  band of H<sub>2</sub><sup>32</sup>S and H<sub>2</sub><sup>34</sup>S for HITRAN applications, *Journal of Quantitative Spectroscopy and Radiative Transfer* 255 (2020) 107236.
- [585] K. L. Chubb, O. Naumenko, S. Keely, S. Bartolotto, S. MacDonald, M. Mukhtar, A. Grachov, J. White, E. Coleman, A. Liu, A. Z. Fazliev, E. R. Polovtseva, V.-M. Horneman, A. Campargue, T. Furtenbacher, A. G. Császár, S. N. Yurchenko, J. Tennyson, MARVEL analysis of the measured high-resolution rovibrational spectra of H<sub>2</sub>S, *Journal of Quantitative Spectroscopy and Radiative Transfer* 218 (2018) 178–186.
- [586] A. A. A. Azzam, S. N. Yurchenko, J. Tennyson, O. V. Naumenko, ExoMol line lists XVI: A Hot Line List for H<sub>2</sub>S, *Mon. Not. R. Astron. Soc.* 460 (2016) 4063–4074.
- [587] M. Mouelhi, A. Cuisset, F. Hindle, C. Jellali, S. Galalou, H. Aroui, R. Bocquet, G. Mouret, F. Rohart, Self and N<sub>2</sub> broadening coefficients of H<sub>2</sub>S probed by submillimeter spectroscopy: Comparison with IR measurements and semi-classical calculations, *Journal of Quantitative Spectroscopy and Radiative Transfer* 247 (2020) 106955.
- [588] J. Waschull, F. Kuhnemann, B. Sumpf, Self-, Air-, and Helium-

- Broadening in the  $\nu_2$  Band of  $\text{H}_2\text{S}$ , *Journal of Molecular Spectroscopy* 165 (1994) 150–158.
- [589] A. Kissel, B. Sumpf, H. D. Kronfeldt, B. A. Tikhomirov, Y. N. Ponomarev, Noble gas induced line-shift and line-broadening in the  $\nu_2$  band of  $\text{H}_2\text{S}$ , *Journal of Molecular Structure* 517-518 (2000) 477–492.
- [590] B. Sumpf, I. Meusel, H. D. Kronfeldt, Noble Gas Broadening in Fundamental Bands of  $\text{H}_2\text{S}$ , *Journal of Molecular Spectroscopy* 184 (1997) 51–55.
- [591] V. I. Starikov, Broadening of vibrational-rotational lines of the  $\text{H}_2\text{S}$  molecule by pressure of monatomic gases, *Optics and Spectroscopy* 115 (2013) 18–27.
- [592] A. Kissel, B. Sumpf, H. D. Kronfeldt, B. A. Tikhomirov, Y. N. Ponomarev, Molecular-Gas-Pressure-Induced Line-Shift and Line-Broadening in the  $\nu_2$  Band of  $\text{H}_2\text{S}$ , *Journal of Molecular Spectroscopy* 216 (2002) 345–354.
- [593] V. I. Starikov, A. E. Protasevich, Broadening of absorption lines of the  $\nu_2$  band of the  $\text{H}_2\text{S}$  molecule by the pressure of atmospheric gases, *Optics and Spectroscopy* 101 (2006) 523–531.
- [594] B. Franco, L. Clarisse, T. Stavrakou, J. Müller, D. Taraborrelli, J. Hadji-Lazaro, J. W. Hannigan, F. Hase, D. Hurtmans, N. Jones, E. Lutsch, E. Mahieu, I. Ortega, M. Schneider, K. Strong, C. Vigouroux, C. Clerbaux, P. Coheur, Spaceborne Measurements of Formic and Acetic Acids: A Global View of the Regional Sources, *Geophysical Research Letters* 47 (2020).
- [595] G. González Abad, P. F. Bernath, C. D. Boone, S. D. McLeod, G. L. Manney, G. C. Toon, Global distribution of upper tropospheric formic acid from the ACE-FTS, *Atmospheric Chemistry and Physics* 9 (2009) 8039–8047.

- [596] C. M. Western, PGOPHER: A program for simulating rotational, vibrational and electronic spectra, *Journal of Quantitative Spectroscopy and Radiative Transfer* 186 (2017) 221–242.
- [597] O. I. Baskakov, E. A. Alekseev, R. A. Motiyenko, J. Lohilahti, V.-M. Horneman, S. Alanko, B. P. Winnewisser, I. R. Medvedev, F. C. De Lucia, FTIR and millimeter wave investigation of the  $7^1$  and  $9^1$  states of formic acid HCOOH and  $H^{13}$ COOH, *Journal of Molecular Spectroscopy* 240 (2006) 188–201.
- [598] K. Hull, T. Wells, B. E. Billinghurst, H. Bunn, P. L. Raston, Synchrotron-based infrared spectroscopy of formic acid: Confirmation of the reassignment of Fermi-coupled  $8\ \mu\text{m}$  states, *AIP Advances* 9 (2019).
- [599] A. Perrin, J. Vander Auwera, An improved database for the  $9\ \mu\text{m}$  region of the formic acid spectrum, *Journal of Quantitative Spectroscopy and Radiative Transfer* 108 (2007) 363–370.
- [600] R. V. Kochanov, I. E. Gordon, L. S. Rothman, S. W. Sharpe, T. J. Johnson, R. L. Sams, Comment on "Radiative forcings for 28 potential Archean greenhouse gases" by Byrne and Goldblatt (2014), *Climate of the Past Discussions* 11 (2015) 1985–2007.
- [601] W. Raballand, M. Rotger, V. Boudon, M. Loëte, Spectroscopy of  $X_2Y_4$  ( $D_{2h}$ ) molecules : Tensorial formalism adapted to the  $O(3) \supset D_{2h}$  chain, Hamiltonian and transition moment operators, *Journal of Molecular Spectroscopy* 217 (2003) 239–248.
- [602] C. P. Rinsland, V. Malathy Devi, D. C. Benner, T. A. Blake, R. L. Sams, L. R. Brown, I. Kleiner, A. Dehayem-Kamadjou, H. S. P. Müller, R. R. Gamache, D. L. Niles, T. Masiello, Multispectrum analysis of the  $\nu_4$  band of  $\text{CH}_3\text{CN}$ : Positions, intensities, self- and  $\text{N}_2$ -broadening, and pressure-induced shifts, *J. Quant. Spectrosc. Radiat. Transfer* 109 (2008) 974–994.

- [603] H. S. P. Müller, A. Belloche, F. Lewen, B. J. Drouin, K. Sung, R. T. Ordu, Garrod, K. M. Menten, Toward a global model of the interactions in low-lying states of methyl cyanide: rotational and rovibrational spectroscopy of the  $\Delta v_4 = 1$  state and tentative interstellar detection of the  $\Delta v_4 = \Delta v_8 = 1$  state In Sgr B2(N), *J. Mol. Spectrosc.* (2021). Resubmitted.
- [604] H. S. P. Müller, L. R. Brown, B. J. Drouin, J. C. Pearson, I. Kleiner, R. L. Sams, K. Sung, M. H. Ordu, F. Lewen, Rotational spectroscopy as a tool to investigate interactions between vibrational polyads in symmetric top molecules: Low-lying states  $\Delta v_8 \leq 2$  of methyl cyanide,  $\text{CH}_3\text{CN}$ , *J. Mol. Spectrosc.* 312 (2015) 22–37.
- [605] M. Carlos, O. Gruson, C. Richard, V. Boudon, M. Rotger, X. Thomas, C. Maul, C. Sydow, A. Domanskaya, R. Georges, P. Souard, O. Pirali, M. Goubet, P. Asselin, T. R. Huet, High-resolution spectroscopy and global analysis of  $\text{CF}_4$  rovibrational bands to model its atmospheric absorption, *Journal of Quantitative Spectroscopy and Radiative Transfer* 201 (2017) 75–93.
- [606] L. Bizzocchi, F. Tamassia, J. Laas, B. M. Giuliano, C. D. Esposti, L. Dore, M. Melosso, E. Canè, A. P. Charney, H. S. P. Müller, H. Spahn, A. Belloche, P. Caselli, K. M. Menten, R. T. Garrod, Rotational and High-resolution Infrared Spectrum of  $\text{HC}_3\text{N}$ : Global Ro-vibrational Analysis and Improved Line Catalog for Astrophysical Observations, *Astrophysical Journal Supplement Series* 233 (2017) 11.
- [607] A. E. Thelen, C. A. Nixon, N. J. Chanover, M. A. Cordiner, E. M. Molter, N. A. Teanby, P. G. Irwin, J. Serigano, S. B. Charnley, Abundance measurements of Titan’s stratospheric HCN,  $\text{HC}_3\text{N}$ ,  $\text{C}_3\text{H}_4$ , and  $\text{CH}_3\text{CN}$  from ALMA observations, *Icarus* 319 (2019) 417–432.
- [608] G. L. Villanueva, K. Magee-Sauer, M. J. Mumma, Modeling of nitrogen compounds in cometary atmospheres: Fluorescence models of ammonia ( $\text{NH}_3$ ), hydrogen cyanide (HCN), hydrogen isocyanide (HNC) and

- cyanoacetylene ( $\text{HC}_3\text{N}$ ), *Journal of Quantitative Spectroscopy and Radiative Transfer* 129 (2013) 158–168.
- [609] X. J. Jiang, J. Z. Wang, Y. Gao, Q. S. Gu,  $\text{HC}_3\text{N}$  observations of nearby galaxies, *Astronomy and Astrophysics* 600 (2017) 15.
- [610] A. Jolly, Y. Benilan, A. Fayt, New infrared integrated band intensities for  $\text{HC}_3\text{N}$  and extensive line list for the  $\nu_5$  and  $\nu_6$  bending modes, *Journal of Molecular Spectroscopy* 242 (2007) 46–54.
- [611] E. Miller-Ricci, S. Seager, D. Sasselov, The atmospheric signatures of super-Earths: how to distinguish between hydrogen-rich and hydrogen-poor atmospheres, *Astrophysical Journal* 690 (2008) 1056–1067.
- [612] P. Wcisło, F. Thibault, N. Stolarczyk, H. Jóźwiak, M. Słowiński, M. Gancewski, K. Stankiewicz, M. Konefał, S. Kass, A. Campargue, Y. Tan, J. Wang, K. Patkowski, R. Ciuryło, D. Lisak, R. Kochanov, L.S. Rothman, I.E. Gordon, The first comprehensive dataset of beyond-Voigt line-shape parameters from *ab initio* quantum scattering calculations for the HITRAN database: He-perturbed  $\text{H}_2$  case study, *Journal of Quantitative Spectroscopy and Radiative Transfer* 260 (2021) 107477.
- [613] E. Roueff, H. Abgrall, P. Czachorowski, K. Pachucki, M. Puchalski, J. Komasa, The full infrared spectrum of molecular hydrogen, *Astronomy & Astrophysics* 630 (2019) A58.
- [614] Z. Lu, G. C. Tabisz, L. Ulivi, Temperature dependence of the pure rotational band of HD: Interference, widths, and shifts, *Physical Review A* 47 (1993) 1159–1173.
- [615] K. Sung, E. H. Wishnow, L. Manceron, B. Drouin, C. Nixon, , Progress report on the measurements of pressure-broadening of HD rotational transitions for Jovian atmospheres, *Bulletin of the AAS* 52 (2020). <https://baas.aas.org/pub/2020n6i103p06>.



- [616] K. Sung, E. H. Wishnow, L. Manceron, B. Drouin, C. Nixon, , Laboratory study of HD R(0) – R(3) transitions broadened by H<sub>2</sub> for Jovian atmospheres, *Journal of Quantitative Spectroscopy and Radiative Transfer In Preparation* (2021).
- [617] C. P. Endres, S. Schlemmer, P. Schilke, J. Stutzki, H. S. P. Müller, The Cologne Database for Molecular Spectroscopy, CDMS, in the Virtual Atomic and Molecular Data Centre, VAMDC, *Journal of Molecular Spectroscopy* 327 (2016) 95–104.
- [618] S. Chandra, W. H. Kegel, R. J. Le Roy, T. Hertenstein, Einstein A-coefficients for vib-rotational transitions in CS., *Astronomy & Astrophysics Supplement* 114 (1995) 175.
- [619] G. Paulose, E. J. Barton, S. N. Yurchenko, J. Tennyson, ExoMol molecular line lists - XII. Line lists for eight isotopologues of CS, *Monthly Notices of the Royal Astronomical Society* 454 (2015) 1931–1939.
- [620] S. Hou, Z. Wei, Line Lists for the  $X\ ^1\Sigma^+$  State of CS, *Astrophysical Journal Supplement Series* 246 (2020) 14.
- [621] B. J. Sandor, R. Todd Clancy, G. Moriarty-Schieven, F. P. Mills, Sulfur chemistry in the Venus mesosphere from SO<sub>2</sub> and SO microwave spectra, *Icarus* 208 (2010) 49–60.
- [622] K. de Kleer, I. de Pater, M. Ádámkovics, Emission from volcanic SO gas on Io at high spectral resolution, *Icarus* 317 (2019) 104–120.
- [623] J. Boissier, D. Bockelée-Morvan, N. Biver, J. Crovisier, D. Despois, B. G. Marsden, R. Moreno, Interferometric imaging of the sulfur-bearing molecules H<sub>2</sub>S, SO, and CS in comet C/1995 O1 (Hale-Bopp), *Astronomy & Astrophysics* 475 (2007) 1131–1144.
- [624] P. F. Bernath, D. M. Bittner, Line list for the  $a^1\Delta-X^3\Sigma^-$  transition of SO: Assignment of the 1.69 micron feature on Io, *Journal of Quantitative Spectroscopy and Radiative Transfer* 240 (2020) 2019–2021.

- [625] M. A. Martin-Drumel, F. Hindle, G. Mouret, A. Cuisset, J. Cernicharo, A complete spectroscopic characterization of SO and its isotopologues up to the terahertz domain, *Astrophysical Journal* 799 (2015) 115.
- [626] E. Raddaoui, L. Troitsyna, A. Dudaryonok, P. Soulard, M. Guinet, H. Aroui, J. Buldyreva, N. Lavrentieva, D. Jacquemart, Line parameters measurements and modeling for the  $\nu_6$  band of CH<sub>3</sub>I: A complete line list for atmospheric databases, *Journal of Quantitative Spectroscopy and Radiative Transfer* 232 (2019) 165–179.
- [627] D. Papoušek, P. Pracna, M. Winnewisser, S. Klee, J. Demaison, Simultaneous Ro-vibrational Analysis of the  $\nu_2$ ,  $\nu_3$ ,  $\nu_5$ , and  $\nu_6$  Bands of H<sub>3</sub><sup>12</sup>CF, *Journal of Molecular Spectroscopy* 196 (1999) 319–323.
- [628] D. Jacquemart and M. Guinet, Line parameters measurements and modeling for the  $\nu_6$  band of CH<sub>3</sub>F: generation of a complete line list for atmospheric databases, *Journal of Quantitative Spectroscopy and Radiative Transfer* 185 (2016) 58–69.
- [629] A. Barbouchi Ramani, D. Jacquemart, P. Soulard, M. Guinet, Measurements and modeling of N<sub>2</sub>-broadening coefficients for the  $\nu_6$  band of CH<sub>3</sub>F, comparison with CH<sub>3</sub>Br and CH<sub>3</sub>Cl molecules, *Journal of Quantitative Spectroscopy and Radiative Transfer* 185 (2016) 58–69.
- [630] A. Adriani, A. Bracco, D. Grassi, M. L. Moriconi, A. Mura, G. Orton, F. Altieri, A. Ingersoll, S. K. Atreya, J. I. Lunine, A. Migliorini, R. Noschese, A. Cicchetti, R. Sordini, F. Tosi, G. Sindoni, C. Plainaki, B. M. Dinelli, D. Turrini, G. Filacchione, G. Piccioni, S. J. Bolton, Two-year observations of the Jupiter polar regions by JIRAM on board Juno, *Journal of Geophysical Research: Planets* 125 (2020) e2019JE006098.
- [631] C. Wenger, V. Boudon, M. Rotger, J. P. Sanzharov, J. P. Champion, XTDS and SPVIEW: Graphical tools for the analysis and simulation of high-resolution molecular spectra, *Journal of Molecular Spectroscopy* 251 (2008) 102–113.

- [632] V. Boudon and T. Grigoryan and F. Philipot and C. Richard and F. Kwabia Tchana and L. Manceron and A. Rizopoulos and J. Vander Auwera and Th. Encrenaz, Line positions and intensities for the  $\nu_3$  band of 5 isotopologues of germane for planetary applications, *Journal of Quantitative Spectroscopy and Radiative Transfer* 205 (2018) 174–183.
- [633] C. Richard and V. Boudon and A. Rizopoulos and J. Vander Auwera and F. Kwabia Tchana, Line positions and intensities for the  $\nu_2/\nu_4$  bands of 5 isotopologues of germane near 11.5  $\mu\text{m}$ , *Journal of Quantitative Spectroscopy and Radiative Transfer* 260 (2021) 107474.
- [634] D. Albert, B. K. Antony, Y. A. Ba, Y. L. Babikov, P. Bollard, V. Boudon, F. Delahaye, G. Del Zanna, M. S. Dimitrijević, B. J. Drouin, M.-L. Dubernet, F. Duensing, M. Emoto, C. P. Endres, A. Z. Fazliev, J.-M. Gorian, I. E. Gordon, P. Gratier, C. Hill, D. Jevremović, C. Joblin, D.-H. Kwon, R. V. Kochanov, E. Krishnakumar, G. Leto, P. A. Loboda, A. A. Lukashevskaya, O. M. Lyulin, B. P. Marinković, A. Markwick, T. Marquart, N. J. Mason, C. Mendoza, T. J. Millar, N. Moreau, S. V. Morozov, T. Möller, H. S. P. Müller, G. Mulas, I. Murakami, Y. Pakhomov, P. Palmeri, J. Penguen, V. I. Perevalov, N. Piskunov, J. Postler, A. I. Privezentsev, P. Quinet, Y. Ralchenko, Y.-J. Rhee, C. Richard, G. Rixon, L. S. Rothman, E. Roueff, T. Ryabchikova, S. Sahal-Bréchet, P. Scheier, P. Schilke, S. Schlemmer, K. W. Smith, B. Schmitt, I. Y. Skobelev, V. A. Srecković, E. Stempels, S. A. Tashkun, J. Tennyson, V. G. Tyuterev, C. Vastel, V. Vujčić, V. Wakelam, N. A. Walton, C. Zeippen, C. M. Zwölf, A decade with VAMDC: Results and ambitions, *Atoms* 8 (2020) 76.
- [635] O. N. Ulenikov and O. V. Gromova and E. S. Bekhtereva and N. I. Raspopova and A. V. Kuznetsov and C. Sydow and S. Bauerecker, High-resolution analysis of  $\text{GeH}_4$  in the dyad region: Ro-vibration energy structure of  $^{70}\text{GeH}_4$  and line strengths of  $^M\text{GeH}_4$  ( $M = 70, 72, 73, 74, 76$ ), *Journal of Quantitative Spectroscopy and Radiative Transfer* 236 (2019) 106581.

- [636] U. Calmonte, K. Altwegg, H. Balsiger, J. J. Berthelier, A. Bieler, G. Ces-  
sateur, F. Dhooghe, E. F. van Dishoeck, B. Fiethe, S. A. Fuselier, S. Gasc,  
T. I. Gombosi, M. Hässig, L. Le Roy, M. Rubin, T. Sémon, C. Y.  
Tzou, S. F. Wampfler, Sulphur-bearing species in the coma of comet  
67P/Churyumov-Gerasimenko, *Monthly Notices of the Royal Astronom-  
ical Society* 462 (2016) S253–S273.
- [637] W. M. Jackson, A. Scodinu, D. Xu, A. L. Cochran, Using the Ultravio-  
let and Visible spectrum of Comet 122P/de Vico to Identify the Parent  
Molecule CS<sub>2</sub>, *Astrophysical Journal* 607 (2004) L139–L141.
- [638] S. K. Atreya, S. G. Edgington, L. M. Trafton, J. J. Caldwell, K. S. Noll,  
H. A. Weaver, Abundances of ammonia and carbon disulfide in the Jovian  
stratosphere following the impact of comet Shoemaker-Levy 9, *Geophys-  
ical Research Letters* 22 (1995) 1625–1628.
- [639] M. Chin, D. D. Davis, Global sources and sinks of OCS and CS<sub>2</sub> and their  
distributions, *Global Biogeochemical Cycles* 7 (1993) 321–337.
- [640] M.O. Andreae, Ocean-atmosphere interactions in the global biogeochem-  
ical sulfur cycle, *Marine Chemistry* 30 (1990) 1–29.
- [641] R. Beauchamp, J. Bus, J. Popp, C. Boreiko, L. Goldberg, A critical  
review of the literature on carbon disulfide toxicity, *Critical Reviews in  
Toxicology* 11(3) (1983) 169–278.
- [642] S. Hernberg, T. Partanen, C. Nordman, P. Sumari, Coronary heart disease  
among workers exposed to carbon disulphide, *Occupational and Environ-  
mental Medicine* 27 (1970) 313–325.
- [643] E. V. Karlovets, I. E. Gordon, R. Hashemi, R. V. Kochanov, R. J. Har-  
greaves, L. S. Rothman, Addition of the line list for carbon disulfide to  
the HITRAN database: line positions, intensities, and half-widths of the  
<sup>12</sup>C<sup>32</sup>S<sub>2</sub>, <sup>32</sup>S<sup>12</sup>C<sup>34</sup>S, <sup>32</sup>S<sup>12</sup>C<sup>33</sup>S, and <sup>13</sup>C<sup>32</sup>S<sub>2</sub> isotopologues, *Journal of  
Quantitative Spectroscopy and Radiative Transfer* 258 (2021) 107275.

- [644] E. V. Karlovets, I. E. Gordon, D. Konnov, A. V. Muraviev, K. L. Vodopyanov, Dual-comb laser spectroscopy of CS<sub>2</sub> near 4.6  $\mu$ m, *Journal of Quantitative Spectroscopy and Radiative Transfer* 256 (2020) 107269.
- [645] G. Blanquet, J. Walrand, J.-F. Blavier, H. Bredohl, I. Dubois, Fourier transform infrared spectrum of CS<sub>2</sub>: Analysis of the  $3\nu_3$  band, *Journal of Molecular Spectroscopy* 152 (1992) 137–151.
- [646] G. Blanquet, J. Walrand, H. Bredohl, I. Dubois, High-Resolution Spectra of Carbon Disulfide <sup>12</sup>C<sup>32</sup>S<sub>2</sub> in the Region of 2  $\mu$ m, *Journal of Molecular Spectroscopy* 198 (1999) 43–51.
- [647] T. Platz, M. Matheis, C. Hornberger, W. Demtröder, High-Sensitivity Overtone Spectroscopy of Carbon Disulfide CS<sub>2</sub>, *Journal of Molecular Spectroscopy* 180 (1996) 81–84.
- [648] W. B. Person, L. C. Hall, Absolute infrared intensities of CS<sub>2</sub> fundamentals in gas and liquid phases. An interpretation of the bond moments of CO<sub>2</sub> and CS<sub>2</sub>, *Spectrochimica Acta* 20 (1964) 771–779.
- [649] S. A. Montzka, S. Reimann, A. Engel, K. Krüger, S. O'Doherty, W. T. Sturges et al., Scientific Assessment of Ozone Depletion: Ozone-Depleting Substances (ODSs) and Related Chemicals, volume Report No. 52 of *Global Ozone Research and Monitoring Project Report*, World Meteorological Organization, Geneva Switzerland, 2011.
- [650] Y. Yokouchi, Y. Nojiri, D. Toom-Saunty, P. Fraser, Y. Inuzuka, H. Tanimoto, H. Nara, R. Murakami, H. Mukai, Long-term variation of atmospheric methyl iodide and its link to global environmental change, *Geophysical Research Letters* 39 (2012) L23805.
- [651] J. Ishikawa, K. Kawaguchi, Y. Maruyama, Analysis for iodine release from unit 3 of Fukushima Dai-ichi nuclear power plant with consideration of water phase iodine chemistry, *Journal of Nuclear Science and Technology* 52 (2015) 308–314.

- [652] A. Perrin, I. Haykal, F. KwabiaTchana, L. Manceron, D. Doizi, G. Ducros, New analysis of the  $\nu_6$  and  $2\nu_3$  bands of methyl iodide ( $\text{CH}_3\text{I}$ ), *Journal of Molecular Spectroscopy* 324 (2016) 28–35.
- [653] F. Kwabia-Tchana, Y. Attafi, L. Manceron, D. Doizi, J. Vander Auwera, A. Perrin, Line intensities for the  $\nu_6$  and  $2\nu_3$  bands of methyl iodide ( $^{12}\text{CH}_3\text{I}$ ), *Journal of Quantitative Spectroscopy and Radiative Transfer* 222-223 (2019) 130–137.
- [654] I. Sadiek, A. Hjältén, F. Senna Vieira, C. Lu, M. Stuhr, A. Foltynowicz, Line positions and intensities of the  $\nu_4$  band of methyl iodide using mid-infrared optical frequency comb fourier transform spectroscopy, *Journal of Quantitative Spectroscopy and Radiative Transfer* 255 (2020) 107263.
- [655] G. Soboń, T. Martynkien, P. Mergo, L. Rutkowski, A. Foltynowicz, High-power frequency comb source tunable from 2.7 to 4.2  $\mu\text{m}$  based on difference frequency generation pumped by an yb-doped fiber laser, *Optics Letters* 42 (2017) 1748–1751.
- [656] A. Khodabakhsh, V. Ramaiah-Badarla, L. Rutkowski, A. C. Johansson, K. F. Lee, J. Jiang, C. Mohr, M. E. Fermann, A. Foltynowicz, Fourier transform and Vernier spectroscopy using an optical frequency comb at 3–5.4 $\mu\text{m}$ , *Optics Letters* 41 (2016) 2541–2544.
- [657] A. Foltynowicz, T. Ban, P. Masłowski, F. Adler, J. Ye, Quantum-noise-limited optical frequency comb spectroscopy, *Physical Review Letters* 107 (2011) 233002.
- [658] P. Masłowski, K. F. Lee, A. C. Johansson, A. Khodabakhsh, G. Kowzan, L. Rutkowski, A. A. Mills, C. Mohr, J. Jiang, M. E. Fermann, A. Foltynowicz, Surpassing the path-limited resolution of Fourier-transform spectrometry with frequency combs, *Physical Review A* 93 (2016) 021802.
- [659] L. Rutkowski, P. Masłowski, A. C. Johansson, A. Khodabakhsh, A. Foltynowicz, Optical frequency comb Fourier transform spectroscopy

- with sub-nominal resolution and precision beyond the Voigt profile, *Journal of Quantitative Spectroscopy and Radiative Transfer* 204 (2018) 63–73.
- [660] E. Raddaoui, P. Soulard, M. Guinet, H. Aroui, D. Jacquemart, Measurements and modeling of air-broadening coefficients for the  $\nu_6$  band of  $\text{CH}_3\text{I}$ , *Journal of Quantitative Spectroscopy and Radiative Transfer* 246 (2020) 106934.
- [661] J. I. Robson, L. K. Gohar, M. D. Hurley, K. P. Shine, T. J. Wallington, Revised IR spectrum, radiative efficiency and global warming potential of nitrogen trifluoride, *Geophysical Research Letters* 33 (2006).
- [662] M. J. Prather, J. Hsu,  $\text{NF}_3$ , the greenhouse gas missing from Kyoto, *Geophysical Research Letters* 35 (2008).
- [663] T. J. Dillon, L. Vereecken, A. Horowitz, V. Khamaganov, J. N. Crowley, J. Lelieveld, Removal of the potent greenhouse gas  $\text{NF}_3$  by reactions with the atmospheric oxidants  $\text{O}(^1\text{D})$ , OH and  $\text{O}_3$ , *Physical Chemistry Chemical Physics* 13 (2011) 18600–18608.
- [664] T. Arnold, J. Mühle, P. K. Salameh, C. M. Harth, D. J. Ivy, R. F. Weiss, Automated measurement of nitrogen trifluoride in ambient air, *Analytical Chemistry* 84 (2012) 4798–4804.
- [665] R. F. Weiss, J. Mühle, P. K. Salameh, C. M. Harth, Nitrogen trifluoride in the global atmosphere, *Geophysical Research Letters* 35 (2008).
- [666] A. Nikitin, J. Champion, V. Tyuterev, L. Brown, G. Mellau, M. Lock, The infrared spectrum of  $\text{CH}_3\text{D}$  between 900 and  $3200\text{ cm}^{-1}$ : extended assignment and modeling, *Journal of Molecular Structure* 517–518 (2000) 1–24.
- [667] O. Egorov, A. Nikitin, M. Rey, A. Rodina, S. Tashkun, V. Tyuterev, Global modeling of  $\text{NF}_3$  line positions and intensities from far to mid-infrared up to  $2200\text{ cm}^{-1}$ , *Journal of Quantitative Spectroscopy and Radiative Transfer* 239 (2019) 106668.

- [668] V. Tyuterev, S. Tashkun, M. Rey, R. Kochanov, A. Nikitin, T. Delahaye, Accurate Spectroscopic Models for Methane Polyads Derived from a Potential Energy Surface Using High-Order Contact Transformations, *Journal of Physical Chemistry A* 117 (2013) 13779–13805.
- [669] A. Nikitin, J. Champion, V. Tyuterev, The MIRS computer package for modeling the rovibrational spectra of polyatomic molecules, *Journal of Quantitative Spectroscopy and Radiative Transfer* 82 (2003) 239–249.
- [670] A. Nikitin, M. Rey, J. Champion, V. Tyuterev, Extension of the MIRS computer package for the modeling of molecular spectra: From effective to full ab initio ro-vibrational Hamiltonians in irreducible tensor form, *Journal of Quantitative Spectroscopy and Radiative Transfer* 113 (2012) 1034–1042.
- [671] N. Boulaftali, N. Sari-Zizi, U. Wötzel, J. Demaison, L. Margulès, H. Harder, H. Mäder, E. MKadmi, H. Bürger, The  $\nu_4 = 1$  State of  $^{14}\text{NF}_3$  at  $493\text{ cm}^{-1}$  Studied by High-Resolution FTIR, Centimeter-Wave, and Millimeter-Wave Spectroscopy, *Journal of Molecular Spectroscopy* 212 (2002) 41–52.
- [672] K. Akkad, N. Ben Sari-Zizi, B. Bakri, J. Demaison, H. Bürger, E. MKadmi, Fourier transform infrared and millimeter-wave study of the  $\nu_2 = 1, 2$  and the  $\nu_2 = \nu_4 = 1$  rovibrational states of  $^{14}\text{NF}_3$ , *Journal of Molecular Spectroscopy* 218 (2003) 36–47.
- [673] N. B. Sari-Zizi, H. Najib, J. Demaison, B. Bakri, J. Colmont, H. Bürger, High-resolution FTIR and MMW study of the  $\nu_4 = 2$  ( $A_1, E$ ) excited state of  $^{14}\text{NF}_3$  near  $985\text{ cm}^{-1}$ : the axial ground state rotational constants derived by the “loop-method”, *Journal of Molecular Spectroscopy* 228 (2004) 511–527.
- [674] W. Höhe, U. Häring, W. A. Kreiner, H. Essig, A. Ruoff, Analysis of the  $\nu_1$  fundamental of  $\text{NF}_3$  combining FT and laser side-band saturation spec-



- troscopy. A secondary standard for the 1000-1060  $\text{cm}^{-1}$  region, Canadian Journal of Physics 72 (1994) 1051–1059.
- [675] H. Najib, N. Ben Sari-Zizi, J. Demaison, B. Bakri, J.-M. Colmont, E. MKadmi, High-resolution infrared and millimeterwave spectra of the  $\nu_3 = 1$  vibrational state of  $^{14}\text{NF}_3$  at 907  $\text{cm}^{-1}$ , Journal of Molecular Spectroscopy 220 (2003) 214–222.
- [676] S. Hmimou, H. Msahal, H. Najib, First high-resolution FTIR study of the  $\nu_1 = \nu_4 = 1$  rovibrational state of  $^{14}\text{NF}_3$  near 1523  $\text{cm}^{-1}$ , Molecular Physics 108 (2010) 787–794.
- [677] H. M. Hamid Najib, Siham Hmimou, High-Resolution Infrared Spectroscopy of the  $\nu_1 + \nu_4$  Band of  $^{14}\text{NF}_3$ : Reductions of the Rovibrational Hamiltonian, Journal of Chemistry 9 (2012) 253–259.
- [678] N. Ben Sari-Zizi, H. Najib, High-resolution infrared study of the  $2\nu_3(\text{A}_1, \text{E})$  and  $\nu_1 + \nu_3(\text{E})$  bands of  $^{14}\text{NF}_3$ , Journal of Molecular Spectroscopy 240 (2006) 210–226.
- [679] I. Bolotova, O. Ulenikov, E. Bekhtereva, S. Albert, S. Bauerecker, H. Hollenstein, P. Lerch, M. Quack, T. Peter, G. Seyfang, A. Wokaun, High resolution analysis of the FTIR spectra of trifluoroamine  $\text{NF}_3$ , Journal of Molecular Spectroscopy 348 (2018) 87–102.
- [680] L. T. Molina, P. J. Wooldridge, M. J. Molina, Atmospheric reactions and ultraviolet and infrared absorptivities of nitrogen trifluoride, Geophysical Research Letters 22 (1995) 1873–1876.
- [681] A. Rodina, O. Egorov, A. Nikitin, M. Rey, V. Serdyukov, L. Sinita, S. Tashkun, Line list for  $\text{NF}_3$  molecule in the 1750–1950  $\text{cm}^{-1}$  region, Journal of Quantitative Spectroscopy and Radiative Transfer 232 (2019) 10–19.
- [682] R. V. Kochanov, I. E. Gordon, L. S. Rothman, K. P. Shine, S. W. Sharpe, T. J. Johnson, T. J. Wallington, J. J. Harrison, P. F. Bernath, M. Birk,

- G. Wagner, K. Le Bris, I. Bravo, C. Hill, Infrared absorption cross-sections in HITRAN2016 and beyond: Expansion for climate, environment, and atmospheric applications, *Journal of Quantitative Spectroscopy and Radiative Transfer* 230 (2019) 172–221.
- [683] P. Bernath, The Atmospheric Chemistry Experiment (ACE), *Journal of Quantitative Spectroscopy and Radiative Transfer* 186 (2017) 3–16. Satellite Remote Sensing and Spectroscopy: Joint ACE-Odin Meeting, October 2015.
- [684] S. A. Montzka, G. S. Dutton, P. Yu, E. Ray, R. W. Portmann, J. S. Daniel, L. Kuijpers, B. D. Hall, D. Mondeel, C. Siso, J. D. Nance, M. Rigby, A. J. Manning, L. Hu, F. Moore, B. R. Miller, J. W. Elkins, An unexpected and persistent increase in global emissions of ozone-depleting CFC-11, *Nature* 557 (2018) 413–417.
- [685] M. Rigby, S. Park, T. Saito, L. M. Western, A. L. Redington, X. Fang, S. Henne, A. J. Manning, R. G. Prinn, G. S. Dutton, P. J. Fraser, A. L. Ganesan, B. D. Hall, C. M. Harth, J. Kim, K.-R. Kim, P. B. Krummel, T. Lee, S. Li, Q. Liang, M. F. Lunt, S. A. Montzka, J. Mühle, S. O’Doherty, M.-K. Park, S. Reimann, P. K. Salameh, P. Simmonds, R. L. Tunnicliffe, R. F. Weiss, Y. Yokouchi, D. Young, Increase in CFC-11 emissions from eastern China based on atmospheric observations, *Nature* 569 (2019) 546–550.
- [686] S. A. Montzka, G. S. Dutton, R. W. Portmann, M. P. Chipperfield, S. Davis, W. Feng, A. J. Manning, E. Ray, M. Rigby, B. D. Hall, C. Siso, J. D. Nance, P. B. Krummel, J. Mühle, D. Young, S. O’Doherty, P. K. Salameh, C. M. Harth, R. G. Prinn, R. F. Weiss, J. W. Elkins, H. Walter-Terrinoni, C. Theodoridi, A decline in global CFC-11 emissions during 2018-2019, *Nature* 590 (2021) 428–432.
- [687] S. Park, L. M. Western, T. Saito, A. L. Redington, S. Henne, X. Fang, R. G. Prinn, A. J. Manning, S. A. Montzka, P. J. Fraser, A. L. Ganesan, C.

- M. Harth, J. Kim, P. B. Krummel, Q. Liang, J. Mühle, S. O'Doherty, H. Park, M. -K. Park, S. Reimann, P. K. Salameh, R. F. Weiss, M. Rigby, A decline in emissions of CFC-11 and related chemicals from eastern China, *Nature* 590 (2021) 433–437.
- [688] J. Mühle, A. L. Ganesan, B. R. Miller, P. K. Salameh, C. M. Harth, B. R. Grealley, M. Rigby, L. W. Porter, L. P. Steele, C. M. Trudinger, P. B. Krummel, S. O'Doherty, P. J. Fraser, P. G. Simmonds, R. G. Prinn, R. F. Weiss, Perfluorocarbons in the global atmosphere: tetrafluoromethane, hexafluoroethane, and octafluoropropane, *Atmospheric Chemistry and Physics* 10 (2010) 5145–5164.
- [689] A. E. J. Harnisch, Natural  $\text{CF}_4$  and  $\text{SF}_6$  on Earth, *Geophysical Research Letters* 25 (1998) 2401–2404.
- [690] Z. Li, P. Varanasi, Measurement of the absorption cross-sections of cfc-11 at conditions representing various model atmospheres, *Journal of Quantitative Spectroscopy and Radiative Transfer* 52 (1994) 137–144.
- [691] J. J. Harrison, New and improved infrared absorption cross sections for trichlorofluoromethane (cfc-11), *Atmospheric Measurement Techniques* 11 (2018) 5827–5836.
- [692] K. Le Bris, J. McDowell, K. Strong, Measurements of the infrared absorption cross-sections of HCFC-141b ( $\text{CH}_3\text{CFCl}_2$ ), *Journal of Quantitative Spectroscopy and Radiative Transfer* 113 (2012) 1913–1919.
- [693] J. J. Harrison, Infrared absorption cross sections for air-broadened 1,1-dichloro-1-fluoroethane (HCFC-141b), *Journal of Quantitative Spectroscopy and Radiative Transfer* 238 (2019) 106489.
- [694] P. Varanasi, Z. Li, V. Nemtchinov, A. Cherukuri, Spectral absorption-coefficient data on HCFC-22 and  $\text{SF}_6$  for remote-sensing applications, *Journal of Quantitative Spectroscopy and Radiative Transfer* 52 (1994) 323–332. Special Issue Atmospheric Spectroscopy Applications.

- [695] J. J. Harrison, New infrared absorption cross sections for the infrared limb sounding of sulfur hexafluoride ( $\text{SF}_6$ ), *Journal of Quantitative Spectroscopy and Radiative Transfer* 254 (2020) 107202.
- [696] V. Nemtchinov, P. Varanasi, Thermal infrared absorption cross-sections of  $\text{CF}_4$  for atmospheric applications, *Journal of Quantitative Spectroscopy and Radiative Transfer* 82 (2003) 461–471. The HITRAN Molecular Spectroscopic Database: Edition of 2000 Including Updates of 2001.
- [697] J. J. Harrison, New infrared absorption cross sections for the infrared limb sounding of carbon tetrafluoride ( $\text{CF}_4$ ), *Journal of Quantitative Spectroscopy and Radiative Transfer* 260 (2021) 107432.
- [698] H. B. Niemann, S. K. Atreya, J. E. Demick, D. Gautier, J. A. Haberman, D. N. Harpold, W. T. Kasprzak, J. I. Lunine, T. C. Owen, F. Raulin, Composition of Titan’s lower atmosphere and simple surface volatiles as measured by the Cassini-Huygens probe gas chromatograph mass spectrometer experiment, *Journal of Geophysical Research (Planets)* 115 (2010) E12006.
- [699] D. Hewett, P. Bernath, J. Zhao, B. Billingham, Near infrared absorption cross sections for ethane broadened by hydrogen and nitrogen, *Journal of Quantitative Spectroscopy and Radiative Transfer* 242 (2020) 106780.
- [700] K. Sung, G. C. Toon, B. J. Drouin, A. W. Mantz, M. A. H. Smith, FT-IR measurements of cold propene ( $\text{C}_3\text{H}_6$ ) cross-sections at temperatures between 150 and 299 K, *Journal of Quantitative Spectroscopy and Radiative Transfer* 213 (2018) 119–132.
- [701] K. Sung, G. C. Toon, A. W. Mantz, M. A. H. Smith, FT-IR measurements of cold  $\text{C}_3\text{H}_8$  cross sections at 7–15  $\mu\text{m}$  for Titan atmosphere, *Icarus* 226 (2013) 1499–1513.
- [702] K. Sung, B. Steffens, G. C. Toon, D. J. Nemchick, M. A. H. Smith, Pseudo-line parameters to represent n-butane ( $\text{n-C}_4\text{H}_{10}$ ) cross-sections measured

- in the 7-15  $\mu\text{m}$  region for the Titan atmosphere, *Journal of Quantitative Spectroscopy and Radiative Transfer* 251 (2020) 107011.
- [703] D. Hewett, P. F. Bernath, A. Wong, B. E. Billinghurst, J. Zhao, N. A. Lombardo, C. A. Nixon, D. E. Jennings,  $\text{N}_2$  and  $\text{H}_2$  broadened isobutane infrared absorption cross sections and butane upper limits on Titan, *Icarus* 344 (2020) 113460.
- [704] D. M. Hewett, P. F. Bernath, B. B. Billinghurst, Infrared absorption cross sections of isobutane with hydrogen and nitrogen as broadening gases, *Journal of Quantitative Spectroscopy and Radiative Transfer* 227 (2019) 226–229.
- [705] D. M. Hewett, P. F. Bernath, B. E. Billinghurst, Erratum to “Infrared absorption cross sections of isobutane with hydrogen and nitrogen as broadening gases” *J Quant Spectrosc Radiat Transf* 227 (2019) 226-229, *Journal of Quantitative Spectroscopy and Radiative Transfer* 242 (2020) 106771.
- [706] P. Bernath, R. Dodangodage, M. Dulick, J. Zhao, B. Billinghurst, Absorption cross sections for neopentane broadened by nitrogen in the 3.3  $\mu\text{m}$  region, *Journal of Quantitative Spectroscopy and Radiative Transfer* 251 (2020) 107034.
- [707] K. Sung, G. C. Toon, T. J. Crawford,  $\text{N}_2$ - and  $(\text{H}_2+\text{He})$ -broadened cross sections of benzene ( $\text{C}_6\text{H}_6$ ) in the 7-15  $\mu\text{m}$  region for the Titan and jovian atmospheres, *Icarus* 271 (2016) 438–452.
- [708] K. Sung, G. C. Toon, T. J. Crawford, Corrigendum to “ $\text{N}_2$ - and  $(\text{H}_2+\text{He})$ -broadened cross sections of benzene ( $\text{C}_6\text{H}_6$ ) in the 7-15  $\mu\text{m}$  region for the Titan and Jovian atmospheres” [*Icarus*, 271 (2016) 438-452], *Icarus* 281 (2017) 476–476.
- [709] R. Dodangodage, P. F. Bernath, J. Zhao, B. Billinghurst, Absorption cross sections for ethane broadened by hydrogen and helium in the 3.3 micron

- region, *Journal of Quantitative Spectroscopy and Radiative Transfer* 253 (2020) 107131.
- [710] A. Wong, D. Hewett, B. B. Billinghamurst, J. N. Hodges, P. F. Bernath, He and H<sub>2</sub> broadened propane cross sections in the 3  $\mu$ m region at cold temperatures, *Journal of Quantitative Spectroscopy and Radiative Transfer* 232 (2019) 104–107.
- [711] A. Wong, D. R. T. Appadoo, P. F. Bernath, IR absorption cross sections of propane broadened by H<sub>2</sub> and He between 150 K and 210 K, *Journal of Quantitative Spectroscopy and Radiative Transfer* 218 (2018) 68–71.
- [712] A. Wong, B. Billinghamurst, P. F. Bernath, Helium broadened propane absorption cross sections in the far-IR, *Molecular Astrophysics* 8 (2017) 36–39.
- [713] A. Wong, R. J. Hargreaves, B. Billinghamurst, P. F. Bernath, Infrared absorption cross sections of propane broadened by hydrogen, *Journal of Quantitative Spectroscopy and Radiative Transfer* 198 (2017) 141–144.
- [714] R. J. Hargreaves, E. Buzan, M. Dulick, P. F. Bernath, High-resolution absorption cross sections of C<sub>2</sub>H<sub>6</sub> at elevated temperatures, *Molecular Astrophysics* 1 (2015) 20–25.
- [715] C. A. Beale, R. J. Hargreaves, P. F. Bernath, Temperature-dependent high resolution absorption cross sections of propane, *Journal of Quantitative Spectroscopy and Radiative Transfer* 182 (2016) 219–224.
- [716] E. M. Buzan, R. J. Hargreaves, P. F. Bernath, High resolution absorption cross sections for propylene in the 3  $\mu$ m region at high temperatures, *Molecular Astrophysics* 3 (2016) 16–20.
- [717] E.-t. Es-sebbar, M. Alrefae, A. Farooq, Infrared cross-sections and integrated band intensities of propylene: Temperature-dependent studies, *Journal of Quantitative Spectroscopy and Radiative Transfer* 133 (2014) 559–569.

- [718] E.-t. Es-sebbar, Y. Benilan, A. Farooq, Temperature-dependent absorption cross-section measurements of 1-butene ( $1\text{-C}_4\text{H}_8$ ) in VUV and IR, *Journal of Quantitative Spectroscopy and Radiative Transfer* 115 (2013) 1–12.
- [719] M. Alrefae, E.-t. Es-sebbar, A. Farooq, Absorption cross-section measurements of methane, ethane, ethylene and methanol at high temperatures, *Journal of Molecular Spectroscopy* 303 (2014) 8–14.
- [720] A. E. Klingbeil, J. B. Jeffries, R. K. Hanson, Temperature-dependent mid-IR absorption spectra of gaseous hydrocarbons, *Journal of Quantitative Spectroscopy and Radiative Transfer* 107 (2007) 407–420.
- [721] C. L. Strand, Y. Ding, S. E. Johnson, R. K. Hanson, Measurement of the mid-infrared absorption spectra of ethylene ( $\text{C}_2\text{H}_4$ ) and other molecules at high temperatures and pressures, *Journal of Quantitative Spectroscopy and Radiative Transfer* 222 (2019) 122–129.
- [722] Y. Ding, W.-W. Su, S. E. Johnson, C. L. Strand, R. K. Hanson, Temperature-dependent absorption cross section measurements for propene, 1-butene, cis-/trans-2-butene, isobutene and 1,3-butadiene in the spectral region  $8.4\text{--}11.7\ \mu\text{m}$ , *Journal of Quantitative Spectroscopy and Radiative Transfer* 255 (2020) 107240.
- [723] Y. Ding, C. L. Strand, R. K. Hanson, High-temperature mid-infrared absorption spectra of methanol ( $\text{CH}_3\text{OH}$ ) and ethanol ( $\text{C}_2\text{H}_5\text{OH}$ ) between  $930$  and  $1170\ \text{cm}^{-1}$ , *Journal of Quantitative Spectroscopy and Radiative Transfer* 224 (2019) 396–402.
- [724] Y. Ding, W. Y. Peng, C. L. Strand, R. K. Hanson, Quantitative measurements of broad-band mid-infrared absorption spectra of formaldehyde, acetaldehyde, and acetone at combustion-relevant temperatures near  $5.7\ \mu\text{m}$ , *Journal of Quantitative Spectroscopy and Radiative Transfer* 248 (2020) 106981.

- [725] G. Wagner, M. Birk, In Preparation, 2021.
- [726] J. Bak, L. Xiong, M. Birk, G. Wagner, I. E. Gordon, K. Chance, Impact of using a new ultraviolet ozone absorption cross-section dataset on OMI ozone profile retrievals, *Atmospheric Measurement Techniques (AMT)* 13 (2020) 5845–5854.
- [727] V. Gorshelev, A. Serdyuchenko, M. Weber, W. Chehade, J. P. Burrows, High spectral resolution ozone absorption cross-sections - Part 1: Measurements, data analysis and comparison with previous measurements around 293 K, *Atmospheric Measurement Techniques* 7 (2014) 609–624.
- [728] J. T. Hodges, J. Viallon, P. J. Brewer, B. J. Drouin, V. Gorshelev, C. Janssen, S. Lee, A. Possolo, M. A. H. Smith, J. Walden, R. I. Wiegolsz, Recommendation of a consensus value of the ozone absorption cross-section at 253.65 nm based on a literature review, *Metrologia* 56 (2019) 034001.
- [729] C. Janssen, H. Elandalousi, J. Gröbner, A new photometric ozone reference in the Huggins bands: the absolute ozone absorption cross section at the 325 nm HeCd laser wavelength, *Atmospheric Measurement Techniques* 11 (2018) 1707–1723.
- [730] A. G. Hearn, The Absorption of ozone in the ultra-violet and visible regions of the spectrum, *Proceedings of the Physical Society* 78 (1961) 932–940.
- [731] M. Birk, G. Wagner, ESA SEOM-IAS – Measurement and ACS database O<sub>3</sub> UV region, Zenodo (2021).
- [732] M. Hermans, A. C. Vandaele, S. Fally, Fourier transform measurements of SO<sub>2</sub> absorption cross sections: I. Temperature dependence in the 24 000–29 000 cm<sup>−1</sup> (345–420 nm) region, *Journal of Quantitative Spectroscopy and Radiative Transfer* 110 (2009) 756–765.



- [733] A. C. Vandaele, M. Hermans, S. Fally, Fourier transform measurements of SO<sub>2</sub> absorption cross sections: II. Temperature dependence in the 29 000-44 000 cm<sup>-1</sup> (227-345 nm) region, *Journal of Quantitative Spectroscopy and Radiative Transfer* 110 (2009) 2115–2126.
- [734] G. Wagner, M. Birk, In Preparation, 2021.
- [735] K. Bogumil, J. Orphal, T. Homann, S. Voigt, P. Spietz, O. C. Fleischmann, A. Vogel, M. Hartmann, H. Kromminga, H. Bovensmann, J. Frerick, J. P. Burrows, Measurements of molecular absorption spectra with the SCIA-MACHY pre-flight model: instrument characterization and reference data for atmospheric remote-sensing in the 230–2380 nm region, *Journal of Photochemistry and Photobiology A: Chemistry* 157 (2003) 167–184.
- [736] M. Birk, G. Wagner, ESA SEOM-IAS - Measurement and ACS database SO<sub>2</sub> UV region, Zenodo (2018).
- [737] C. E. Sioris, C. D. Boone, R. Nassar, K. J. Sutton, I. E. Gordon, K. A. Walker, P. F. Bernath, Retrieval of carbon dioxide vertical profiles from solar occultation observations and associated error budgets for ACE-FTS and CASS-FTS, *Atmospheric Measurement Techniques* 7 (2014) 2243–2262.
- [738] J. Chimot, J. P. Veefkind, T. Vlemmix, J. F. de Haan, V. Amiridis, E. Proestakis, E. Marinou, P. F. Levelt, An exploratory study on the aerosol height retrieval from OMI measurements of the 477 nm O<sub>2</sub>–O<sub>2</sub> spectral band using a neural network approach, *Atmospheric Measurement Techniques* 10 (2017) 783–809.
- [739] F. Kataoka, D. Crisp, T. Taylor, C. O’Dell, A. Kuze, K. Shiomi, H. Suto, C. Bruegge, F. Schwandner, R. Rosenberg, L. Chapsky, R. Lee, The Cross-Calibration of Spectral Radiances and Cross-Validation of CO<sub>2</sub> Estimates from GOSAT and OCO-2, *Remote Sensing* 9 (2017) 1158.

- [740] J.-M. Hartmann, C. Boulet, G. C. Toon, Collision-induced absorption by  $\text{N}_2$  near  $2.16 \mu\text{m}$ : Calculations, model, and consequences for atmospheric remote sensing, *Journal of Geophysical Research: Atmospheres* 122 (2017) 2419.
- [741] I. Ortega, L. K. Berg, R. A. Ferrare, J. W. Hair, C. A. Hostetler, R. Volkamer, Elevated aerosol layers modify the  $\text{O}_2\text{--O}_2$  absorption measured by ground-based MAX-DOAS, *Journal of Quantitative Spectroscopy and Radiative Transfer* 176 (2016) 34–49.
- [742] E. Spinei, A. Cede, J. Herman, G. H. Mount, E. Eloranta, B. Morley, S. Baidar, B. Dix, I. Ortega, T. Koenig, R. Volkamer, Direct sun and airborne MAX-DOAS measurements of the collision induced oxygen complex,  $\text{O}_2\text{--O}_2$  absorption with significant pressure and temperature differences, *Atmospheric Measurement Techniques Discussions* 7 (2014) 10015–10057.
- [743] V. S. Meadows, Reflections on  $\text{O}_2$  as a Biosignature in Exoplanetary Atmospheres, *Astrobiology* 17 (2017) 1022–1052.
- [744] M. Abel, L. Frommhold, Collision-induced spectra and current astronomical research gas of  $\text{H}_2$ , *Canadian Journal of Physics* 91 (2013) 0532.
- [745] P. J. Godin, R. M. Ramirez, C. L. Campbell, T. Wizenberg, T. G. Nguyen, K. Strong, J. E. Moores, Collision-Induced Absorption of  $\text{CH}_4\text{--CO}_2$  and  $\text{H}_2\text{--CO}_2$  Complexes and Their Effect on the Ancient Martian Atmosphere, *Journal of Geophysical Research: Planets* 125 (2020).
- [746] R. Wordsworth, Y. Kalugina, S. Lokshtanov, A. Vigasin, B. Ehlmann, J. Head, C. Sanders, H. Wang, Transient reducing greenhouse warming on early Mars, *Geophysical Research Letters* 44 (2017) 665.
- [747] C. Richard, I. E. Gordon, L. S. Rothman, M. Abel, L. Frommhold, M. Gustafsson, J. M. Hartmann, C. Hermans, W. J. Lafferty, G. S. Orton,

- K. M. Smith, H. Tran, New section of the HITRAN database: Collision-induced absorption (CIA), *Journal of Quantitative Spectroscopy and Radiative Transfer* 113 (2012) 1276–1285.
- [748] T. Karman, I. E. Gordon, A. van der Avoird, Y. I. Baranov, C. Boulet, B. J. Drouin, G. C. Groenenboom, M. Gustafsson, J.-M. Hartmann, R. L. Kurucz, L. S. Rothman, K. Sun, K. Sung, R. Thalman, H. Tran, E. H. Wishnow, R. Wordsworth, A. A. Vigasin, R. Volkamer, W. J. van der Zande, Update of the HITRAN collision-induced absorption section, *Icarus* 328 (2019) 160–175.
- [749] M. Abel, L. Frommhold, X. Li, K. L. C. Hunt, Collision-induced absorption by  $\text{H}_2$  pairs: From hundreds to thousands of Kelvin, *Journal of Physical Chemistry A* 115 (2011) 6805–6812.
- [750] L. N. Fletcher, M. Gustafsson, G. S. Orton, Hydrogen dimers in giant-planet infrared spectra, *Astrophysical Journal Supplement Series* 235 (2018) 24.
- [751] M. Abel, L. Frommhold, X. Li, K. L. C. Hunt, Infrared absorption by collisional  $\text{H}_2$ –He complexes at temperatures up to 9000 K and frequencies from 0 to 20 000  $\text{cm}^{-1}$ , *Journal of Chemical Physics* 136 (2012) 044319.
- [752] M. Gustafsson, L. Frommhold, The  $\text{H}_2$ –H infrared absorption bands at temperatures from 1000 K to 2500 K, *Astronomy & Astrophysics* 400 (2003) 1161–1162.
- [753] M. Gustafsson, L. Frommhold, Infrared absorption spectra of collisionally interacting He and H atoms, *Astrophysical Journal* 546 (2001) 1168.
- [754] A. Borysow, L. Frommhold, Theoretical collision-induced rototranslational absorption spectra for the outer planets:  $\text{H}_2$ – $\text{CH}_4$  pairs, *Astrophysical Journal* 304 (1986) 849–865.

- [755] E. Bar-Ziv, S. Weiss, Translational Spectra Due to Collision-Induced Overlap Moments in Mixtures of He with CO<sub>2</sub>, N<sub>2</sub>, CH<sub>4</sub>, and C<sub>2</sub>H<sub>6</sub>, *Journal of Chemical Physics* 57 (1972) 34.
- [756] T. Odintsova, E. Serov, A. Balashov, M. Koshelev, A. Koroleva, A. Simonova, M. Tretyakov, N. Filippov, D. Chistikov, A. Finenko, S. Lokshitanov, S. Petrov, A. Vigasin, CO<sub>2</sub>–CO<sub>2</sub> and CO<sub>2</sub>–Ar continua at millimeter wavelengths, *Journal of Quantitative Spectroscopy and Radiative Transfer* 258 (2021).
- [757] R. H. Taylor, A. Borysow, L. Frommhold, Concerning the rototranslational absorption spectra of He–CH<sub>4</sub> pairs, *Journal of Molecular Spectroscopy* 129 (1988) 45.
- [758] R. E. Samuelson, N. R. Nath, A. Borysow, Gaseous abundances and methane supersaturation in Titan’s troposphere, *Planetary and Space Science* 45 (1997) 959–980.
- [759] A. Borysow, L. Frommhold, Collision-induced rototranslational absorption spectra of CH<sub>4</sub>–CH<sub>4</sub> pairs at temperatures from 50 to 300 K, *Astrophysical Journal* 318 (1987) 940–943.
- [760] M. Gruszka, A. Borysow, Roto-translational collision-induced absorption of CO<sub>2</sub> for the atmosphere of Venus at frequencies from 0 to 250 cm<sup>−1</sup>, at temperatures from 200 to 800 K, *Icarus* 129 (1997) 172.
- [761] Y. Baranov, A. Vigasin, Collision-induced absorption by CO<sub>2</sub> in the region of  $\nu_1$ ,  $2\nu_2$ , *Journal of Molecular Spectroscopy* 193 (1999) 319 – 325.
- [762] Y. Baranov, G. T. Fraser, W. J. Lafferty, A. Vigasin, Collision-induced absorption in the CO<sub>2</sub> fermi triad for temperatures from 211 K to 296 K, in: C. Camy-Peyret, A. Vigasin (Eds.), *Weakly Interacting Molecular Pairs: Unconventional Absorbers of Radiation in the Atmosphere*, Springer, 2003, pp. 149–158. doi:10.1007/978-94-010-0025-3.

- [763] Y. I. Baranov, Collision-induced absorption in the region of the  $\nu_2+\nu_3$  band of carbon dioxide, *Journal of Molecular Spectroscopy* 345 (2018) 11–16.
- [764] A. Borysow, L. Frommhold, Theoretical collision-induced rototranslational absorption spectra for modeling Titan’s atmosphere:  $\text{H}_2\text{--N}_2$  pairs, *Astrophysical Journal* 303 (1986) 495–510.
- [765] D. N. Chistikov, A. A. Finenko, S. E. Lokshtanov, S. V. Petrov, A. A. Viggasin, Simulation of collision-induced absorption spectra based on classical trajectories and ab initio potential and induced dipole surfaces. I. Case study of  $\text{N}_2\text{--N}_2$  rototranslational band, *Journal of Chemical Physics* 151 (2019).
- [766] Y. I. Baranov, W. J. Lafferty, G. T. Fraser, Investigation of collision-induced absorption in the vibrational fundamental bands of  $\text{O}_2$  and  $\text{N}_2$  at elevated temperatures, *Journal of Molecular Spectroscopy* 233 (2005) 160–163.
- [767] W. J. Lafferty, A. M. Solodov, A. Weber, W. B. Olson, J.-M. Hartmann, Infrared collision-induced absorption by  $\text{N}_2$  near  $4.3\ \mu\text{m}$  for atmospheric applications: measurements and empirical modeling, *Applied Optics* 35 (1996) 5911.
- [768] K. Sung, E. Wishnow, M. Venkataraman, L. R. Brown, I. Ozier, D. C. Benner, T. J. Crawford, A. Mantz, M.-A. H. Smith, Progress in the measurement of temperature-dependent  $\text{N}_2\text{--N}_2$  collision-induced absorption and  $\text{H}_2$ -broadening of cold and hot  $\text{CH}_4$ , in: *AAS/Division for Planetary Sciences Meeting Abstracts #48*, volume 48 of *AAS/Division for Planetary Sciences Meeting Abstracts*, 2016, p. 424.11.
- [769] Y. I. Baranov, W. Lafferty, G. Fraser, Infrared spectrum of the continuum and dimer absorption in the vicinity of the  $\text{O}_2$  vibrational fundamental in  $\text{O}_2/\text{CO}_2$  mixtures, *Journal of Molecular Spectroscopy* 228 (2004) 432 – 440.

- [770] Maté, B. and Lugez, C. and Fraser, G. T. and Lafferty, W. J., Absolute intensities for the O<sub>2</sub> 1.27  $\mu$ m continuum absorption, *Journal of Geophysical Research: Atmospheres* 104 (1999) 30585–30590.
- [771] T. Karman, M. A. J. Koenis, A. Banerjee, D. H. Parker, I. E. Gordon, A. van der Avoird, W. J. van der Zande, G. C. Groenenboom, O<sub>2</sub>–O<sub>2</sub> and O<sub>2</sub>–N<sub>2</sub> collision-induced absorption mechanisms unravelled, *Nature Chemistry* 10 (2018) 549.
- [772] F. R. Spiering, W. J. van der Zande, Collision induced absorption in the a<sup>1</sup> $\Delta(\nu=2) \leftarrow X^3\Sigma_g^-(\nu=0)$  band of molecular oxygen, *Physical Chemistry Chemical Physics* 14 (2012) 9923–9928.
- [773] H. Tran, C. Boulet, J.-M. Hartmann, Line mixing and collision-induced absorption by oxygen in the A-band: Laboratory measurements, model, and tools for atmospheric spectra computations, *Journal of Geophysical Research* 111 (2006) D15210.
- [774] F. R. Spiering, M. B. Kiseleva, N. N. Filippov, L. van Kesteren, W. J. van der Zande, Collision-induced absorption in the O<sub>2</sub> B-band region near 670 nm, *Physical Chemistry Chemical Physics* 13 (2011) 9616–9621.
- [775] R. Thalman, R. Volkamer, Temperature dependent absorption cross-sections of O<sub>2</sub>–O<sub>2</sub> collision pairs between 340 and 630 nm and at atmospherically relevant pressure, *Physical Chemistry Chemical Physics* 15 (2013) 15371.
- [776] F. Thibault, V. Menoux, R. Le Doucen, L. Rosenmann, J.-M. Hartmann, C. Boulet, Infrared collision-induced absorption by O<sub>2</sub> near 6.4  $\mu$ m for atmospheric applications: measurements and empirical modeling, *Applied Optics* 36 (1997) 563.
- [777] J. J. Orlando, G. S. Tyndall, K. E. Nickerson, J. G. Calvert, The temperature dependence of collision-induced absorption by oxygen near 6  $\mu$ m, *Journal of Geophysical Research: Atmospheres* 96 (1991) 20 755–20 760.

- [778] V. Menoux, R. L. Doucen, C. Boulet, A. Roblin, A. M. Bouchardy, Collision-induced absorption in the fundamental band of  $N_2$ : temperature dependence of the absorption for  $N_2$ - $N_2$  and  $N_2$ - $O_2$  pairs., *Applied optics* 32 (1993) 263–268.
- [779] J.-M. Hartmann, C. Boulet, D. D. Tran, H. Tran, Y. Baranov, Effect of humidity on the absorption continua of  $CO_2$  and  $N_2$  near  $4\ \mu m$ : Calculations, comparisons with measurements, and consequences for atmospheric spectra, *Journal of Chemical Physics* 148 (2018) 054304.
- [780] A. Borysow, C. Tang, Far infrared CIA spectra of  $N_2$ - $CH_4$  pairs for modeling of Titan’s atmosphere, *Icarus* 105 (1993) 175–183.
- [781] M. Vangvichith, H. Tran, J.-M. Hartmann, Line-mixing and collision induced absorption for  $O_2$ - $CO_2$  mixtures in the oxygen A-band region, *Journal of Quantitative Spectroscopy and Radiative Transfer* 110 (2009) 2212–2216.
- [782] T. Karman, E. Miliordos, K. L. Hunt, G. C. Groenenboom, A. van der Avoird, Quantum mechanical calculation of the collision-induced absorption spectra of  $N_2$ - $N_2$  with anisotropic interactions, *Journal of Chemical Physics* 142 (2015) 1–12.
- [783] L. Frommhold, *Collision Induced Absorption in Gases*, Cambridge University Press, 2006.
- [784] J. Borysow, M. Moraldi, L. Frommhold, The collision induced spectroscopies: Concerning the desymmetrization of classical line shape, *Molecular Physics* 56 (1985) 913–922.
- [785] P. Schofield, Space-time correlation function formalism for slow neutron scattering, *Physical Review Letters* 4 (1960) 239–240.
- [786] A. Borysow, L. Frommhold, Collision-induced Rototranslational Absorption Spectra of  $N_2$ - $N_2$  Pairs for Temperatures from 50 to 300 K, *Astrophysical Journal* 311 (1986) 1043.

- [787] E. A. Serov, A. A. Balashov, M. Y. Tretyakov, T. A. Odintsova, M. A. Koshelev, D. N. Chistikov, A. A. Finenko, S. E. Lokshantov, S. V. Petrov, A. A. Vigasin, Continuum absorption of millimeter waves in nitrogen, *Journal of Quantitative Spectroscopy and Radiative Transfer* 242 (2020) 106774.
- [788] A. I. Meshkov, F. C. De Lucia, Laboratory measurements of dry air atmospheric absorption with a millimeter wave cavity ringdown spectrometer, *Journal of Quantitative Spectroscopy and Radiative Transfer* 108 (2007) 256–276.
- [789] B. Maté, C. L. Lugez, A. M. Solodov, G. T. Fraser, W. J. Lafferty, Investigation of the collision-induced absorption by O<sub>2</sub> near 6.4  $\mu\text{m}$  in pure O<sub>2</sub> and O<sub>2</sub>–N<sub>2</sub> mixtures, *Journal of Geophysical Research Atmospheres* 105 (2000) 22225–22230.
- [790] D. V. Oparin, N. N. Filippov, I. M. Grigoriev, A. P. Kouzov, Effect of stable and metastable dimers on collision-induced rototranslational spectra: Carbon dioxide - rare gas mixtures, *Journal of Quantitative Spectroscopy and Radiative Transfer* 196 (2017) 87–93.
- [791] M. Turbet, H. Tran, O. Pirali, F. Forget, C. Boulet, J. M. Hartmann, Far infrared measurements of absorptions by CH<sub>4</sub>+CO<sub>2</sub> and H<sub>2</sub>+CO<sub>2</sub> mixtures and implications for greenhouse warming on early Mars, *Icarus* 321 (2019) 189–199.
- [792] M. Turbet, C. Boulet, T. Karman, Measurements and semi-empirical calculations of CO<sub>2</sub>+CH<sub>4</sub> and CO<sub>2</sub>+H<sub>2</sub> collision-induced absorption across a wide range of wavelengths and temperatures. Application for the prediction of early Mars surface temperature, *Icarus* 346 (2020) 113762.
- [793] D. Mondelain, C. Boulet, J. M. Hartmann, The binary absorption coefficients for H<sub>2</sub>+CO<sub>2</sub> mixtures in the 2.12-2.35  $\mu\text{m}$  spectral region determined by CRDS and by semi-empirical calculations, *Journal of Quantitative Spectroscopy and Radiative Transfer* 260 (2021) 107454.



- [794] A. A. Finenko, I. E. Gordon, D. N. Chistikov, E. K. Conway, S. E. Lokshtanov, Y. N. Kalugina, S. V. Petrov, A. A. Vigasin, Trajectory-based simulation of  $\text{CH}_4\text{--N}_2$  collision-induced band profiles relevant to the atmosphere of Titan, in: AGU Fall Meeting Abstracts, 2020, pp. P067–0013. URL: <https://agu.confex.com/agu/fm20/webprogram/Paper686857.html>, american Geophysical Union 2020 Fall Meeting (San Francisco, CA, 1-17 Dec 2020).
- [795] A. Banerjee, J. Mandon, F. Harren, D. H. Parker, Collision-induced absorption between  $\text{O}_2\text{--CO}_2$  for the  $a^1\Delta_g(v=1) \leftarrow X^3\Sigma_g^-(v=0)$  transition of molecular oxygen at 1060 nm, Physical Chemistry Chemical Physics (Incorporating Faraday Transactions) 21 (2019) 1805–1811.
- [796] D. Mondelain, S. Kassi, A. Campargue, Accurate Laboratory Measurement of the  $\text{O}_2$  Collision-Induced Absorption Band Near  $1.27\text{ }\mu\text{m}$ , Journal of Geophysical Research: Atmospheres 124 (2019) 414–423.
- [797] G. Thomas, K. Stamnes, Radiative Transfer in the Atmosphere and Ocean, Cambridge University Press, Cambridge, 1999. URL: <http://www.cambridge.org/us/academic/subjects/earth-and-environmental-science/atmospheric-science-and-meteorology/radiative-transfer-atmosphere-and-ocean>. doi:10.1063/1.1333301.
- [798] G. Brasseur, S. Solomon, Aeronomy of the Middle Atmosphere, Springer, Dordrecht, 2005. URL: <http://www.springer.com/la/book/9781402032844>. doi:10.1007/1-4020-3824-0.
- [799] R. Fenn, S. Clough, W. Gallery, R. Good, F. Kneizys, J. Mill, L. Rothman, E. Shettle, Optical and infrared properties of the atmosphere, in: A. Jursa (Ed.), Handbook of geophysics and the space environment, National Technical Information Service, Springfield, 1985, p. 1038. URL: [ntrl.ntis.gov/NTRL/dashboard/searchResults/titleDetail/ADA167000.xhtml](http://ntrl.ntis.gov/NTRL/dashboard/searchResults/titleDetail/ADA167000.xhtml).

- [800] H. D. Downing, D. Williams, Optical constants of water in the infrared, *Journal of Geophysical Research* 80 (1975) 1656–1661.
- [801] R. Wagner, S. Benz, O. Möhler, H. Saathoff, M. Schnaiter, U. Schurath, Mid-infrared Extinction Spectra and Optical Constants of Supercooled Water Droplets, *Journal of Physical Chemistry A* 109 (2005) 7099–7112.
- [802] S. G. Warren, R. E. Brandt, Optical constants of ice from the ultraviolet to the microwave: A revised compilation, *Journal of Geophysical Research* 113 (2008) D14220.
- [803] M. L. Clapp, D. R. Worsnop, R. E. Miller, Frequency-dependent optical constants of water ice obtained directly from aerosol extinction spectra, *Journal of Physical Chemistry* 99 (1995) 6317–6326.
- [804] R. T. Tisdale, D. L. Glandorf, M. A. Tolbert, O. B. Toon, Infrared optical constants of low-temperature  $\text{H}_2\text{SO}_4$  solutions representative of stratospheric sulfate aerosols, *Journal of Geophysical Research: Atmospheres* 103 (1998) 25353–25370.
- [805] C. E. Lund Myhre, D. H. Christensen, F. M. Nicolaisen, C. J. Nielsen, Spectroscopic Study of Aqueous  $\text{H}_2\text{SO}_4$  at Different Temperatures and Compositions: Variations in Dissociation and Optical Properties, *Journal of Physical Chemistry A* 107 (2003) 1979–1991.
- [806] C. E. Lund Myhre, H. Grothe, A. A. Gola, C. J. Nielsen, Optical Constants of  $\text{HNO}_3/\text{H}_2\text{O}$  and  $\text{H}_2\text{SO}_4/\text{HNO}_3/\text{H}_2\text{O}$  at Low Temperatures in the Infrared Region, *Journal of Physical Chemistry A* 109 (2005) 7166–7171.
- [807] R. F. Niedziela, R. E. Miller, D. R. Worsnop, Temperature- and Frequency-Dependent Optical Constants for Nitric Acid Dihydrate from Aerosol Spectroscopy, *Journal of Physical Chemistry A* 102 (1998) 6477–6484.

- [808] L. J. Richwine, M. L. Clapp, R. E. Miller, D. R. Worsnop, Complex refractive indices in the infrared of nitric acid trihydrate aerosols, *Geophysical Research Letters* 22 (1995) 2625–2628.
- [809] O. B. Toon, M. A. Tolbert, B. G. Koehler, A. M. Middlebrook, J. Jordan, Infrared optical constants of H<sub>2</sub>O ice, amorphous nitric acid solutions, and nitric acid hydrates, *Journal of Geophysical Research* 99 (1994) 25631.
- [810] R. Wagner, T. Ajtai, K. Kandler, K. Lieke, C. Linke, T. Müller, M. Schnaiter, M. Vragel, Complex refractive indices of Saharan dust samples at visible and near UV wavelengths: a laboratory study, *Atmospheric Chemistry and Physics* 12 (2012) 2491–2512.
- [811] R. Grainger, D. Peters, G. Thomas, A. Smith, R. Siddans, E. Carboni, A. Dudhia, Measuring Volcanic Plume and Ash Properties from Space. In: *Remote Sensing of Volcanoes and Volcanic Processes: Integrating Observation and Modeling* (Pyle D, Mather T, edit.), Special Publ Geo Soc (2013).
- [812] A. Deguine, D. Petitprez, L. Clarisse, S. Gudmundsson, V. Outes, G. Villarosa, H. Herbin, Complex refractive index of volcanic ash aerosol in the infrared, visible, and ultraviolet, *Applied Optics* 59 (2020) 884.
- [813] P. F. Liu, N. Abdelmalki, H.-M. Hung, Y. Wang, W. H. Brune, S. T. Martin, Ultraviolet and visible complex refractive indices of secondary organic material produced by photooxidation of the aromatic compounds toluene and m-xylene, *Atmospheric Chemistry and Physics* 15 (2015) 1435–1446.
- [814] P. Liu, Y. Zhang, S. T. Martin, Complex Refractive Indices of Thin Films of Secondary Organic Materials by Spectroscopic Ellipsometry from 220 to 1200 nm, *Environmental Science & Technology* 47 (2013) 13594–13601.
- [815] C. E. Lund Myhre, C. J. Nielsen, Optical properties in the UV and

visible spectral region of organic acids relevant to tropospheric aerosols, *Atmospheric Chemistry and Physics* 4 (2004) 1759–1769.

- [816] D. T. L. Alexander, P. A. Crozier, J. R. Anderson, Brown Carbon Spheres in East Asian Outflow and Their Optical Properties, *Science* 321 (2008) 833–836.
- [817] R. A. Sutherland, R. K. Khanna, Optical Properties of Organic-based Aerosols Produced by Burning Vegetation, *Aerosol Science and Technology* 14 (1991) 331–342.
- [818] B. I. Magi, Q. Fu, J. Redemann, A methodology to retrieve self-consistent aerosol optical properties using common aircraft measurements, *Journal of Geophysical Research* 112 (2007) D24S12.
- [819] B. Stagg, T. Charalampopoulos, Refractive indices of pyrolytic graphite, amorphous carbon, and flame soot in the temperature range 25° to 600°C, *Combustion and Flame* 94 (1993) 381–396.
- [820] H. Chang, T. T. Charalampopoulos, Determination of the Wavelength Dependence of Refractive Indices of Flame Soot, *Proceedings of the Royal Society A: Mathematical, Physical and Engineering Sciences* 430 (1990) 577–591.
- [821] M. Query, Optical constants of minerals and other materials from the millimeter to the ultraviolet, Technical Report, Chemical Research Development and Engineering Center, Aberdeen: Chemical Research, Development Engineering Center, CRDEC-CR-88009, 1987. URL: <https://apps.dtic.mil/sti/citations/ADA192210>.
- [822] O. B. Toon, J. B. Pollack, C. Sagan, Physical properties of the particles composing the Martian dust storm of 1971-1972, *Icarus* 30 (1977) 663–696.
- [823] B. Khare, C. Sagan, E. Arakawa, F. Suits, T. Callcott, M. Williams, Optical constants of organic tholins produced in a simulated Titanian

- atmosphere: From soft x-ray to microwave frequencies, *Icarus* 60 (1984) 127–137.
- [824] S. Ramirez, I. Coll, A. da Silva, R. Navarro-Gonzalez, J. Lafait, F. Raulin, Complex Refractive Index of Titan’s Aerosol Analogues in the 200–900 nm Domain, *Icarus* 156 (2002) 515–529.
  - [825] H. Imanaka, D. P. Cruikshank, B. N. Khare, C. P. McKay, Optical constants of Titan tholins at mid-infrared wavelengths (2.5–25  $\mu\text{m}$ ) and the possible chemical nature of Titan’s haze particles, *Icarus* 218 (2012) 247–261.
  - [826] T. Henning, H. Mutschke, Low-temperature infrared properties of cosmic dust analogues., *Astronomy & Astrophysics* 327 (1997) 743–754.
  - [827] S. Zeidler, T. Posch, H. Mutschke, Optical constants of refractory oxides at high temperatures, *Astronomy & Astrophysics* 553 (2013) A81.
  - [828] B. Begemann, J. Dorschner, T. Henning, H. Mutschke, J. Gurtler, C. Kompe, R. Nass, Aluminum Oxide and the Opacity of Oxygen-rich Circumstellar Dust in the 12–17 Micron Range, *Astrophysical Journal* 476 (1997) 199–208.
  - [829] T. Henning, B. Begemann, H. Mutschke, J. Dorschner, Optical properties of oxide dust grains., *Astronomy & Astrophysics Supplement Series* 112 (1995) 143–149.
  - [830] T. Posch, F. Kerschbaum, D. Fabian, H. Mutschke, J. Dorschner, A. Tamanai, T. Henning, Infrared Properties of Solid Titanium Oxides: Exploring Potential Primary Dust Condensates, *Astrophysical Journal Supplement Series* 149 (2003) 437–445.
  - [831] L. A. G. of the AIU Jena, Database of Optical Constants for Cosmic Dust, Unpublished data, 2012. URL: <http://www.astro.uni-jena.de/Laboratory/OCDB/mgfeoxides.html{\#}C>.

- [832] L. A. G. of the AIU Jena, Database of Optical Constants for Cosmic Dust, Unpublished data, 2012. URL: <http://www.astro.uni-jena.de/Laboratory/OCDB/crsilicates.html{#}C>.
- [833] D. Fabian, T. Henning, C. Jäger, H. Mutschke, J. Dorschner, O. Wehrhan, Steps toward interstellar silicate mineralogy, *Astronomy & Astrophysics* 378 (2001) 228–238.
- [834] D. Fabian, T. Posch, H. Mutschke, F. Kerschbaum, J. Dorschner, Infrared optical properties of spinels, A study of the carrier of the 13, 17 and 32 micron emission features observed in ISO-SWS spectra of oxygen-rich AGB stars., *Astronomy & Astrophysics* 373 (2001) 1125–1138.
- [835] C. Jäger, J. Dorschner, H. Mutschke, T. Posch, T. Henning, Steps toward interstellar silicate mineralogy VII. Spectral properties and crystallization behaviour of magnesium silicates produced by the sol-gel method., *Astronomy & Astrophysics* 408 (2003) 193–204.
- [836] S. Zeidler, T. Posch, H. Mutschke, H. Richter, O. Wehrhan, Near-infrared absorption properties of oxygen-rich stardust analogs: The influence of coloring metal ions., *Astronomy & Astrophysics* 526 (2011) A68.
- [837] T. Posch, F. Kerschbaum, H. Mutschke, D. Fabian, D. Clément, J. Dorschner, Features of oxide dust particles in circumstellar shells of AGB stars, in: *Exploiting the ISO Data Archive, Infrared Astronomy in the Internet Age*, Sigüenza, Spain, June 24-27, 2002, p. 14. URL: <http://adsabs.harvard.edu/abs/2003ESASP.511..141P>.
- [838] L. Kou, D. Labrie, P. Chylek, Refractive indices of water and ice in the 0.65- to 2.5- $\mu$ m spectral range, *Applied Optics* 32 (1993) 3531.
- [839] A. Sinyuk, O. Torres, O. Dubovik, Combined use of satellite and surface observations to infer the imaginary part of refractive index of Saharan dust, *Geophysical Research Letters* 30 (2003).

- [840] J. H. Dingle, S. Zimmerman, A. L. Frie, J. Min, H. Jung, R. Bahreini, Complex refractive index, single scattering albedo, and mass absorption coefficient of secondary organic aerosols generated from oxidation of biogenic and anthropogenic precursors, *Aerosol Science and Technology* 53 (2019) 449–463.
- [841] K. J. Zarzana, D. O. De Haan, M. A. Freedman, C. A. Hasenkopf, M. A. Tolbert, Optical Properties of the Products of  $\alpha$ -Dicarbonyl and Amine Reactions in Simulated Cloud Droplets, *Environmental Science & Technology* 46 (2012) 4845–4851.
- [842] R. F. Niedziela, M. L. Norman, C. L. DeForest, R. E. Miller, D. R. Worsnop, A Temperature- and Composition-Dependent Study of  $\text{H}_2\text{SO}_4$  Aerosol Optical Constants Using Fourier Transform and Tunable Diode Laser Infrared Spectroscopy, *Journal of Physical Chemistry A* 103 (1999) 8030–8040.
- [843] U. M. Biermann, B. P. Luo, T. Peter, Absorption Spectra and Optical Constants of Binary and Ternary Solutions of  $\text{H}_2\text{SO}_4$ ,  $\text{HNO}_3$ , and  $\text{H}_2\text{O}$  in the Mid Infrared at Atmospheric Temperatures, *Journal of Physical Chemistry A* 104 (2000) 783–793.
- [844] K. F. Palmer, D. Williams, Optical Constants of Sulfuric Acid; Application to the Clouds of Venus?, *Applied Optics* 14 (1975) 208.
- [845] M. L. Norman, J. Qian, R. E. Miller, D. R. Worsnop, Infrared complex refractive indices of supercooled liquid  $\text{HNO}_3/\text{H}_2\text{O}$  aerosols, *Journal of Geophysical Research: Atmospheres* 104 (1999) 30571–30584.
- [846] M. R. Query, I. L. Tyler, Reflectance and complex refractive indices in the infrared for aqueous solutions of nitric acid, *Journal of Chemical Physics* 72 (1980) 2495–2499.
- [847] E. E. Remsberg, D. Lavery, B. Crawford, Optical constants for sulfuric

- and nitric acids, *Journal of Chemical & Engineering Data* 19 (1974) 263–265.
- [848] C. A. Hasenkopf, M. R. Beaver, M. G. Trainer, H. Langley Dewitt, M. A. Freedman, O. B. Toon, C. P. McKay, M. A. Tolbert, Optical properties of Titan and early Earth haze laboratory analogs in the mid-visible, *Icarus* 207 (2010) 903–913.
  - [849] C. Bohren, D. Huffman, *Absorption and Scattering of Light by Small Particles.*, John Wiley and Sons, New York, 1983. doi:10.1002/9783527618156.
  - [850] H. R. Wakeford, D. K. Sing, Transmission spectral properties of clouds for hot Jupiter exoplanets, *Astronomy & Astrophysics* 573 (2015) A122.
  - [851] S. Massie, M. Hervig, HITRAN 2012 refractive indices, *Journal of Quantitative Spectroscopy and Radiative Transfer* 130 (2013) 373–380.
  - [852] F. M. Skinner, I. E. Gordon, C. Hill, R. J. Hargreaves, K. E. Lockhart, L. S. Rothman, Referencing Sources of Molecular Spectroscopic Data in the Era of Data Science: Application to the HITRAN and AMBDAS Databases, *Atoms* 8 (2020) 16.
  - [853] C. R. Harris, K. J. Millman, S. J. van der Walt, R. Gommers, P. Virtanen, D. Cournapeau, E. Wieser, J. Taylor, S. Berg, N. J. Smith, R. Kern, M. Picus, S. Hoyer, M. H. van Kerkwijk, M. Brett, A. Haldane, J. F. del Río, M. Wiebe, P. Peterson, P. Gérard-Marchant, K. Sheppard, T. Reddy, W. Weckesser, H. Abbasi, C. Gohlke, T. E. Oliphant, Array programming with NumPy, *Nature* 585 (2020) 357–362.
  - [854] H. Tran, N. H. Ngo, J. M. Hartmann, Efficient computation of some speed-dependent isolated line profiles, *Journal of Quantitative Spectroscopy and Radiative Transfer* 129 (2013) 199–203.
  - [855] H. Tran, N. H. Ngo, J. M. Hartmann, Erratum to “Efficient computation of some speed-dependent isolated line profiles” [ *J. Quant. Spectrosc. Ra-*



- diat. Transfer 129 (2013) 199-203], Journal of Quantitative Spectroscopy and Radiative Transfer 134 (2014) 104–104.
- [856] S. A. Clough, M. J. Iacono, J.-L. Moncet, Line-by-line calculations of atmospheric fluxes and cooling rates: Application to water vapor, Journal of Geophysical Research: Atmospheres 97 (1992) 15761–15785.
  - [857] E. J. Mlawer, V. H. Payne, J. L. Moncet, J. S. Delamere, M. J. Alvarado, D. C. Tobin, Development and recent evaluation of the MT\_CKD model of continuum absorption, Philosophical Transactions of the Royal Society of London Series A 370 (2012) 2520–2556.
  - [858] D. Paynter, V. Ramaswamy, Investigating the impact of the shortwave water vapor continuum upon climate simulations using GFDL global models, Journal of Geophysical Research: Atmospheres 119 (2014) 10720–10737.
  - [859] E. A. Serov, T. A. Odintsova, M. Y. Tretyakov, V. E. Semenov, On the origin of the water vapor continuum absorption within rotational and fundamental vibrational bands, Journal of Quantitative Spectroscopy and Radiative Transfer 193 (2017) 1–12.
  - [860] A. A. Vigasin, Water vapor continuum: Whether collision-induced absorption is involved?, Journal of Quantitative Spectroscopy and Radiative Transfer 148 (2014) 58–64.
  - [861] S. A. Clough, F. X. Kneizys, R. W. Davies, Line shape and the water vapor continuum, Atmospheric Research 23 (1989) 229–241.
  - [862] Y. Baranov, W. Lafferty, The water-vapor continuum and selective absorption in the 3–5  $\mu\text{m}$  spectral region at temperatures from 311 to 363K, Journal of Quantitative Spectroscopy and Radiative Transfer 112 (2011) 1304–1313.
  - [863] I. V. Ptashnik, R. A. McPheat, K. P. Shine, K. M. Smith, R. G. Williams, Water vapor self-continuum absorption in near-infrared windows derived

- from laboratory measurements, *Journal of Geophysical Research* 116 (2011) D16305.
- [864] Y. I. Baranov, The continuum absorption in  $\text{H}_2\text{O}+\text{N}_2$  mixtures in the 2000–3250  $\text{cm}^{-1}$  spectral region at temperatures from 326 to 363 K, *Journal of Quantitative Spectroscopy and Radiative Transfer* 112 (2011) 2281–2286.
- [865] Y. I. Baranov, W. J. Lafferty, The water vapour self-and water-nitrogen continuum absorption in the 1000 and 2500  $\text{cm}^{-1}$  atmospheric windows, *Philosophical Transactions of the Royal Society A: Mathematical, Physical and Engineering Sciences* 370 (2012) 2578–2589.
- [866] I. V. Ptashnik, R. A. McPheat, K. P. Shine, K. M. Smith, R. Gary Williams, Water vapour foreign-continuum absorption in near-infrared windows from laboratory measurements, *Philosophical Transactions of the Royal Society A: Mathematical, Physical and Engineering Sciences* 370 (2012) 2557–2577.
- [867] I. V. Ptashnik, T. E. Klimeshina, A. A. Solodov, A. A. Vigasin, Spectral composition of the water vapour self-continuum absorption within 2.7 and 6.25  $\mu\text{m}$  bands, *Journal of Quantitative Spectroscopy and Radiative Transfer* 228 (2019) 97–105.
- [868] M. Birk, G. Wagner, J. Loos, K. P. Shine, 3  $\mu\text{m}$  Water vapor self- and foreign-continuum: New method for determination and new insights into the self-continuum, *Journal of Quantitative Spectroscopy and Radiative Transfer* 253 (2020) 107134.
- [869] A. Campargue, S. Kass, D. Mondelain, S. Vasilchenko, D. Romanini, Accurate laboratory determination of the near-infrared water vapor self-continuum: A test of the MT\_CKD model, *Journal of Geophysical Research: Atmospheres* 121 (2016) 13180–13203.

- [870] L. Lechevallier, S. Vasilchenko, R. Grilli, D. Mondelain, D. Romanini, A. Campargue, The water vapour self-continuum absorption in the infrared atmospheric windows: new laser measurements near 3.3 and 2.0  $\mu\text{m}$ , *Atmospheric Measurement Techniques* 11 (2018) 2159–2171.
- [871] D. Mondelain, A. Aradj, S. Kassi, A. Campargue, The water vapour self-continuum by CRDS at room temperature in the 1.6  $\mu\text{m}$  transparency window, *Journal of Quantitative Spectroscopy and Radiative Transfer* 130 (2013) 381–391.
- [872] D. Mondelain, S. Manigand, S. Kassi, A. Campargue, Temperature dependence of the water vapor self-continuum by cavity ring-down spectroscopy in the 1.6  $\mu\text{m}$  transparency window, *Journal of Geophysical Research: Atmospheres* 119 (2014) 5625–5639.
- [873] D. Mondelain, S. Vasilchenko, P. Čermák, S. Kassi, A. Campargue, The self- and foreign-absorption continua of water vapor by cavity ring-down spectroscopy near 2.35  $\mu\text{m}$ , *Physical Chemistry Chemical Physics (Incorporating Faraday Transactions)* 17 (2015) 17762–17770.
- [874] T. A. Odintsova, M. Y. Tretyakov, O. Pirali, P. Roy, Water vapor continuum in the range of rotational spectrum of  $\text{H}_2\text{O}$  molecule: New experimental data and their comparative analysis, *Journal of Quantitative Spectroscopy and Radiative Transfer* 187 (2017) 116–123.
- [875] T. A. Odintsova, M. Y. Tretyakov, A. O. Zibarova, O. Pirali, P. Roy, A. Campargue, Far-infrared self-continuum absorption of  $\text{H}_2^{16}\text{O}$  and  $\text{H}_2^{18}\text{O}$  (15–500  $\text{cm}^{-1}$ ), *Journal of Quantitative Spectroscopy and Radiative Transfer* 227 (2019) 190–200.
- [876] S. Vasilchenko, A. Campargue, S. Kassi, D. Mondelain, The water vapour self- and foreign-continua in the 1.6  $\mu\text{m}$  and 2.3  $\mu\text{m}$  windows by CRDS at room temperature, *Journal of Quantitative Spectroscopy and Radiative Transfer* 227 (2019) 230–238.

- [877] K. P. Shine, A. Campargue, D. Mondelain, R. A. McPheat, I. V. Ptashnik, D. Weidmann, The water vapour continuum in near-infrared windows - Current understanding and prospects for its inclusion in spectroscopic databases, *Journal of Molecular Spectroscopy* 327 (2016) 193–208.
- [878] D. J. Paynter, V. Ramaswamy, An assessment of recent water vapor continuum measurements upon longwave and shortwave radiative transfer, *Journal of Geophysical Research: Atmospheres* 116 (2011) D20302.
- [879] J. C. Mast, M. G. Mlynczak, R. P. Cageao, D. P. Kratz, H. Latvakoski, D. G. Johnson, D. D. Turner, E. J. Mlawer, Measurements of downwelling far-infrared radiance during the RHUBC-II campaign at Cerro Toco, Chile and comparisons with line-by-line radiative transfer calculations, *Journal of Quantitative Spectroscopy and Radiative Transfer* 198 (2017) 25–39.
- [880] R. Rizzi, T. Maestri, C. Arosio, Estimate of Radiosonde Dry Bias From Far-Infrared Measurements on the Antarctic Plateau, *Journal of Geophysical Research: Atmospheres* 123 (2018) 3205–3211.
- [881] T. A. Odintsova, M. Y. Tretyakov, A. A. Simonova, I. V. Ptashnik, O. Pirali, A. Campargue, Measurement and temperature dependence of the water vapor self-continuum between 70 and 700  $\text{cm}^{-1}$ , *Journal of Molecular Structure* 1210 (2020) 128046.
- [882] H. Dekker, S. D’Odorico, A. Kaufer, B. Delabre, H. Kotzlowski, Design, construction, and performance of UVES, the echelle spectrograph for the UT2 Kueyen Telescope at the ESO Paranal Observatory, in: M. Iye, A. F. Moorwood (Eds.), *Optical and IR Telescope Instrumentation and Detectors*, volume 4008 of *Society of Photo-Optical Instrumentation Engineers (SPIE) Conference Series*, 2000, pp. 534–545. doi:10.1117/12.395512.

## Appendix A. Abbreviations

When describing the inclusion of data into HITRAN, the following abbreviations, acronyms and initialisms have been used at various points throughout the article:

- 4TR – Four-temperature range
- ABSCO – Absorption coefficient [314]
- ACE – Atmospheric Chemistry Experiment [20]
- API – Application programming interface
- ARIEL – Atmospheric Remote-sensing Infrared Exoplanet Large-survey [46]
- ARTS – Atmospheric Radiative Transfer Simulator [30]
- ASCII – American standard code for information interchange
- CCSD(T) – Coupled-cluster singles, doubles, and perturbative triples
- CDMS – Cologne Database for Molecular Spectroscopy [335]
- CDSD – Carbon Dioxide Spectroscopic Database [135]
- CFC – Chlorofluorocarbon
- CIA – Collision-induced absorption
- CLS – Canadian Light Source
- CRDS – Cavity ring-down spectroscopy
- DLR – Deutsches Zentrum für Luft und Raumfahrt (German Aerospace Center)
- DMS – Dipole moment surface
- DOI – Digital object identifier

- DPL – Double-power law
- EDTM – Effective dipole transition moment
- EH – Effective Hamiltonian
- EPG – Exponential power gap
- ESA – European Space Agency
- FIR – Far-infrared
- FORUM – Far-infrared Outgoing Radiation Understanding and Monitoring [23]
- FTIR – Fourier transform infrared
- FTS – Fourier transform spectrometer
- GARLIC – Generic Atmospheric Radiation Line-by-line Infrared Code [31]
- GeCaSDa – Germane Calculated Spectroscopic Database [581]
- GEISA – Gestion et Etude des Informations Spectroscopiques Atmospheriques (Management and Study of Atmospheric Spectroscopic Information) [405]
- GEMS – Geostationary Environment Monitoring Spectrometer [22]
- GENLN – General Line-by-line Atmospheric Transmittance and Radiance Model [28]
- GOSAT – Greenhouse Gases Observing Satellite [19]
- HAPI – HITRAN Application Programming Interface [51]
- HAPIEST – HITRAN Application Programming Interface and Efficient Spectroscopic Tools
- HCFC – Hydrochlorofluorocarbon
- HDF-5 – Hierarchical Data Format version 5

- HITRAN – High-resolution transmission molecular absorption database [15]
- HITEMP – High-temperature molecular spectroscopic database [52]
- HR – High-resolution
- HT – Hartmann–Tran
- HTTPS – Hypertext transfer protocol secure
- IAO – Institute of Atmospheric Optics
- IASI – Infrared Atmospheric Sounding Interferometer [185]
- ICB – Laboratoire de l’Université de Bourgogne
- IDL – Interactive Design Language
- IR – Infrared
- JIRAM – Jovian Infrared Auroral Mapper [630]
- JPL – Jet Propulsion Laboratory
- JSON – JavaScript Object Notation
- JWST – James Webb Space Telescope [45]
- LBL – Line-by-line
- LBLRTM – Line-by-line Radiative Transfer Model [26]
- LERMA – Laboratoire d’étude du rayonnement et de la matière en astrophysique
- LIDAR – Light detection and ranging
- LISA – Laboratoire Interuniversitaire des Systèmes Atmosphériques
- MARVEL – Measured Active Rotational-Vibrational Energy Levels [57, 58]

- MATS – Multi-spectrum analysis tool for spectroscopy [236]
- MCRB – Modified complex Robert–Bonamy
- MIR – Mid-infrared
- MODTRAN – Moderate resolution atmospheric transmission code [27]
- MT\_CKD – Mlawer-Tobin Clough-Kneizys-Davies [857]
- MW – Microwave
- NASA – National Aeronautics and Space Administration
- NDSD-1000 – Nitrogen Dioxide Spectroscopic Data Bank at 1000 K [386, 387]
- NEMESIS – Non-linear optimal estimator for multivariate spectral analysis [34]
- netCDF – Network common data form
- NIR – Near-infrared
- NIST – National Institute of Standards and Technology
- NMHC – Non-methane hydrocarbon
- NOSD-1000 – Nitrous Oxide Spectroscopic Data Bank at 1000 K [241]
- NSO – National Solar Observatory
- OCO – Orbiting Carbon Observatory [16, 17]
- ODU – Old Dominion University
- ORM – Object-relational mapping
- PES – Potential energy surface
- PNNL – Pacific Northwest National Laboratory



- PSC – Polar stratospheric cloud
- PSG – Planetary Spectrum Generator [36]
- rCMDS – Requantized Classical Molecular Dynamics Simulation
- REST API – Representational state transfer application programming interface
- RFM – Reference Forward Model [29]
- RI – Refractive indices
- RKR – Rydberg–Klein–Rees
- RMS – Root mean square
- RT – Rototranslational
- S&MPO – Spectroscopy and Molecular Properties of Ozone [192]
- SB RAS - Siberian Branch, Russian Academy of Sciences
- SDV – Speed-dependent Voigt
- SEOM-IAS – Scientific Exploitation of Operational Missions — Improved Atmospheric Spectroscopy Databases
- SHeCaSDa – Sulfur Hexafluoride Calculated Spectroscopic Database [581]
- SNR – Signal to noise ratio
- SOA – Secondary organic aerosol
- SRP – Standard reference photometer
- TCCON – Total Carbon Column Observing Network [145, 146]
- TEMPO – Tropospheric Emissions: Monitoring of Pollution [24]
- TES – Tropospheric Emission Spectrometer [18]

- TFMeCaSDa – TetraFluoro-Methane Calculated Spectroscopic Database [581]
- TheoReTS – Theoretical Reims-Tomsk Spectral data [302]
- TIPS – Total Internal Partition Sums
- TROPOMI – Tropospheric Monitoring Instrument [21]
- UCL – University College London
- ULB – Université Libre de Bruxelles
- UV – Ultraviolet
- UVES – Ultraviolet-Visual Echelle Spectrograph [882]
- VAMDC – Virtual Atomic and Molecular Data Centre [634]
- VLIDORT – Vector Linearized Discrete Ordinate Radiative Transfer [33]
- VP – Voigt profile